Physics of Anisotropic Materials Under Pressure

Hung-Chung Hsueh

A thesis submitted in fulfilment of the requirements

for the degree of Doctor of Philosophy

to the

University of Edinburgh

1997

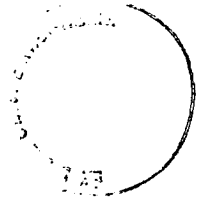

Abstract

The structural, vibrational, and electronic properties of anisotropic materials under compression are comprehensively investigated in this thesis. Recent developments in the techniques of high-pressure X-ray diffraction and Raman scattering, and significant advances in first principle simulations provide detailed high-pressure studies of condensed matter systems. In view of the widely disparate strength of cohesive forces, these studies consist of ionic compounds, quasi-two dimensional semiconductors, quasi-molecular solids, and end with liquid crystals. As a result of the coexistence of different heirarchical interactions in anisotropic systems, evidence of preferential pressure-induced enhancement of weak bonding is found not only in the structural response to external hydrostatic pressure but also in vibrational and electronic behaviour. Further, the understanding of pressure-induced breakdown of rigid-layer vibrations (explored in layered compounds), pressure-induced electron transfer in molecular crystals, and strong overlap of inter- and intra-molecular vibrational modes of liquid crystals provides insight into the essential physics of flexible molecular systems.

Declaration

This thesis has been composed by myself and it has not been submitted in any previous application for a degree. The work reported within was executed by me, unless otherwise stated.

March 1997

Acknowledgements

It is not possible for me to list all the people who encouraged and helped me during my studying and researching career. I apologise in advance for any omissions.

First of all, I want to thank my parents for their generous support in all aspects including finance. My great appreciation must also go to my supervisor, Dr. J. Crain, for his invaluable supervision, endless patience, and encouragement during my research and thesis writing. In addition, I would like to acknowledge to Prof. G. S. Pawley in Edinburgh, Dr. Simon C. Lin in Academia Sinica, and Prof. J. A. Lin in Tamkang University for enriching my essential physical concepts and inspiration.

During these last three years, I have also received helpful assistance and advice from outstanding experimentalists and theorists. I am especially indebted to Prof. R. J. Nelmes, Dr. M. I. McMahon, Dr. H. D. Liu, and Mr. S. A. Belmonte at the Daresbury SRS for their help with high-pressure X-ray experiments, and also to Dr. G. J. Ackland, Dr. S. J. Clark, Ms. M. C. Warren in Edinburgh, and Dr. M. H. Lee in Tamkang for their kind support on the pseudopotential scheme. I am also grateful to Mr. H. Vass in Edinburgh for his "magic" assistance in the Raman scattering laboratory.

Many thanks to Mrs. Eleanor McKirdy and Mr. J. R. Maclean for their warm friendship and constantly enthusiastic help for everything. Also, I appreciate the guys who enjoyed the exhausting badminton and basketball games with me. It was really good fun and healthy.

Finally, I would like to give my deep thanks to my dear wife, Huei-Ju. This thesis would not have been successful without her encouragement and understanding.

Contents

Chapter 1

Pressure Effects on Solids: Overview

1.1 Introduction

In thermodynamics, the equations of state of substances play an essential role connecting the macroscopic measurements and microscopic quantum mechanical models. All equations of state can be expressed in terms of the thermodynamical variables pressure, volume, and temperature. Temperature and pressure have been applied to materials to identify the energy state of a system for many years. However, the temperature factor is easily coupled with other intrinsic physical variables which complicates the thermal effects on systems. On the contrary, hydrostatic pressure furnishes a "clean" variable with which to explore the phase behaviour of materials. In addition to condensed matter science, high pressure studies have been also of sustained interest in geo and planetary physics where relevant pressures reach as much as several Mbar (1Mbar $= 10^6$ atm $= 10^{12}$ dyne/cm^2 = 100 Gigapascal (GPa)).

Recent progress in pressure equipment and techniques extended static pressure regimes to $\sim$ 5 Mbar [1] which already exceeds the pressure at the earth's centre ($\sim$

3.5 Mbar) and has provided a wide enough compression regime to explore phase transitions of all well-known elements and compounds [1]. On the other hand, recent advancement in computational schemes (with the support of increasing computer power) makes quantum-mechanical calculations for large scale electronic systems feasible. The application of the modern first principles calculations assists us in understanding material properties. Moreover, the marriage of new high-pressure experimental and computational technologies has led to successful interpretation of subtle pressure effects in many solids characterised predominately by isotropic bonding.

Nevertheless, for high pressure studies, there still exists a frontier – anisotropic materials which have not been systematically studied at pressure. Based on the mature high pressure methodologies pointed out above, the obstacles to studying anisotropic materials can be circumvented. Therefore, it is a suitable time and also the main goal of this thesis to perform extensive studies of anisotropic matter under compression.

1.2 Heirarchical Cohesion in Materials

The physical and chemical properties of substances under hydrostatic pressure are dominated by the nature of the interaction among individual basic constituents. Therefore, information on heirarchical cohesion is a vital background for understanding pressure effects on materials. In general, coupling can be categorised briefly in terms of the strength of cohesive forces as follows.

ionic bond: In an ionic crystal, like NaCl, the ions are coupled to each other by means of the transfer of electrons between cations and anions. Since the valence electrons associated with each ion are not appreciably distorted, the strong ionic bonding force is in essence contributed from the very long-range electrostatic Columbic attractive potential between heteropolar ions. The strength of this ionic bond is estimated to be about $7 \sim 16$ eV/molecule.

covalent bond: Covalent bonding arises from the sharing of valence charges between homopolar atoms. This interaction is due to the hybridisation of various electron orbitals between same species of atoms which then forms a directional bond to construct a covalent solid, such as diamond. The binding energy of the covalent bond mechanism can be calculated from its band structure and it is in the range of $5 \sim 12$ eV/molecule.

metallic bond: For the metallic elements, the valence electrons of atoms are easily released to form nearly-free electrons among metallic cores composed of a nucleus and inner electrons. Hence, the metal solid is built by nondirectional metallic bonds which hold the positively charged atom cores together by mutual attraction to free valence electrons. The strength of metallic bonds is about $1 \sim 8$ eV/molecule.

hydrogen bond: A hydrogen bond corresponds to a specific configuration in which a hydrogen atom is a joint connecting two ions together. Therefore, this asymmetric bond is characterised by partly covalent and partly ionic bonding type. The hydrogen bond plays a central role in ice crystals and the secondary structure of protein molecules and DNA molecules. The binding energy of this relatively weak cohesion is approximate 0.2 eV/molecule.

van der Waal's force: In the noble gases or molecular crystals, the gas atoms or identifiable molecular subunits are held together by van der Waal's forces which are due to the quantum-mechanical dipole fluctuations between polarised atoms or molecules. This long-range secondary attractive cohesion is proportional to the product of atomic polarisabilities and decays with interatomic or intermolecular distance as r^{-6}. The magnitude of van der Waal's attraction is of order ~ 0.1 eV/molecule.

thermal-Casimir force and exponential force: In conventional thermotropic liquid crystals, two secondary attractive forces, other than the van der Waal's force, have been reported recently [2]. As with van der Waal's interactions, the dipole-dipole interactions between the thermal fluctuation induced dipole moments of the liquid crystal molecules accounts for the long-range thermal-Casimir forces. Corresponding to different mesomorphic phases of liquid crystals, there exist the nematic- and the smectic-thermal-Casimir force. The strength of these forces is of the same order as that of van der Waal's force, however, it dies off as r^{-5} at large separation. Another effective force observed in phase transitions of liquid crystals is due to the surface-enhanced exponential decays of smectic the order parameter [3]. This effective force is therefore recognised as an exponentially decaying short-range force.

1.3 Generic Pressure Effects in Isotropic Semiconductors

The structure of isotropic crystals is predominately formed by a specific type of cohesion discussed previously. For instance, under ambient conditions, Silicon (Si) adopts a diamond structure. It is a typical isotropic tetrahedral semiconductor which is specified by a covalent bonding geometry. The hydrostatic pressure effects on Si can be represented by three characteristics: pressure-induced dense polymorphs, phonon-frequency shift, and metallisation.

From sensitive high-pressure structural determinations [4], diamond structure Si was found to undergo a phase transition to a more packed configuration with a six-fold β-Sn crystal structure at 125 kbar. However, the generic pressure-induced phase transition route in Si is more complicated with hysteresis effects which have been discussed in detail in some review works [5]. In addition, the vibrational character of diamond Si can be displayed in its Raman spectra at different pressure. It is found that the first-order Raman peaks, such as the mode at 520 cm^{-1}, shift linearly toward higher energy

with increasing hydrostatic pressure from ambient to 125 kbar [6] but without changing shape. This phenomena can be interpreted as the enhancement of strength of covalent bonds in Si by compression. Furthermore, the semiconductor electronic properties of ambient Si are also affected by the application of pressure. In fact, as the result of the resistivity measurements of Si during pressurisation process [7], a pressure-induced metallisation has been found and the Si with β-Sn structure corresponds to a metallic phase.

1.4 Anisotropic Materials under High Pressure

Many materials are formed or synthesised by condensing atoms or molecules in such a way that their structures are principally governed by a variety of bonding types. For example, a crystal of I_2 includes covalent bonds to hold two isolated iodines together and a weak intermolecular force to bond the individual molecules to form the crystalline structure. According to the admixture of heirarchical cohesion, the properties of these materials will show some degree of anisotropy at equilibrium. Further, this anisotropy is expected to be substantially enhanced by perturbations because of the different types of bonds. In view of the advantages of recently developed high pressure techniques, insight into manifold bonding forces can be obtained systematically by the application of compression to general anisotropic matters.

As with isotropic crystals, the influence of external pressure on anisotropic materials is reflected in structural, vibrational, and electronic properties. To obtain a comprehensive picture of compressional effects, both experimental and theoretical methods dedicated to high pressure investigations for anisotropic solids are employed in this thesis. Before exploring several case studies, an outline of well-established experimental techniques and devices for determining the structural details and zone-centre phonons of materials as a function of pressure is given in Chapter 2. The theoretical analysis methods are discussed in Chapter 3 which are used to perform the quantum-mechanical

calculations of structural stability and lattice dynamics of solids under high pressure.

From the consideration of macroscopic network dimensionality, the remainder of this thesis is organised as follows. In Chapter 4, the structural and electronic properties of the less anisotropic three-dimensional ionic semiconductor CuCl under hydrostatic compressional circumstance are discussed. It is shown that the calculated high-pressure polymorphism of this tetrahedral compound is consistent with experimental observations. Subsequently, anisotropic layered semiconductors are studied in Chapter 5 and 6. The structural and electronic responses to pressure of typical quasi-two-dimensional layered semiconductors, GeS and GeSe, are displayed in Chapter 5, whereas the extensive studies of pressure-dependent vibrational properties of these layered solids are presented in Chapter 6. To further explore pressure effects on highly anisotropic matter, examples of zero-dimensional quasi-molecular crystals of Group-V metal triiodides are given in the first part of Chapter 7. However, for a soft condensed matter system, such as a liquid crystal, correspondly rich phase behaviour can be achieved by applying relatively low pressure. The strength of the perturbation provided by this low pressure range is easily accessible in experiments. Therefore, in the second part of Chapter 7, the vibrational properties of liquid crystals are discussed, and the further extension of this research is given at the end of this thesis.

Chapter 2

High-Pressure Experimental Techniques

2.1 Introduction

The progressive developments of high pressure technology over last few decades provide a unique means by which to study materials because, generally, hydrostatic pressure offers a stronger and more direct perturbation on materials than does temperature. Under compression, the static and dynamic properties of materials will undergo a dramatic change such as pressure-induced volume collapse, phase transition, frequency shift of the vibrational spectra, etc.. In order to construct a high pressure environment, not only are specific devices which can bear high compression required but also mature high-pressure techniques are necessary. This chapter is concerned with the experimental techniques and equipment which are devoted to structural and vibrational studies under external hydrostatic pressure. The principles pressure devices will be highlighted in the following section.

2.2 Pressure Instrumentation and Calibration

The rich physical phenomena under pressure has attracted much attention from scientists for a long time. The more interesting pressure region is much higher than ambient pressure, therefore, the specific pressure equipment is necessary to support the high pressure investigations. Recently, significant improvements in the diamond anvil cell technique make the ultra-high pressure ($\sim$ Mbar) feasible and the diamond device is still at the forefront of modern compression technologies.

2.2.1 Diamond Anvil Cell (DAC)

Since the pioneering work using diamonds for high-pressure studies up to 20 kbar [8] the DAC has opened a fruitful field of high pressure science. The importance of the DAC is not only because diamond has a inherent high compressive strength but also because diamond possesses a natural wide transmission range to radiation sources. These characters of diamond guarantee the capabilities for ultra-high-pressure generation. After the innovations in DAC techniques, pressures up to a few Mbar can be produced for specific purposes. The rapid extension of the pressure range provides opportunities to tackle sophisticated studies of pressure-induced phase transitions and other high-pressure phenomena of materials.

The basic idea of the DAC is to use two diamond anvils to squeeze materials from opposite directions and the hydrostatic pressure is formed inside the materials. The generic arrangement of a DAC is shown in Fig. 2.1(a). In general, the diamond is cut specially to form a diamond anvil with a small culet face(the diameter about few hundreds μm) shown in Fig. 2.1(b). The shape and the area of culet face depends on the different type of DAC and determines the maximum pressure of the specific DAC. Research for higher pressure and large volume points to larger diamonds. On the contrary, the price and the purity of diamond will limit the size of itself. Some typical designs of DAC for different purposes are presented as follows.

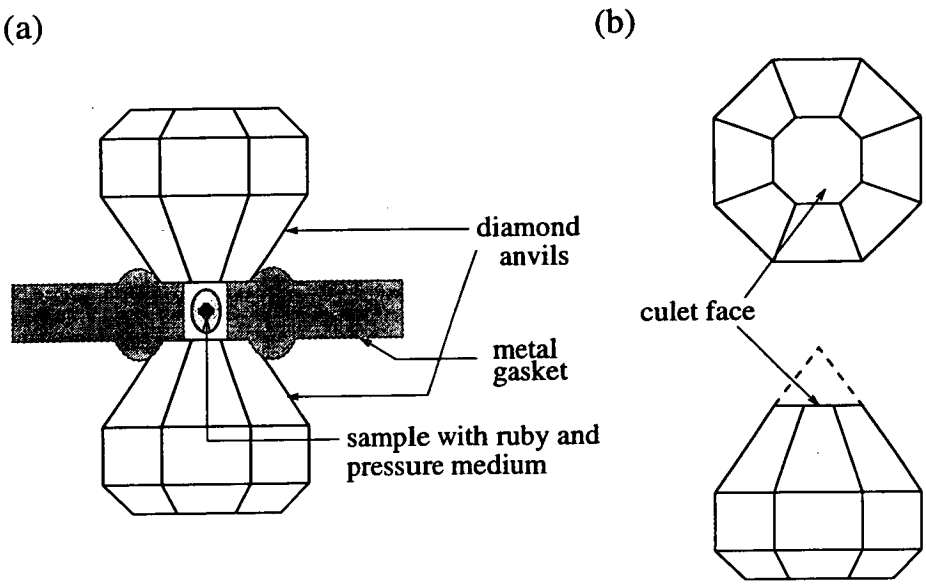

Figure 2.1. Schematic diagram of (a) DAC and (b) basic design a diamond anvil

Merrill-Bassett Cell

Based on similar design to the Bridgman anvil [9], the compact Merrill-Bassett cell [10] has been extensively used in high-pressure X-ray diffraction studies. As shown in Fig. 2.2(a), two diamond anvils are set in the beryllium (Be) supports which fit individually into two steel platens. The wide conical angle (100°) of this cell facilitates more data collection of angle-dispersive X-ray diffraction. After careful centering and alignment of diamonds, the sample is placed between anvils which can be pressurised by tightening the three symmetrically located (120° apart) screws. The Merrill-Bassett cell can be mounted easily on an X-ray goniometer head for an X-ray diffraction setup. The upper pressure limit of a standard Merrill-Bassett with 400 μm-diameter culet face is about 200 kbar.

DXR X-ray Cell

The arrangement of the DXR cell is similar to the Merrill-Bassett cell but a few improvements have been made. As shown in Fig. 2.2(b), this piston-cylinder type cell

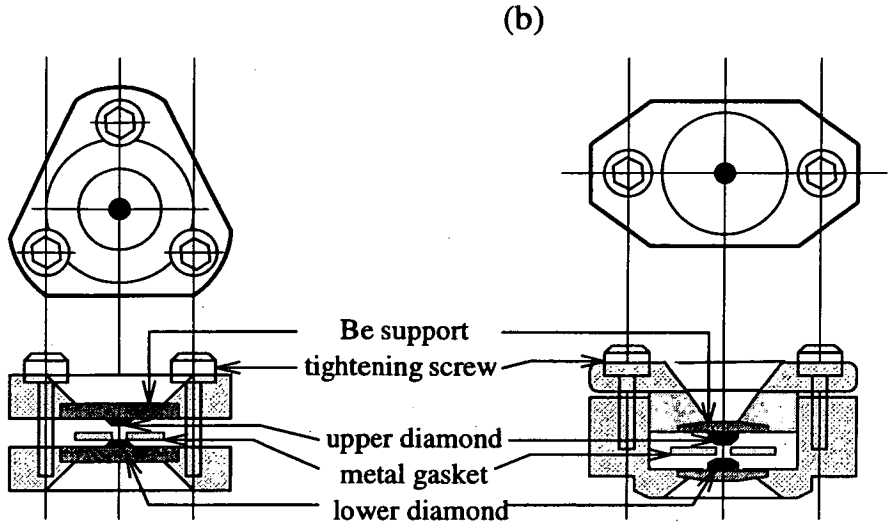

Figure 2.2. (a)Merrill-Bassett cell and (b) DXR X-ray cell

preserves diamond alignment easily during pressure increase. A further contribution comes from the new design of the Be backing plates which sustain a stronger stress and also make the light path equal within Be. Pressure is applied from the two symmetrically situated screws. Normally, pressures up to 300~400 kbar can be reached using a DXR cell with 400μm diameter diamonds.

Diacell B-05 Diamond Anvil Cell

This specific version of DAC is similar to a versatile pressure cell developed by Weir *et al.* [11]. For high-pressure spectroscopic measurements, type IIa diamonds (low fluorescence) with 500μm diameter culet face have been chosen to be the optical window of the Diacell B-05 DAC because of its highly transparent property over a wide spectral range. In Fig. 2.3, the applied force from the screwing knob can be transferred via the lever-arm to push the piston of the Diacell (shown in Fig. 2.3). This optical pressure cell has been tested as high as 500 kbar.

Different types of DAC have been built for various applications. For instance, the DAC for single crystal [12] and powder [13] X-ray diffraction, Raman scattering [14],

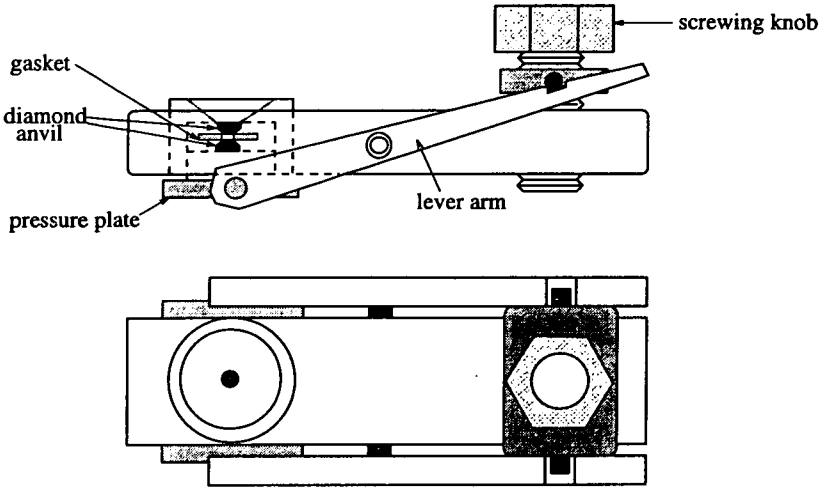

Figure 2.3. A cross-sectional view of Diacell B-05 DAC.

high-pressure measurements with thermal perturbation [15], etc. The details of DAC techniques can be found elsewhere [16, 17].

2.2.2 Pressure Transmitting Media and Metal Gasket

In order to generate uniform stress on the samples, a pressure-transmitting medium is needed to translate the uniaxial thrust into hydrostatic pressure. Considering the constraints of the pressure medium, such as chemical inertness, low compressibility, easy filling in gasket aperture, etc., some candidate organic fluid mixtures [18] and condensed gases [19] have been studied. It was found that a 4:1 methanol-ethanol mixture maintains pressure homogeneity when pressurised up to 200 kbar [18]. This pressure medium has been widely used for the last twenty years. However, many pressure media are not suitable for the samples with moisture sensitivity.

Beside the pressure transmitting fluid, the gasket is another auxiliary device in DACs. Before the use of metal gaskets, high-pressure studies only could be implemented in a DAC without a pressure medium and the pressure gradient in the sample was very high. Indeed, the lower pressure regions of sample around the edges of diamond culet

faces act as a supporting gasket for the central high-pressure area. The first metal gasket in the DAC was developed to maintain a hydrostatic medium within the sample space of the DAC. As depicted in Fig. 2.1(a), the metal gasket with a few-hundred-μm diameter hole for sample and compression medium has been indented between the diamond anvils and the extruded metal forms a supporting ring around the edge of the diamond culet face. This extruded ring protects the diamond-face edge from the concentration of stresses at the edge under high pressure. Mao and Bell [20] proposed beveling the edges of the diamond anvils to reduce the stress gradients more efficiently to reach higher pressure. Usually, harder material, such as tungsten (W), is needed for ultra-high pressure experiments.

2.2.3 The Ruby Pressure Gauge

How to determine the magnitude of pressure with accuracy is a crucial for high pressure research. A trivial way to measure the pressure is to use the primary pressure gauge which is based on the fundamental definition of pressure, force per unit area. However, the uncertainties in force measurement inside the pressure cell prohibit this method. Alternatively, using the systematic property change of materials with compression, a secondary pressure gauge provides a more reliable determination of pressure. The ruby pressure gauge is one of the secondary pressure gauges and is widely used in the DAC.

The ruby pressure static scale measures the pressure response of sharp ruby (R_1 line) fluorescence (at 6942Å). It was developed by Forman *et al.* The main advantage of using the ruby pressure scale is the linear dependence between R_1 line shift ν and external hydrostatic pressure P over a modest pressure-region (0 to 100 kbar) [21],

$$P(kbar) = -1.321(\nu - \nu_0)(cm^{-1}) \tag{2.1}$$

where ν_0=1/6942 cm^{-1}. The accepted pressure-induced shift rate (0.757 cm^{-1}/kbar) and sharp linewidth (7.5 Å) of the ruby R_1 fluorescence yield a reasonably precise

pressure determination. Due to the high intensity of the ruby R_1 line only a small ruby chip ($\sim 2.7 \times 10^{-5} mm^3$) is needed to make the pressure measurement accessible especially in the small working volume within a DAC.

However, there are different arguments concerning the linearity of the extrapolated dependence of pressure-induced ruby R_1 line shift beyond 200 kbar [22, 23]. Mao *et al.* [24] have done the ruby pressure calibration up to 1 Mbar and observed that the linear ruby scale underestimates by about 10% at high pressure. They suggested a new calibration curve to fit the ruby data,

$$P(kbar) = 3.808 \left[(\frac{\nu_0}{\nu})^5 - 1 \right] (cm^{-1}) \tag{2.2}$$

Beside the uncertainty of ruby calibration at very high pressure, the doublet spin transition($^2E \rightarrow {}^2A_4$) and significant temperature sensitivity($(d\lambda/dT)/(d\lambda/dP)$= 0.186 kbar/K) [25] of ruby fluorescence also limit the precision of ruby pressure scale.

Although corrections to the ruby scale will certainly be required, the ruby sensor is still generally accepted up to 200 kbar. For the case studies in this thesis, which are mainly below 200 kbar, the ruby sensor is especially convenient and reliable.

2.3 Angle-dispersive X-ray Powder Diffraction Method

Since the invention of X-rays in 19th century, X-ray has been used frequently to probe the atomic world. The most successful application of X-ray techniques is to elucidate the structural detail of materials. Lots of diffraction methods have been developed and the most direct evidence of crystal structure can be read from a single crystal diffraction method. However, during high pressure structural studies, the pressure gradient inside the specimen will increase dramatically. This effect causes strong stresses on single crystals, and impedes high-pressure single crystal diffraction. Therefore, the powder method is more suitable for high pressure study. The angle-dispersive powder method using a fixed monochromatic X-ray beam will be discussed in this section.

2.3.1 Powder Diffraction

The mechanism of powder diffraction method is similar to the single crystal diffraction except the specimen is in polycrystalline form. Traditionally, the powder method was suited to materials for which single crystal forms are not available. However, the technique has attracted more interest since the introduction of modern refinement techniques which can accurately extract 3-dimensional information of materials from 1-dimensional powder diffraction pattern. The rapid development of data analysis enlarges the application field of the powder method and nowadays, the powder diffraction technique is extensively used in material science.

X-ray Scattering from Crystals

The basic mechanism of X-ray diffraction by crystalline materials is represented clearly by W. L. Bragg who explained the diffraction phenomena with a simple model in which atoms of perfect crystals are arranged regularly to form many parallel lattice planes with an infinite boundary condition. In this model, constructive diffraction can happen only if the reflections of a strictly monochromatic X-ray from successive planes are coherent, i.e. the difference of X-ray path between two neighbouring lattice planes must be an integral number of incident X-ray wavelengths (as shown in Fig. 2.4). Then, the Bragg's law can be formulated as,

$$n\lambda = 2d\sin\theta \tag{2.3}$$

where λ is the wavelength of incident X-ray. d is the space between lattice planes. θ is the angle between incident X-ray and the lattice surface. The integer n is the order of the corresponding reflection. Using the monochromatic X-ray source, the diffracted sharp peaks with special diffraction angles provide information on the possible shape and size of the unit cell.

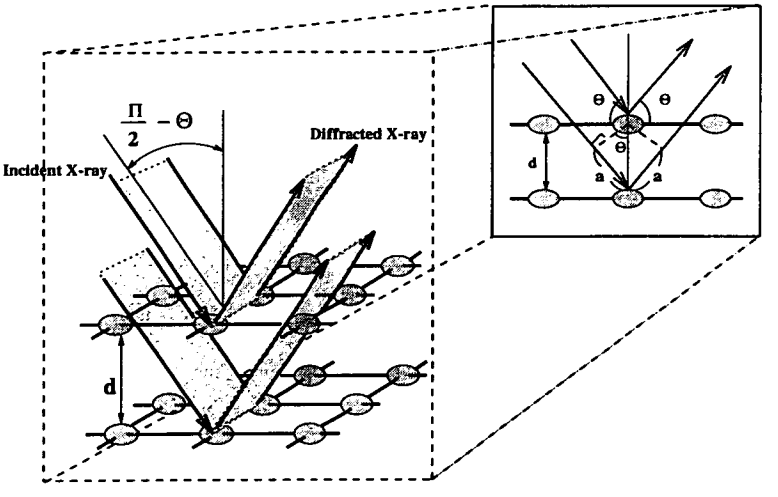

Figure 2.4. Diffraction of X-rays by a crystal. θ is the half of diffraction angle and d is the distance between two parallel lattice planes. The light path difference is $2a$ where $a = d \sin \theta$.

Angle-dispersive Powder Method

Under the stringent requirement of the Bragg's law, the incident fixed λ X-ray brings about only a few observable diffraction events for a given crystal. By changing θ during the experiment, the angle-dispersive powder diffraction method can overcome this obstacle. The powdered sample is a assemblage of tiny crystals with random orientations with respect to the incident X-ray. The randomly oriented polycrystalline arrangement is equivalent to a single crystal rotating around each possible axes. The crystal rotation with a specific axis generates a conical sheet of diffraction for which the cone angle is equal to twice the corresponding diffraction angle. A whole diffracted sphere is built up by superimposing all diffracted rings if the powder stacking is random enough to diffract the incident beam in all possible directions (as shown in Fig. 2.5). The angle-dispersive powder method is more suitable for the sample under high pressure because the stress gradient on powder is much lower than on single crystals. Nevertheless, the

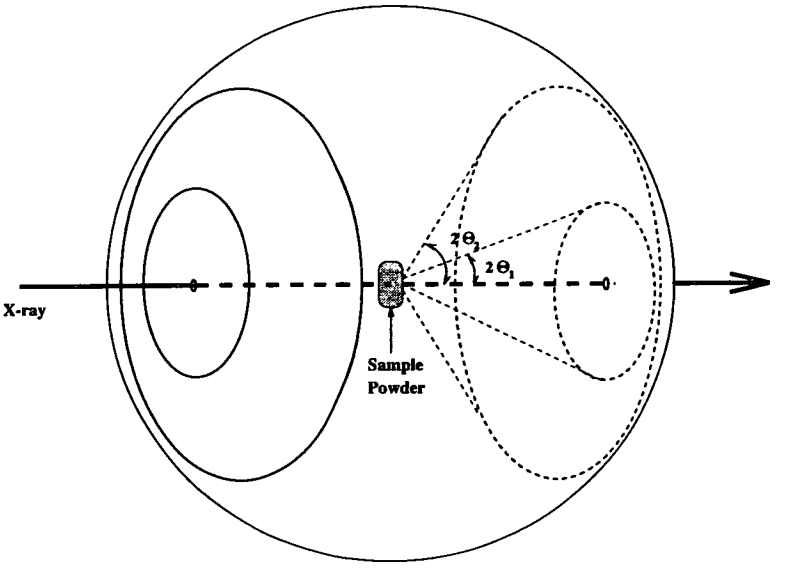

Figure 2.5. Formation of a diffracted sphere of radiation in the angle-dispersive powder method. $2\theta_1$ and $2\theta_2$ denote the diffraction angle with respect to two different diffracted cones.

full picture of crystal structure is deduced from the combination of the unit cell determination and the intensity knowledge of each diffraction peaks which is dominated by the atomic arrangement in the unit cell. The detail of the diffraction profile will now be discussed.

The Output of X-ray Powder Diffraction

Following the rigorous condition of the Bragg's law, the profile of each diffraction of the ideal crystal using pure monochromatic X-ray should be a sharp δ function for which intensity depends on the radiation source and structural parameters within a unit cell. However, the intrinsic imperfection of samples and the extrinsic perturbation, such as the nominally monochromatic X-ray and instrument geometry, cause peak broadening curves and unavoidable background scattering. Then, the measurement of the *integrated intensities* defined as the areas under diffraction curves are more important than the maximum intensities.

Table 2.1. The important factors affecting the integrated intensity of random powder scattering. N is the number of atoms within the basis of unit cell. The f_n and $\mathbf{r}_n = (x_n, y_n, z_n)$ are the form factor and the positional vector of the nth atom, respectively. The *hkl* represents a special reflection with Miller index *hkl* which corresponds to a reciprocal vector **K** with respect to a diffraction angle is 2θ. The parameter p depends on the polarisation of the incident beam (*e.g.* $p = 1$ for an unpolarised X-ray). The thermal agitation parameter M is a function of the half-diffracted angle θ and the thermal vibration amplitude u.

Structure factor	$F_{hkl} = \sum_{n=1}^{N} f_n \exp^{2\pi i(hx_n+ky_n+lz_n)} = \sum_{n=1}^{N} f_n \exp^{i\mathbf{K}\cdot\mathbf{r}_n}$
Lorentz-polarisation factor	$LP = \frac{1+p\cos^2\theta}{\sin^2\theta\cos\theta(1+p)}$
Multiplicity factor	m_{hkl}
Absorption factor	$A(\theta)$
Temperature factor	$T(u,\theta) = \exp^{-M(u,\theta)}$

Rather than for a single crystal, there are more crucial parametrised factors [26] listed in Table 2.1 which must be taken into account in calculating the the integrated intensity of diffraction peaks in the powder diffraction method because of the randomised crystalline distribution of powdered sample. As formulated in Table 2.1, the structure factor F_{hkl} depends on atomic scattering form factors f_n which decreases rapidly while $\sin\theta/\lambda$ increases. The Lorentz-polarisation factor describes the geometrical condition of the sample and the polarisation of the incident radiation. The multiplicity is a factor which concerns the contribution from reflection planes with different Miller indices having the same geometric spacing. The absorption factor is considered to multiply the calculated intensity. Moreover, the thermal diffuse background of diffraction pattern resulting from the thermal fluctuation can be modeled as a Debye form [26].

Therefore, the basic expression of the integrated intensity at $2\theta_i$ corresponding the

hkl reflection of a randomly distributed powder sample using X-ray can be written as

$$I_{cal}(2\theta_i) = \frac{I_o \lambda^3 v}{V^2} |F_{hkl}|^2 m_{hkl} A(\theta) T(u,\theta) LP \tag{2.4}$$

where I_o and λ are the intensity and the wavelength of the incident X-ray, respectively. The V is the volume of the unit cell and the v is the diffracting sample volume.

From Eqn. (2.4), the 3-dimensional information of the atom arrangement can be systematically studied from the measurement of each 1-dimensional diffraction peak. However, in the total pattern, the peak-overlapping from neighbouring reflections exists and this '*scrambling*' feature becomes more severe when the density of the reflection lines increases. In order to figure out the individual integrated intensity, a robust method which can correctly simulate the contribution of neighbouring diffraction lines is necessary and will be discussed in Sec. 2.3.3.

2.3.2 Instrumentation

The instrumentation for high-pressure powder diffraction includes synchrotron radiation and the image plate system. Owing to the advantages of strong intensity, small cross section and tunable wavelength of output X-ray radiation, synchrotron radiation has been widely accepted for detailed structure study of materials. Another crucial technique, the image plate, has been developed recently and provides a promising result for high pressure study. Both techniques will be described as follows.

Generation of X-rays in a Synchrotron Radiation Source

The basic idea of synchrotron radiation is that electromagnetic radiation is emitted from accelerating charged particles. The radiation frequency can be extended to the X-ray region when light charged particles, such as electrons, are accelerated to close to the speed of light c. ($c \simeq 3 \times 10^8$ m/sec).

The outline of the facility at SRS Daresbury is shown in Fig. 2.6. The electrons

are generated and speeded up from a linear accelerator, then boosted in the booster in order to be injected into the storage ring in which the charges circulate around for several hours. Under the magnetic field of the long bending magnets, the electrons will lose energy and emit radiation which energy can be enhanced by a insertion magnetic device, wiggler. The lost energy is compensated when the electrons go through a radio-frequency cavity inside the ring. According to the Lorentz transformation, the output photon with the instantaneous velocity v emitted along the tangent of the electron orbit with momentum $P_{||}$ and energy E will induce an effective momentum on the plane perpendicular to the the tangent direction in the laboratory frame

$$P_{lab||} = P_{||} \tag{2.5}$$

$$P_{lab\perp} = \frac{\frac{v}{c}E}{c\sqrt{1-\frac{v^2}{c^2}}} = \frac{\gamma\beta E}{c} \tag{2.6}$$

where, for photons, $\beta = \frac{v}{c} \approx 1$, and $P_{||}c = E$ beacuse of the Einstein relativity formula. Then, the radiation can be detected within a emission cone with a very small cone angle Ψ (< 1 mrad)

$$\Psi \approx \tan\Psi = \frac{P_{lab||}}{P_{lab\perp}} \approx \frac{1}{\gamma} \tag{2.7}$$

Within the small cross-section corresponding to the cone angle, synchrotron radiation provides a brighter source than the conventional electron-impact X-ray generator does. Synchrotron radiation with a strong intensity source will shrink the exposure time and produce high-resolution data. Another remarkable advantage of using SRS is that the synchrotron generates X-rays not only a shorter wavelength but also with a wide working range of tunable radiation which can be used to probe small polycrystalline structures.

As shown in Fig 2.6, the X-ray source on Powder Diffraction Station 9.1 at the SRS Daresbury comes from a multipole 5 Tesla wiggler magnet and then through a

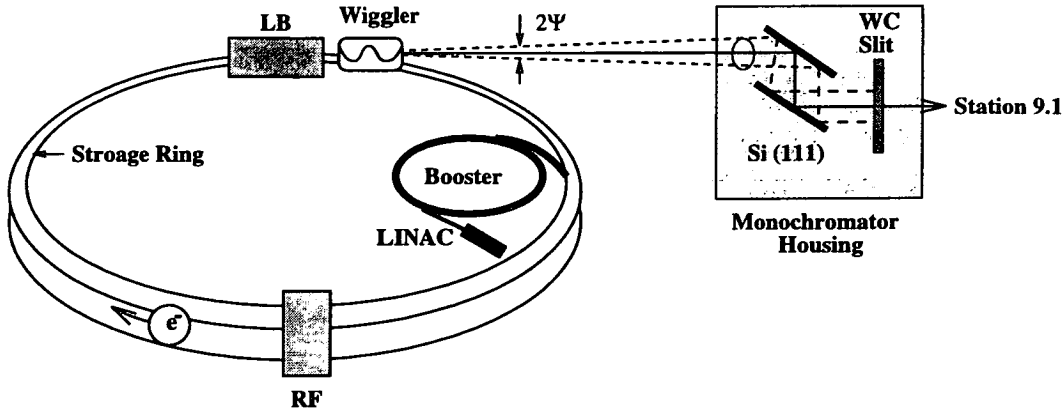

Figure 2.6. Schematic diagram of SRS at Daresbury. LINAC is the linear accelerator. RF and LB denotes the radio-frequency cavity and the long bending magnets.

monochromator housing to allow a proper size and wavelength of collimated beam. The monochromator housing is composed of a Si(111) monochromator which selects the operating wavelength ($0.42 \sim 0.9$ Å) and tungsten-carbide (WC) slits which reduce the beam size ($0.5 \times 0.5\text{mm}^2$).

Image-Plate Detector

At high pressure, the very small sample volume is of order $5 \times 10^5 \mu\text{m}^3$ within the DAC. This gives a fairly weak signal and a poor powder average which limits the quality of one-dimensional data collection by a conventional Debye-Scherrer film. In order to accumulate enough scattering intensity, a modern two-dimensional area detector technique, image-plate (IP) system, has been developed recently [27, 28] and used to perform angle-dispersive powder diffraction under pressure [29].

The design of the synchrotron-based IP system on Station 9.1 is illustrated in Fig 2.7. The stray radiation of the collimated beam from the monochromator housing is absorbed by a Pb shield and then passes through a WC tube. At the end of the

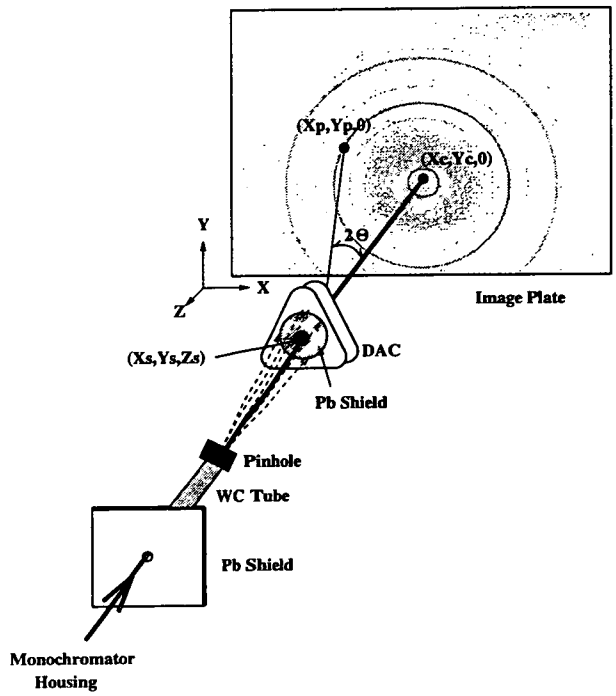

Figure 2.7. A schematic diagram of a image-plate setup at SRS. The pinhole is mounted on a motorised XYZ stage and the pressure cell on another adjustable stage where both are not shown here. The axes used to define beam and plate geometry are also defined in this diagram.

WC tube, a pinhole with a spark-eroded hole 300μm was mounted to eliminate the contamination from $\lambda/3$ radiation which surrounds the incident λ beam. The characteristic K-absorption edge of Pt (at 0.15817 Å) is more suitable for this attenuation for $\lambda < 0.4745$ Å . However, a further reduction of the $\lambda/3$ *halo* is implemented by another small Pb shield with a tiny hole (1mm) attached at the front of DAC window. Then, a cleaner beam results and the full diffracted cone is detected by a $20 \times 25cm^2$ Kodak storage-phosphor image plate.

The two-dimensional pattern recorded on an image plate is read by means of a Molecular Dynamics 400A PhosphorImager which extracts the 2800×2000 pixels data from the A4 sheet image plate. As shown in Fig. 2.7, the relationship between pixel position $(X_p, Y_p, 0)$ and the Bragg diffracted angle θ for a ideal flat plate geometry is

formulated as,

$$\cos 2\theta = \frac{(X_c - X_s, Y_c - Y_s, -Z_s) \cdot (X_p - X_s, Y_p - Y_s, -Z_s)}{|(X_c - X_s, Y_c - Y_s, -Z_s)|\ |(X_p - X_s, Y_p - Y_s, -Z_s)|} \tag{2.8}$$

where the sample position and the center of strike beam are represented as (X_s, Y_s, Z_s) and $(X_c, Y_c, 0)$ respectively.

However, in real cases, the intensity integration of a 2-dimensional Debye-Scherrer ring is still affected by a few uncertainties from the geometry and a robust algorithm is needed to overcome this hamper. The PLATYPUS program developed at Edinburgh is a powerful and reliable program to translate 2D image data into 1D diffraction profiles. Using PLATYPUS, the raw 2800 × 2000 pixels data are firstly divided into 160 sectors and the data size is reduced to 160 × 2500 points. Then, the uncertain parameters (such as the sample to image plate distance and the unit direction vector of the incident beam) are adjusted by a algorithm designed to maximise profile sharpness [27]. After determining all unknown parameters, the 2D pixels are rebinned into 1D pixels pattern (shown in Fig. 2.8). Moreover, the converting relation of the pixel number into 2θ coordinates can be obtained by collecting the pattern of a material (*e.g.* Si) with well-defined lattice parameters and index of each reflection at the given distance. After this calibration, the diffraction profile as a function of 2θ is eventually deduced.

2.3.3 Structure Determination

The comprehensive characters of diffraction patterns include mainly two components: the diffraction line positions and line intensities. The unit cell parameters are determined by the angular positions of all diffraction lines. Meanwhile, the detailed location of atoms within a unit cell is dominated by the relative intensity of the lines. In order to decipher detail of the crystal structure, the diffraction pattern is modeled as a function of structural parameters and a matching process between the observed and calculated

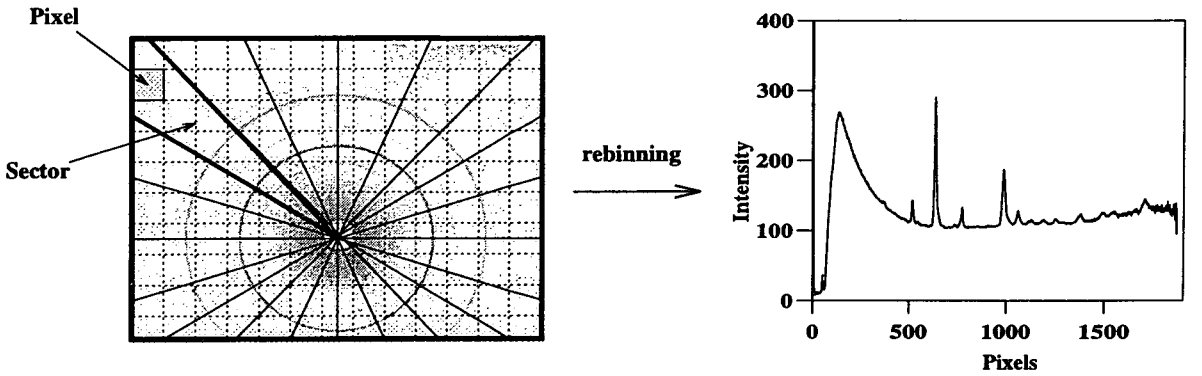

Figure 2.8. The procedure of the data conversion algorithm in PLATYPUS.

pattern is repeated until the accurate structure is found.

The structure-searching procedure can be implemented straightforwardly on a computer as an iterative programme to minimumise the difference between calculated and observed results. Before searching the optimal structural parameters, an appropriate initial trial structure which is close to the destination structure is needed to reduce the computation cost. In general, this initial trial configuration of an unknown structure can be obtained by means of, for example, a pattern indexing program DICVOL91 [30] in which the size and shape of a unit cell is determined by an optimised successive scheme. However, most structural studies in this thesis were started from well-defined configurations and the initial structural parameters for finding real structures can be acquired from previous structural surveys [31].

Once the possible size and shape of the unit cell have been found, the detailed structure can be determined by a refinement procedure which can routinely search the possible structural solutions. A profile refinement method introduced initially by Rietveld in 1969 [32] is accepted widely and applied in many fields. There are a lot of computer programs based on Rietveld's method have been developed and widely used. Two *Rietveld method programs*, MPROF [33] and DBWS [34], are employed to do the

profile refinement in this thesis.

The Rietveld method is a minimisation technique which looks for an optimised line-profile matching between calculation and observation. Before the searching of the correct structure detail, a precise model of the observed diffraction pattern is needed. For total pattern fitting, the reflection lines contain structural and nonstructural parts in Rietveld's model. As pointed out in Sec. 2.3.1, the structural information is included in the intensity of an idealised individual diffraction peak which is expressed as a function of structural parameters (Eqn. (2.4)). The nonstructural component of Rietveld model is an analytical function. Thus, the Rietveld method does not require the integrated intensity for each reflection. In other words, the whole diffraction profile is calculated.

Considering the overlap from neighbouring contributing reflections, the Rietveld calculated intensity of $2\theta_i$ is

$$S_{cal}(2\theta_i) = \sum_j I_{cal}(2\theta_j) Y(\Delta 2\theta_{ij}) + B(2\theta_i) \tag{2.9}$$

where Y is the analytical profile function which is normalised to unit area and $\Delta 2\theta_{ij} = 2\theta_i - 2\theta_j$. $B(2\theta_i)$ is the background at $2\theta_i$ and can be simulated by a function of the polynomial fitting of chosen observed background intensities. The summation is over all Bragg peaks which neighbour and contribute the intensity at $2\theta_i$.

There are different types of analytical profile functions commonly used, such as Gaussian function [32], Pearson VII function [35], Voigt function [36], etc.. All of the analytical functions are basicly composed by a combination of the Lorentzian function and the Gaussian function which are defined as

$$\text{Lorentzian:} \quad Y_l(\Delta 2\theta) = Y(\theta_0) \frac{(FWHM_l)^2}{(FWHM_l)^2 + 4(\Delta 2\theta)^2} \tag{2.10}$$

$$\text{Gaussian:} \quad Y_g(\Delta 2\theta) = Y(\theta_0) \exp -4ln2(\frac{\Delta 2\theta}{FWHM_g})^2 \tag{2.11}$$

where the subscripts l and g represent the Lorentzian and the Gaussian function, respectively. $Y(\theta_0)$ is the maximum intensity the function at θ_0 and $\Delta 2\theta$ is the difference from position of maximum position. FWHM is the full width at half maximum intensity and is a function of angular position [37]

$$(FWHM(\theta))^2 = U\tan^2(\theta) + V\tan(\theta) + W \tag{2.12}$$

where U, V and W are the halfwidth parameters.

The widely accepted Pseudo-Voigt function [38] which is also used throughout this thesis is a linear combination of the Lorentzian and the Gaussian. The profile is formulated as

$$Y_{P-V}(\Delta 2\theta) = \eta Y_l(\Delta 2\theta) - (1-\eta)Y_g(\Delta 2\theta) \quad , \quad 0 \leq \eta \leq 1 \tag{2.13}$$

where η is the pseudo-voigt mixing parameter.

The distribution of stacking directions in a powder has to be considered as well in pattern modeling. Especially in anisotropic materials which is the focus of this thesis, the sample is easily cleaved along a special axis and the crystallites tend to have rod- or disk-like shape. This anisotropic character will lead a natural preferred orientation of sample crystallites during the sample loading.

The preferred orientation effect can be reduced by careful sample preparation but cannot be removed completely. In this case, the calculated intensity in Eqn. (2.9) should be modified as

$$S_{cal}(2\theta_i) = \sum_j I_{cal}(2\theta_j)Y(\Delta 2\theta_{ij})P_j + B(2\theta_i) \tag{2.14}$$

where P_j is a preferred-orientation function corresponding the reflection at $2\theta_j$. Two different correction schemes for preferred orientation effects are introduced in MPROF

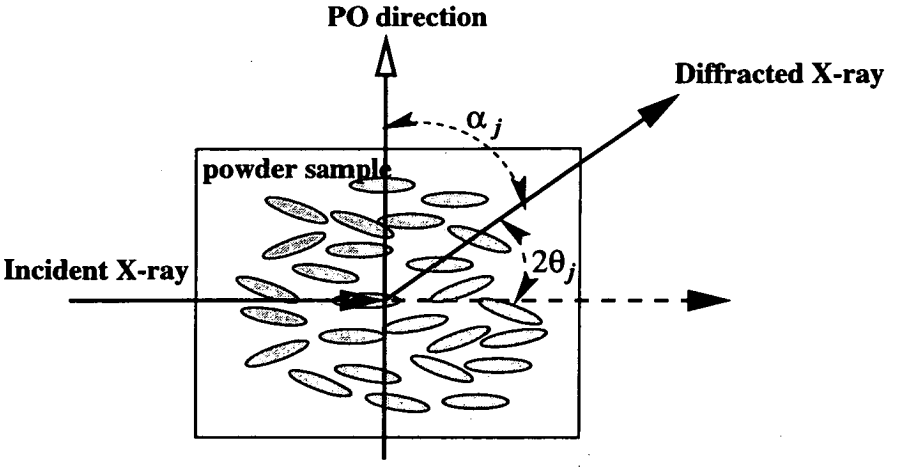

Figure 2.9. A schematic diagram showing the preferred-orientational (PO) geometry in a powder diffraction for an anisotropic material.

and DBWS individually. In MPROF, the original Rietveld form is taken,

$$P_j = exp(-G\alpha_j^2) \tag{2.15}$$

On the other hand, a empirical preferred orientation correction, March-Dollase function [39], is used in DBWS within a commercial package CERIUS,

$$P_j = (r^2 \cos^2 \alpha_j + r^{-1} \sin^2 \alpha_j)^{-3/2} \tag{2.16}$$

where G and r are adjustable coefficients. α_j is the angle between the scattering vector at $2\theta_j$ and the preferred-orientational direction (as sketched in Fig. 2.9).

Thus, the minimisation process of the Rietveld method is implemented by a least-squares fitting between the calculated and observed intensities of the whole pattern. The cost function F which has to be minimised with respect to all structural and nonstructural parameters discussed above is

$$F = \sum_i W(2\theta_i)\{S_{obs}(2\theta_i) - S_{cal}(2\theta_i)\}^2 \quad , \quad W(2\theta_i) = \frac{1}{S_{obs}(2\theta_i)} \tag{2.17}$$

where $W(2\theta_i)$ is the observation weight of the reflection at $2\theta_i$. The summation is over all the independent observations. The quality of minimisation can be evaluated by different reliability factors [40]. The R-weighted pattern factor R_{wp} is normally used to indicate the goodness-of-fit and is defined as

$$R_{wp} = 100 \times \sqrt{\frac{\sum_{i=1}^{N}(S_{obs}(2\theta_i) - S_{cal}(2\theta_i))^2}{\sum_{i=1}^{N}(S_{obs}(2\theta_i))^2}} \tag{2.18}$$

where N is the number of observations.

Starting from a proper initial point in the configuration space with respect to all refined parameters, the Rietveld refinement process is carried out with different trial parameters set until the R_{wp} factor converges to a minimum. A small value of R_{wp} represents a good fitting between calculated and observed profiles. Another complementary indicating factor χ^2 which is a ratio of the cost function F (Eqn. (2.17)) to the number of degrees of freedom is also used in MPROF method. The value of χ^2 closes to unity when the fitness is very good. Furthermore, based on the Gaussian statistic model within the least-squares algorithm, the error of each refined parameter p_i is described by an estimated standard deviation $\sigma(p_i)$

$$\sigma(p_i) \sim \sqrt{\frac{1}{M_{ii}(N - P + C)}} \tag{2.19}$$

where M_{ii} is the matrix of the least-squares algorithm, N is the number of observations, P denotes the number of adjustable parameters during refinement, and C is the number of constraints.

2.4 High-resolution Raman Scattering

In order to study the dynamics of materials, the technique of vibrational spectroscopy has been developed and broadly used. In accordance with different mechanisms, the vibrational spectroscopic technique can be classified as two branches: light absorption

and light scattering. Unlike light absorption using infrared radiation, the techniques of light scattering spectroscopy are basicly designed to detect the induced fluctuations of charge density of a medium during the light scattering process. Raman scattering is a standard spectroscopic tool to study the inelastic light scattering process. The first part of this section is devoted to the Raman effect. This is followed by description of pressure-induced Raman effects and experimental considerations.

2.4.1 Raman Effect

The Raman effect studied first by C. V. Raman in 1921 describes the interaction of electromagnetic radiation with materials. When electromagnetic radiation impacts on matter, the atoms within the system are perturbed by the applied electric field and oscillate around their equilibrium positions. The vibrations which are in phase of all the atoms are observed in spectroscopy as a band and named as *normal modes of vibration.* The total number of normal modes of a general three-dimensional system comprised N atoms is 3N-6 which is derived from the number of degrees of freedom of N atoms minus those of three pure translations and of another three pure rotations of the whole system.

For each normal mode of vibration of the atoms, the charge distribution within the system undergoes a deformation and an induced dipole moment is generated. Based on the classical electromagnetic theory, the creation of the induced dipole moment $\boldsymbol{\mu_i}$ is deduced from the variation of an electric field,

$$\boldsymbol{\mu_i} = \boldsymbol{\alpha E} = \boldsymbol{\alpha E_0} \cos(2\pi\nu_0 t) \tag{2.20}$$

where $\mathbf{E_0}$ is a vector of the amplitude of electric field of incident radiation. ν_0 is frequency of incident monochromatic radiation and t is time. $\boldsymbol{\alpha}$ is the polarisability

which can be expressed in the Cartesian coordinate system as,

$$\boldsymbol{\alpha} = \alpha_{ij} = \begin{pmatrix} \alpha_{xx} & \alpha_{xy} & \alpha_{xz} \\ \alpha_{yx} & \alpha_{yy} & \alpha_{yz} \\ \alpha_{zx} & \alpha_{zy} & \alpha_{zz} \end{pmatrix} \tag{2.21}$$

where the second rank tensor α_{ij} depends on the nature of structure and direction of bonds within material. For example, the polarisability of an isotropic material adopts spherical symmetry and is represented as a symmetric tensor with equal diagonal elements,$\alpha_{xx} = \alpha_{yy} = \alpha_{zz}$. Then, the average polarisability $\bar{\alpha}$ is

$$\bar{\alpha} = \frac{1}{3}(\alpha_{xx} + \alpha_{yy} + \alpha_{zz}) = \alpha_{xx} \tag{2.22}$$

However, for an anisotropic system, the polarisability tensor is an ellipsoid symmetry and this deviation can be evaluated by the anisotropy γ

$$\gamma^2 = \frac{1}{2}[(\alpha_{xx} - \alpha_{yy})^2 + (\alpha_{yy} - \alpha_{zz})^2 + (\alpha_{zz} - \alpha_{xx})^2 + 6(\alpha_{xy}^2 + \alpha_{yz}^2 + \alpha_{zx}^2)] \tag{2.23}$$

Based on the adiabatic approximation, the polarisability tensor can be expanded as a Taylor's series in normal coordinate $\mathbf{Q}$,

$$\boldsymbol{\alpha} = \boldsymbol{\alpha}_0 + (\frac{\partial \boldsymbol{\alpha}}{\partial \mathbf{Q}})_0 \mathbf{Q} + \textit{high order terms} \tag{2.24}$$

where $\boldsymbol{\alpha}_0$ is the polarisability associate with the equilibrium of the system. The small atomic vibration of the normal coordinate $\mathbf{Q}$ with amplitude $\mathbf{q}$ and frequency ν_{ph} is given by

$$\mathbf{Q} = \mathbf{q}\cos(2\pi\nu_{ph}t) = \hat{\boldsymbol{q}}|q|\cos(2\pi\nu_{ph}t) \tag{2.25}$$

where $\hat{\boldsymbol{q}}$ and $|q|$ is the unit vector and the value of the amplitude vector $\mathbf{q}$, respectively.

Under the vibration $\mathbf{Q}$, the polarisability $\boldsymbol{\alpha}_0$ oscillates and the induced dipole moment is formed as

$$\boldsymbol{\mu_i} = \boldsymbol{\alpha}_0 \mathbf{E}_0 \cos(2\pi\nu_0 t) + \frac{1}{2}(\frac{\partial \boldsymbol{\alpha}}{\partial \mathbf{Q}})_0 \mathbf{q} \mathbf{E}_0 \{\cos[2\pi(\nu_0 - \nu_{ph})t] + \cos[2\pi(\nu_0 + \nu_{ph})t]\} + \textit{high order terms} \quad (2.26)$$

where the first order term on the right side accounts for the one-phonon process with a fundamental frequency shift (ν_{ph}), whereas the two-phonon scattering referred to as an overtone is described by the high order term.

Consequently, in Eqn. (2.26), three components with respect to three different types of scattered radiation which can be observed. The elastic Rayleigh Scattering is described by the first term of μ_i with the same frequency μ_0 as the incident radiation. The second and the third term with a specific frequency-shift from ν_0 corresponds to two inelastic scatterings in which Stokes Raman scattering is specified by the frequency $\nu_0 - \nu_{ph}$ and anti-Stokes Raman scattering by $\nu_0 + \nu_{ph}$. Then, the Rayleigh band, Stokes Raman band, and anti-Stokes Raman band are separated by a reasonable distance in frequency axes and make themselves detectable using a spectrometer with enough resolution. Actually, the inelastic Raman scatterings happen only under the condition $(\partial\boldsymbol{\alpha}/\partial\mathbf{Q})_0 \neq 0$ which is different from the constraint necessary condition for the infrared absorption $(\partial\boldsymbol{\mu}/\partial\mathbf{Q}) \neq 0$.

The phenomenon of Raman scattering is easily understood by taking into account the interaction between photons and phonons (which are the quantisations of atomic vibrations). As the schematic interpretations in Fig. 2.10, the Rayleigh scattering is explained as follows. The material with initial energy $h\nu_{v=0}$ is excited up to a virtual state by incident radiation $h\nu_0$ and then returns to the original state accompanied by scattered radiation without any energy loss. However, in Stokes Raman scattering, the

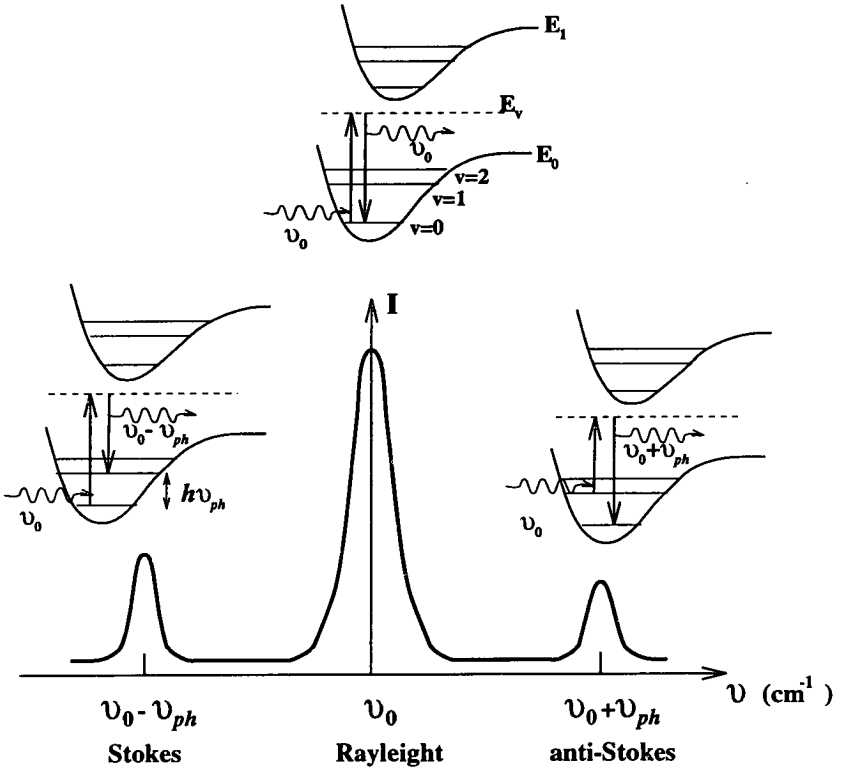

Figure 2.10. Transition between the vibrational energy levels with respect to scattering bands. E_0, E_v, and E_1 denotes the energy level of the ground electronic state, virtual state, and excited electronic state, respectively. v is the vibrational level. The incident and the phonon frequency is represented by ν_0 and ν_{ph} respectively.

inelastic scattering process is due to phonon absorption during the energy transition between initial and final state which is constrained by the selection rule for the fundamental transition, $\Delta v = \pm 1$, and thus the scattered frequency is $\nu_0 - (\nu_{v=0} - \nu_{v=1}) = \nu_0 - \nu_{ph}$. Also, the anti-Stokes Raman scattering is characterised by phonon emission within the transition and increases the frequency of scattered radiation to $\nu_0 + \nu_{ph}$. Furthermore, under conservation of wavevector during the scattering process, the wavevector of the induced phonon $k_{ph} \sim 0$, therefore, the general one-phonon Raman scattering permits routine studies of the zone-center phonons.

By classical electromagnetic theory, the intensity of an oscillating dipole moment is defined as

$$I = \frac{16\pi^4\nu^4}{3c^3}\mu^2 \sim |(\partial\alpha/\partial\mathbf{Q})_0\hat{q}|^2|q|^2 \tag{2.27}$$

where $(\partial\alpha/\partial\mathbf{Q})_0\hat{q}$ is defined as a Raman tensor wich is a second rank tensor possessing all point group symmetry of the material. The power spectrum is denoted by $|q|^2$ and, for the one-phonon Stokes process, is expressed as

$$|q|^2 = \frac{h}{4\pi N\nu_{ph}}(n_{ph} + 1)L_{ph}(\nu) \tag{2.28}$$

where N is the number of phonons in the specimen. n_{ph} and $L_{ph}(\nu)$ is the Bose thermal population factor and the Lorentzian line-shape function.

$$n_{ph} = \frac{1}{exp(\frac{h\nu_{ph}}{2\pi KT} - 1)} \tag{2.29}$$

$$L_{ph}(\nu) = \frac{(FWHM)^2}{(FWHM)^2 + (\nu_{ph} - \nu)^2} \tag{2.30}$$

Due to the Placzek's theory [41], $\nu_{ph} \ll \nu_0$ and $h\nu_0$ is much smaller than the energy difference between two electric states, the intensity of Rayleigh scattering is about a

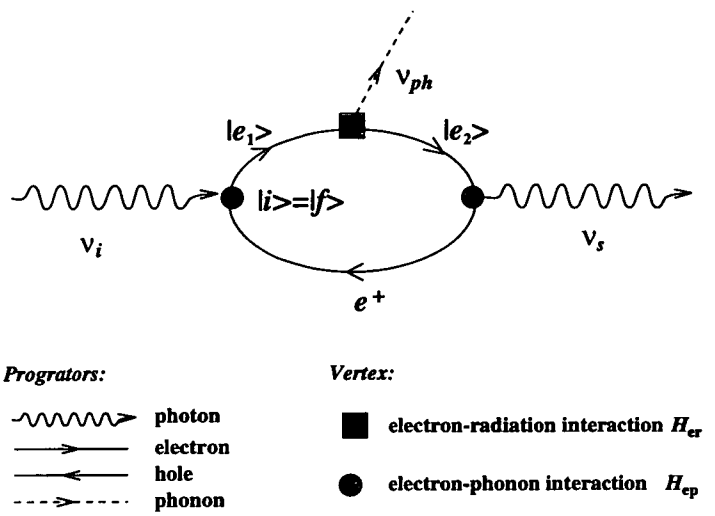

Figure 2.11. One possible Feynman diagram for one-phonon Stokes scattering process. $|i>$ and $|f>$ are initial and final states of the system. $|e_1>$ and $|e_2>$ denotes the first and the second intermediate state, respectively. e^+ represents the hole which will recombine with electron eventually. ν_i, ν_s, and ν_{ph} stands for the frequency of the incident, scattered, and phonon, respectively.

thousand times that of Stokes Raman scattering. Also, the intensity ratio of Stokes to anti-Stokes Raman scattering is larger than unity because there is a greater population of oscillators in the lowest energy state.

In addition to the classical picture mentioned above, the detailed procedure of Raman scattering does include the electron-photon and electron-phonon interactions. Using quantum field theory, the Raman scattering process for one-phonon generation can be expressed by a Feynman diagram shown in Fig. 2.11.

The scattering probability at each vertex can be expressed in a perturbation theory series via the Fermi Golden Rule [42]. For example, the scattering probability at the first vertex of Fig. 2.11 referring to the transition between initial state $|i>$ and the first intermediate state $|e_1>$ is,

$$\left| \sum_{|e1>} \frac{< e_1|H_{er}|i >}{[h\nu_i - (E_{e1} - E_i)]} \right|^2 \tag{2.31}$$

where H_{er} is the electron-radiation interaction Hamiltonian and E_n is the energy of state n. Then the magnitude of the polarisability which is a function of scattering probability of the whole Feynman loop can be calculated by third order perturbation theory [43] as proportional to,

$$\sum_{|e1>,|e2>} \frac{< f|H_{er}|e_2 >< e_2|H_{ep}|e_1 >< e_1|H_{er}|i >}{[h\nu_i - h\nu_{ph} - (E_{e2} - E_i)][h\nu_i - (E_{e1} - E_i)]} \tag{2.32}$$

where H_{ep} is the electron-phonon interaction Hamiltonian.

The polarisation properties of materials contribute strongly to the scattered radiation especially for crystal structure and therefore, each Raman-active mode can be identified by measuring the depolarisation ratio ρ of scattered radiation which is given by

$$\rho = \frac{I_\perp}{I_{||}} \tag{2.33}$$

where $I_\perp$ is the component of scattered intensity which is perpendicular to the polarisation of incident radiation and $I_{||}$ is parallel component of scattered intensity. Thus, the different compositions of polarisations of the incident radiation and the specimen permit the measurement of ρ which yields the assignment of each vibrational mode by using group theory.

Besides the general Raman effect discussed above, there are other special Raman techniques which are widely applied in different systems. For example, the *prereso-nance* and *resonance Raman effect* [44] and *Surface-enhanced Raman Spectroscopy* [44] which has been used to study the biomolecules absorbed on a metallic surface. Thus, the versatility of Raman effect proves that it is a sophisticated method to investigate materials.

2.4.2 Pressure-induced Modification of Raman Effect

As described above, during one-phonon Raman scattering, the scattered Raman lines mainly arise from the Raman tensor and the power spectrum. The Raman tensor reflects symmetry and the interactions within the specimen and the power spectrum describes the frequency and the output profile of each Raman line. It is expected that these two factors will be affected when external pressure is applied and can be observed from the Raman spectrum.

Firstly, the force constants of the bonds inside the structure are modified under compression and the pressure-induced spectral shifts of Raman lines with specific force constants are expected. Moreover, the rate of pressure-induced phonon frequency shift is used to define the Grüneisen parameter which characterises the nature of different types of bonds and the cohesion arising from each chemical bond. These can be classified by scaling laws which will be discussed in detail in Chapter 6. Also, considering the anharmonic interactions, the lifetime of the phonons is affected and the profile of Raman line will be changed by pressure.

Secondly, the magnitude of each component of the Raman tensor will be also affected substantially by pressure. Taking into account Eqn. (2.32), the electron-phonon interaction can be described schematically in Fig. 2.12. The direct electronic bandgap $h\nu_g (= E_{e2} - E_i$ in Eqn. (2.32)) will be modified by applying the compression and then the components of Raman tensor are changed which yield a pressure-induced intensity variation. Finally, the symmetry of Raman tensor components and Raman selection rules will change while a pressure-induced structural phase transition corresponding to the change of space group takes place.

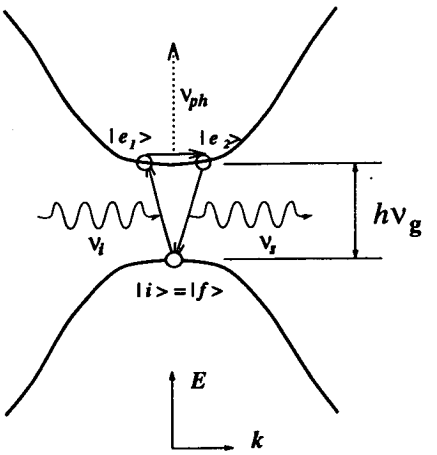

Figure 2.12. Schematic diagram of two-band process of Raman scattering. **k** and **E** denotes the wavevector and energy respectively. ν_g is the frequency corresponding to the energy gap. $|i>=|f>$ locates at the valence band and $|e_1>$(or $|e_2>$) at the conduction band. The rest notations are the same as Fig 2.11

2.4.3 Experimental Aspects of Raman Scattering

A typical setup for a general Raman scattering experiment includes three main apparatuses: the exciting source, auxiliary optics, and the spectrometer. Unlike the conventional Raman scattering, the *Light Amplification by Stimulated Emission of Radiation* (LASER) is widely used as a modern exciting source to routinely study the Raman effect. Also, various optics have also been designed to enhance the Raman signal and to identify the polarisation of the Raman peak. Meanwhile, the recent developments of optical techniques provide high-resolution spectrometers which enrich the application fields of the Raman scattering dramatically. The discussion of these three parts used in this thesis is given as follows. In addition, different scattering geometries for specific purposes will be exhibited at the end of this section.

Exciting Source: LASER

A laser is a device that depends on emission by stimulated processes. The basic design of a typical laser is to use a plasma tube with two end mirrors to confine and excite

specific gas atoms. In this evacuated glass tube, the photons emitted by some gas atoms ricochet backward and forward between two end mirrors to induce more photons. Once sufficient numbers of photon accumulate to penetrate one partially transparent ending mirror , a laser light source can be tapped. In principle, the emission process inside a laser tube is described briefly as follows.

1. *Optical Pumping* – The atoms or ions are initially stay in ground state and then, are excited up to the excited state by photons till the majority population of atoms are in the high electronic level.

2. *Spontaneous Emission* – Few atoms in the excited state emit the energy and return to the lower state during this process in order to trigger the stimulated emission.

3. *Stimulated Emission* – This effect is due to a spontaneous and synchronising emission from all atoms in the excited state. This procedure gives rise to a directly polarised and coherent output radiation with high power.

According to the nature of the above procedure, the emitted radiation of a laser is a monochromatic, highly coherent and high power light source with a well-defined polarisation and a small cross section. These properties of the laser overcome the problem of the low efficiency of Raman scattering and the wide frequency working range makes the Raman studies of semiconductors feasible.

Depending on the property of emitted radiation, there are two types of lasers, continuous-wave(CW) and pulsed, which are normally used. In this thesis work, two CW types of Ar^+ and Kr^+ lasers are chosen where emission frequencies include, 5145, 5017, 4880, 4765 and 4579 Å , and 6764, 6471, 5682, 5309 and 4762 Å regions, respectively.

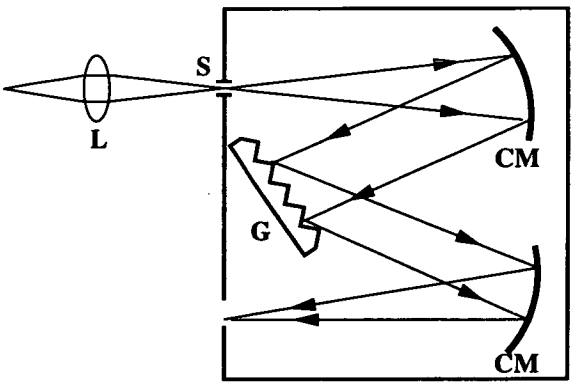

Figure 2.13. Schematic of a laser filter monochromater. The light with a special frequency can be chosed by tuning the grating (G). L, S, and CM denotes the lens, slit, and concave mirror, respectively.

Auxiliary Optics

As discussed in Sec. 2.4.1, the Raman effect is intrinsically weak and directly related to the polarisability of specific materials. In order to fit the requirement of depolarisation and also to improve the intensity of spectra, some optical devices shown as follows are necessary.

1. *Laser Filter Monochromater* - Although the laser light source is highly monochromatic, the output laser line with a specific frequency is still admixed with weak nonlasing lines which will affect the sensitive Raman signal. However, this contamination can be reduced by introducing a laser filter monochromater (as shown in Fig. 2.13) which can separate the admixture of light with very close frequencies and then block the noise from the laser plasma.

2. *Focus Lens* - For the applications, *eg.* DAC, which require a small sample volume, a focus lens is usually placed at front of the sample to increase photon density at the sample. By adjusting the position of the focus lens, the Raman signal can be substantially enhanced when the sample is situated at the focus of the lens.

3. *Polariser* – In solid state, the existence of specific Raman peaks is determined by the geometry of the substance. This depolarisation measurement can be performed using the polariser which eliminates the component of light whose direction of the electric field vector differs from that of the required orientation. Normally, the polarisers are set at front of the focus lens and the at spectrometer to specify the polarisation of the incident and scattered light, respectively.

Spectrometer: Coderg T800

Modern spectrometers are composed of high resolution optical devices which help to detect the weak Raman signal and also reduce the background noise. As a commercial triple-grating scanning spectrometer, the Coderg T800, has been built up in Edinburgh University with three important components and is shown in Fig. 2.14

1. *Monochromator* – It is a device of diffraction gratings to allow the dispersion of radiation. More gratings give low noise from imperfection in the ruling of gratings. In the Coderg T800, three monochromators are arranged as shown in Fig. 2.14 and the first two monochromators are symmetrically mounted.

2. *Photomultiplier* – It is designed to make the original low intensity of Raman signals detectable. Utilisation of the photocathode, the consecutive arranged dynodes, and the anode increases the weak signal up to six orders of magnitude. Two photomultiplier devices, phototubes, are supplied in the Coderg T800 and an automatic exciting line suppression device is mounted at the front of the phototubes to prevent the overloading of phototubes from stray light.

3. *Recoder* – The output of photomultiplier is detected by the detection amplifier and then fed into the external PC controller for data recording.

The scan range of 10000-24500 (cm^{-1}) can be achieved by accurately tunning three gratings inside Coderg T800. In addition, the mechanical slit width which can be

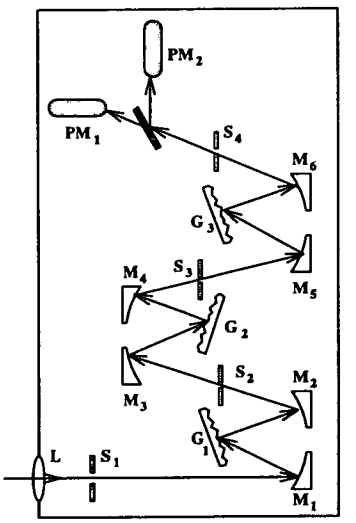

Figure 2.14. Diagram of the Coderg T800 spectrometer. The three monochromators are composed of mirrors(M) and gratings(G). The signal is collected by the entrance lens(L) and then filtered by four slits(S). The output photons is finally detected by two photomultipliers(PM).

adjusted over the range from 0 to 2000 μm determines the resolution of output data from a calibration curve of slit width versus wavelength accuracy. Moreover, the balance between scanning speed, slit width, and the time constant imposed needs to be kept to enhance the quality of spectrum.

Scattering Geometry

For different applications, two scattering geometries have been performed in Edinburgh for pressure and temperature Raman studies. The arrangements are presented as follows

1. *Backscattering Geometry* – As discussed in Sec. 2.2.1, only two optical windows are available for DAC and, thus, the optimised setup for the high-pressure Raman study is the backscattering (180° scattering) geometry. According to the limitation of the DAC, an extra mirror and focus lens is needed to change the route of laser to pass through the window of the DAC. The experimental setup is shown in Fig. 2.15(a).

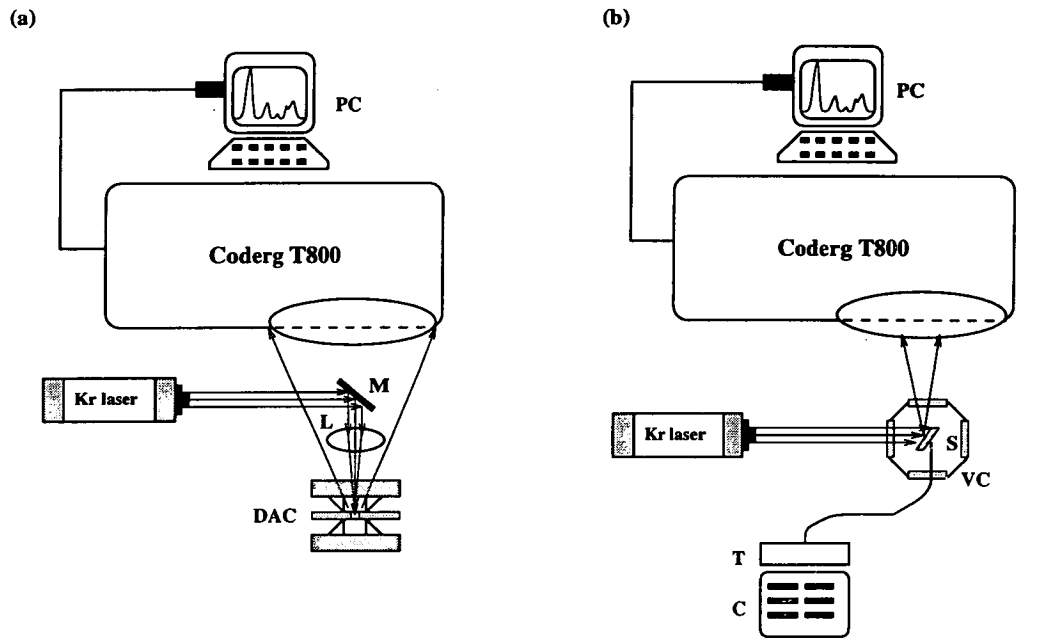

Figure 2.15. Schematic diagrams of experimental arrangements for (a) high-pressure backscattering and (b) low-temperature 90° scattering Raman spectroscopies. In (a), M and L denote the mirror and the lens. S, VC, T, and C in (b) represents the sample, vacuum chamber, temperature controller, and cryostat, respectively.

2. 90° *Scattering Geometry* – To study temperature effects on Raman scattering, the specimen is fitted in a vacuum chamber with four optical windows and is mounted directly to a cryostat and a temperature controller. Then, the 90° scattering geometry is a simple setup for low temperature study. The arrangement is depicted in Fig.2.15(b).

Chapter 3

First Principles Computer Simulations

3.1 Introduction

Certain material equilibrium properties such as crystal structure, lattice dynamics and binding energy are directly related to the ground state total energy. For theoretical high-pressure studies of materials, total energy calculations provide scope to explore physical features under compression. For example, in equilibrium, the static structural properties of solids, like bulk modulus B, can be obtained by fitting the total energy (E_{total})-volume (V) curve to an equation of state (EOS). The Murnaghan EOS is often used according to which :

$$E_{total}(V) = \left\{ \frac{BV}{B'(B'-1)} \left[B' \left(\frac{V - V_0}{V} \right) + \left(\frac{V_0}{V} \right)^{B'} - 1 \right] \right\} E_{total}(V_0) \qquad (3.1)$$

where B' is the pressure derivative of bulk modulus and V_0 is the equilibrium volume. In addition, the relative structural stability of different phases can be determined by comparing associated E vs V curves in which the structure with minimum total energy corresponds to the equilibrium one. Furthermore, pressure-induced phase transition

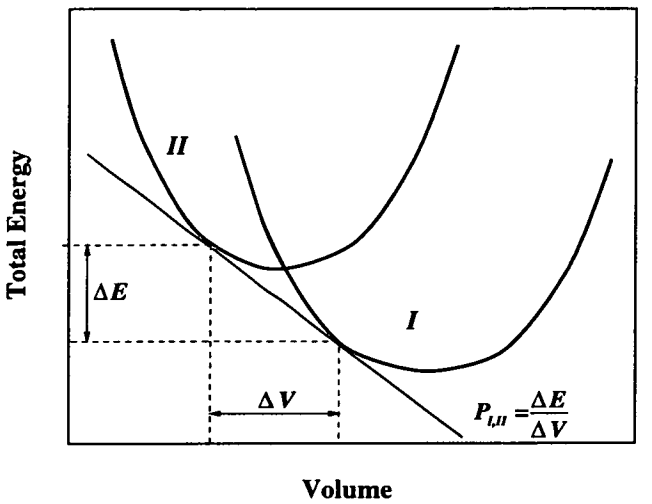

Figure 3.1. $E - V$ diagram for a pressure-induced structural phase transition. The transition occurs at the pressure $P_{I,II}$ for which the common-tangents of the energy-volume curves of phase I and II.

can also be represented by the Gibbs free energy G in terms of total energy, thermal and compressional contributions

$$G = E_{total} - TS + PV \tag{3.2}$$

and the transition pressure $P_{I,II}$ between phase I and II can be evaluated from a common tangent to both EV curves as shown in Fig. 3.1

Hence, the quality of theoretical studies of high pressure physics relies on the accuracy of total energy calculations. However, the total energy is a many-body quantum-mechanical quantity which implies that the exact solution can never be achieved by brute-force solving a many-body Schrödinger equation. Therefore, some intelligent approximations must be involved in order to make the calculations feasible. Much effort has been invested in modelling accurate potentials in terms of analytically parameterised forms [45]. These models are known as empirical potential models which brought spectacular success in electronic band structure calculations, phonon studies, etc., with relatively cheap computation cost. For example, the pair potential in an empirical pseudopotential model (EPM) is usually parameterised three terms which

can be determined by fitting data to associated experiments. Based on the EPM, pressure-induced phase transitions, surface reconstructions, and defect formation can be systematically studied [46]. Nevertheless, the main drawback of all empirical treatments is that the empirical potentials lack transferability which limits the applications of these models.

Instead of empirical models, potentials can be also constructed from a knowledge of atomic wavefunctions and the corresponding quantum-mechanical modelling is called '*first principles*' method. There exist a wide variety of first principles (or *ab initio*) calculations which have been built to deal with this computational challenge. One of the outstanding schemes, *ab initio* total-energy pseudopotential calculation, will be discussed in detail in this chapter. Based on this robust technique, pressure-induced structural, vibrational, and electronic properties of materials can be comprehensively studied not only for small atomic systems but also for large-scale condensed matter.

3.2 Structure Study: *Ab-initio* Total-energy Calculations

Total energy calculations of crystals always deal with systems having coupling between electrons and nuclei. However, the large difference between electronic and ionic mass yield a useful assumption in which the nuclei can be treated as an adiabatic background for instantaneous motion of electrons. This adiabatic principle is known as the Born-Oppenheimer (BO) approximation and it is adopted by almost all quantum-mechanical calculations. Unfortunately, the total energy calculations are still impossible if only the BO approximation is included. To perform an accurate and efficient *ab initio* total energy calculation, other assumptions and computational skills are necessary and are explained as follows

3.2.1 Density Functional Formalism – An Efficient Approach for Many-electron Systems

The method of handling the multi-electron system is the density-functional (DF) approach which treats electrons as continuous media, like jelly, and then all physical properties can be represented as a functional of the total electron density $\rho(\mathbf{r})= |\Psi|^2$. The advantage of DF theorem is to replace the N-dimensional electron wave function of the N-electron system by a simple three-dimensional electron density. The idea of DF methods is proposed by Thomas and Fermi to derive the ground-state electron configuration of N-electron atoms. In the traditional Thomas-Fermi (TF) model, the Hamiltonian of an atom with N electrons contains the kinetic energy (T_{TF}), electron-nucleus attractive energy ($V_{ne(TF)}$), and electron-electron repulsive energy ($V_{ee(TF)}$). Based on a locally homogeneous electron approximation, the functional T_{TF} can be determined exactly. Also, the explicit form of $V_{ne(TF)}$ and $V_{ee(TF)}$ can be derived from the classical electromagnetic model. Thus, the TF total energy functional ($E_{TF}[\rho]$) is given by

$$\begin{aligned} E_{TF}[\rho(\mathbf{r})] &= T_{TF}[\rho(\mathbf{r})] + V_{ne(TF)}[\rho(\mathbf{r})] + V_{ee(TF)}[\rho(\mathbf{r})] \\ &= \frac{3}{10}(3\pi^2)^{2/3}\int \rho^{5/3}(\mathbf{r}) - Z\int \frac{\rho(\mathbf{r})}{\mathbf{r}}d\mathbf{r} + \frac{1}{2}\int\int \frac{\rho(\mathbf{r}_1)\rho(\mathbf{r}_2)}{|\mathbf{r}_1 - \mathbf{r}_2|}d\mathbf{r}_1 d\mathbf{r}_2 \quad (3.3) \end{aligned}$$

where Z is the valence and $\mathbf{r}_1$,$\mathbf{r}_2$ denote locations of different electrons. According to the variational principle, the ground state electron density of an atom can be obtained from minimising the energy functional subject to the constraint of charge conservation. The constrainted variational principle and the Euler-Lagrange equation of the Lagrange multiplier, λ_{TF}, are formulated as

$$\delta\left\{E_{TF}[\rho(\mathbf{r})] - \lambda_{TF}\left(\int \rho(\mathbf{r})d\mathbf{r} - N\right)\right\} = 0 \quad (3.4)$$

$$\lambda_{TF} = \frac{\delta E_{TF}[\rho(\mathbf{r})]}{\delta\rho(\mathbf{r})} = \frac{1}{2}(3\pi^2)^{2/3}\rho^{2/3}(\mathbf{r}) - \frac{Z}{\mathbf{r}} + \int \frac{\rho(\mathbf{r}')}{|\mathbf{r}\text{-}\mathbf{r}'|}d\mathbf{r}' \tag{3.5}$$

However, this oversimplified model and subsequent modifications cannot provide the precisely quantitative predictions in most cases.

The renaissance of the DF scheme was revived by Hohenberg and Kohn (HK) in their remarkable density-functional theory (DFT) for nondegenerate systems [47]. First, the HK-DFT proved rigorously that the charge density $\rho(\mathbf{r})$ is a well-defined basic variable which determines all ground-state physical properties. The rationale of the HK-DFT is to reformulate the exact energy functional E_{HK} of an N-electron system under the external potential $v_{ion}(\mathbf{r})$ in terms of the v_{ion}-dependent and v_{ion}-independent components.

$$\begin{aligned} E_{HK}[\rho(\mathbf{r})] &= \{T[\rho(\mathbf{r})] + V_{ee}[\rho(\mathbf{r})]\} + V_{ne}[\rho(\mathbf{r})] \\ &= F_{HK}[\rho(\mathbf{r})] + V_{ne}[\rho(\mathbf{r})] \\ &= F_{HK}[\rho(\mathbf{r})] + \int v_{ion}(\mathbf{r})\rho(\mathbf{r})d\mathbf{r} \end{aligned} \tag{3.6}$$

where T (kinectic energy) and V_{ee} (electron-electron interaction energy) are both v_{ion}-independent, however, V_{ne} which represents the interaction between electrons and an external field contributed from nuclei is solely determined by the external potential v_{ion}. This energy functional suggests a universal functional $F_{HK}[\rho]$ can be applied to any multi-electron system once the explicit form of F_{HK} is obtained.

In the 2nd HK theorem, the ground state can be achieved by an energy variational principle (like Eqn. (3.4)) and the associated Euler-Lagrange equation is

$$\lambda_{HK} = \frac{\delta E_{HK}[\rho(\mathbf{r})]}{\delta\rho(\mathbf{r})} = v_{ion}(\mathbf{r}) + \frac{\delta F_{HK}[\rho(\mathbf{r})]}{\delta\rho(\mathbf{r})} \tag{3.7}$$

where λ_{HK} is the Lagrange multiplier with respect to the electron number conservation

constraint

$$N = \int \rho(\mathbf{r}) d\mathbf{r} \tag{3.8}$$

The HK theorems have also been confirmed in a more general degenerate system in which the ground state density is not associated with the external potential $v_{ion}(\mathbf{r})$ only [48, 49]. However, the N-representable total electron density of this general system is not as well-behaved as the v_{ion}-representable charge density in a simple nondegenerate system. The modified universal functional F'_{HK} corresponds to the minimum value of F_{HK} which is obtained from different wave functions Ψ associated with a particular density ρ

$$F'_{HK}[\rho] \equiv \min_{\Psi \to \rho} < \Psi | \widehat{T} + \widehat{V}_{ee} | \Psi > \tag{3.9}$$

where $\widehat{T}$ and $\widehat{V}_{ee}$ is the operator corresponding to $T[\rho]$ and $V_{ee}[\rho]$, respectively. This generalisation of HK theorems also gives the possibility to build up the finite-temperature DFT [50].

Based on the HK theorems, an independent-particle form of the DFT was proposed by Kohn and Sham [51]. In the Kohn-Sham (KS) model, the kinetic energy ($T_s[\rho]$) derived from noninteracting electrons is included in the KS universal functional F_{KS}. In addition, the electron-electron interaction V_{ee} is separated into a classical electron-electron repulsive energy $J[\rho]$ and a quantum-mechanical exchange-correlation energy $G_{xc}[\rho]$. So, the KS total energy functional $E_{KS}[\rho]$ is

$$\begin{aligned} E_{KS}[\rho(\mathbf{r})] &= F_{KS}[\rho(\mathbf{r})] + V_{ne}[\rho(\mathbf{r})] \\ &= T_s[\rho(\mathbf{r})] + J[\rho(\mathbf{r})] + G_{xc}[\rho(\mathbf{r})] + \int v_{ion}(\mathbf{r})\rho(\mathbf{r}) d\mathbf{r} \end{aligned} \tag{3.10}$$

The total electron density still satisfies the constraint of Eqn. (3.8). Thus, the Euler

equation of the KS model becomes

$$\begin{aligned}\lambda_{KS} &= \left\{v_{ion}(\mathbf{r}) + \frac{\delta J[\rho(\mathbf{r})]}{\delta\rho(\mathbf{r})} + \frac{\delta G_{xc}[\rho(\mathbf{r})]}{\delta\rho(\mathbf{r})}\right\} + \frac{\delta T_s[\rho(\mathbf{r})]}{\delta\rho(\mathbf{r})} \\ &= \left\{v_{ion}(\mathbf{r}) + \int \frac{\rho(\mathbf{r}')}{|\mathbf{r}\text{-}\mathbf{r}'|}d\mathbf{r}' + v_{xc}(\mathbf{r})\right\} + \frac{\delta T_s[\rho(\mathbf{r})]}{\delta\rho(\mathbf{r})} \\ &= v_{eff}(\mathbf{r}) + \frac{\delta T_s[\rho(\mathbf{r})]}{\delta\rho(\mathbf{r})} \end{aligned} \tag{3.11}$$

where v_{xc} and v_{eff} is the exchange-correlation potential and effictive potential, respectively. From Eqn. (3.11), the real multi-electron interacting system can be simulated by the noninteracting electrons under the influence of the effective potential v_{eff}. Thereby, the total electron density of the N-electron system can be decomposed into N single-particle wavefunction ψ of each independent electron

$$\rho(\mathbf{r}) = \sum_{i=1}^{N} \psi_i^*(\mathbf{r})\psi_i(\mathbf{r}) \tag{3.12}$$

In this expression, the KS kinetic energy functional $T_s[\rho]$ can be calculated indirectly but exactly as

$$\begin{aligned} T_s[\rho(\mathbf{r})] &= \sum_{i=1}^{N} < \psi_i(\mathbf{r})|(-\frac{1}{2}\nabla^2)|\psi_i(\mathbf{r}) > \\ &= \sum_{i=1}^{N}(-\frac{1}{2})\int \psi_i^*(\mathbf{r})\nabla^2\psi_i(\mathbf{r})d\mathbf{r} \end{aligned} \tag{3.13}$$

The variation principle therefore leads to a one-electron KS equation for a specific wavefunction $\psi_i(\mathbf{r})$

$$\left\{-\frac{1}{2}\nabla^2 + v_{eff}(\mathbf{r})\right\}\psi_i(\mathbf{r}) = \epsilon_i\psi_i(\mathbf{r}) \tag{3.14}$$

where ϵ_i is the KS eigenvalue which, strictly speaking, has no simple physical meaning. Hence, the self-consistent one-electron wavefunction ψ_i can be obtained by iteratively solving the KS equation Eqn. (3.14), just like the Hartree-Fock scheme but without

any coupling between different orbitals, and the total electron density is determined from Eqn. 3.12. The ground-state total energy can be derived from calculated KS eigenvalues ϵ_i and the ground-state electron density $\rho(\mathbf{r})$

$$E = \sum_{i}^{N} \epsilon_i - \frac{1}{2} \int \frac{\rho(\mathbf{r})\rho(\mathbf{r}')}{|\mathbf{r}\text{-}\mathbf{r}'|} + G_{xc}[\rho(\mathbf{r})] - \int v_{xc}(\mathbf{r})\rho(\mathbf{r})d\mathbf{r} \tag{3.15}$$

However, the solution of the canonical KS equation (Eqn. (3.14)) is feasible provided that the effective potential v_{eff} is known. Among the components of v_{eff} (Eqn. 3.11), the explicit form for $\delta J[\rho]/\delta\rho$ and v_{ion} can be regarded as the electrostatic potentials. The challenge is to describe the exchange-correlation component v_{xc} precisely. The simplest but essential assumption of the exchange-correlation energy is the local density approximation (LDA) in which $G_{xc}[\rho]$ is a function of g_{xc} – the exchange-correlation energy per particle of a uniform electron gas of density ρ. Then, the local representation of the nonlocal exchange-correlation energy functional and corresponding potential v_{xc} are

$$G_{xc}^{LDA}[\rho(\mathbf{r})] \equiv \int \rho(\mathbf{r}) g_{xc}[\rho(\mathbf{r})] d\mathbf{r} \tag{3.16}$$

$$v_{xc}^{LDA}(\mathbf{r}) = \frac{\delta G_{xc}^{LDA}[\rho(\mathbf{r})]}{\delta\rho(\mathbf{r})} = g_{xc}[\rho(\mathbf{r})] + \rho(\mathbf{r}) \frac{\delta g_{xc}[\rho(\mathbf{r})]}{\delta\rho(\mathbf{r})} \tag{3.17}$$

where the functional $g_{xc}[\rho]$ can be split into two parts: exchange component $g_x[\rho]$ and correlation component $g_c[\rho]$. The analytic form for g_x and g_c can be determined from the Hartree-Fock exchange-energy functional [50] and quantum Monte Carlo calculations [52], respectively.

Moreover, the generic quantum-mechanical nonlocal electron-correlation effect in real systems can be visualised by the exchange and correlation hole in the real-space electrostatic integral expression of G_{xc} [53]

$$G_{xc} = \frac{1}{2} \int \rho(\mathbf{r}) \left\{ \int \frac{\rho_{xc}(\mathbf{r}, \mathbf{r}')}{|\mathbf{r}\text{-}\mathbf{r}'|} d\mathbf{r}' \right\} d\mathbf{r} \tag{3.18}$$

where $\rho_{xc}(\mathbf{r}, \mathbf{r}')$ is composed of the exchange hole density $\rho_x(\mathbf{r}, \mathbf{r}')$ and the correlation hole density $\rho_c(\mathbf{r}, \mathbf{r}')$. The $\rho_x(\mathbf{r}, \mathbf{r}')$ describing Pauli-exclusion parallel-spin electrons around a given electron is strictly negative. Nevertheless, $\rho_c(\mathbf{r}, \mathbf{r}')_{\mathbf{r}'\to\mathbf{r}} < 0$ according to the Columbic repulsion between electrons with same spins, and $\rho_c(\mathbf{r}, \mathbf{r}')_{\mathbf{r}'\gg\mathbf{r}} > 0$ is due to the accumulation of repelled charges. Indeed, the ρ_x and ρ_c satisfies

$$\int \rho_x(\mathbf{r}, \mathbf{r}')d\mathbf{r}' = -1 \tag{3.19}$$

$$\int \rho_c(\mathbf{r}, \mathbf{r}')d\mathbf{r}' = 0 \tag{3.20}$$

Therefore, any proper model for exchange-correlation effect must satisfy the sum rules of Eqn. (3.19) and (3.20). This is the main reason to account for the significant success of the simple KS-LDA model. Further, an improved local-spin-density (LSD) approximation including an extra variable of spin has also been developed [54] and which allows different electron distributions with respect to various spin configuration. The comparison between the exchange-correlation hole of LDA and LSD is made and illustrated in Fig. 3.2.

However, the LDA (or LSD) takes into account the strictly localised electron behaviour only and ignores the nonlocal contribution of total energy. This approximation gives rise to an underestimate of calculated equilibrium structure parameters (*eg.* lattice constants) within LDA. Recently, a nonphenomenological gradient functional, generalised gradient approximation (GGA), was introduced to extend the strict localisation of LDA into a semi-local region [55]. In GGA, the exchange-correlation energy G_{xc}^{LDA} of Eqn. (3.17) is replaced by a general form which includes the variable of the gradient of electron density

$$G_{xc}^{GGA}[\rho(\mathbf{r})] = \int \mathcal{G}[\rho(\mathbf{r}), \nabla\rho(\mathbf{r})]d\mathbf{r} \tag{3.21}$$

where $\mathcal{G}$ is a functional of two functions ρ and $\nabla\rho$. For small atomic and molecular

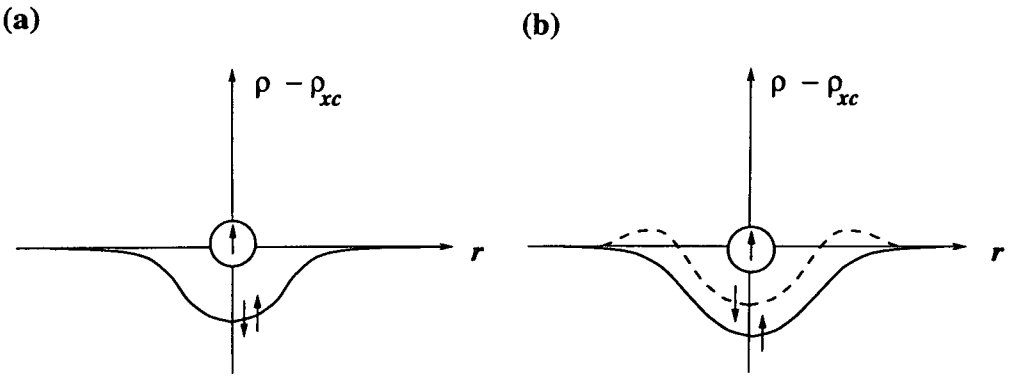

Figure 3.2. Schematic diagram for the exchange-correlation hole in LDA (a) LSD (b). A given electron is denoted as a circle and small arrows represent electron spins. It can be seen that the charge distribution , $\rho - \rho_{xc}$, in LDA is an average of ones which has parallel-spin (solid curve) and antiparallel-spin (dashed curve) with respect to the given electron, respectively, in LSD

systems, the GGA gives more precise predictions of physical quantities than does LDA [56]. However, in the stronger long-range interacting solids, a more generalised consideration of the fully-nonlocal model is needed to obtain the exact exchange-correlation energy.

The applications of DFT are exploited in many fields, such as atoms, molecules, clusters, surface properties, liquids, plasmas, and even superconductors. Recent developments lift the zero-temperature limitation of the original DFT explained above and also enable the calculations including realivistic effects [57]. Also, the progressive growth of time-dependent DFT [58] provides a computational technique to tackle the dynamical properties of materials. Furthermore, the DFT extension into van der Waals interactions regime [59] implies that DFT is a versatile approach for complex many-body systems.

3.2.2 Periodic Boundary Conditions

In spite of the decoupling of electron-electron mutual interactions in the DFT, the total charge density in the form of Eqn. (3.12) is still formidable since there exist an enormous number of non-interacting electrons in typical materials ($N \approx 10^{23}$). However, in crystalline solids having highly long-range order, this impractical problem can be overcome by involving Bloch's formulation [60]. In this theorem, Bloch's electrons obey the one-electron Schrödinger equation (like Eqn. (3.14)) with a periodic background potential. Each associated wavefunction can be expressed by a product of a wavelike component and a cell-periodic function $f(\mathbf{r})$ expanded as a discrete plane-wave basis set

$$\begin{aligned} \psi_j(\mathbf{r}) &= f_j(\mathbf{r})\ exp[i\mathbf{k}\cdot\mathbf{r}] \\ &= \left\{\sum_K c_{j,\mathbf{K}}\ exp[i\mathbf{K}\cdot\mathbf{r}]\right\}\ exp[i\mathbf{k}\cdot\mathbf{r}] \\ &= \sum_K c_{j,\mathbf{k}+\mathbf{K}}\ exp[i(\mathbf{K}+\mathbf{k})\cdot\mathbf{r}] \end{aligned} \tag{3.22}$$

where $\mathbf{k}$ is the wave vector of the wavelike part and $\mathbf{K}$ is the reciprocal lattice vectors of the crystal. According to the periodicity of the crystal structure, only a set of $\mathbf{k}$ points within the first Brillouin zone in the reciprocal space are needed for electronic states calculations. However, the electronic potential in the bulk solid is composed of finite electronic states at each point of the infinite $\mathbf{k}$-point set and the infinity of the plane-wave expansion of electron wavefunction of Eqn. (3.22) remains. Therefore, another approximation must be introduced to make large scale electronic structure calculations available.

In view of the continuity of electron wavefunctions, the $\mathbf{k}$-space can be discretised as finite domains in which the electron wavefunctions associated with different $\mathbf{k}$ points in the same region are almost identical and the whole BZ can be approximated by a finite set of special $\mathbf{k}$ points corresponding to specific $\mathbf{k}$-space domains. Based on this

assumption, the infinite electron states calculation is mapped onto a feasible calculation of electron wavefunctions at finite special k points. It is obvious that the error of this simplification can be systematically reduced by using a more dense special k-point set. Many methods [61, 62, 63] have been employed to construct efficient special sets of k points at which occupied electronic states give rise to very accurate approximations to the electronic potential and the contribution to the total energy. A common scheme for BZ integrations proposed by Monkhorst and Pack [64] was implemented in the following calculations in this thesis.

In the Monkhorst-Pack method, the BZ is discretised as a three-dimensional grid in which only a few special k-space lattice points are needed to describe the average behaviour of the BZ integral for any physical quantity. In the general case, a cubic Monkhorst-Pack grid of size N^3 is used and the wave vector for each lattice point within a coordinate frame having a central origin is defined as

$$\mathbf{k}_{MP}(n_i) = \frac{2n_1 - N - 1}{2N}\mathbf{b}_1 + \frac{2n_2 - N - 1}{2N}\mathbf{b}_2 + \frac{2n_3 - N - 1}{2N}\mathbf{b}_3 \tag{3.23}$$

where $\{\mathbf{b}_i | i = 1, 2, 3\}$ is the set of primitive reciprocal vectors and $\{n_i | i = 1, 2, 3\}$ is the index of each Monkhorst-Pack lattice point. Thus, any smoothly varying periodic function in reciprocal space $\mathcal{F}(\mathbf{k})$ can be expanded in terms of a Fourier series

$$\mathcal{F}(\mathbf{k}_{MP}) = \sum_{m=1}^{\infty} \mathcal{F}_m \; exp[i\mathbf{k}_{MP}(m) \cdot \mathbf{r}] \tag{3.24}$$

where $\mathcal{F}_m$ is the Fourier coefficient. Under the effects of the lattice point group operations $\{T_i | i = 1 \cdots n_T\}$, the periodic function has complete symmetry of lattice is formulated as

$$\begin{aligned} \mathcal{F}(\mathbf{k}_{MP}) &= \frac{1}{n_T}\sum_i \mathcal{F}(T_i\mathbf{k}_{MP}) \\ &= \frac{1}{n_T}\sum_{m=1}^{\infty} \mathcal{F}_m \sum_{|\mathbf{r}|=\mathbf{C_m}} exp[i\mathbf{k}_{MP} \cdot \mathbf{r}] \end{aligned}$$

$$= \sum_{m=1}^{\infty} \mathcal{F}_m A_m(\mathbf{k}_{MP}) \tag{3.25}$$

where the new basis A_m is a set of lattice vectors within the k-space shell of a radii C_m. In addition, the average value of the Fourier coefficient $\overline{\mathcal{F}}_m$ corresponding to a specific C_m can be evaluated by

$$\overline{\mathcal{F}}_m = \frac{1}{N^3} \sum_{j=1}^{p(N)} w_j \mathcal{F}(\mathbf{k}_j) A_m(\mathbf{k}_j) \tag{3.26}$$

where $p(N)$ is the symmetry-dependent number of points $\mathbf{k}_j$ in $\mathbf{k}_{MP}$. w_j is the weight associated with $\mathbf{k}_j$ and is the ratio of the order of the whole $\{T_i\}$ to the order of the point group of the wave vector at $\mathbf{k}_j$. So, the average value of the BZ integration for $\mathcal{F}$ can be implemented by summing up average values of $\mathcal{F}_m$ with respect to different radius within the primitive cell volume v

$$\frac{v}{8\pi^3} \int_{BZ} \overline{\mathcal{F}}(\mathbf{k}) d\mathbf{k} = \overline{\mathcal{F}} = \sum_{m=1}^{\infty} \overline{\mathcal{F}}_m A_m(\mathbf{k}) \tag{3.27}$$

However, the infinity in Eqn. (3.27) can be removed since the orthonormal A_m satisfies the restriction

$$|r_j| < \frac{N}{2} \longrightarrow |\mathbf{r}| = C_m < \frac{\sqrt{3}}{2} N \text{ (in the cubic grid)} \tag{3.28}$$

Hence, for a chosen Monkhorst-Pack grid $\{\mathbf{K}_{MP}\}$, the special point $\mathbf{k}_i$ which represents all the points $\mathbf{k}_j$ in the set of $p(N)$ (in Eqn. (3.26)) is determined from symmetry elements of the crystal. From Eqn. (3.26), the weight factors of different special k points can be obtained from the lattice point group. The physical properties (such as electron density, electron wave function, etc) over whole BZ are therefore derived from

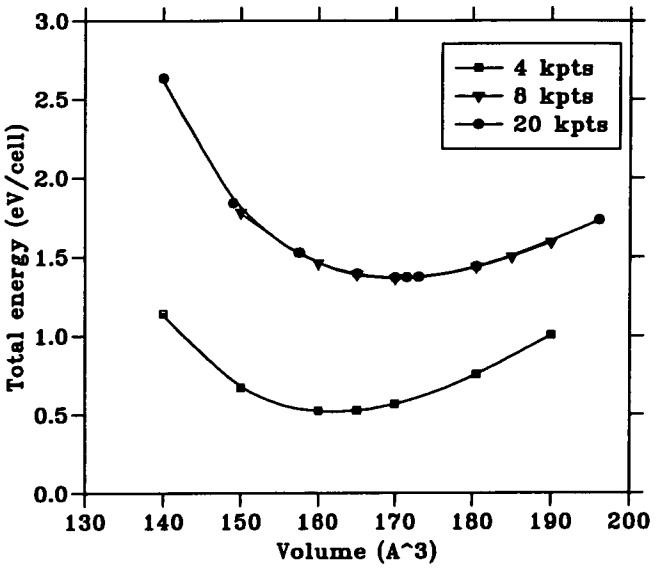

Figure 3.3. Graphs showing relative total energy versus unit cell volume for several different special k-point sets of GeSe. The results for the 4-, 8-, and 20-k-point set are shown as squares, triangles, and circles, respectively. However, the unit cell parameters were not optimised at every volume in these convergence tests. The curves through the calculated data are guides to the eye.

Eqn. (3.27) and evaluated by summing finite terms which satisfy Eqn. (3.28)

$$\int_{BZ} \mathcal{F}(\mathbf{k}_i) = \sum_m \overline{\mathcal{F}}_m A_m(\mathbf{k}_i) \tag{3.29}$$

Further, for some less-symmetric Bravais lattices, a noncubic Monkhorst-Pack grid may be chosen to get a more appropriate interpolation for the associated BZ.

Usually, the Monkhorst-Pack k-point sampling scheme provides an accurate approximation for the total energy of insulators and semiconductors. The error due to a inadequately coarse grid of **k** points can be reduced by using a finer mesh **k** points. For example, the calculated total energy of a semiconductor GeSe as a function of volume for different k-point samplings is shown in Fig. 3.3. Three Monkhorst-Pack grids, $2 \times 4 \times 4$, $4 \times 4 \times 4$ and $4 \times 4 \times 10$ corresponding to 4, 8, and 20 special **k** points, respectively, are used. It is evident that only a few **k** points are needed to give converged total energies of semiconductors. However, extremely large numbers of **k** points are required for metallic systems since the periodic functions are not smooth around the

Fermi surface and, actually, they become discontinuous at the Fermi surface [65].

Another issue of the computational difficulty comes from the infinite discrete plane-wave basis set as shown in Eqn. (3.22). This disadvantage of the choice of basis set can be removed using a kinetic energy cut-off $E_{cut-off}$ to truncate the infinite series of plane waves since the coefficients $c_{j,\mathbf{k}+\mathbf{K}}$ in Eqn. (3.22) referred to higher kinetic energy $(\hbar^2/2m)|\mathbf{k}+\mathbf{K}|$ are very small while comparing with the terms with lower kinetic energy. The magnitude of error due to the introduction of the kinetic energy cut-off can always be diminished and by increasing the value of $E_{cut-off}$. Thus, the KS equation (Eqn. (3.14)) can be reformulated in terms of finite Bloch's electron wavefunctions

$$\sum_{\mathbf{K}'}\left[\frac{\hbar^2}{2m}|\mathbf{k}+\mathbf{K}|^2\delta_{\mathbf{K}\mathbf{K}'}+v_{eff}(\mathbf{K}\text{-}\mathbf{K}')\right]c_{i,\mathbf{k}+\mathbf{K}'}=\epsilon_i c_{i,\mathbf{k}+\mathbf{K}}$$
$$H_{\mathbf{k}-\mathbf{K},\mathbf{k}-\mathbf{K}'}c_{i,\mathbf{k}+\mathbf{K}'}=\epsilon_i c_{i,\mathbf{k}+\mathbf{K}} \qquad (3.30)$$

where $v_{eff}(\mathbf{K}\text{-}\mathbf{K}')$ is the recriprocal expression of the effective potential in Eqn. (3.11). The solution of the secular equation Eqn. (3.30) is obtained by a diagonalisation of the Hamiltonian matrix H. However, the complexity of solving this secular equation scales as $\mathcal{O}(N^3)$ and a higher kinetic energy cut-off giving a large size of matrix H makes Eqn. (3.30) intractable. In order to reduce the matrix size of H and decrease the cutoff energy, the pseudopotential approximation which describes the core and valence electrons is introduced and will be discussed in Sec. 3.2.3. Moreover, the periodic treatment presented in this section can be generalised to apply to aperiodic configurations of atoms by simply constructing a large unit cell containing this special configuration in the space having virtual periodicity [66].

3.2.3 Pseudopotential Approximation for Electron-Ion Interactions

It is well known that most physical and chemical properties of solids are governed mainly by the valence as opposed to core electrons. However, inside the core region,

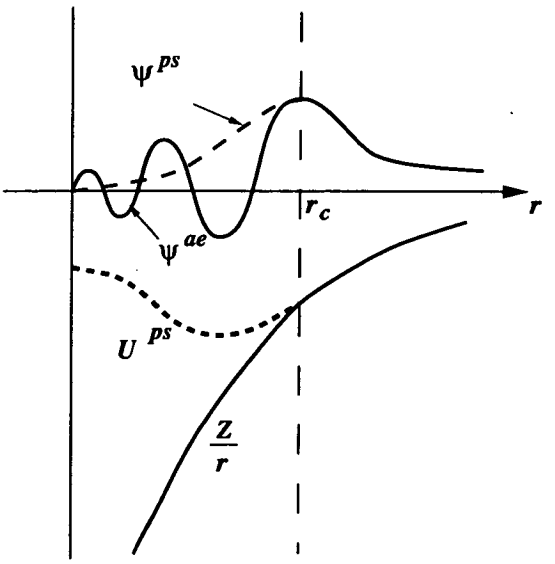

Figure 3.4. Schematic illustration of the pseudoelectron ψ^{PS} (dashed curves) and real all-electron ψ^{ae} (solid curves) wavefunctions and associated potentials U^{PS} and Z/r as a function of r. The pseudoelectron is identical to a real one while r beyonds the core radius r_c.

the tightly bound core orbitals and the rapidly oscillating valence wavefunctions are always represented by a large number of plane waves. As pointed out in the preceding discussion, this requirement for the plane-wave expansion of core electrons yields computational impracticality. In order to remove this hurdle, a pseudopotential (introduced initially by Fermi) is used to separate electrons into outer valence and inner core types. In fact, in the pseudopotential approximation, the core electrons are removed and the strong ionic potential is replaced by a weaker and smooth pseudopotential acting on an associated pseudo wavefunction in the core region. A schematic illustration of all-electron and pseudoelectron potentials and their corresponding wavefunctions is depicted in Fig. 3.4

Generally, based on the fundamental quantum-mechanical collision theory [67], the asymptotic form of a electron wave function ψ_l with particular angular momentum l

scattered by an attractived potential U is given by

$$\psi_l(r) \approx Y_{lm}(\theta, \phi) \left\{ \frac{1}{r} \sin \left[kr - \frac{l\pi}{2} + \delta_l(k) \right] \right\} \tag{3.31}$$

where $Y_{lm}(\theta, \phi)$ is the special harmonic and δ_l is the scattering phase shift. The corresponding l-dependent potential U_l is thus derived from inverting a radial Schrödinger equation

$$U_l(r) = \frac{\hbar^2}{2\mu\psi_l(r)} \left[\frac{d^2\psi_l(r)}{dr^2} \right] + E_l - \frac{l(l+1)}{r^2} \tag{3.32}$$

where μ and E_l denotes the reduced mass and the eigenvalue with respect to occupied orbitals ψ_l, respectively. Thereby, for the pseudopotential within the core region, the phase shift produced by the radial nodeless pseudo wavefunction ψ_l^{ps} depends on various angular momenta and, thus, a general form for the associated l-dependent pseudopotential U_{NL}^{ps} referred to nonlocal pseudopotential is

$$U_{NL}^{ps} = \sum_{lm} |Y_{lm} > U_l < Y_{lm}| \tag{3.33}$$

where U_l is the pseudopotential for angular momentum l and the bra ($|Y_{lm}>$) and ket ($< Y_{lm}|$) project out the l, m component of ψ_l^{ps}. A special case in which the pseudopotential is a constant for different angular momentum components is called a local pseudopotential U_L^{ps}. Using the U_L^{ps}, the complexity of the operation of Hamiltonian on the wavefunction expanded as N plane waves can be substantially reduced from $\mathcal{O}(N^2)$ of U_{NL}^{ps} to $\mathcal{O}(N \ln N)$ [68]. However, this local pseudopotential is not appropriate for every atom.

As shown in Fig. 3.4, the pseudopotential and the pseudo wavefunctions should be identical to the true ionic potential and the true valence wavefunctions, respectively, beyond the core radius r_c to preserve the scattering phase shifts of real valence electrons. Also, the equality of valence electron density of pseudo electrons and of true electrons

outside the core is necessary for maintaining the accurate description of the exchange-correlation energy functional G_{xc}. Taking into account the above restrictions, two constraints [69] should be satisfied for any generated pseudo wavefunction $\psi^{ps}(r)$

$$\int_0^{r_c} |\psi(r)|^2 r^2 d^3r = \int_0^{r_c} |\psi_{ps}(r)|^2 r^2 d^3r \tag{3.34}$$

and

$$\frac{d}{d\epsilon}\left(\frac{d}{dr}\ln\psi_l\right)_{r_c} = \frac{d}{d\epsilon}\left(\frac{d}{dr}\ln\psi_l^{ps}\right)_{r_c} \tag{3.35}$$

where Eqn. (3.34) indicating the conservation of the pseudo and real electron density within the core region is referred to the *norm conservation* requirement. Also, the well-behaved logarithmic derivative of the l-component of a good pseudo wavefunction in Eqn. (3.35) guarantees that the scattering phase shifts are the same to 1st order in energy and the associated potential is transferable. The corresponding pseudopotential derived from the above pseudo wavefunctions is named the *norm-conserving pseudopotential* which can be applied in various atomic situations.

In view of the expensive computational cost of implementing the nonlocal pseudopotential in Eqn. (3.33), Kleinman and Bylander [70] suggested an efficient transformation to generate the U_{NL}^{ps}. In Kleinman-Bylander pseudopotentials U_{NL}^{KB}, the l-component of a norm-conserving pseudopotential is separated into a local part U_L and a small variation δU_l

$$U_{l,NL}^{KB} = U_L + \delta U_l \tag{3.36}$$

and, under the LDA given in Sec. 3.2.1, Eqn. 3.33 can be rewritten as

$$U_{NL}^{KB} = U_L + \sum_{lm} \frac{|\phi_m^0 \delta U_l >< \delta U_l \phi_m^0|}{< \phi_m^0 |\delta U_l| \phi_m^0 >} \tag{3.37}$$

where ϕ_m^0 are the wavefunctions of the pseudoatom. Since the U_{NL}^{KB} projects the wavefunction onto a single basis state rather than a radically complete basis set for spherical harmonic components, the degree of transferability of the Kleinman-Bylander pseudopotential is not high [71]. This low transferability can be improved by some modifications: a proper choice of U_L, reducing the core radius r_c, etc [72].

Concerning the characteristic requirements of pseudopotentials mentioned above, much effort [73, 74] has been devoted to generate good pseudopotentials, especially soft ones, which lead to rapid convergence in solids. Among different schemes, the recently developed *kinetic energy filter tuning*, also called Q_c tuning, method [75] was used here to generate optimised pseudopotentials. Like other contemporary approaches, the Q_c tuning scheme starts from an all-electron atomic calculation with a selected exchange-correlation energy, G_{xc}^{LDA} or G_{xc}^{GGA}, to determine all the atomic states of a given configuration. In this procedure, the all-electron valence charge wavefunction ψ^{ae} can be obtained and will be the basis to generate a pseudo wavefunction. Following the criterion of the continuity of pseudopotentials proposed by Rappe *et.al* [73], the l-component pseudo wavefunction ψ_l^{ps} inside the core regime can be described by a linear combination of specially chosen spherical Bessel functions $j_l(k_i r)$ with a boundary condition in which the logarithmic derivates of $j_l(k_i r)$ match those of $\psi_l^{ae}(r)$ at r_c

$$\psi_l^{ps}(r) = \sum_{i=1}^{n} \alpha_i j_l(k_i r) \text{ (for } 0 < r < r_c) \; ; \; \frac{j_l'(k_i r_c)}{j_l(k_i r_c)} = \frac{\psi_l^{ae\prime}(r_c)}{\psi_l^{ae}(r_c)} \tag{3.38}$$

Beyond the core radius, the pseudo wave function is identical to the all-electron one

$$\psi_l^{ps}(r) = \psi_l^{ae}(r) \text{ (for } r \geq r_c) \tag{3.39}$$

In addition to the constraints of the norm conversation and the continuity of the first

derivate of $\psi_l^{ps}(r)$ at $r = r_c$

$$\left.\frac{d\psi_l^{ps}(r)}{dr}\right|_{r_c} = \left.\frac{d\psi_l^{ae}(r)}{dr}\right|_{r_c} \tag{3.40}$$

The proper soft pseudo wavefunction is thus generated from the minimisation of the kinetic energy beyond the adjustable cutoff parameter Q_c

$$\min \int_{Q_c}^{\infty} k^2 |\psi_l^{ps}(k)|^2 d^3k \;=\; \min \left\{ -\int_0^{\infty} \psi_l^{ps*}(r) \nabla^2 \psi_l^{ps}(r) d^3r - \int_0^{Q_c} k^2 |\psi_l^{ps}(k)|^2 d^3k \right\} \tag{3.41}$$

The improvement the Q_c tuning method achieved is that only three Bessel functions are utilised in Eqn. (3.38) and Q_c was found as an effective controlling parameter to minimise Eqn. (3.41). Hence, for a good choice of r_c which assures the high transferability of the pseudopotential, the pseudo wavefunctions can be determined by tuning Q_c to obtain the best fit of the logarithmic derivate curve of the all-electron wavefunction. Once the pseudo wavefunctions are found, the optimised pseudopotential is derived by inverting Schrödinger equation (like Eqn. (3.32)). A minor difficulty of the Q_c tuning approach is that the logarithmic derivate test is r_c-independent and cannot provide any hint of the value of r_c. Thus, for various applications, systematic tests for the optimised pseudopotentials with respect to different r_c must be done to verify the pseudopotential approximation in solid state calculations. The examples of some ionic-pseudopotential tests can be found elsewhere [75].

3.2.4 Molecular Dynamics for Electronic Ground-state

Although the pseudopotential approximations significantly reduce the size of plane-wave expansion of electron wave functions, the computational cost of total energy calculations is still dominated by a conventional matrix diagonalisation for obtaining KS orbitals (Eqn. (3.30)) which needs $\mathcal{O}(N^3)$ operations. An efficient procedure, the

Car-Parrinello scheme [76] determines the KS eigenstates for a given ionic configuration by solving a set of molecular-dynamics equations of motion.

On the BO potential energy surface, Car and Parrinello introduced the electron wavefunctions as dynamical variables. Then, as with classical molecular dynamics, the fictitious dynamics of wavefunctions and the KS energy functional E_{KS} (Eqn. (3.10)) accounts for the kinetic-energy and potential terms, respectively, and the specialised Car-Parrinello Lagrangian $\mathcal{L}'_{CP}$ for the electronic system is defined as

$$\mathcal{L}'_{CP} = \sum_i \frac{m_f}{2} < \frac{\partial \psi_i(\mathbf{r},t)}{\partial t} | \frac{\partial \psi_i(\mathbf{r},t)}{\partial t} > - E_{KS}[\{\psi_i\},\{\mathbf{R}_I\},\{\alpha_v\}] \tag{3.42}$$

where m_f is the fictitious mass of the electron wavefunction ψ_i. $\mathbf{R}_I$ and α_v is the ionic configuration and the unit cell parameters, respectively. Moreover, in order to ensure orthonormality of wavefunctions propagating along associated molecular-dynamics paths, the constrained Lagrangian $\mathcal{L}'_{CP-con}$ is

$$\begin{aligned} \mathcal{L}'_{CP-con} &= \sum_i \frac{m_f}{2} < \frac{\partial \psi_i(\mathbf{r},t)}{\partial t} | \frac{\partial \psi_i(\mathbf{r},t)}{\partial t} > - E_{KS}[\{\psi_i\},\{\mathbf{R}_I\},\{\alpha_v\}] + \\ & \sum_{i,j} \Lambda_{ij} \left\{ \int \psi_i^*(\mathbf{r},t)\psi_j(\mathbf{r},t) d^3r - \delta_{i,j} \right\} \end{aligned} \tag{3.43}$$

where Λ_{ij} is the Lagrange multiplier. According to the fixed ionic and unit-cell configuration, the parameters of $\mathbf{R}_I$ and α_v are constants with respect to wavefunctions and the constrained molecular-dynamics equation of motion for the wavefunctions is therefore derived from the Lagrange equations of motion

$$\begin{aligned} m_f \frac{\partial^2 \psi_i(\mathbf{r},t)}{\partial t^2} &= -\frac{\delta E_{KS}}{\delta \psi_i^*(\mathbf{r},t)} + \sum_j \Lambda_{ij} \psi_j(\mathbf{r},t) \\ &= -\left[H_{KS} - \sum_j \Lambda_{ij} \right] \psi_j(\mathbf{r},t) \end{aligned} \tag{3.44}$$

where H_{KS} is the KS Hamiltonian.

In practice, the orthonormal constraint is implemented by two steps: normalisation and orthogonalisation to avoid evaluating Λ_{ij} at infinitely small time steps. First, The normalisation procedure is performed by relaxing the orthogonality in the constrained equations of motion Eqn. (3.44) and thus the partially constrained equations of motion can be derived

$$m_f \frac{\partial^2 \psi_i(\mathbf{r},t)}{\partial t^2} = -\left[H_{KS} - < \psi_i(\mathbf{r},t)|H_{KS}|\psi_i(\mathbf{r},t) >\right]\psi_j(\mathbf{r},t) \tag{3.45}$$

After the integration of Eqn. (3.45) at the end of each time step, the orthogonality of wavefunctions is imposed using the Gram-Schmidt orthogonalisation scheme [77] in which the orthonormal wavefunction is constructed by a set of linearly independent wavefunctions from the intergration of the equations of motion and is ensured to be orthogonal to all lower-energy states. Thereby, for a given ionic configuration and an initial set of trial wavefunctions, the KS eigenstates are obtained from the iterative processes of solving Eqn. (3.45) and orthonormalisation until the wavefunctions are stationary and the corresponding minimum of $E_{KS}[\rho]$ is consequently recognised as the total energy of the solid.

However, in the multidimensional configuration space of $E_{KS}[\rho]$, the indirect search for the self-consistent H_{KS} described above will lead the problem of instability and fluctuation of the min $E_{KS}[\rho]$ in large scale systems due to an improper choice of time step in integrating equations of motion. This disadvantage can be overcome using direct minimisation of $E_{KS}[\rho]$ since it is believed that the $E_{KS}[\rho]$ has a global well-defined minimum value. In current numerical methods, a well-established optimisation scheme, conjugate-gradients method [78], provides an efficient searching strategy to find the extremum of functions. Superior to the conventional steep-descents method [78], the conjugate-gradients searching approach surveies all independent directions determined from the local minimum values and their derivates of previous searches. This algorithm gives an upper bound on the number of minimisation steps which is equal to

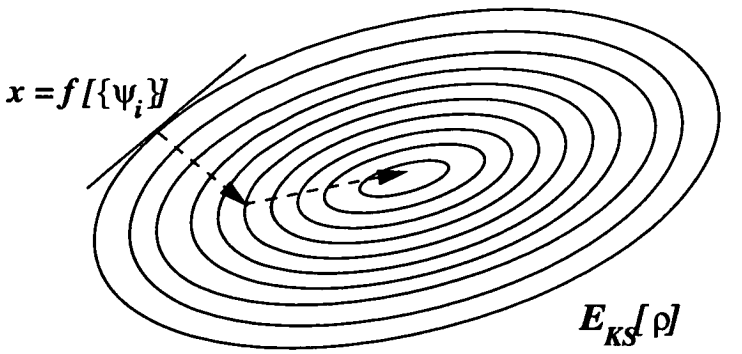

Figure 3.5. Schematic illustration for the minimisation of the Kohn-Sham energy functional $E_{KS}[\rho]$ by means of a conjugate-gradients scheme. The searching directions (dashed lines) are a functional of a set of wavefunctions $\{\psi_i\}$.

the dimensionality of the configuration space. The search procedure of applying the conjugate-gradients method on the total energy calculations is shown schematically in Fig. 3.5. Considering that the ill-conditioned conjugate-gradiented operator (associated with H_{KS} in total energy calculations) causes expensive computation in every minimisation step, a preconditioned conjugate-gradients technique is proposed [79] to speed up the convergence of direct minimisations by reshaping the conjugate-gradients operator as a well-conditioned one which has a relatively narrow spectrum of eigenvalues. So, the minimisation of E_{KS} with large number of plane-wave basis sets and higher cutoff energies is tractable.

3.2.5 Structural Relaxation

The constraints of frozen ionic positions and the fixed unit cell are now removed and the whole structure of the solid is allowed to relax to its equilibrium configuration while introducing additional structural degrees of freedom $\{\mathbf{R}_I\}$ and $\{\alpha_\upsilon\}$. Then, the original Car-Parrinello Lagrangian containing the kinetic energy terms of the ion and unit cell

can be derived from Eqn. (3.42)

$$\begin{aligned}\mathcal{L}_{CP} &= \mathcal{L}'_{CP} + \left[\sum_I \frac{1}{2} M_I (\frac{\partial R_I}{\partial t})^2 + \sum_v \frac{1}{2}\eta_v (\frac{\partial \alpha_v}{\partial t})^2\right] \\ &= \sum_i \frac{m_f}{2} < \frac{\partial \psi_i(\mathbf{r},t)}{\partial t} | \frac{\partial \psi_i(\mathbf{r},t)}{\partial t} > + \sum_I \frac{1}{2} M_I (\frac{\partial R_I}{\partial t})^2 + \\ &\quad \sum_v \frac{1}{2}\eta_v (\frac{\partial \alpha_v}{\partial t})^2 - E_{KS}[\{\psi_i\}, \{\mathbf{R}_I\}, \{\alpha_v\}] \end{aligned} \tag{3.46}$$

where M_I is the physical mass of the ion I and η_v is a fictitious mass of specific unit cell defined by $\{\alpha_v\}$. Two further sets of equations of motion related to structural parameters can be generated: first sets describe the force acting on an ion will induce a acceleration along the direction of the applied force,

$$M_I \frac{\partial^2 R_I}{\partial t^2} = -\frac{\partial E_{KS}}{\partial R_I} \tag{3.47}$$

and another sets present the stress-induced changes of lattice parameters

$$\eta_v \frac{\partial^2 \alpha_v}{\partial t^2} = -\frac{\partial E_{KS}}{\partial \alpha_v} \tag{3.48}$$

At first glance, the above two equations imply that ionic and volume-strain relaxation could be achieved simultaneously by simplely integrating equations of motion and the equilibrium structure could be obtained trivially. Nevertheless, the mutual interaction between electronic and ionic configurations in the dynamics of ions and the electron-volume coupling in stresses calculations restrict the direct integrations of Eqn. (3.47) and (3.48). These quantum-mechanical considerations for ionic and unit-cell coordinates will be addressed as follows and these features play an essential role in implementing *ab-initio* dynamical simulations of solids.

Ionic Position Relaxation

As displayed in Sec 3.2.4, the minimum of KS energy functional E_{KS} has physical meaning only within the BO approximation. Any change of the ionic configuration must be accompanied by a redistribution of the electron density with respect to the modification of the set of electron wavefunction $\{\psi_i\}$ in order to hold the whole system on the BO energy surface. This change in the wavefunction set affects the minimum value of E_{KS} and contributes to the force on ions situated at the instantaneous positions. Therefore, the general form of the force acting on an ion at R_I can be given by

$$\begin{aligned} F_I &= -\frac{dE_{KS}}{d\mathbf{R}_I} \\ &= -\frac{\partial E_{KS}}{\partial \mathbf{R}_I} - \left[\sum_i \frac{\partial E_{KS}}{\partial \psi_i}\frac{\partial \psi_i}{\partial \mathbf{R}_I} + \sum_i \frac{\partial E_{KS}}{\partial \psi_i^*}\frac{\partial \psi_i^*}{\partial \mathbf{R}_I}\right] \end{aligned} \tag{3.49}$$

In the special case where ψ_i is an exact eigenstate of H_{KS}, the component of F_I inside the square brackets of Eqn. 3.50 is equivalent to a function of the derivative $\partial < \psi_i|\psi_i > /\partial \mathbf{R}_I$ which is cancelled due to the normalisation of ψ_i. According to the Hellmann-Feynman theorem, the force on the ion I is expressed as

$$F_{HF,I} = -\frac{\partial E_{KS}}{\partial \mathbf{R}_I} \tag{3.50}$$

and is called Hellmann-Feynman force. Under the constraint of BO approximation, the Hellmann-Feynman theorem therefore enforces that the calculations of forces cannot be performed until the wavefunctions converge completely.

For the ionic relaxation, the force on each ion in the initial ionic configuration can be simply determined from Eqn. (3.50) when the electron wavefunctions are near their ground states. Then, the ions are driven by the calculated Hellmann-Feynman forces toward a new configuration which satisfies the equations of motion Eqn. (3.47). This molecular dynamics of ionic relaxation is performed by a general conjugate-gradients

minimisation scheme. Furthermore, the electron wavefunctions must be recalculated for the new ionic configuration to ensure the system remains on the BO surface. Therefore, this procedure is implemented iteratively until the ionic system is relaxed to a minimum energy configuration which is associated with the equilibrium ionic structure. However, the inevitable deviation of the electron wavefunctions from ground states in a self-consistent calculation will propagate into $F_{HF,I}$ which may cause the ionic configuration to drift away from the local minimum. Therefore, a fine tolerance of convergence of the wavefunctions is necessary in each ionic relaxation step to prevent instabilities.

Strictly speaking, the force F_I is also influenced by the variation of the basis set of the electron wavefunction. Actually, a correction term attributed to the derivative of the basis states ϕ_i with respect to the ionic positions for the Hellmann-Feynman force $F_{HF,I}$ is needed to account for this contribution and Eqn. (3.50) can be revised as

$$F'_{HF,I} = -\frac{\partial E_{KS}}{\partial \mathbf{R}_I} + \sum_i \frac{\partial E_{KS}}{\partial \phi_i} \frac{d\phi_i}{d\mathbf{R}_I} \tag{3.51}$$

The second term on the right-hand-side of Eqn. (3.51) is named the Pulay force [80]. Usually, this Pulay force cannot be ignored and the direct calculation is awkward using general basis sets. However, $d\phi_i/\mathbf{R}_I$ vanishes for the plane-wave basis set since they are independent of ionic positions. So, the Pulay force is zero for a plane wave basis set.

Unit Cell Optimisation

Now, we consider the degrees of freedom related to the unit cell and the computational techniques for relaxing the unit cell are introduced. Similar to the F_{HF} in Eqn. (3.50), a Hellmann-Feynman integrated stress $\tilde{\sigma}_{HF,v}$ can be obtained

$$\tilde{\sigma}_{HF,v} = \frac{\partial E_{KS}}{\partial \alpha_v} \tag{3.52}$$

If the unit cell is treated as a classical continuum object, the dynamics of unit cell can be presented by the stresses on it. For a general unit cell defined by a tensor $\widetilde{h_0}$ comprising three lattice constants $\{\mathbf{a}, \mathbf{b}, \mathbf{c}\}$, a small strain α with respect to a deformed tensor $\widetilde{h} = (1+\alpha)\widetilde{h_0}$ is induced by a stress $\tilde{\sigma}$ which can be formulated generally as Eqn. (3.52)

$$\sigma_{\mu\nu} = \frac{1}{\Xi}\frac{dE_{KS}}{d\alpha_{\mu\nu}} \tag{3.53}$$

where Ξ is the volume of the unit cell and $\mu\nu$ denotes the specific components of the stress tensor $\tilde{\sigma}$. The equilibrium structure is therefore achieved by relaxing the unit cell until the all the components of $\tilde{\sigma}$ are identical to zero.

In view of the change of the size and shape of unit cell in real space during relaxation, the basis set of wavefunctions in reciprocal space will be affected as will E_{cutoff}. In principle, this effect is expected to be minor if the E_{cutoff} is sufficiently large. However, this disadvantage of finite basis sets can be overcome by the introduction of an explicit correction [81]. For the stress calculations, the procedure of using a constant E_{cutoff} is performed for updating the basis set because the change of unit cell causes increasing number of basis states which give more reliable results. In practice, the calculation can be split into two components with respect to constant numbers of basis set (N_{PW}) and constant cutoff energy (E'_{cutoff}). Under the approximation of homogeneous distribution of plane waves, the corrected stress $\widetilde{\sigma_c}$ is derived from Eqn. 3.53

$$\begin{aligned} \widetilde{\sigma_c} &= \frac{\partial E_{KS}}{\partial \alpha}|_{N_{PW}} + \frac{\partial E_{KS}}{\partial N_{PW}}|_{E'_{cutoff}}\frac{dN_{PW}}{d\alpha} \\ &= \tilde{\sigma}_{N_{PW}} + \sigma_P \end{aligned} \tag{3.54}$$

where constant-N_{PW} stress $\tilde{\sigma}_{N_{PW}}$ is determined from the quantum-mechanical calculations [82] and the isotropic correction, Pulay stress (σ_P), is

$$\sigma_P = \frac{2}{3\Xi}\frac{\partial E_{KS}}{\partial(\ln E_{cutoff})} \tag{3.55}$$

and the associated Pulay correction to total energy can be obtained by integrating $\widetilde{\sigma_c}$ over the unit cell

$$E_{KS}(E_{cutoff}) = E_{KS}(N_{PW}) - \frac{2}{3}\frac{\partial E_{KS}(E_{cutoff})}{\partial(\ln E_{cutoff})}\ln(\frac{N_{ac}}{N_t}) \tag{3.56}$$

where N_{ac} is the number of plane waves actually used in calculations and N_t is a theoretical number of homogeneously distributed plane waves in the unit cell of a cell volume Ξ.

A further molecular dynamics scheme which optimise the size and shape of unit cell under the stress effects has been developed recently [83, 84]. For a unit cell specified by a lattice tensor $\tilde{h}$ = {**a**,**b**,**c**} with a cell volume Ξ, the individual ionic position $\mathbf{r}_i$ of N ions can be represented by the fractional coordinates $\mathbf{s}_i$ in which $\mathbf{r}_i = \tilde{h}\mathbf{s}_i$. In order to separate the ionic and unit cell parameters, a metric tensor $\tilde{g} = \tilde{h}^T\tilde{h}$ is utilised. A fictitious unit-cell mass **W** is also used to construct a Lagrangian. Since the deformation of unit cell is derived by the stresses which act on the cell faces, a further tensor $\widetilde{f_0} = \widetilde{\Omega_0}^T\widetilde{\Omega_0}$ (where initial cell faces are defined by $\widetilde{\Omega_0} = \{\mathbf{b}_0\times\mathbf{c}_0, \mathbf{c}_0\times\mathbf{a}_0, \mathbf{a}_0\times\mathbf{b}_0\}$) is introduced as a variable and then a Lagrangian invariant against different choice of the unit cell is defined as

$$\mathcal{L}_{inv} = \sum_{i=1} N\frac{m_i}{2}(\frac{d\mathbf{s}_i}{dt})^T\tilde{g}(\frac{d\mathbf{s}_i}{dt}) - U(\mathbf{r}_i) + \frac{\mathbf{W}}{2}\mathbf{Tr}\left[(\frac{d\tilde{h}}{dt})\widetilde{f_0}(\frac{d\tilde{h}}{dt})^T\right] - P\Xi \tag{3.57}$$

where P is an external isotropic pressure. In Eqn. (3.57), the first term accounts for the ionic kinetic energy, the potential energy is given in the second term. Particularly, a fictitious kinetic energy of the unit cell is also included in this Lagrangian and the

external compressional perturbation is allowed at the end. This Lagrangian can be regarded as a generalisation of $\mathcal{L}_{CP}$ (Eqn. (3.46)). Hence, the equations of motion for describing the dynamics of the lattice tensor $\widetilde{h}$ can be obtained from the Lagrange's equation and is given by

$$\frac{d^2\widetilde{h}}{dt^2} = \frac{1}{\mathbf{W}}[\widetilde{\sigma} - P]\widetilde{\Omega}\widetilde{f_0}^{-1} \tag{3.58}$$

where $\widetilde{\sigma}$ is the *ab-initio* stress tensor.

Integration of Eqn. (3.58) in performed by the Verlet algorithm [85] and $\mathbf{W}$ is a function of the integrating time step. Further, as explained previously, the effect of the basis-set change in performing the unit cell dynamics requires a modification of E_{cutoff} and $\widetilde{\sigma}$ is approximated by the corrected stress $\widetilde{\sigma_c}$ of Eqn. (3.54). The Pulay component of the stress can be obtained straightforwardly from the derivative of total energy E_{KS} with respect to the logarithm of cutoff energy E_{cutoff}. Moreover, the optimal unit cells with respect to various pressures are also determined using this atomic first principles structural relaxation approach under different compressional conditions. In addition, a quenched molecular dynamics scheme is used here to find the equilibrium lattice parameters. However, it is found that the alternate relaxation of the ionic and unit cell parameters can achieve a faster convergence which may be attributed to the coupling between ionic and unit cell degrees of freedom.

3.3 Lattice Dynamics Study: Zone-centre Phonon Calculations

The traditional theoretical studies for the lattice dynamics of crystals are performed with the help of group theory. However, this symmetry method gives only a qualitative picture of lattice vibrations. On the contrary, quantitative descriptions of phonons in crystals can be generated from either empirical or first principles modelling. In the

empirical approach, the potential in solids is modelled by a series of parameters which are determined from experimental measurements. On the other hand, reliable lattice dynamics calculations can be also obtained using the results of accurate ionic and unit cell relaxations generated from *ab initio* molecular dynamics simulations given in preceding sections. Some empirical models and the first principles calculation for the vibrational studies of materials are included here.

3.3.1 Empirical Models

Calculation of vibrational properties in crystals have been made by many empirical models. The common requirement is to fit the parameters of models to experimentally determined physical quantities and each model serve to extrapolate from these observations to the whole lattice dynamics of materials. A complete survey for various empirical phonon modelling schemes can be found elsewhere [86]. Here, only some successful models which are still widely used are outlined.

To account for the electronic polarisability, a shell model was developed by Dick *et al.* and Cochran. In this model, the ionic system is split into a non-polarisable core and a electronic shell formed by the valence charge. As illustrated in Fig. 3.6(a), each core and valence shell is coupled to each other by a simple spring model with the specific force constant. Hence, the interaction between ions contains both short-range couplings and long-range Coulomb interactions. Usually, the potential requires about 10 parameters and can provide reasonably good results. However, this shell picture is not suitable for covalent solids in which valence electrons are shared between different ions rather than localised on ionic positions. This disadvantage of the shell model limits its application no matter how many parameters are used to expand the potentials.

Another popular approach is the valence force field (VFF) model which analyses the lattice vibrations in terms of the valence force fields for the effect of bond stretching and bond bending. For example, the phenomenological potential within a unit cell

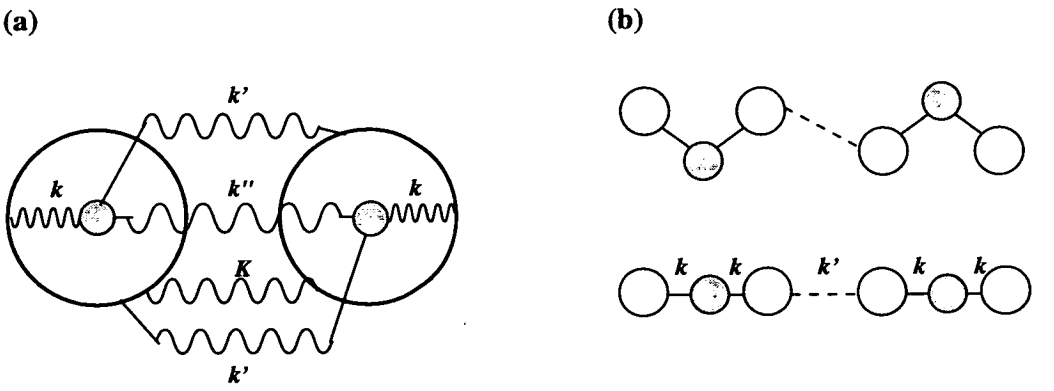

Figure 3.6. Illustrations for two empirical models: shell model (a) and linear-chain model (b). In the shell model, the coupling force constant for nearest electron-nucleus, electron-electron, nucleus-nucleus, and next-nearest electron-nucleus interaction is denoteds as k, K, k", and k', respectively. In the linear-chain model (b), an example of layered MoS_2 is depicted in which Mo and S atoms are designated by small grey and large blank circles, respectively. The intralayered (solid lines) force constant is k, whereas the weaker interlayer (dashed lines) is k'.

containing only two atoms X, Y can be expressed as

$$\begin{aligned} U^{VFF} &= \frac{1}{2}\,[\, k_{r_{ij}} \sum_{i,j} (\delta r_{ij})^2 + k_{r_{ik}} \sum_{i,k} (\delta r_{ik})^2 + r_0^2 k_{\Theta_{ijk}} \sum_{YXY} (\delta\Theta_{ijk})^2 \\ &\quad + r_0^2 k_{\Theta_{jkl}} \sum_{XYX} (\delta\Theta_{jkl})^2 + r_0 k_{r_{ij}\Theta_{ijk}} \sum_{YXY} (\delta\Theta_{ijk})(\delta r_{ij}) \\ &\quad + r_0 k_{r_{jk}\Theta_{jkl}} \sum_{XYX} (\delta\Theta_{jkl})(\delta r_{jk}) + \cdots \,] \end{aligned} \tag{3.59}$$

where the indices j, k denotes the nearest and next-nearest neighbours of the atom i; δr_{ij} is the change of bond length from its equilibrium value r_0 and $\delta\Theta_{ijk}$ is the corresponding change of the angles between the $i-j$ and $i-k$ bonds. $k_{r_{ij}}$, $k_{\Theta_{ijk}}$, and $k_{r_{ij}\Theta_{ijk}}$ is the the force constant for the interaction between bonds, angles, and bond–angle, respectively. Fortunately, the vibrational behaviour for a specific bond is mainly characterised by the bond-stretch and bond-bending force constant and this VFF model is easily transferred into other molecular systems containing the same type of bonds.

For some particular atomic arrangements, there may exist a special empirical model (not the general case) which provides a particularly efficient means to obtain the force constants and phonon frequencies. A typical model for layered solids is the linear-chain model [87]. This model transfers the layered structure, *eg.* MoS_2, into a simple one-dimensional chain which connects the atoms by the springs with different force constants. The schematic diagram of the linear-chain model is depicted in Fig. 3.6(b). Based on the eigenvectors determined from group theoretical analysis, the force constants with respect to different types of spring can be obtained from fitting the parameters to a few observed zone-centre modes frequencies. However, layered solids treated by means of the linear-chain model must satisfy the following requirements: the ions of unit cells should lie on a series of parallel planes in which every plane contains only one ion; the eigenvectors for normal modes should be parallel or normal to the chain, and the cohesion across adjacent layers should be restricted to nearest neighbours.

3.3.2 First Principles Calculations

Despite of the efficiency of some empirical methods, most have very low transferability between different structures. From this view point, *ab initio* methods are necessary to gain insight into lattice vibrations. Once the Hellmann-Feynman forces on ions are determined very precisely by *ab initio* scheme shown in Sec 3.2.5, a dynamical matrix diagonalisation method based on quantum-mechanical calculations is possible accomplished to evaluate the frequencies of phonons. The central concept of this phonon calculation originates from a classical harmonic approximation in which the Hamiltonian H for a perfect crystal can be expressed as

$$H \approx H_0 + H_{harm} \tag{3.60}$$

where H_0 is the Hamiltonian with respect to all the ions at equilibrium positions and H_{harm} is due to the small ionic dispacements. For a given configuration, the

displacement from the equilibrium of the νth ion with a mass M_ν in the μth unit cell is $\mathbf{u}_{\mu\nu}$. Within the harmonic approximation H_{harm} is

$$H_{harm} = \frac{M_\nu}{2}(\frac{d\mathbf{u}_{\mu\nu}}{dt})^2 + \frac{1}{2}\sum_{\mu'\nu'} \mathbf{u}_{\mu\nu} \cdot \mathcal{K}_{\mu\nu,\mu'\nu'} \cdot \mathbf{u}_{\mu'\nu'} \tag{3.61}$$

where $\mathcal{K}_{\mu\nu,\mu'\nu'}$ describe the interaction between $\mathbf{u}_{\mu\nu}$ and $\mathbf{u}_{\mu'\nu'}$. The equations of motion for ion $\mathbf{u}_{\mu\nu}$ is derived and the force on it can be defined as

$$\mathbf{F}_{\mu\nu} = M_\nu(\frac{d^2\mathbf{u}_{\mu\nu}}{dt^2}) = \sum_{\mu'\nu'} \mathcal{K}_{\mu\nu,\mu'\nu'}\mathbf{u}_{\mu'\nu'} \tag{3.62}$$

and $\mathcal{K}$ is therefore regarded as the force constant.

However, the displacement $\mathbf{u}_{\mu\nu}$ of the νth ion at $\mathbf{x}_{\mu\nu}$ in the μth unit cell can be related to the displacement $\mathbf{u}_{0\nu}$ of the corresponding ion in the origin unit cell. It can be formulated as

$$\mathbf{u}_{\mu\nu} = \mathbf{u}_{0\nu}\ exp[i\mathbf{q}\cdot(\mathbf{x}_{\mu\nu} - \mathbf{x}_{0\nu}) - \omega t] \tag{3.63}$$

where $\mathbf{q}$ and ω denotes the wave vector and frequency, respectively. By substituting Eqn. (3.63) into (3.61), the equations of motion for $\mathbf{u}_{0\nu}$ becomes

$$M_\nu\omega^2\mathbf{u}_{0\nu} = \sum_{\mu,\nu'} \mathcal{K}_{\mu\nu,0\nu'}\ exp[i\mathbf{q}\cdot(\mathbf{x}_{\mu\nu} - \mathbf{x}_{0\nu'})]\mathbf{u}_{0\nu'} \tag{3.64}$$

Following a mass-modified Fourier transformation of $\mathcal{K}$, the dynamical matrix $D_{\nu\nu'}(\mathbf{q})$ is obtained. If the directions of displacements are taken care, the general dynamical matrix is

$$D_{\alpha\beta}\begin{pmatrix}\mathbf{q}\\ \nu\nu'\end{pmatrix} = \frac{1}{\sqrt{M_\nu M_{\nu'}}}\sum_{\mu} \mathcal{K}_{\mu\nu_\alpha,0\nu'_\beta}\ exp[-i\mathbf{q}\cdot(\mathbf{x}_{\mu\nu} - \mathbf{x}_{0\nu'})] \tag{3.65}$$

where α, β represent the displacing directions of ions. Consequently, Eqn. 3.64 can be

transformed as a secular equation of the form

$$\sum_{\nu'_\beta} \left\{ D_{\alpha\beta}\begin{pmatrix}\mathbf{q}\\ \nu\nu'\end{pmatrix} - \omega^2 \delta_{\nu_\alpha \nu'_\beta} \right\} \zeta_{0\nu'_\beta} = 0 \tag{3.66}$$

where $\zeta_{0\nu'_\beta} = \sqrt{M_{\nu'}}\mathbf{u}_{0\nu'_\beta}$ is the phonon eigenvector. So, at each wave vector $\mathbf{q}$, the eigenvalues ω^2 and associated eigenvectors are determined from a diagonalisation of the dynamical matrix $D_{\alpha\beta}(\begin{smallmatrix}\mathbf{q}\\ \nu\nu'\end{smallmatrix})$. Further, the resultant eigenvalue as a function of wave vector gives the phonon dispersion curves within the first Brillouin zone.

However, this clumsy calculation is reduced to a one unit cell simulation if only the zone-centre phonons (Γ-point modes) are concerned. The dynamical matrix $\mathbf{D}(\begin{smallmatrix}\mathbf{0}\\ \nu\nu'\end{smallmatrix})$ is thus simplified and its elements can be evaluated directly from forces. Based on Newton's third law, a small displacement τ of the ν'th ion from equilibrium along β will induce a force on the νth ion along α. The same procedure is employed under the Hellmann-Feynman theorem for which detail was given in Sec. 3.2.5. In general, the dynamical matrix for a unit cell of N ions needs 3N displacing operations to fill the matrix. Each component of this 3N $\times$ 3N matrix is given

$$D_{\alpha\beta}(\nu\nu') = \frac{1}{\sqrt{M_\nu M_{\nu'}}} \frac{F^{HF}_{\nu\alpha}}{\tau_\beta} \tag{3.67}$$

and the zone-centre phonons are derived from diagonalising the matrix. The computation effort of this *ab initio* force constants calculations can be reduced even further by introducing symmetry operations. If a set of symmetry elements $\mathbf{S} = \{S_i\}$ map the ith and the jth ion to the kth and the lth ion, respectively, within a unit cell, then the force constants can be propagated by

$$\mathcal{K}_{kl} = S\mathcal{K}_{ij}S^T \tag{3.68}$$

Once a subset of the possible 3N distortions are performed, the full dynamical matrix is then constructed by the symmetry mapping of Eqn. 3.68. It should be noted that

the symmetry of transformation matrices may be lower than that of the point group adopted by the equilibrium structure because of the possible symmetry breaking of the displaced configuration.

In the harmonic approximation, the magnitude of the distorted displacement should match this criterion. Hence, the tests for the appropriate value of τ have to be done to ensure the phonon calculations within the harmonic regime. In practice, this testing scheme is performed by displacing the ion in opposite directions with the same magnitude for different τ. The merit of each τ can be judged by the difference of $\left|F_{\nu\alpha}^{HF}\right|$ related to each pair of distortions. Moreover, to minimise the effect of the possible residual force of equilibrium configuration from incomplete convergence of calculated Hellmann-Feynman forces, the largest value of the displacement satisfying the harmonic requirement is used. Ultimately, diagonalisation of the resulting appropriate dynamical matrix gives all 3N eigenvalues and eigenvectors of Γ-point modes and this method can be extended for calculating arbitrary wave-vector modes by using a superlattice calculation.

3.3.3 Frozen Phonon Method

Before the modern quantum-mechanical phonon calculations introduced above, Γ point phonon frequencies were calculated by an *indirect* approach known as the frozen phonon method. In this method, a specific phonon frequency is deduced from the total energy difference between the equilibrium structure and the distorted lattice with a particular displacement pattern. For example, Wendel *et al.* [88] calculated the total energies of the equilibrium structure of silicon (Si) and the deformed structure in which two sublattices are distorted by a displacement τ along [111] direction. The energy difference can be expanded in terms of τ

$$E_\tau - E_0 = \frac{\mu_{Si}}{2}\omega_{TO}(\Gamma)^2\tau^2 + \frac{A_{xyz}}{\sqrt{27}}\tau^3 + \cdots \tag{3.69}$$

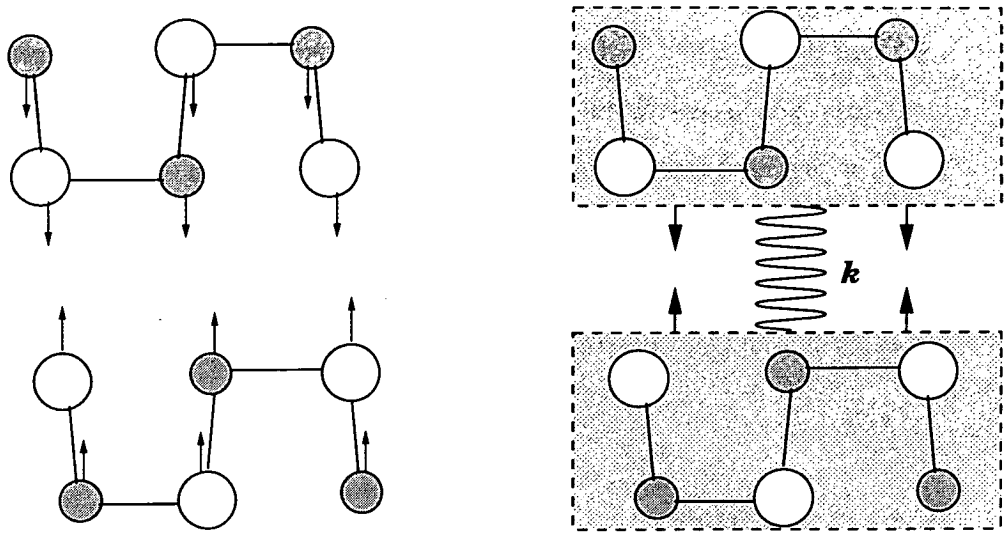

Figure 3.7. Schematic diagram for the frozen phonon calculation of a typical layered semiconductor GeS. The Ge and S atoms are represented by small and large circles, respectively. A Γ-mode corresponding to a compressive shift of the rigid layers against to each other can be simplified as a spring model in which a pair of slabs are linked by a spring with force constant k.

where μ_{Si} is the reduced mass of Si and A_{xyz} is a coefficient. The Γ-point transverse optical modes $\omega_{TO}(\Gamma)$ is thereby obtained. Also, It has been shown that the other modes can be calculated from various static displacements [88, 89].

Based on this concept, a *direct* frozen-phonon calculation can be implemented by combining first principles force calculations and the fixed displacement pattern for a specific zone-centre phonon. For instance, instead of building up the dynamical matrix, the calculation of the rigid-layer compressive phonon frequency of a typical layered semiconductor GeS (detail see Sec 6.5.3) can be performed by the Hellmann-Feynman forces calculations for a displacement pattern which assumes that the layers shift rigidly against to each other (shown in Fig. 3.7). After a sufficient convergence of calculated force, the Ge and S atoms in the same layer are displaced as a rigid unit and the effective force on this layer is approximated by a summation of individual forces on each atom. As illustrated in Fig. 3.7, the frequency of this rigid-layer compressive mode is therefore determined directly by a simple Hook's law.

Since the harmonic criterion is also held in this method, the appropriate displacement tests are necessary to guarantee the calculation is within the harmonic regime. However, frozen phonon approach cannot provide detailed eigenvectors of vibrational modes. In fact, it utilises assumed eigenvectors, usually from the group theoretical analysis, as the input condition for the calculation and its accuracy will be easily affected by nonambient environments. This essential issue will be addressed in Chapter 6.

3.4 Summary

From reviewing the background techniques for *ab initio* total energy pseudopotential simulations in this chapter, it is found that the quantum-mechanical calculations for the ground-state electronic configurations of large systems are accessible by density functional theory, plane-wave basis set, pseudopotential, k-point sampling, and Car-Parrinello molecular dynamics scheme. Further, the stable structure is determined by the Hellmann-Feynman forces and the corrected stresses which can be derived from the minimum of Kohn-Sham total energy and self-consistent wavefunctions. All the features have been implemented computationally in *ab initio* molecular dynamics package -- CAmbridge Serial Total Energy Package (CASTEP) [68]. A flow chart of the calculation procedure of CASTEP is briefly shown in Fig. 3.8.

Also, based on this *ab initio* modelling, insight into zone-centre vibrational modes can be probed by the first principles phonons calculation. The computational procedure is sketched in Fig. 3.9. Superior to empirical approaches, the first principle dynamical matrix diagonalisation method provides not only eigenvalues but also eigenvectors which the detail displacement patterns for specific vibrational modes. In addition, the dispersion curves can be obtained by performing this calculation on a supercell environment.

It is worth to mention that the infrared-active vibrations may involve long-range

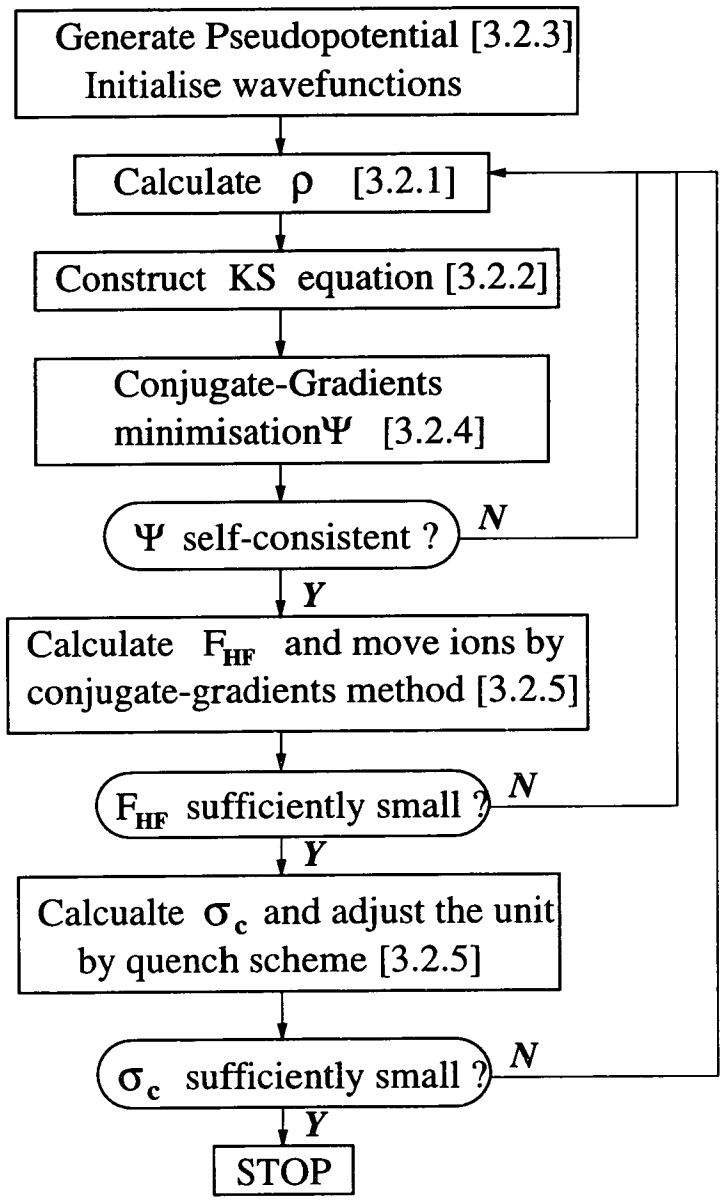

Figure 3.8. Flow chart describing the procedure for the electronic, ionic, and unit cell relaxation of solids with *ab initio* molecular dynamics simulation. The computational detail of processes can be found in the related sections which are noted in square brackets.

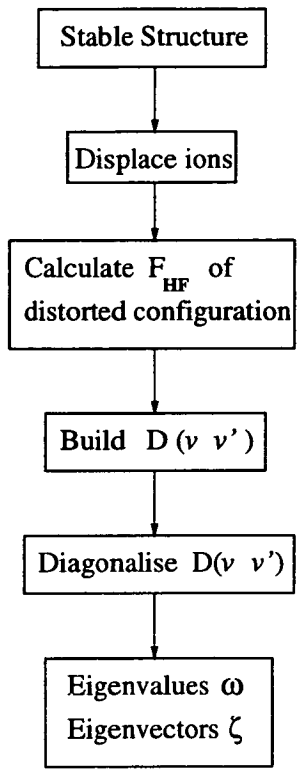

Figure 3.9. Flow diagram for the first principles phonons calculation.

dipolar forces which will affect the calculated infrared eigenvalues. Nevertheless, this dipolar effect was not included in our first principles phonon calculations. On the contrary, Raman-active modes with respect to the inversion symmetry are free from dipolar forces and the corresponding phonon calculations should be more accurate. Recently, a technique combining density functional theory with linear-response technique has been developed [90] to impelment lattice-dynamics calculations in semiconductors. It would be of interest to apply this density functional perturbation approach to address the missing long-range dipolar force effect in phonon calculations.

Chapter 4

Pressure Studies of Ionic Semiconductor: CuCl

4.1 Introduction

The CuCl is one of the most ionic of tetrahedral semiconductors. According to its strong ionicity, the CuCl is easily influenced by external fields. Therefore, complexity of structural and electronic properties is expected to be found in CuCl under pressure and temperature. In fact, the high-pressure structural, chemical and electrical properties of CuCl have been the subject of extensive experimental study [91, 92]. Also, unusual vibrational properties of CuCl associated with the extreme anharmonicity [93], unexpectedly large negative thermal expansion [94], and anomalies in the first-order Raman spectrum [95], have been of sustained interest for many years. Further, it is anticipated that the electronic properties of CuCl will differ from the covalent tetrahedral materials. These have been already investigated in detail elsewhere [96, 97].

CuCl is distinct from its III-V or II-VI counterparts in that copper $3d$ electrons hybridise strongly with chlorine $3p$ states. The hybridisation causes more electrons to be involved in bonding and this situation leads to a serious computational obstacle to the application of the conventional pseudopotential method. Nevertheless, advances in

ab-initio pseudopotential total energy calculations given in previous chapter make it possible to theoretically study the structural and electronic properties of this complex system. Hence, in this chapter, entirely parameter-free calculation is used to prospect the detail of pressure-induced polymorphs of CuCl.

In addition to the perception of exotic behaviour of CuCl itself, another motivation of this study is to elucidate the pressure effects on the three-dimensional ionic network semiconductors in which cohesion is much larger than the typical anisotropic solids. In view of cohesive strength, it is worth probing the influence of hydrostatic pressure on the highly ionic solids before entering the pressure studies of highly anisotropic materials of the next chapters.

Thus, this chapter is organised as follows. The theoretical definition of ionicity and the prediction of structural stability are reviewed in Sec.4.2. In Sec.4.3 the structural detail of CuCl-IV and *ab-initio* structural studies are outlined. The study of electronic properties is also presented in Sec.4.4. Consequently, a conclusion is made in Sec.4.5.

4.2 Ionicity of The Bond in Crystals: Historical Perspective

The nature of chemical bonds in crystals has been studied for many years since they provide an understanding of fundamental crystalline properties. In order to study the characteristic of chemical bonds, the concept of ionicity of bond has been introduced. However, as a non-directly observable quantity, different scales of ionicity have been proposed in terms of thermochemical criteria [98] and dispersion theory [99]. Recently, a measure of asymmetry of charge density distribution derived from first-principle calculations has been also used to gauge the ionicity of bond [100]. A comparison between various ionicity scales of the ionic semiconductor CuCl at ambient condition is made in this section. Moreover, using total-energy calculations, the structural stability of tetrahedral compounds under compression can be expressed as a function of ionicity

and bondlength [101]. The methodology to predict the pressure-induced phase transition of binary compounds $A^N B^{8-N}$ using pseudopotential calculations coupled with an empirical ionicity scale is reviewed. As a result of this calculation, the empirical scales of the transition pressure of CuCl from ambient structure to a high-pressure phase are shown here as well.

4.2.1 Ionicity Scales for Octet Binary Compounds $A^N B^{8-N}$

Considering the formation of bonds connecting individual atoms, the ionicity of chemical bonds was initially defined by Pauling [98] as a function of the atomic electronegativity. The concept of electronegativity (X) as a scale to measure the power of electron-attraction of an atom and can be determined from the formation energies (D) of the bonding. In principle, the relationship of bond formation energies and the difference between elemental electronegativities of the bonding atom A and B , $X_A - X_B$, is given by

$$|X_A - X_B| \propto \sqrt{D_{AB} - \frac{D_{AA} + D_{BB}}{2}} \tag{4.1}$$

where D_{AB}, D_{AA}, and D_{BB} denotes the heat of formation for the AB, AA, and BB bond, respectively. Thus, Pauling's ionicity ($I_{Pauling}$) of bonds in $A^N B^{8-N}$ crystals with the coordination number M is defined as

$$I_{Pauling}(AB) = \frac{M - Ne^{\frac{-|X_A - X_B|^2}{4}}}{M} \quad \text{and} \quad 0 \leq I_{Pauling}(AB) < 1 \tag{4.2}$$

However, the Pauling's ionicity scale includes not only individual bond energies but also the energies due to bond-bond interactions which will introduce the inaccuracy of the ionic character of a chemical bond [102].

An improved definition of ionicity, Phillips' ionicity scale, was established from spectroscopic dispersion [99]. This scale of ionicity is obtained from the transition energy

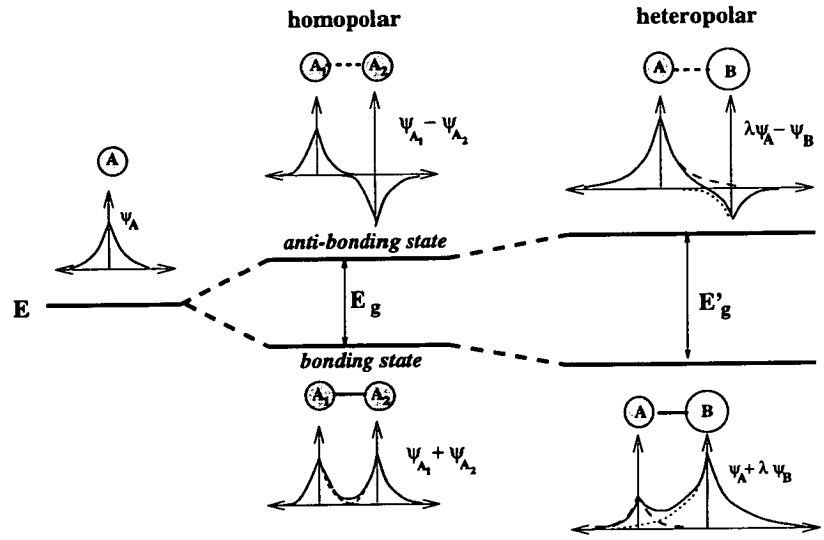

Figure 4.1. A sketch of the energy gap between the bonding and antibonding state as a function of ionic properties of the given bond. The gap for the homopolar and heteropolar diatomic system is denoted as E_g and E'_g, respectively. The schematic wave function which can be described as a linear combination of ground state ψ_A and ψ_B of individual atom A and B with a combination coefficient λ is also shown for the corresponding state.

between bonding and antibonding states of semiconductors. Based on the fundamental quantum-mechanical model for diatomic systems, the ground state of each electron in the diatomic molecular potential can be separated into bonding and antibonding levels and this gives rise to an energy gap between two diatomic states [103]. Fig. 4.1 shows that the bonding state with respect to lower energy is specified by heaping up the wavefunctions between two atoms while the antibonding state with higher energy corresponds to the antisymmetric wave function with a cusp within the bond region.

For more quantitative studies, in homopolar diatomic molecules, the band gap of bonding-antibonding splitting corresponding to the bond between identical atoms A_1 and A_2 is characteristed by the hopping intergal $E_h = 2H_{A_1A_2} = 2 < \psi_{A_1}|H|\psi_{A_2} >$ which is the off-diagonal element of the Hamiltonian matrix. However, as illustrated in Fig. 4.1 , the energy gap will be enhanced according to the difference between on-site Hamiltonian matrix elements on unlike bonding atoms in heteropolar molecules. Hence,

the average valence-conduction band gap E_g in $A^N B^{8-N}$ crystals can be formulated as

$$E_g = \sqrt{E_h^2 + C^2} \tag{4.3}$$

where C is a function of $| < \psi_A|H|\psi_A > - < \psi_B|H|\psi_B > |$. Therefore the ionicity of the bond, $I_{Phillips}$, is defined as

$$I_{Phillips} = \frac{C^2}{E_g^2} = \frac{C^2}{E_h^2 + C^2} \tag{4.4}$$

where E_h and C are responsible for the covalent and ionic components of the average band gap E_g, respectively. In practice, the homopolar part E_h depends on the lattice constant a and can be estimated from the optical gap of a pure covalent system, such as Si, in which $E_g = E_h$

$$\log \frac{E_h}{E_h(Si)} = 2.5 \log \frac{a(Si)}{a} \tag{4.5}$$

Further, based on the theoretical calculations of the response functions [104], the average energy gap $E_g(AB)$ of $A^N B^{8-N}$ compounds can be obtained spectroscopically from the real part of complex electronic dielectric constant $\epsilon_0(AB)$,

$$\epsilon_0(AB) - 1 \propto E_g(AB)^{-2} \tag{4.6}$$

Then, the $C(AB)$ can be derived from Eqn. (4.3). In addition, Phillips defined an ionicity phase angle φ ($\tan\varphi = C/E_h$) and found a critical angle φ_c giving $I_{\varphi_c} = 0.785$ which identifies a boundary separating the domain of fourfold coordinated structures from the stable region of sixfold coordinated structures of $A^N B^{8-N}$ crystals on the C versus E_h diagram.

In addition to empirical definitions of ionicity, the character of charge asymmetry in

crystals can be evaluated by first-principles calculations [100]. Theoretically, by choosing the origin at the middle of the bond, the symmetric and antisymmetric component of the calculated valence charge density $\rho(\mathbf{r})$ contributing to the covalent and ionic properties of the given bond, respectively, are expressed as

$$\rho_{symm.}(\mathbf{r}) = \frac{\rho(\mathbf{r}) + \rho(-\mathbf{r})}{2} \tag{4.7}$$

$$\rho_{antisymm.}(\mathbf{r}) = \frac{\rho(\mathbf{r}) - \rho(-\mathbf{r})}{2} \tag{4.8}$$

Technically, the charge asymmetry calculation is performed using the Fourier transformation of the valence charge density. Then, the symmetric and antisymmetric part of charge density in reciprocal space $\mathbf{G}$ are given by

$$\rho_{symm.}(\mathbf{G}) = \frac{\rho(\mathbf{G}) + \rho^*(\mathbf{G})}{2} \tag{4.9}$$

$$\rho_{antisymm.}(\mathbf{G}) = \frac{\rho(\mathbf{G}) - \rho^*(\mathbf{G})}{2} \tag{4.10}$$

where $\rho^*(\mathbf{G})$ is the complex conjugate of the charge desnity. The charge asymmetry coefficient g, a measure of ionicity, is therefore defined as

$$g^2 = \frac{S_{antisymm.}}{S_{symm.}} = \frac{\sum_{\mathbf{G}} |\rho_{antisymm.}(\mathbf{G})|^2}{\sum_{\mathbf{G}} |\rho_{symm.}(\mathbf{G})|^2} \tag{4.11}$$

where the $S_{symm.}$ and $S_{antisymm.}$ represents the value of symmetric and antisymmetric charge density over whole unit cell, respectively.

As the result of calculations, the g values of $A^N B^{8-N}$ compounds were found very close to corresponding $I_{Phillips}$ except for the compounds containing first-row elements without core p states. However, a clear structural separation still can be obtained using charge asymmetry calculations: similar to the parameters of E_h and C in Phillips' ionicity, $S_{symm.}$ and $S_{antisymm.}$ can be used to group the stable structures of $A^N B^{8-N}$ compounds having the same coordination as the separated lines on the $S_{symm.}$-$S_{antisymm.}$

phase diagram.

Using empirical and first-principle scales defined above, different values of ionicity for CuCl are determined as $I_{Pauling}$(CuCl) = 0.67, $I_{Phillips}$(CuCl) = 0.746, and g(CuCl) = 0.741. The ionicity of CuCl in the Phillips scale is smaller than the critical value of 0.785 and suggests CuCl will favour the fourfold zinc-blende structure under ambient condition. This conclusion is consistent with the result of the first-principle charge asymmetry calculation. Further, $I_{Phillips}$(CuCl) is close to the critical value I_{φ_c}at which zinc-blende structure becomes unstable with respect to the more closely packed structures, wurtzite or rocksalt. This inherent structural stability implies the possibility of a large number of pressure- or temperature-induced polymorphs existing for CuCl which will be outlined in Sec. 4.3.

4.2.2 Prediction of High-Pressure Phase Transition in Tetrahedral Semiconductors: The Ionicity Scale Method

High-pressure structure stability of tetrahedral semiconductors in diamond or zinc-blende structures was systematicly studied by Chelikowsky using a combination of $ab - initio$ total energy calculations and the empirical Phillips ionicity scale [101]. Following Chelikowsky's approach, the phase transitions in binary compounds $A^N B^{8-N}$ from zinc-blende structure to either the metallic β-Sn structure or the ionic rocksalt structure under compression can be well-defined by the parameters of bondlength and ionicity. In general, the transition pressures of the binary octets family predicted by this methodology are in good agreement with observed results. Before determining the pressure-induced structural trends of CuCl, the background of this treatment is addressed below.

In order to understand the effect of ionicity on the structural properties, Chelikowsky performed total-energy calculations using a self-consistently screened ionic pseudopotential [69] in a structure-independent Gaussian basis set. The ionicity of the potential could be gradually modified by changing the Gaussian potential well on

both anions and cations. Thus, stability of different crystal structures at a specific pressure is determined from the minimisation of calculated total-energies of various electronic configurations. However, to obtain a more precise description of phase behaviour of zinc-blende semiconductors, Chelikowsky rescaled the calculated transition pressure P_i^α which represents the transition from zinc-blend structure to high-pressure structure α at a given reference volume V_i by a volume-independent scaling factor S^α. The transition pressure P_t^α is therefore formulated as

$$P_t^\alpha(I_{Phillips}, V) = P_i^\alpha(I_{Phillips}, V_i)S^\alpha(V - V_i) \tag{4.12}$$

where $I_{Phillips}$ is the Phillips ionicity scale (defined in Eqn. (4.4)) and V is the volume. α denotes only two possible types of structure, β-Sn and rocksalt, in Chelikowsky's investigation.

As a result of this calculation applyed to various species of octet binary compounds, a global phase diagram (shown in Fig. 4.2) of high-pressure transitions for zinc-blende materials is constructed in terms of bondlength and ionicity. In this diagram, compounds located in the ionic domain corresponding to a larger value of the ionicity ($I_{Phillips} \geq 0.6$) are predicted to undergo a transition to the ionic rocksalt structure while more covalent semiconductors transform predominately to the metallic β-Sn structure under hydrostatic pressure. As displayed in Fig. 4.2, the range of bondlengths was set from 2.25 to 2.8 Å according to the scaling law of Eqn. (4.12) is no more appropriate for structures having bondlength less than 2.25 Å and, on the other hand, systems with longer bondlength than 2.8 Å become unstable in zinc-blende structure at ambient pressure. In addition, the calculated transition pressure increases with decreasing bondlength for constant ionicity.

With the coordinate specified by the bondlength of 2.35 Å and the ionicity of 0.746, the zinc-blende CuCl was predicted to transform from the zinc-blende structure to rocksalt type structure at 63.5 kbar. However, the calculated transition pressure

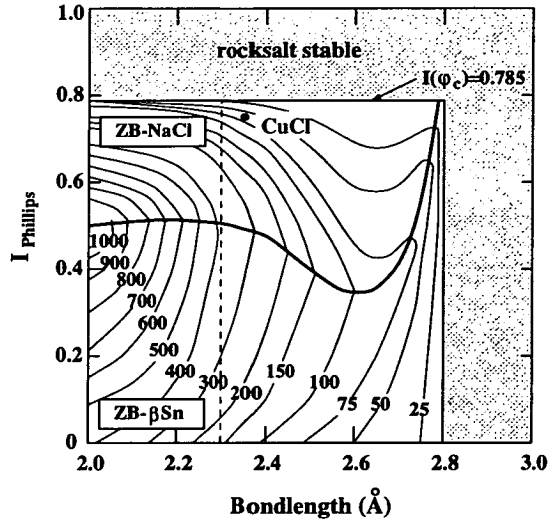

Figure 4.2. High-pressure domains for tetrahedral semiconductors with a contour of calculated transition pressures. The location of CuCl indicates that structure of CuCl will transform from the zinc-blende to the rocksalt modification at 63.5 kbar.

is not consistent with the experimental data for which an intermediate phase of CuCl was observed at about 50 kbar. This missing prediction reveals an oversimplification of Chelikowsky's phase diagram since it includes only two high-pressure structures. It therefore can not provide detailed pressure behaviour of tetrahedral compounds with intermediate phases like CuCl. A first principle method which will be discussed in the next section is therefore needed to explore the structural response of CuCl to external pressure.

4.3 First-principle structural Stability Determination for Exotic Structures of CuCl

The phase behaviour of the ionic binary compound CuCl has been extensively studied under external pressure and temperature [92, 91, 105]. The *P-T* phase diagram of CuCl was reported by Merrill [106] and is shown in Fig. 4.3. As illustrated in this diagram, a wurtzite structure phase (CuCl-I) has been found at high temperature (400 $\sim$ 425 °C) and ambient pressure [92]. Decreasing the temperature to the ambient, CuCl

has been observed in the zinc-blende structure (CuCl-II) having space group $F\bar{4}3m$. During the pressurising procedure, a phase transition from CuCl-II to a more dense rocksalt structure is expected by the theoretical ionicity prediction as discussed in the preceding section. However, unlike III-V and group-IV compounds which exhibit a direct transformation between fourfold zinc-blende structures to sixfold rocksalt-type or eightfold CsCl-type metallic modifications [5], an intermediate tetrahedrally coordinated phase has been observed in CuCl using high-pressure X-ray diffraction [107]. The crystal structure of CuCl-IV was then recognised as a tetragonal structure although no atomic positions could be assigned. Recently high pressure powder neutron measurements revealed that the CuCl-IV can be represented as a simple cubic crystal structure [108] for which structural details will be given latter.

In this section, the vital structural information of CuCl-IV is described in detail in order to compare with the relevant structures of the Group-IV and III-V family of semiconductors. To determine the structural phase transitions from CuCl-II to CuCl-IV and then to CuCl-V, the pseudopotential method is therefore performed for total energy calculations of all three structures. The computational details and calculated results are presented in the second part of this section. It is found that structural properties and relative stability of three modifications of CuCl are fairly well described by this *ab-initio* pseudopotential approach.

4.3.1 Structural Detail of CuCl-IV

Similar to the BC8 structure which is a dense metastable polymorph found in Si and Ge after decompression from metallic phases [5], a simple cubic SC16 structure was found to be adopted by the CuCl-IV [108]. The analogy between the BC8 structure and the SC16 structure is drawn in Fig. 4.4. As displayed in Fig. 4.4(a), the BC8 structure is body-centered cubic containing 16 identical atoms per conventional cell or 8 atoms per primitive cell. The nature of bonding for homopolar solids in the

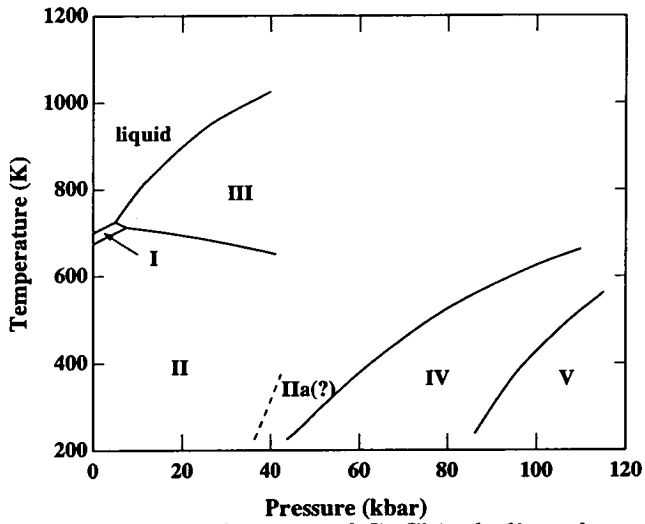

Figure 4.3. The $P-T$ phase diagram of CuCl including the ambiguous superconductive phase CuCl-IIa.

BC8 structure is dominated by a four-fold bonding feature which gives rise to a even-member ring feature. The binary version of BC8 is derived from replacing 8 atoms in the conventional cell with another species of atom which results in a simple cubic structure with a basis of 16 atoms as shown in Fig. 4.4(b). However, a distorsion of the perfect binary analogue of the BC8 structure is induced by the different electronic properties between two species of atoms. Then, the SC16 structure with bonds between unlike species of atoms having lower symmetry than BC8 is illustrated in Fig. 4.4(c).

Unlike the perfect BC8 structure (shown in Fig. 4.4(c)), the SC16 CuCl-IV is composed of eight CuCl formula units (16 atoms). The CuCl-IV structure has spacegroup $Pa\bar{3}$ and is fully specified by a single lattice constant parameter and two free atomic positional parameters (u_{Cu} and u_{Cl}) for anions and cations, respectively. The locations of each species of atom are at the $8c$ sites of the $Pa\bar{3}$ spacegroup and expressed as

$$\begin{aligned} \pm(u,u,u) \quad & \pm(\frac{1}{2}-u,\frac{1}{2}+u,u) \\ \pm(u,\frac{1}{2}-u,\frac{1}{2}+u) \quad & \pm(\frac{1}{2}+u,u,\frac{1}{2}-u) \end{aligned} \tag{4.13}$$

In the special case for which the anion and cation are identical and $|u_{anion}-u_{cation}| = 1/2$, the SC16 structure reduces to the BC8 with spacegroup $Ia\bar{3}$ like Si-III and Ge-IV.

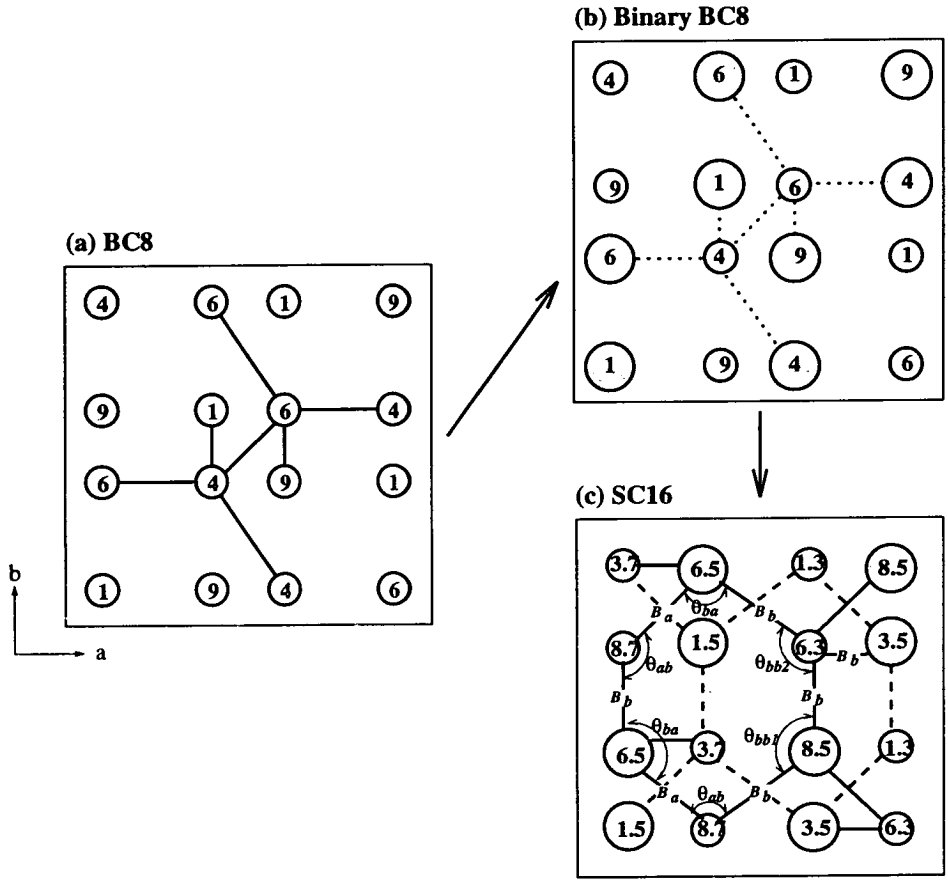

Figure 4.4. Structural similarity between the (a) BC8 for group-IV semiconductors, the (b) binary version of BC8, and the (c) binary analogue SC16 for the I-VII compound, eg. CuCl. The cations and anions are denoted as large and small circles, respectively. Elevations in fractional units of c/10 are indicated by the numbers inside the circles. The fourfold bonding feature of BC8 is represented by solid lines in (a) whereas the virtual bonds in the binary version of BC8 are shown as dotted lines in (b). In (c), a sixfold ring of SC16 structure is displayed as solid and dashed lines for different depth along the c-axis direction. Two characteristic bonds (B_a and B_b) with four bond angles (θ_{ab}, θ_{ba}, θ_{bb1}, and θ_{bb2}) are also indicated in (c).

Moreover, Fig. 4.4(c) shows that the bonding of the SC16 CuCl-IV structure without centrosymmetry is characterised by two different bondlengths B_a and B_b

$$B_a = a_0\sqrt{3}[1-(u_{Cu}+u_{Cl})] \tag{4.14}$$

$$B_b = a_0\sqrt{2[1-(u_{Cu}+u_{Cl})]^2-[1-(u_{Cu}+u_{Cl})]+1/4} \tag{4.15}$$

where a_0 is the lattice constant of the simple cubic structure.

As a result of the structural refinement of the neutron powder spectra at 55.2 kbar, the unit cell parameter and two internal structural parameters u_{Cu} and u_{Cl} was determined to be 6.416 Å , 0.6297(3) and 0.1527(3), respectively. Using these parameters, a three-dimensional illustration of the CuCl-IV in SC16 structure is therefore depicted in Fig. 4.5. The bondlengths B_a and B_b derived from the structural parameters are given as 2.42 and 2.29 Å , respectively, which comprise of a sixfold ring with two pairs of bond angles of $\theta_{ab} = 93.9^o$ and $\theta_{ba} = 98.2^o$ and two other close angles $\theta_{bb_1} = 118.0^o$ and $\theta_{bb_2} = 119.5^o$ defined in Fig. 4.4(c). The average bond length of SC16 CuCl-IV similar to that found in zinc-blend CuCl-II structure (2.35 Å). Nevertheless, the nearest non-bonded separation of Cu^+-Cu^+ (2.88 Å) and Cl^--Cl^- (3.44 Å) along the [111] direction of SC16 CuCl-IV are much smaller than the corresponding non-bonded distance in zinc-blende CuCl-II (3.83 Å). Further, the response of u_{Cu} to pressure is insignificant, being within quoted experimental uncertainties, whereas the u_{Cl} increases slightly to 0.1540(3) at a pressure of 92.4 kbar [108].

4.3.2 *Ab-initio* Study of Pressure-Induced Polymorphism in CuCl

In addition to the first-principle determination of phase transitions presented in Sec. 4.2.2, relative structural stability of the zinc-blende CuCl-II and rocksalt CuCl-V phases have also been investigated by means of the three-body potential model associated with the effect of charge-transfer mechanism under compression [109]. This three-body interactions improve the prediction of the transition pressure give a better description

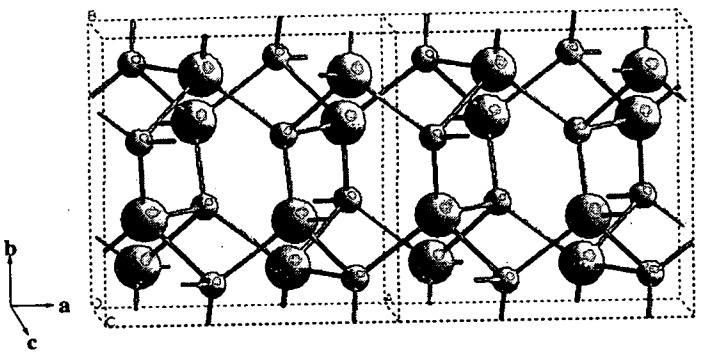

Figure 4.5. Illustration of the SC16 structure for CuCl-IV containing two unit cells along the a-axis direction. The Cu and Cl atoms are denoted as small and large spheres, respectively.

of high-pressure elastic behaviour of CuCl [110]. More recently the structural polymorphism of CuCl including CuCl-IV has been fairly well described using *ab-initio* structural stability calculations combined with the pseudopotential and full-potential models [111].

To perform the total-energy pseudopotential calculations for CuCl, nonlocal, norm-conserving ionic pseudopotentials for copper and chlorine are necessary. As shown in Sec. 3.2.3, the Kleinman-Bylander separation method is implemented to handle the nonlocal pseudopotential. The soft pseudopotential for Cl was generated using a RRKJ optimisation scheme [73]. The electronic configuration for the s, p, and d potential of Cl was $3s^{2.00}3p^{5.00}$, $3s^{2.00}3p^{5.00}$, and $3s^{1.00}3p^{3.75}3d^{0.25}$, respectively. The core radius was 0.9 Å . However, another scheme for generating optimised pseudopotentials [112, 113], Q_c tuning method (highlighted in Sec 3.2.3), was employed to build the pseudopotential of Cu. The electronic configuration for all s, p, and d potentials of Cu was $3d^{9.00}4s^{0.75}4p^{0.25}$ with cutoff radius of 1.06 Å . Using the tuning parameters of $q_c(s) = 0.8$, $q_c(p) = 1.0$, and $q_c(d) = 1.175$, the pseudopotential of the copper is

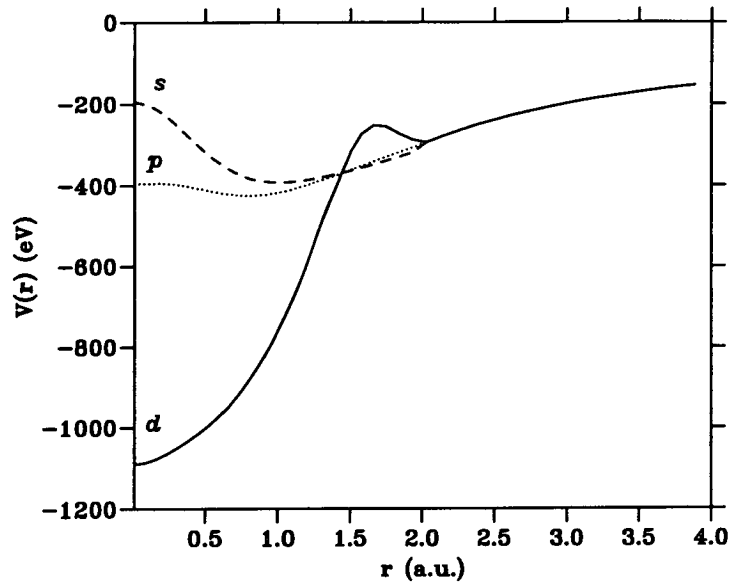

Figure 4.6. Nonlocal pseudopotential for Cu with a core radius of 1.06 Å (2.00 a.u.). The $3d$, $4s$, and $4p$ eigenstate of Cu is denoted as the solid, dashed and dotted line, respectively.

shown in Fig. 4.6. Before implementing *ab-initio* total energy calculations of CuCl, the optimised Cu pseudopotential was tested in the calculation of metallic copper using an $8 \times 8 \times 8$ Monkhorst-Pack k-point grid with a face-centered-cubic unit cell containing four atoms. The calculated total energy was found to be converged to 0.1 eV for the energy cutoff of 650 eV and gave rise to an underestimate of lattice constant of 0.3% with a small overestimate of bulk modulus by 1.8% [114]

In view of the hybridisation of Cu-$3d$ states and Cl-$3p$ states, ten $3d$ electrons of Cu were involved in the calculation and the number of valence electrons per formula unit of CuCl becomes 18. Thus, the total energy calculations of different phases of CuCl are performed using the Perdew-Zunger parametrisation [115] of the Cepperley-Alder exchange-correlation potential [116]. To perform the Brillouin Zone intergrations, a $4 \times 4 \times 4$ Monkhorst-Pack grid corresponding to 10, 4, and 10 special k points for zinc-blende, SC16, and NaCl structure, respectively, has been used to give convergence of total energy calculations to 0.01 eV/cell. Electronic degrees of freedom for all phases of CuCl were relaxed using a preconditioned conjugate-gradient scheme (shown in Sec 3.2.4). Unlike the well-defined internal structural coordinates of the zinc-blend and

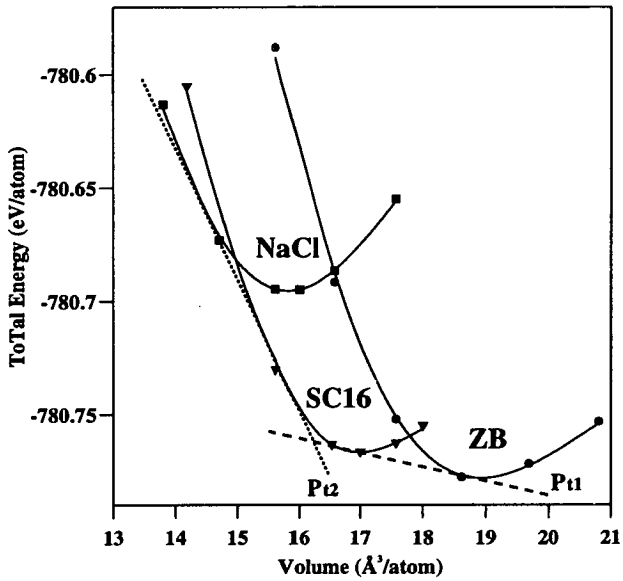

Figure 4.7. The unit cell volume dependence of total energy for the zinc-blende (circles), SC16 (triangles), and rocksalt (squares) structure of CuCl. The Murnaghan fitting of data for each structure is indicated by a solid curve. The common-tangent construction for the pressure-induced phase transition of zincblende-SC16 and SC16-rocksalt is denoted as P_{t1} and P_{t2}, respectively.

rocksalt phase, the equilibrium atomic positions of SC16 CuCl-IV were optimised by relaxing ions under the Hellmann-Feynman forces (see Sec. 3.2.5) at different volumes. The calculated total energy as a function of the unit cell volume for CuCl-II (zinc-blende), CuCl-IV (SC16), and CuCl-V (rocksalt) is displayed in Fig. 4.7

As the calculated results in Fig. 4.7, the zinc-blende structure (CuCl-II) transforms first to the SC16 (CuCl-IV) while CuCl is pressurised up to 12 kbar. The stability of the SC16 structure of CuCl persists up to 94 kbar where the rocksalt structure is expected to be more favourable. The calculated equilibrium lattice constants, bulk modulus, and transition pressures for three phases of CuCl are listed in Table 4.1 in which a comparison with experimental data is also made.

From the data of Table 4.1, it can be found that the *ab-initio* pseudopotential method accounts for the structural behaviour of three phases of CuCl as does the full potential linear augmented plane-wave (FP-LAPW) technique [117, 111]. However, both first-principle simulations lead to an underestimate of transition pressures

Table 4.1. Calculated structural parameters for the zinc-blende (ZB), SC16, and rocksalt (NaCl) phases of CuCl as determined using the pseudopotential and FP-LAPW methods. Experimental results are also shown for comparison. The unit for lattice constant (a_0), bulk modulus (B_0), and transition pressure (P_t) are in Å , Mbars, and kbars, respectively.

Method	a_0			B_0			P_t		
	ZB	SC16	NaCl	ZB	SC16	NaCl	ZB	SC16	NaCl
FP-LAPW [111]	5.273	6.421	4.893	0.756	0.839	0.927	-	37	87
Pseudopotential	5.343	6.483	5.021	0.619	0.636	0.803	-	12	94
Expert. [108]	5.424	6.418	4.929	0.650	0.660	-	-	55	105

between zinc-blende and SC16 and between SC16 and rocksalt structure. There are some possible reasons to account for these disagreements between theoretical and experimental results. Firstly, the hysteresis effects in the experiment may lead to an overestimate of the transition pressure upon upstroke. Unfortunately, no measurement of the transition pressures during decompression has been done for CuCl to determine the magnitude of this effect. However, they are not expected to be as pronounced as in covalent network compounds such as InSb [29] and GaAs [118].

Another possible cause is that the formation of local regions of SC16 CuCl may occur at pressures lower than the pressure at which the long-range order of the high pressure phase has been established. Indirect evidence suggests that a minority of SC16 CuCl has been found at a lower pressure of 49.8 kbar in neutron scattering measurements [108]. Nevertheless, the similarity between bond lengths in zinc-blende and SC16 CuCl will bring about a disadvantage for the precise identification of this pressure-induced short-range structural changes.

According to the high temperature-sensitivity of CuCl, the observations of elastic properties shows a strong pressure-temperature coupling effect on the phase behaviour of CuCl [119]. It implies that temperature effects could give the dominant reason for the underestimate of calculated transition pressures. These measurements suggested that

the transition pressure between CuCl-II and CuC-IV decreases substantially with decreasing temperature. Very recent reports on two-phonon absorption in CuCl show that the characteristic luminescence peak from CuCl-IV can be observed at pressure about 40 kbar when the sample is cooled down to 6 K [120]. Hence, the zero-temperature condition of our *ab-initio* calculations presented here is responsible for the lower calculated transition pressures than those found experimentally at ambient temperature.

4.4 Electronic Properties of CuCl polymorphs

The electronic properties of modifications of CuCl are essentially characterised by the admixture of the copper-3d and chlorine-3p orbitals. As a result of calculations, the valence charge density of SC16 CuCl indicates that the bonding in this strongly hybridised compound can be accurately described by the nonlocal ionic pseudopotentials. Moreover, upon close inspection of electronic band structures, this $p-d$ hybridisation taking place close to the Fermi energy will affect the energy gap between the top of valence band and the bottom of conduction band. Indeed, the orbital-overlapping of CuCl associated with a band gap of few eV is stronger than that of family IV and III-V semiconductors in which d orbitals corresponding to very low energies can be treated as localised core states [117]. In order to explore the change in the electronic properties of CuCl under pressure, the band structures of different phases of CuCl are discussed in detail here.

4.4.1 Valence Charge Density of CuCl-IV

It is well known that the charge density gives detailed information of bonding properties which are of interest to structural chemists. The bonding in SC16 CuCl-IV can be explained using *ab-initio* pseudopotential calculations given in the preceding section.

Since calculations for SC16 CuCl-IV are performed including d orbitals, the charge density illustrated in Fig. 4.8 is composed of the contributions from Cu($3d^{10}4s^1$) and

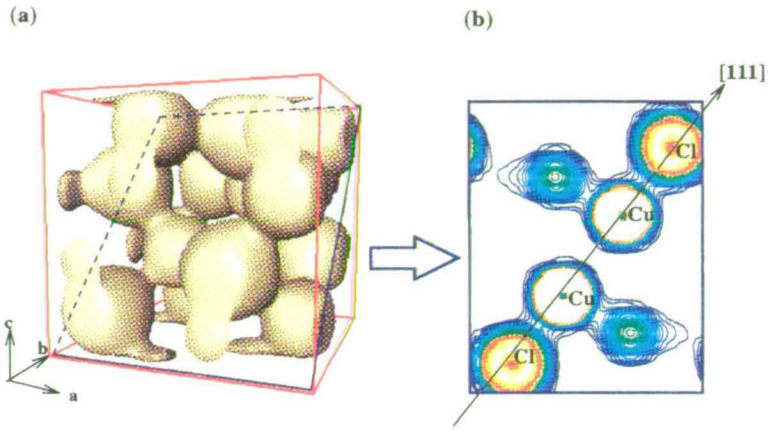

Figure 4.8. Valence charge density of SC16 CuCl-IV in the three-dimensional isosurface (a) and a two-dimensional contour map of the $(0\bar{1}1)$ plane (b). The direction of [111] is indicated as a solid arrow.

Cl($3s^2 3p^5$) states. A three-dimensional picture of valence electron density of SC16 phase is shown Fig. 4.8(a) which presents a fourfold bonding feature agreeing with the structure shown in Fig. 4.4(c). In addition, the characteristic sixfold rings are also observable at the centre of this unit cell. The character of bonds between unlike atoms is studied in more detail by the topology of charge density along specific directions. As a slice of $(0\bar{1}1)$ plane, Fig. 4.8(b) displays a two-dimensional charge density contour map which includes the [111] direction. The chemical bonds along the [111] direction correspond to the B_a defined in Fig. 4.4(c) and are found to be not as symmetric as highly covalent bonds in family IV and III-V compounds. It is a consequence of the fact that the $3d$ electrons of Cu are not so localised as the ones of elemental covalent semiconductors. Moreover, the charge asymmetry coefficient g (defined in Sec.4.2.1) for 18 valence charges within this bond B_a is calculated as a value of 0.582 which implies this bond remains highly ionic.

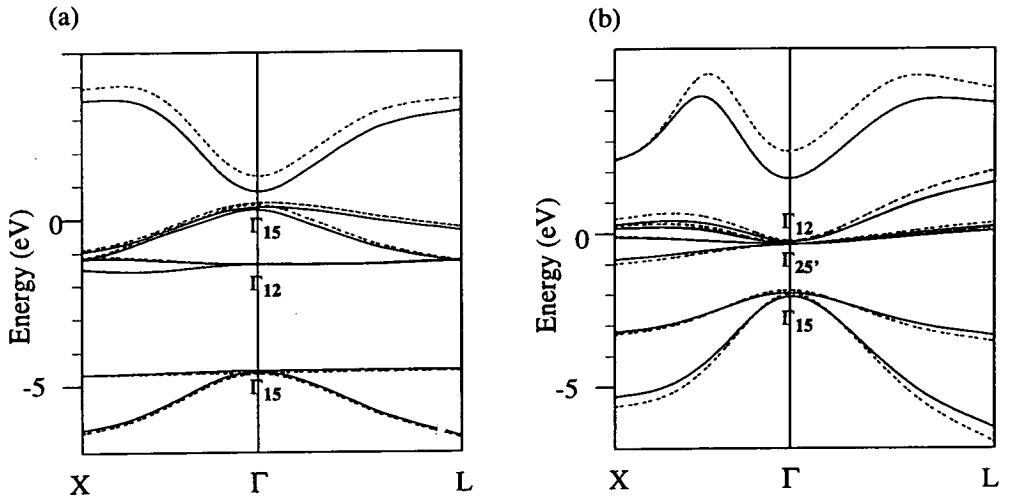

Figure 4.9. Band structure of CuCl in the zinc-blende (a) and rocksalt (b) modifications as determined from pseudopotential (solid line) and all-electron (dashed line) methods. Two calculated band structures are aligned at the twofold degenerate d level Γ_{12}.

4.4.2 Band Structure Calculations

Electronic band structures for the CuCl-II (zinc-blende) and CuCl-V (rocksalt) are calculated using *ab-initio* pseudopotential method with respect to the relevant equilibrium lattice constant shown in Table 4.1. The results are compared with all-electron FP-LAPW calculations. In view of the interaction between $3p$ and $3d$ states of Cl and Cu, respectively, only the valence bands are shown here. The calculated band structures along the high-symmetry directions for these two modifications of CuCl are given in Fig. 4.9. The band structure of SC16 CuCl-IV obtained from FP-LAPW method is also shown in Fig. 4.10.

In Fig. 4.9, two methods show similar band structures in which the lowest-energy band gaps are direct in the zinc-blende phase and indirect in the rocksalt phase. Both phases are found to be insulating without band overlap in the Brillouin-zone regions studies. The result of Fig. 4.10 also indicates that CuCl-IV is not metallic. These results are consistent with the previous self-consistent scalar-relativistic linear muffin-tin-orbitals (LMTO) combination and the non-self-consistent Korringa-Kohn-Rostoker

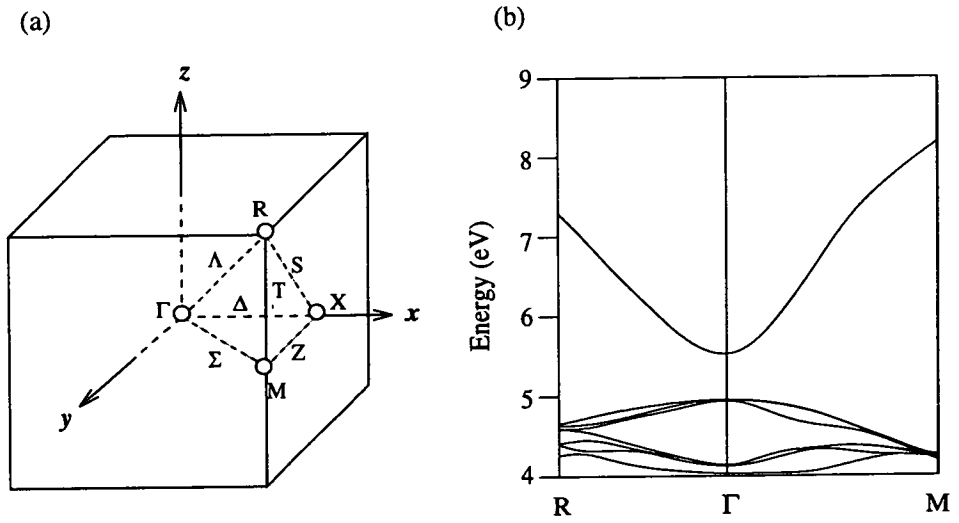

Figure 4.10. Brillouin zone of the SC16 structure (a) and band structure of SC16 CuCl-IV as determined from all-electron calculations (b).

(KKR) methods [121]. More convincing evidence comes from the optical measurements of absorption edges [122] and electrical studies [123] which found no metallic phase of CuCl under compression up to 120 kbar.

From a more careful inspection of band structures, the influence of the *p-d* hybridisation on CuCl in different phases can be qualitatively determined by symmetry considerations. Based on the tight-binding approximation [124], the energy band can be interpreted as a linear combination of orbital interactions (also called *overlap parameters*) with coefficients of the geometrical structural factor. Also, the degeneracies of bands at specific k point (eg. Γ) are predominantly determined by the structural symmetry. Therefore, the absence of the inversion symmetry of zinc-blende CuCl-II is responsible for the splitting of top five $3d$ bands at Γ point, shown in Fig. 4.9(a), which corresponds to the $p-d$ interaction. Similar band behaviour is also found in the band structure of CuCl-IV (Fig. 4.10) adopting the SC16 structure without the inversion symmetry. However, this $p-d$ hybridisation is not allowed for rocksalt CuCl-V at the zone centre since the inversion symmetry of the rocksalt structure excludes the $p-d$ mixing according to the different parities of the two states. The top d bands of the

rocksalt phase are unmixed and degenerate as shown in Fig. 4.9(b). In addition, the symmetry forbidden *p-d* hybridisation accounts for the indirect band gap of the rocksalt modification of CuCl [121].

Considering the quantitative description of band structures, the comparison of the lowest band gap obtained from various theoretical methods and optical measurements is made for all three phases of CuCl and listed in Table 4.2. It can be seen that three self-consistent band calculations (pseudopotential, FP-LAPW, and LMTO) give a discrepancy between the calculated and observed energy gap. Further, by comparing the band gaps and band structures of the zinc-blende structure calculated by pseudopotential and FP-LAPW methods, the inequivalence is deduced from different minimum energy lattice constants as given in Table 4.1. Actually, the resulting differences in calculated band structures are found to be consistent with the deformation potentials of CuCl in this structure [121]. However, in the rocksalt phase, not only the change of bandwidths but also the maximum of the valence band obtained from two calculations are different. Again, the change of bandwidths in the rocksalt modification of CuCl is a consequence of deformation potentials. Moreover, the indirect band gap of $\Gamma \rightarrow L$ and $L \rightarrow X$ predicted by pseudopotential and FP-LAPW approach, respectively, is similar to the indirect transition obtained from LMTO ($L \rightarrow X$) and KKR ($\Gamma \rightarrow L$) methods [121]. Since the KKR method provided more accurate energy gap and deformation potential, the $\Gamma \rightarrow L$ indirect band gap determined by this non-self-consistent calculation is therefore regarded as the actual indirect transition.

4.5 Conclusion

The structural and electronic behaviour of the pressure-induced modifications of the highly ionic compounds CuCl have been comprehensively studied by the first-principles method using nonlocal ionic pseudopotentials. Results from calculations successfully account for the observed pressure-induced transition sequence observed experimentally

Table 4.2. The lowest band gaps calculated by pseudopotential (Pseudop.), FP-LAPW, self-consistent LMTO, ans non-self-consistent KKR methods for three phases of CuCl. The results of optical measurements are also included for comparison. According to different conclusions obtained from these calculations (see in text), the indirect band gap of the rocksalt modification is indicated in individual parenthesis. The unit for energy is in electron-volt (eV).

Structure	Pseudop.	FP-LAPW [111]	LMTO [121, 117]	KKR [121]	Expt. [121]
zinc-blende ($\Gamma \rightarrow \Gamma$)	0.351	0.707	0.5	3.21	3.17
SC16 ($\Gamma \rightarrow \Gamma$)	-	0.526	1.66*	-	2.9
rocksalt (indirect gap)	0.224 ($\Gamma \rightarrow L$)	0.577 ($L \rightarrow X$)	0.6 ($\Gamma \rightarrow L$)	3.97 ($L \rightarrow X$)	3.0

* calculation for the PbO-like structure of CuCl-IV [117]

in this material. The prediction and observation implies that the SC16 structure is a stable high-pressure polymorph of both III-V and I-VII compound semiconductor families though it appears that kinetic factors preclude its formation in the III-V compounds [5]. The observed differences in structure adoption therefore appear to depend sensitively on the details of the transition mechanisms. Moreover, the electronic energy band structures of different dense polymorphs have been also discussed in this chapter. The issue of electron-orbital hybridisation corresponding to energy band gaps still can be well addressed by *ab-initio* band structure calculations although the main simplification of this approach (density functional theory) is only appropriate for ground-state calculations. Finally, in view of the substantial pressure effects on highly ionic solids, a potentially fruitful issue will be to investigate the response of highly anisotropic materials to hydrostatic compression which will be concentrated upon in the rest of this thesis.

Chapter 5

Compressional Mechanism and Pressure-induced Electronic Effects in Layered Compounds

5.1 Introduction

In view of the coexistence of different heirarchical cohesion in some structures, quasi-two-dimensional layered materials have been the subject of sustained interest for many years. For more open-type structure of layered solids (than those of covalently bonded semiconductors), knowledge of the weak interlayer and stronger intralayer interaction is a preliminary stage to the study of more complex materials, such as chained materials, molecular solids, liquid crystals, etc., with potential applications.

Recent developments in both experimental and computational methods achieved a great successful step in understanding the pressure-induced structural and electronic effects in semiconductors, such as structural polymorphism of III-V semiconductors [125] and CuCl presented in previous chapter. However, with respect to the unique bonding properties of anisotropic structures, even stronger and richer pressure effects

in layered compounds are expected. This gives another motivation to implement high pressure techniques on quasi-two-dimensional layered semiconductors.

Therefore, in this chapter, modern established measurement techniques and simulation schemes have been used to probe the structural and electronic properties of layered compounds, GeS and GeSe, under compression. The organisation of this chapter is as follows. A fundamental discussion of the layered crystal structure of GeS and GeSe is introduced in Sec. 5.2. Experimental and computational detail will be also included here. In Sec. 5.3, systematic studies of the pressure-induced structural behaviour will be presented. Finally, the electronic properties corresponding to these anisotropic structures will be investigated under pressure.

5.2 Homology of Structure in GeS and GeSe at Ambient Pressure

5.2.1 Structural Details and Theoretical Classification

The ambient pressure structures of two germanium chalcogenides, GeS and GeSe, have been studied using a conventional single crystal X-ray diffraction method [126, 127] and the analysis showed the crystal structures of both GeS and GeSe are characterised by a black-phosphorus-like layered structure which is often regarded as a distorsion of a rocksalt configuration. In fact, the isostructural semiconductors GeS and GeSe adopt a double-layered orthorhombic crystal structure with the $Pcmn(D_{2h}^{16})$ at ambient pressure. There are eight atoms(four Ge and four chalcogens) contained in the unit cell. Choosing the c-axis to be perpendicular to the plane of layers, the atomic positions can be completely determined by the space group symmetry. The locations of four Ge(or chalcogens) are defined by the additional specification of two free atomic positional parameters(u and v) and are expressed as

$$\pm(u, \frac{1}{4}, v) \text{ and } \pm(\frac{1}{2} - u, \frac{1}{4}, \frac{1}{2} + v) \tag{5.1}$$

Thus, the ambient pressure crystal structure of the orthorhombic germanium chalcogenides is illustrated in Fig. 5.1.

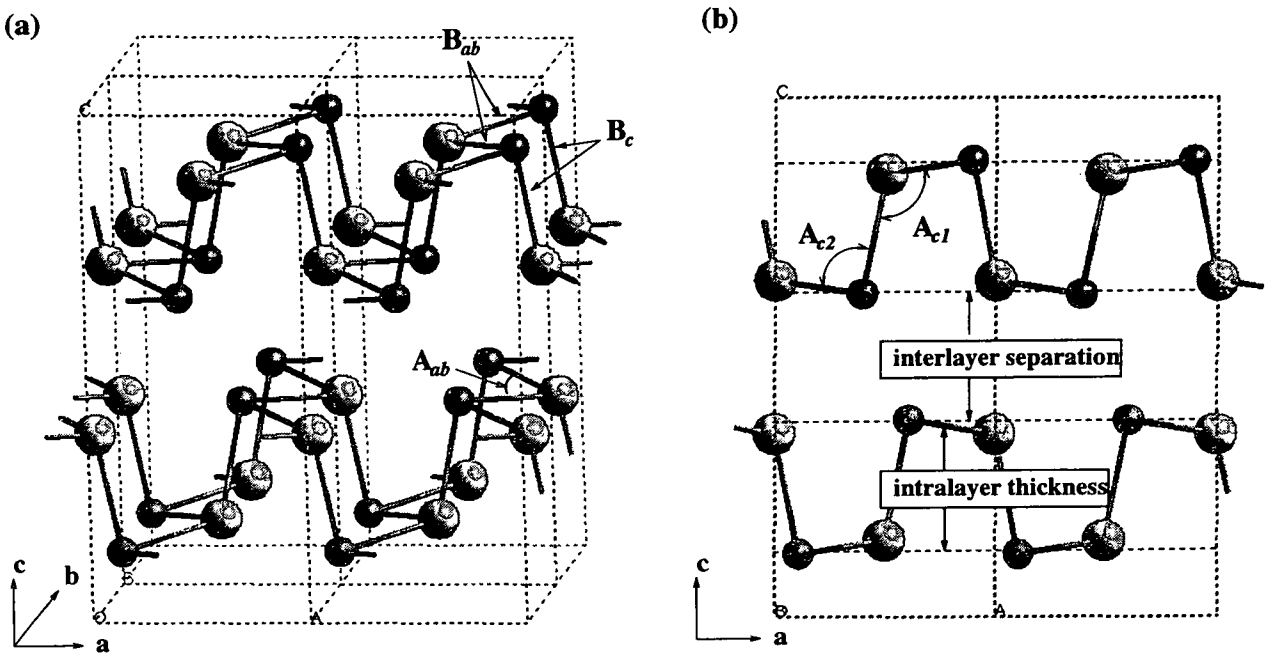

Figure 5.1. (a) Illustration of the germanium chalcogenide orthorhombic crystal structure showing the threefold covalent coordination in the layers. Four unit cells are shown (doubled in the a and b direction). In (b), it is shown a projection of the structure of space group *Pcmn* along the b axis. Ge and S (or Se) are represented as small and big spheres, respectively. The B_{ab} bond and B_c bond are specified in (a). Three distinct bond angles (A_{ab}, A_{c1}, and A_{c2}) are defined in both (a) and (b). The intralayer thickness and the interlayer separation are also shown in (b).

In Fig. 5.1, each unit cell consists of two double layers which are formed by covalently bonded anion(chalcogens)-cation(Ge) pairs with threefold coordinated atoms. There are two distinct bond lengths which are specified to be normal and parallel to the layer plane and denoted as B_c and B_{ab} in Fig 5.1 , respectively. Three bond angles related to the threefold bonded structure can be also observed inside each layer unit. However, the cohesion between layers is a weak interaction (with strength of the

same order as for van der Waal's interactions) which accounts for the easy cleavage of the crystal perpendicular to c-axis and also for the substantial anisotropic properties. The interlayer separation and intralayer thickness is defined as $2v_{Ge}$c and $2(\frac{1}{4} - v_{Ge})$c, respectively.

The structural stability of compounds can be theoretically classified by a quantum mechanical dual-coordinate scheme [128] which takes into account the covalency and ionicity of the material itself. In order to examine the chemical trends, Littlewood has proposed two modified coordinates to study the correlations between three phases of nine IV-VI semiconductors [129]. These two coordinates are formulated by the linear combinations of the radii of s and p orbitals to evaluate the electronegativity difference and the s-p energy splitting between Ge and chalcogen. It was found that a relativistic effect enhances the s-p splitting and then yields the stable rocksalt structure of the heavy members, Pb chalcogenides, of the IV-VI family. The strong ionicity referring to the larger s-p splitting suppresses the sp hybridisation and results in the formation of sixfold ionic p orbitals. Nevertheless, the relativistic effect becomes weaker for the lighter compounds and the reduction of s-p energy splitting enhances the directional s-p orbitals. Therefore, the covalently bonded orthorhombic structure is allowed and expected to be more stable for the lighter IV-VI semiconductors, GeS and GeSe.

5.2.2 Experimental Structural Determination

Angle-dispersive powder X-ray diffraction method (with the image plate technique) (Sec. 2.3) has been used to determine the crystal structure of GeS [130] and GeSe [131] under ambient pressure. The powder samples of GeS and GeSe were obtained by grinding a melt-grown single-crystal sample at liquid nitrogen temperature. The uniform finest powders(grain size $< 5\mu m$) were placed in DACs and careful loadings of samples were maintained to reduce the preferred orientation for both layered compounds GeS and GeSe. Using the Si **(111)** monochromator, the wavelength of the synchrotron beam was set to 0.4447Å for GeS and 0.4652Å for GeSe individually. The

incident beam was collimated to a diameter of 75 μm and the distance between the sample and the image plate was approximately 300 mm for each experimental setup. The exposure time was about 4 hours in length. The PLATYPUS software package (Sec. 2.3.2) was employed to integrate the two-dimensional image patterns and convert those to one-dimensional diffraction patterns. The observed powder patterns of GeS and GeSe at ambient pressure are presented in Fig. 5.2.

During the subsequent Rietveld refinement procedures, the preferred orientation correction was taken into account to record accurate relative intensities of the diffraction peaks. The preferential directional staking of disk-shaped samples deduced from the easy cleavage normal to the c-axis of the layered crystals is responsible for a certain degree of misrepresentation of the relative intensities of the relevant **(hkl)** reflections. Therefore, it is naturally expected that the **(00l)** axis is the dominant preferred orientational direction of GeS and GeSe. However, there is no guarantee that the incident beam direction and preferred orientation direction coincide. To find the appropriate preferred orientation axis, many trial preferred orientation directions have been examined and it was found a pure **(00l)** does fit the observed data best.

Indeed, the real preferred orientational direction is composed of either several preferred orientation axes or a distribution of such directions. These complex phenomena can be dealt with using recently developed sophisticated preferred orientation analysis methods [132, 133]. However, it is shown that, in these cases, a single preferred direction provides a reasonable approximation to the combination of different preferred orientation axes.

The MPROF Rietveld method using the form of preferred orientation correction in Eqn. (2.15) with **(00l)** preferred direction was used to refine both GeS and GeSe data. The refinement reliability can be evaluated by two parameters: R_{wp} and χ^2 which are given from the output of MPROF package. In the cases of GeS and GeSe, R_{wp}(GeS)=14.80% and χ^2(GeS)=0.076 while R_{wp}(GeSe)=14.63% and χ^2(GeSe)=0.147. The least-squares fits to the ambient powder patterns are shown in Fig. 5.2 and the

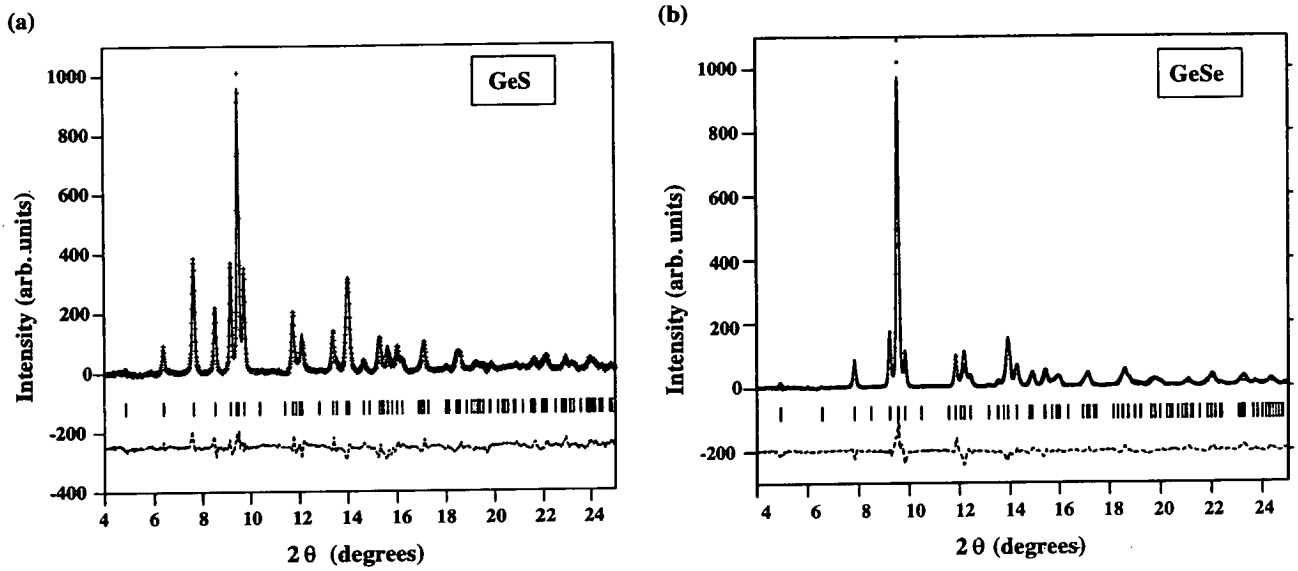

Figure 5.2. Rietveld refinements of powder patterns of (a) GeS and (b) GeSe obtained at ambient pressure. The wavelength of the incident beam was 0.4447 Å and 0.4652 Å for GeS and GeSe, respectively. The fit shown here has been obtained using a **(001)** preferred orientation correction for both GeS and GeSe. The observed data are denoted as '+' symbols and the symbol of '|' represents the calculated reflection. The solid line is the calculated profile. The dashed line is the difference between the calculation and observation.

details of structural parameters of GeS and GeSe determined by refinement procedures are shown in Table 5.1. For comparison, the previous single crystal data are also exhibited in this table.

The bond lengths and bond angles at ambient pressure can be completely determined from the information contained in Table 5.1. In the case of GeS, the B_{ab} and B_c bond lengths defined in Fig 5.1 are 2.494Å and 2.283Å respectively, and which are 2.578Å and 2.439Å in GeSe. Three distinct bond angles in the GeS structure, A_{ab}, A_{c1} and A_{c2} are measured as 95.4°, 105.5°, and 91.1°, respectively, and the revalent data are 95.9°, 105.4°, and 90.1° for GeSe. As shown in Fig 5.1, a double-layer presents two nonbonded separations between the next nearest neighbours of different species. These distances are approximately 3.305Å and 3.94Å for GeS and 3.494Å and 4.034Å for

Table 5.1. Observed structural parameters for GeS and GeSe at ambient conditions. For comparison, the previous single crystal results are also shown. The units for cell dimensions (a, b, and c) are in Å and the positional parameters are in fractional coordinate units.

Compound	Data	a	b	c	u_{Ge}	v_{Ge}	$u_S(u_{Se})$	$v_S(v_{Se})$
GeS	this work	4.29	3.64	10.46	0.123	0.123	0.498	-0.153
	[134]	4.30	3.64	10.47	0.127	0.122	0.499	-0.151
	[135]	4.30	3.65	10.44	0.106	0.121	0.503	-0.148
GeSe	this work	4.38	3.83	10.85	0.110	0.124	0.504	-0.156
	[135]	4.40	3.85	10.82	0.111	0.121	0.500	-0.146

GeSe, respectively. Also, two double-layers constitute a unit cell and are characterised by an interlayer separation and intralayer thickness. The experimental value of the interlayer separation of GeS and GeSe is 2.656Å and 3.038Å respectively, whereas the intralayer thickness is 2.573Å in GeS and 2.387Å in GeSe at ambient pressure.

5.2.3 First-principle Simulation of Structure

The computational determination of the equilibrium structures were performed using *ab-initio* pseudopotential total-energy package, CASTEP, which is already discussed in detail in Chapter 3. In CASTEP, the local density approximation (LDA) based on the parameterisation of Perdew and Zunger [136] form was employed to describe the exchange-correlation interactions, G_{xc}, within the Kohn-Sham equation (Eqn. (3.14)). The nonlocal ionic pseudopotentials of Ge, S, and Se are in the Kleinman-Bylander form and were generated by the Q_c tunning approach (Sec. 3.2.3). Then, a preconditioned conjugate gradient scheme was used to minimise the total energy of the system and to relax the ions under the influence of the Hellmann-Feynman forces (Sec. 3.2.4).

For both GeS and GeSe, the energy cutoff of 300 eV for the plane wave basis set expansion has been tested and implemented. This cutoff value corresponds to approximately 2000 and 2500 plane waves per band per k-point in GeS and GeSe,

respectively. It was found that the total energies at this cutoff converge to better than 0.1 meV/ cell in GeS and 0.2 meV/cell in GeSe. In order to perform the Brillouin zone(BZ) integrations, the Monkhorst-Pack special points scheme (Sec. 3.2.2) was used. After the examination of the k-point sampling, the $4 \times 4 \times 4$ and $4 \times 4 \times 10$ grid corresponding to 8 and 20 special k points provide full convergence of total energies of GeS and GeSe, respectively.

However, two different strategies were performed to search the equilibrium structure configurations of GeS and GeSe individually. To find the equilibrium structural parameters at ambient pressure, a *unit cell optimisation* method which parameterises the external pressure as an input factor was employed in the studies of the GeS structure. As discussed in Sec. 3.2.5, this automatic searching technique relaxes and optimises the lattice constants under the stresses on the unit cell which can be calculated from first principles. During this *ab-initio* simulation process, the change of cell parameters is accompanied by a change of the plane basis set which gives rise to a modification of the energy cutoff, E_{cutoff}. This effect can be balanced by adding a Pulay correction to the stress calculation. Based on the definition of the Pulay correction in Eqn. (3.55), the correction coefficient, $\partial E/\partial(lnE_{cutoff})$, of GeS is derived from the slope of a linear fitting curve in Fig. 5.3 and it is found the value of the derivative is -2.85. Thus, a quenched molecular dynamics scheme with alternate relaxation of the cell and structural parameters is launched from a set of reasonable initial parameters to find the stable structure.

As a test of this automatic relaxation method, a conventional exhaustive searching scheme is applied to determine the equilibrium configuration of the GeSe structure. An efficient approach is to calculate the best ratio of lattice constants which corresponds to the local minimum of total-energy for a fixed volume size and then repeat this process for different volumes. Therefore, the total-energy of the system is described as a function of volume and the pressure of each calculated volume can be determined

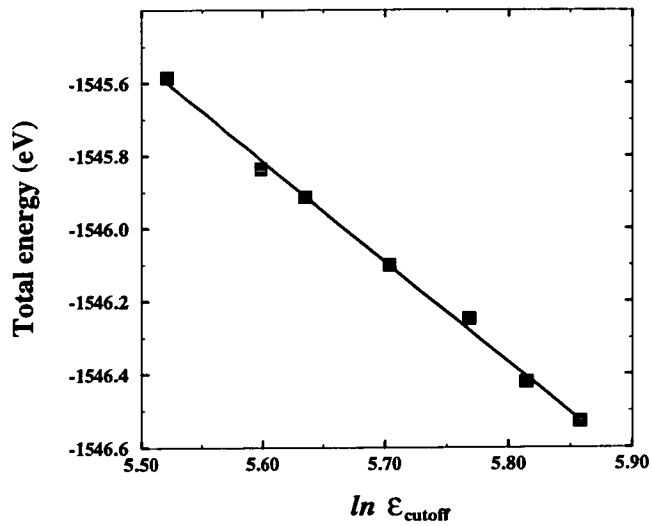

Figure 5.3. The calculated total energy as a function of the logarithm of the cutoff energy. The calculated total energies corresponding to different cutoff energies are denoted as solid squares. The solid line is a linear fit to the calculated data and is defined as the Pulay coefficient.

from the tangent of the energy-volume curve at the relative volume. Thus, a well-defined global minimum of the total-energy with respect to the optimum volume size and cell parameters can be easily found from the minimum of the energy-volume curve to specify the calculated ambient system.

The calculated ambient structural parameters of GeS and GeSe are both shown in Table. 5.2. Comparing with the experimental data in Table. 5.1, it is evident that the calculated lattice constants are roughly 2% smaller than room temperature experimental values. Because this first-principles method corresponds to zero temperature condition, a part of this discrepancy can be contributed from the effect of thermal expansion. However, it is believed that this underestimate is dominately attributed to the well-known tendency of the LDA methods to *overbind* (Sec. 3.2.1).

Table 5.2. Calculated structural parameters for GeS and GeSe at ambient pressure. The units for cell dimensions (a, b, and c) are in Å and the positional parameters are in fractional coordinate units.

	a	b	c	u_{Ge}	v_{Ge}	$u_S(u_{Se})$	$v_S(v_{Se})$
GeS	4.184	3.556	10.123	0.123	0.117	0.499	-0.148
GeSe	4.293	3.744	10.576	0.107	0.118	0.498	-0.146

5.3 Structural Response to Pressure: Experiment and Computation

This section will include experimental and theoretical studies of the structural response of GeS and GeSe to hydrostatic pressures. The equations of state for both Ge chalcogenides will be described and the compressional mechanism of these anisotropic materials will be explained by the calculated structural parameters corresponding to different pressure.

5.3.1 Equations of State for GeS and GeSe

Under compression, the equations of state (EOS) for GeS and GeSe can be studied experimentally using synchrotron powder X-ray diffraction with image plate area detectors for optimal signal to noise ratios and accurate relative peak intensities. The powder samples are placed in the DAC with a chip of ruby for pressure determination and a 4:1 methanol-ethanol mixture as the pressure transmitting fluid for generating hydrostatic pressures. The detail of experimental techniques and setup can be found in Chapter 2. The structural properties of GeS and GeSe have been studied up to 94 and 130 kbar, respectively. The observed profiles and refinement patterns of GeS at 94 kbar and of GeSe at 130 kbar are both shown in Fig. 5.4.

From the powder diffraction data, it was found that the GeS structure retains the

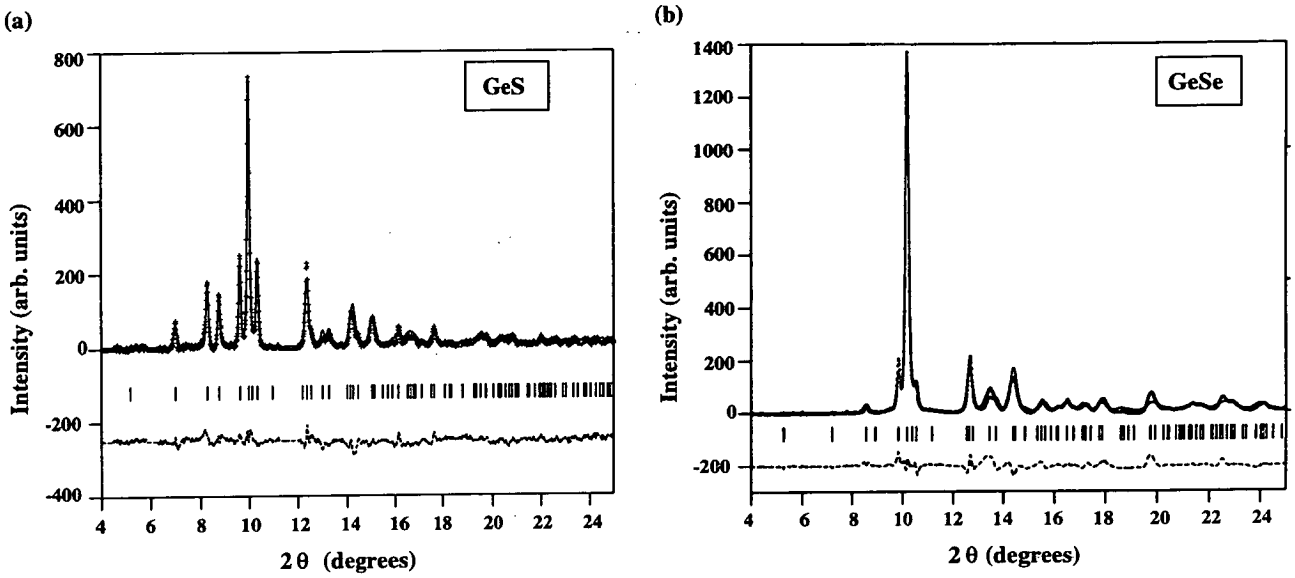

Figure 5.4. Rietveld refinements of powder patterns of (a) GeS obtained at 94 kbar and (b) GeSe obtained at 130 kbar. The radiation sources and the preferred orientation directions have been mentioned in Fig. 5.2. The observed data (shown as '+'), calculated reflections (shown as '|'), calculated pattern (solid line), and discrepancy (dashed line) are exhibited and the refinement reliability factor R_{wp} of GeS and GeSe is 16.03 and 15.63, respectively.

layered orthorhombic crystal structure up to 94 kbar. Also, there is no evidence in these experiments to reveal a pressure-induced structural phase transformation of GeSe up to 130 kbar. Decompression of both GeS and GeSe from high pressure to ambient pressure was also studied. It resulted in diffraction patterns almost identical to those obtained from the starting material albeits only with slightly broadened peaks.

Using *ab initio* simulations, the structure stability can be systematically studied by comparing with the calculated total energies of different structure phases. Two possible crystal structures of Ge chalcogenides, rocksalt (NaCl) and orthorhombic, were taken into account. The computational parameters are the same as the ambient calculation presented in Sec. 5.2.3. The results of calculated total energy as a function of unit cell volume of the two phases are shown in Fig. 5.5. It is revealed that the orthorhombic

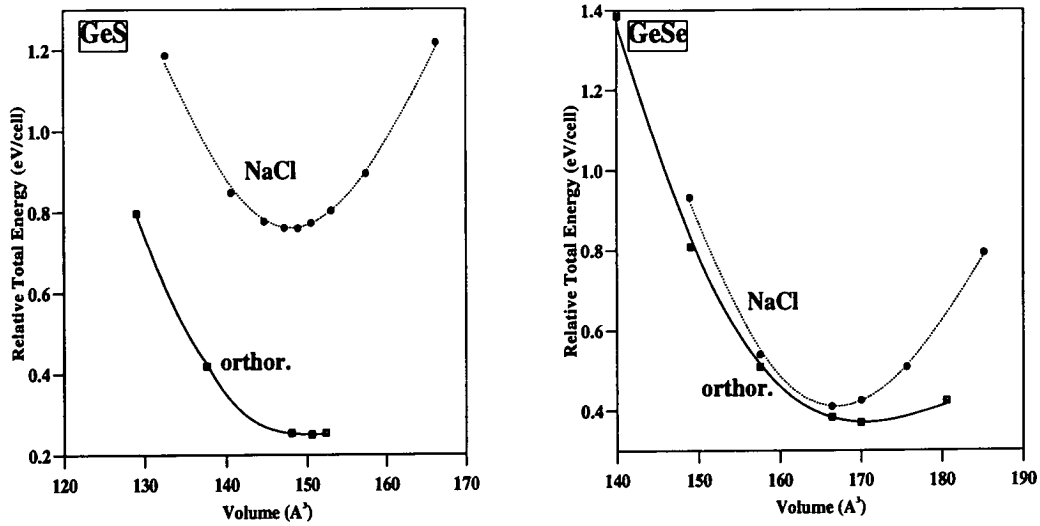

Figure 5.5. Relative total energy versus the unit cell volume determined by *ab initio* calculations. The hydrostatic pressure response was determined by optimisation of the unit cell parameters. At every volume, internal ionic positional parameters were relaxed under the influence of Hellmann-Feynman forces. The calculated total energies of orthorhombic and NaCl structure are denoted as solid squares and circles, respectively. The solid and dashed lines are the third-order polynomial fit to the total energy versus unit cell volume.

structure of two Ge chalcogenides is more stable than the NaCl phase and there is no tendency of pressure-induced structural transformation from the orthorhombic to the rocksalt phase under hydrostatic pressure. Furthermore, in Fig. 5.5, the decreasing of total energy difference between orthorhombic and NaCl structure with going down the Group-VI family implies that the stable structure of the heavier Ge chalcogenide, GeTe, favours the NaCl-like crystal structure. Indeed, the equilibrium GeTe has been found to adopt a rhombhedral structure which can be regarded as a distortion of the NaCl type [137].

Thus, the EOS for GeS and GeSe can be clearly described by results of the refinement data from X-ray diffraction patterns and *ab-initio* calculations as shown in Fig. 5.6. Fig. 5.6 shows the variation of the unit cell volume as a function of pressure for GeS and GeSe. It is seen that the pressure response of unit cell volumes of these orthorhombic crystal structures can be well accounted for by first-principle calculations.

In order to obtain the bulk modulus B_0 and its pressure derivative B_0' at ambient pressure, the 3rd-order Birch-Murnaghan EOS form [138] has been fitted to the curves.

$$P = 3B_0x(1+2x)^{5/2}[1+cx] \tag{5.2}$$

where

$$\begin{aligned} x &= \frac{1}{2}\left[\left(\frac{V_0}{V}\right)^{2/3} - 1\right] \\ c &= \frac{3}{2}(B_0' - 4) \end{aligned}$$

The fitting curves of experimental data are also shown in Fig. 5.6 and the bulk modulus and their 1st derivative for GeS and GeSe are listed in Table 5.3. Nevertheless, the overestimate of bulk modulus in *ab-initio* calculations in Table 5.3 is the consequence of the underestimate of unit cell volumes in calculations with the LDA approximation.

Table 5.3. The experimental and calculated bulk modulus (B_0) of GeS and GeSe. under ambient condition. The 1st-order derivative of B_0 to pressure (B_0') are also shown here.

Compound	Data	B_0 (kbar)	B_0'
GeS	expt.	399	4.8
	calc.	461	4.3
GeSe	expt.	379	5.3
	calc.	412	5.1

Both experimental and computational results of the EOS of GeS and GeSe are consistent with Chattopadhyay's measurements [139] in which the structures of GeS and GeSe are studied using energy-dispersive X-ray diffraction where no structural transition has been found up to 340 kbar. Furthermore, the bulk modulus at zero-pressure reported in [139] are higher than present work because the previous data were

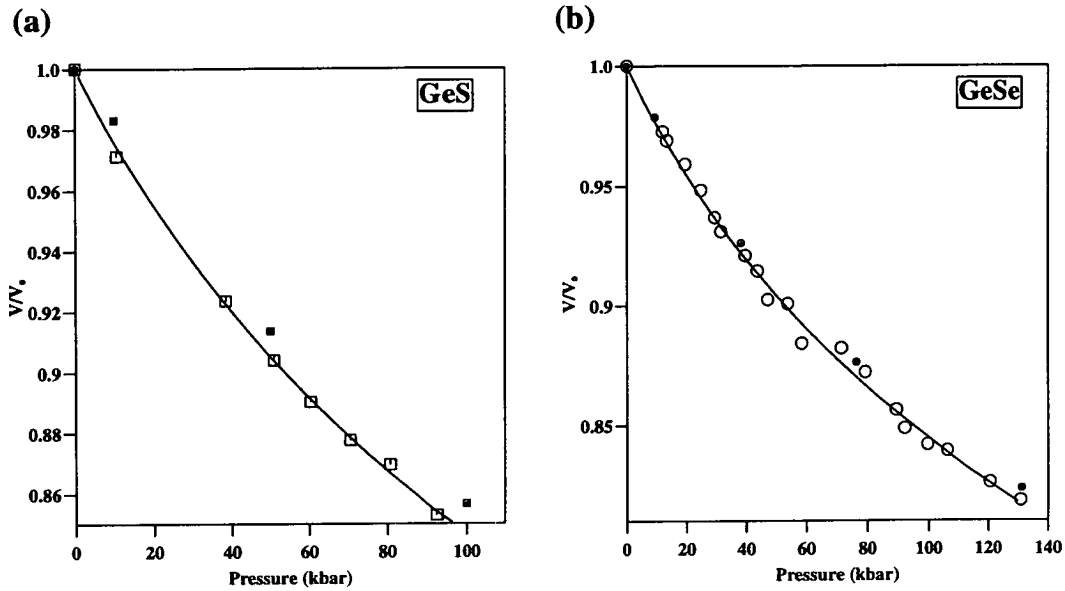

Figure 5.6. The dependence of normalised unit cell volume, V/V_0 (V_0 is the equilibrium unit cell volume at ambient pressure), as a function of hydrostatic pressure of (a) GeS up to 100 kbar and of (b) GeSe up to 130 kbar. The open symbols represent the experimental data as determined using angle-dispersive powder X-ray diffraction and solid ones denote *ab-initio* calculations. The solid lines are the fitting curves of experimental points to the 3rd-order Birch-Murnaghan equation which gives the information of the bulk modulus shown in Table 5.3.

obtained over a much wider pressure range ($\sim$ 50 kbar).

However, the above compressional behaviour of Ge chalcogenides is in contrast to the observations of Bhatia *et al.* [140] who report a significant drop of resistivity for GeSe under presure. The authors claim that a single crystal GeSe undergoes a pressure-induced first-order structural phase transition to a metallic NaCl structure at approximate 60 kbar. Moreover, Bhatia *et al.* found the equilibrium lattice constant of NaCl-like GeSe after decompression to be 7.37 Å which is substantially larger than the first-principle value (5.483 Å) which corresponds to the minimum of the total energy curve of GeSe in the NaCl structure shown in Fig. 5.5. It is believed that the phase transitions reported in Bhatia's paper suffers from nonhydrostaticity and that the recovered sample has a more complex structure rather than a simple NaCl-like structure. The isostructural metallisation transition of GeS and GeSe will be discussed

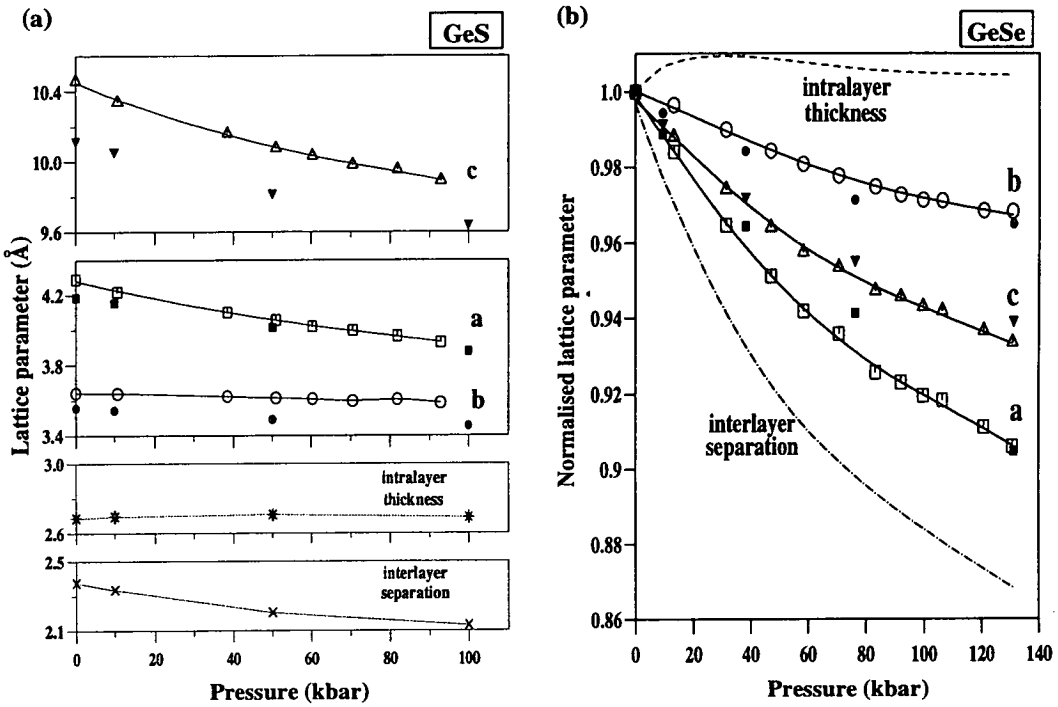

Figure 5.7. Variation of unit cell parameters with pressure of (a) GeS and (b) GeSe. In (a), cell parameters of GeS refined from experimental data are shown as open symbols and the calculated lattice constants, intralayer thickness, and interlayer separation is denoted as solid symbols, '*', and 'X', respectively. Solid and dotted lines are guides to eye. In (b), the normalised experimental and calculated lattice constants of GeSe are denoted as open and solid symbols, respectively. The dashed and dash-dotted lines represent the calculated intralayer thickness and interlayer separation, respectively.

in Sec. 5.4.

5.3.2 Pressure Dependence of Layered Structure Properties

The pressure dependences of unit cell parameters of GeS and GeSe as a function of hydrostatic pressure up to 94 and 130 kbar, respectively, are shown in Fig. 5.7. The results of first-principle calculations are also included in this figure for comparison.

First of all, an anisotropic pressure response of the unit cell under hydrostatic pressure is expected because of the anisotropic features of the layered structure. As is

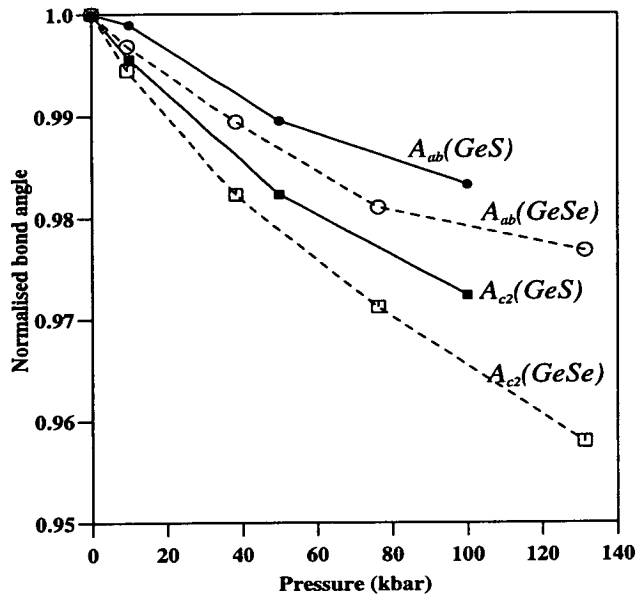

Figure 5.8. The calculated hydrostatic pressure response of the normalised bond angles of GeS and GeSe. The bond angle in the a-b plane (A_{ab})and along the c-axis direction (A_{c2}) is denoted as solid circles and squares for GeS and open circles and squares for GeSe, respectively. The solid and dashed lines are guides to eye.

evident from Fig. 5.7, for both Ge chalcogenides , the a axis is the most compressible direction among three lattice constants, whereas the b axis is least sensitive to pressure. The calculated interlayer separation and intralayer thickness are also presented in Fig. 5.7 and, as would be expected, the interlayer separation corresponding to a weak cohesion is the most rapidly pressure-induced decreasing while the intralayer thickness is insensitive to external pressures.

However, as shown in Fig. 5.7, the surprise is that the c axis (to which the layer planes are normal) is not the most pressure sensitive in spite of the most compressible parameter (interlayer separation) being along the c-axis direction. This unexpected pressure dependent phenomena can be understood by inspecting the compressional behaviour of bond angles. As an example, the calculated pressure dependence of two bond angles, defined as A_{ab} and A_{c2} in Fig. 5.1, are shown in Fig. 5.8 for both GeS and GeSe. It is found that the angle for the intralayer bond (A_{c2}) is much softer than the angle for the bond in the a-b plane (A_{ab}) under compression. This result suggests

that the dominant compression mechanism of the layered Ge chalcogenides is due to the bending of intralayer bonds along the a-axis direction.

Also, the calculated internal positional parameters of GeS and GeSe, u_{Ge}, v_{Ge}, u_S(or u_{Se}), and v_S(or v_{Se}), as a function of pressure are shown in Figs. 5.9(a)- 5.9(d), separately. It reveals that not only the pressure response of global structural parameters (lattice constants), but also the variation of fine structural parameters (fractional atomic positions) of two Ge chalcogenides are very similar to each other.

On the other hand, the hydrostatic variation of two intralayer-bond lengthes, B_{ab} and B_c(shown in Fig. 5.1), and two shortest interlayer atomic separations are shown in Fig. 5.10. The results suggest the compression mechanism performed by pushing layers together yields to the interlayer atomic separation approaching to the intralayer bond length and implies the loss of structural anisotropy while these two distances are comparable under very high pressure. However, in Fig. 5.10, the calculated data show that the interlayer atomic distances are larger than the intralayer bonds and this suggests the structures of two Ge chalcogenides are still characterised by highly anisotropic bonding under the highest pressure studied here.

5.4 Electronic Structure under Compression

The electronic properties of materials can be systematically studied from the careful inspection of the band structures. According to the marked anisotropy, the electron bands of GeS and GeSe will show a unique pattern to reflect the layered crystal structure. Corresponding to the pressure-induced structural behaviour studied in the previous section, the electron distribution will be affected by external compression and it can be observed using band structure calculations. In this section, the method and symmetry consideration for the band structure calculations of GeS and GeSe are highlighted initially. A comparison between experimental and calculated results are also provided.

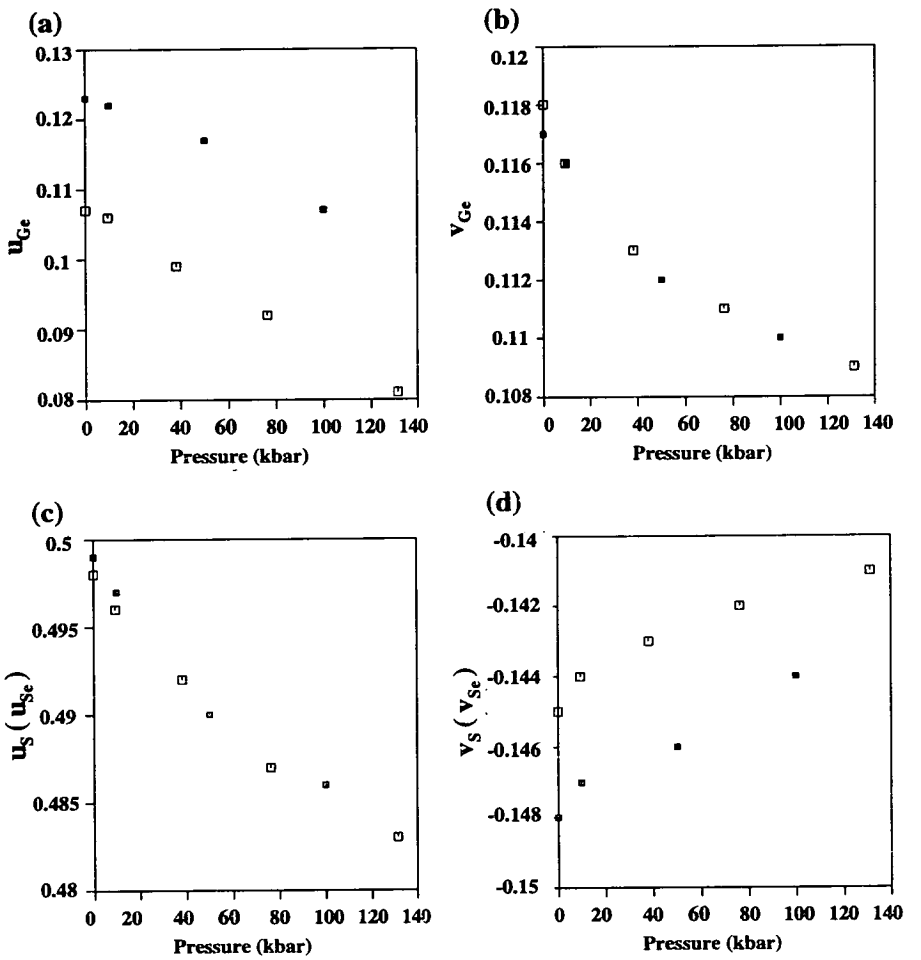

Figure 5.9. The variation of the calculated internal structural parameters of GeS and GeSe with pressure. For GeS, u_{Ge}, v_{Ge}, u_S, and v_S, are denoted as solid symbols, whereas, open symbols represent the u_{Ge}, v_{Ge}, u_{Se}, and v_{Se} of GeSe. Four parameters are shown in (a), (b),(c), and (d) independently. The internal structural parameters are in the fractional unit.

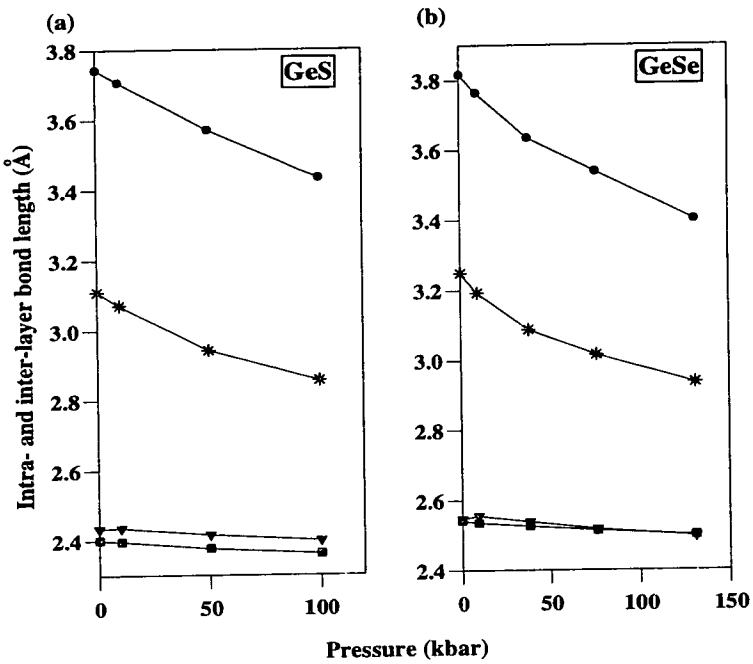

Figure 5.10. Pressure dependence of the intra and interlayer bond length of (a) GeS and (b) GeSe. Solid squares and triangles represent the intralayer bond on a-b plane (B_{ab}) and along the c-axis direction (B_c), respectively. Two shortest distances between atoms of unlike species within different double layers are denoted as the symbols of solid circles and '*'. The solid lines are guides to eye.

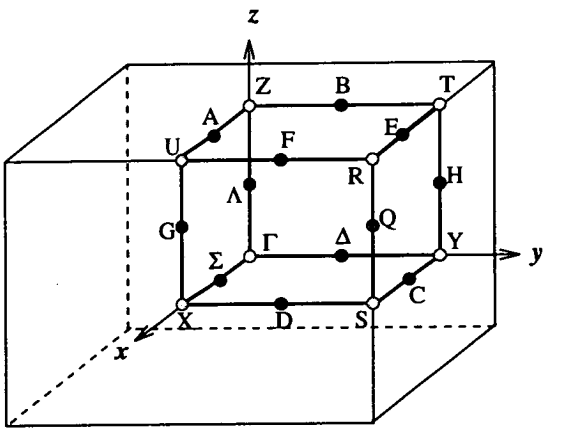

Figure 5.11. Brillouin zone for the primitive orthorhombic structure with high symmetry points and directions labelled. In this convention, the x, y, and z directions correspond to c, b and a crystallographic axes, respectively.

Then, the pressure effects on electron bands will be demonstrated and finally, the nature of bonding will be interpreted by the valence charge densities at different pressure conditions.

5.4.1 Electronic Structure Study - Band Structure Calculations

The band structures of GeS and GeSe were calculated using the density functional formalism. In order to evaluate band energies at many k points along high-symmetry directions in the Brillouin zone (BZ), the self consistent eigenfunctions of the Kohn-Sham Hamiltonian corresponding to the full relaxed structural parameters shown in last sections were used and the correct Hamiltonian can be constructed. Meanwhile, unlike variational total-energy calculations discussed in Chapter 3, a full matrix diagonalisation method is performed to calculate eigenvalues at each k point in the BZ.

Before implementing the band structure calculations, it is worth showing the symmetry properties of the points and lines inside the BZ for the orthorhombic GeS and GeSe. In Fig. 5.11, the high symmetry vertices and edges of the irreducible $\frac{1}{8}$ BZ are

well characterised by the nonsymmorphic group D_{2h}^{16}. Taking both space-group symmetry and time-reversal symmetry into account, all the vertices are double degenerate except Γ (singlet), S (fourfold degenerate) and R (fourfold degenerate). Also, there are three singlet edges (Σ, Δ, and Λ) and one fourfold-degenerate edge (Q) which are different from the double degenerate symmetry of the rest [141].

At ambient pressure, the calculated energy band structures of GeS and GeSe are both shown in Fig. 5.12 along different symmetry lines in the BZ. As the members of the IV-VI family, GeS and GeSe with four Ge-chalcogen pairs in the unit cell provide 40 valence electrons which can be filled in 20 electron bands which are shown at the Γ point in Fig. 5.12. In these calculations, bands were degenerated at some special high symmetry k points, such as the double degeneracy of Z and fourfold degeneracy of S. The degeneracy of calculated eigenvalues at each k point is consistent with the previous symmetry analysis. In addition, X-ray photoemission (XPS) valence-band spectra of GeS [141, 142] and GeSe [143] and relative calculated density of states (DOS) are shown in Fig. 5.12 for comparison. The measured calculated energies of the DOS peaks for GeS and GeSe are also listed in Table 5.4. Remarkable agreement between the observed photoemission density of states (PDOS) and *ab-initio* calculations was found.

Moreover, an indirect band gap between the top of the valence bands and the lowest conduction band has been found along the Λ direction (between Γ and Z) in both GeS and GeSe. However, the calculated indirect band gap E_g^i of GeS and GeSe is 0.65 and 0.36 eV, respectively, which is smaller than the experimental measurements (E_g^i(GeS) 1.65 eV [144] and E_g^i(GeSe)=1.1 eV [145]). This underestimate of band gap is to be expected in view of that the the unoccupied excited states cannot be described properly using the density functional theory.

The response of band structure of GeS to pressure is shown in Fig. 5.13. As is evident from Fig. 5.13 , the indirect energy gap decreases more dramatically than the other valence bands with increasing pressure. As a matter of fact, the calculated band gap of GeS is closed at 50 kbar. The same presure-induced indirect band closure can

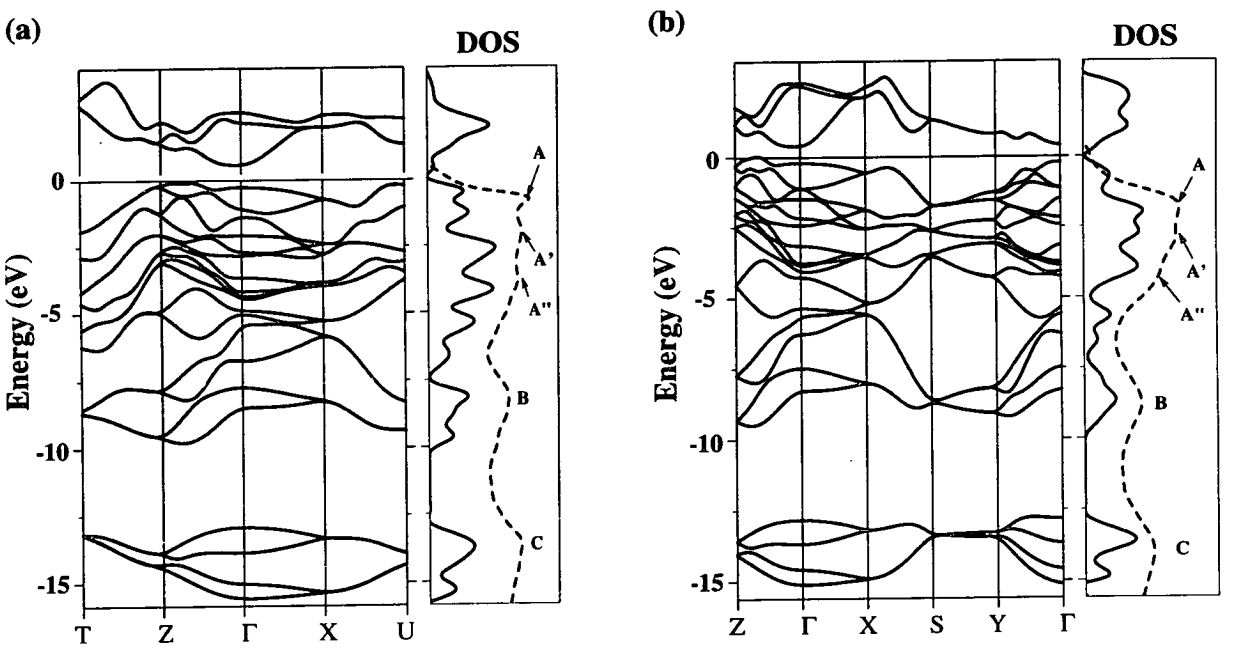

Figure 5.12. Calculated band structure for (a) GeS and (b) GeSe. 20 valence bands and 3 conduction bands are presented here. Calculated DOS (solid line) and PDOS (dashed line) obtained from XPS (using X-ray with $h\nu = 1486.6$ eV [141, 143]) for GeS and GeSe are also shown in (a) and (b), respectively. Calculated energies are referred to the top of the valence bands and experimental energies are referred to the Fermi level of the spectrometer. Five observed peaks are denoted as A, A', A", B, and C.

Table 5.4. Observed (E(XPS)) and calculated (E(calc.)) energies of DOS peaks for GeS and GeSe. The energy in the unit of eV is referred to the top of the valence bands and notation of peaks is the same as Fig. 5.12

Compound	Peak	E(calc.)	E(XPS)
GeS	A	1.3	1.2
	A'	2.5	2.4
	A"	4.0	4.2
	B	8.1	8.5
	C	13.6	13.1
GeSe	A	1.3	1.2
	A'	2.7	2.4
	A"	4.0	3.7
	B	8.6	8.3
	C	13.6	13.5

be also found in GeSe [131] under modest pressure ($\sim$ 40 kbar). The calculated results suggest that GeS and GeSe undergo a semiconductor-to-semimetal phase transition under compression. This conclusion can explain the large drop in electrical resistivity of GeSe at 60 kbar observed by Bhatia *et al* [140]. However, the calculated metallisation pressure may also be subject to underestimates arising from the overbinding of LDA within first principle calculations.

5.4.2 Nature of bonding - Valence Charge Densities

The information on bonding can be extracted from inspection of the valence charge distribution. As mentioned above, the lowest 20 valence bands of layered Ge chalcogenides are occupied by 40 valence electrons contributed from four Ge($4s^2 4p^2$) and four S ($3s^2 3p^4$) (or Se($4s^2 4p^4$)) within the unit cell. To understand the roles of different valence bands playing in the bonding picture, at ambient pressure, a portion of band structure (along line Λ) of GeSe shown in Fig. 5.12(b) was chosen as an example and the 20 valence bands of GeSe were separated into five independent groups. The valence

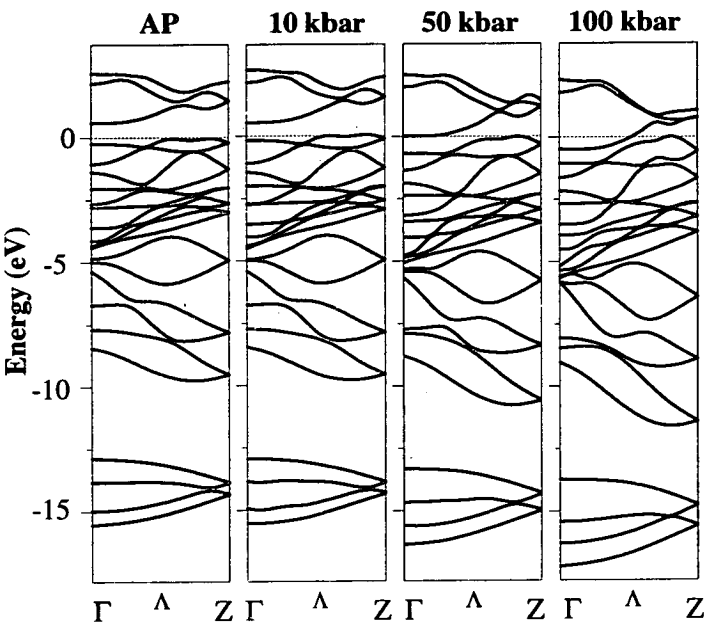

Figure 5.13. Evolution of the electron band structure of GeS at different pressures. The pressure is indicated at the top of each separated window of bands. A pressure-induced closure of indirect band gap between vertices Γ and Z has been predicted in these calculations. Energies are referred to the top of the valence bands which is represented as the dashed lines.

charge densities for each groups was a by-product of the band structure calculation. The three-dimensional electron densities for five groups are presented independently in Fig. 5.14. As a result in Fig. 5.14(a), it is clear that the lowest four bands with little dispersion correspond to a predominately spherical charge distribution around the Se atoms and are referred to the deeper s orbital of Se. In Fig. 5.14(b), the second lowest four bands are mainly derived from the Ge s level. The remaining three groups correspond to the combinations of $4p$ orbitals of Ge and Se. From the Fig. 5.14, the majority of the charge of group (c) (band 9-10), (d) (band 11-16), and (e) (band 17-20) is obviously located along three crystallographic c, b, and a axes, respectively. Also, these three groups display more information of bonding character of the orthorhombic crystal structure.

It should be mentioned that the lower bands of GeSe along the lines Δ and D are very similar to each other. As shown in Fig. 5.15, the nearly parallel nature of the lower bands along Δ implies a splitting from the bands along relative higher symmetry line, D, and the splitting within a pair of bands is small (0.5 eV for the Se($4s$) bands and 0.8 eV for Ge($4s$) bands). The same feature can be found in GeS along Λ and G and the energy splitting is 0.5 and 0.8 eV for S($3s$) and Ge($4s$) bands, respectively. This similarity can be also found in any pair of lines which are normal to the x direction of the BZ. The reason for this effect is that the weak electronic interaction between two double-layers will lift the degeneracy of energy bands along the edge normal to the x direction of the BZ (corresponding to the direction of layer plane in real space). If a single layer is treated, without any cohesion between layers, the space group D_{2h}^{16} will be reduced to the point group C_{2v} and the dispersion of bands along line Δ should be identical to which along line D. Therefore, the band energy splitting of can be proposed as a reasonable measure of the interlayer interaction.

Finally, the three-dimensional valence electron density of the whole 20 valence bands of GeSe at ambient pressure is shown in Fig. 5.16(a). Four unit cells (double the a and b crystallographic axis) are shown. It is evident that a significant amount of electron

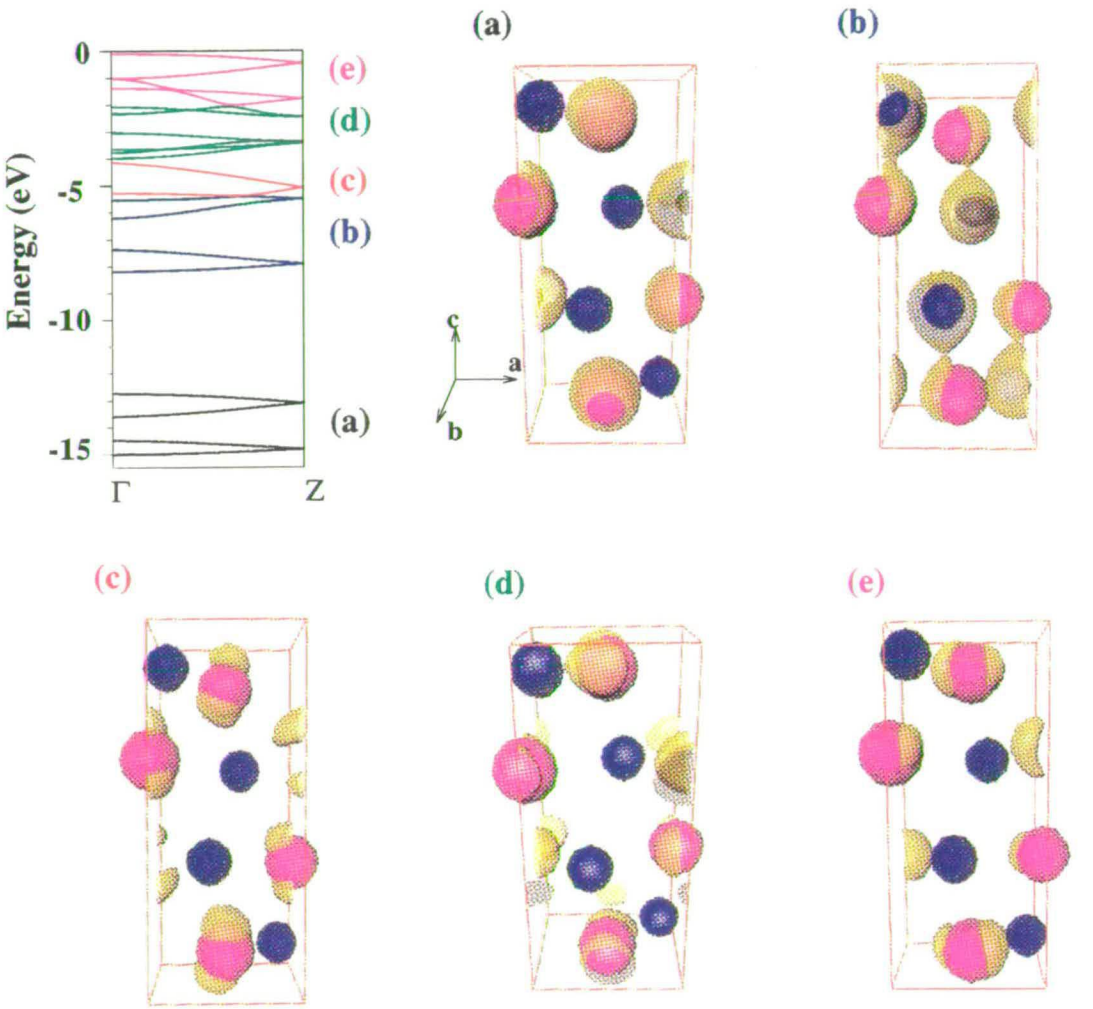

Figure 5.14. Valence band structure and charge densities of GeSe at ambient condition. For clarity, five different groups of bands are represented independently as black, blue, red, green, and pink lines in band structure and relative charge density is shown in (a), (b), (c), (d), and (e), respectively. Ge and Se is shown as a smaller blue and larger pink sphere, respectively, and valence charge distribution is shown as the yellow cloud.

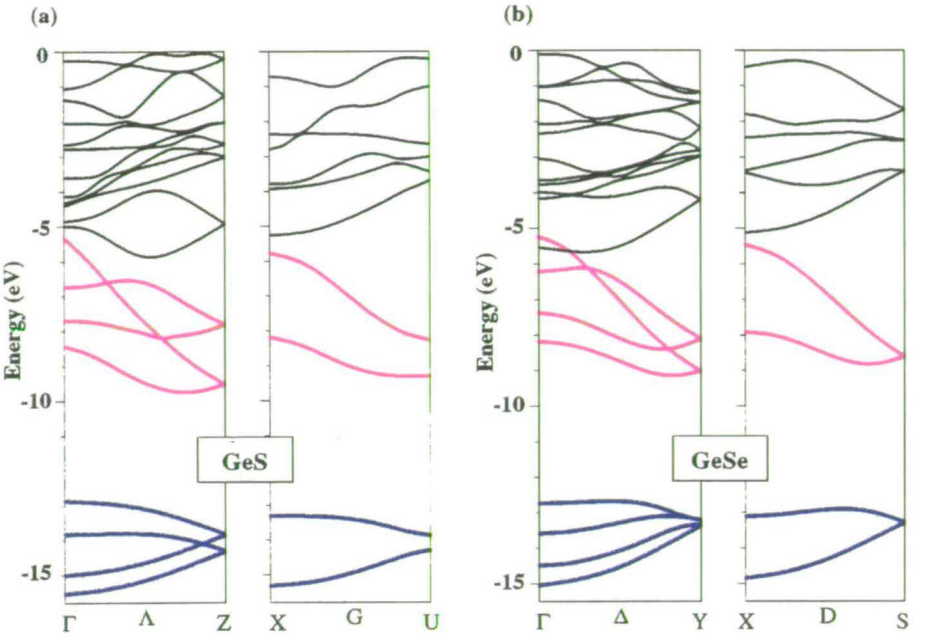

Figure 5.15. Band structure of (a) GeS along symmetry lines Λ, G and (b) GeSe along Δ and D. The bands of s orbitals for Ge and S (or Se) are shown as the pink and the blue lines, respectively, for comparison. A band splitting can be found along two parallel edges (Λ-G or Δ-D) of BZ.

centered around the individual atom positions is shared in the bonds. Moreover, within a given separate double layer, the charge densities form a threefold coordinated covalent bonding structure. It can be seen clearly in Fig. 5.16(a) that there is negligible charge density between the layers despite without special care of modelling the weak interaction in these calculations. However, as shown in Fig 5.16(b), only slight bridging of the electron distribution of GeSe across the different layers has been observed under high pressure ($\sim$ 130 kbar) and the electron distribution still maintains the orthorhombic layered bonding feature.

5.5 Conclusion

In this chapter, the high-pressure effects on the structural properties of the anisotropic layered IV-VI semiconductors, GeS and GeSe, have been extensively studied using a

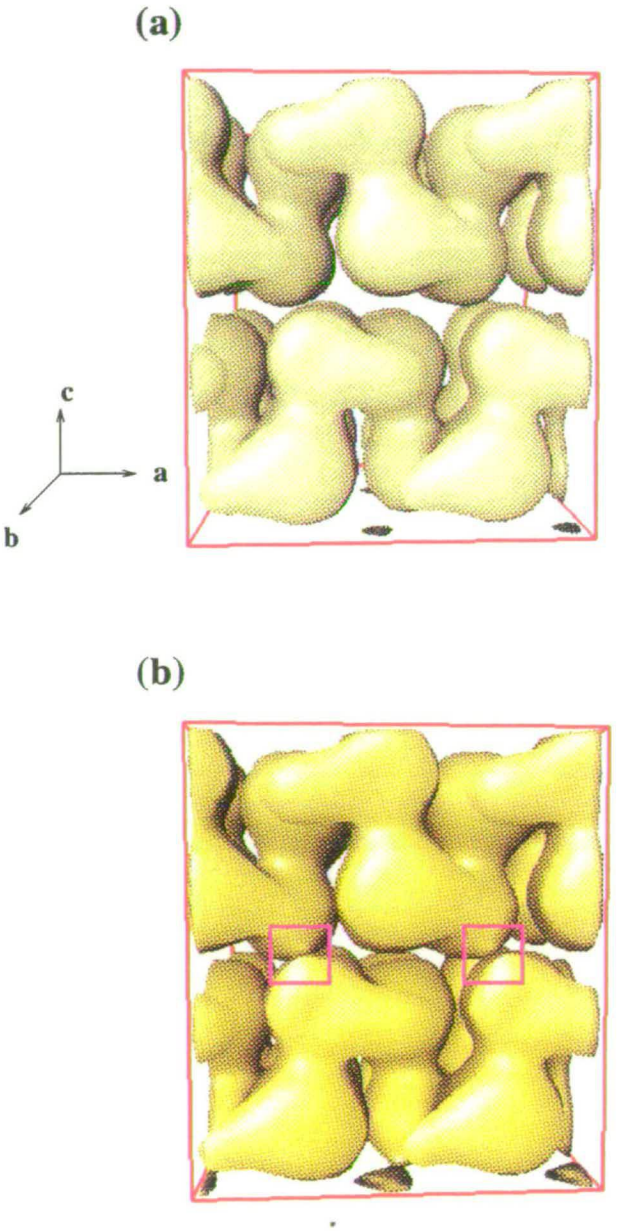

Figure 5.16. Valence charge distribution in GeSe at (a) ambient pressure and (b) 130 kbar as viewed normal to the c axis. As shown in these figures, each atoms is threefold coordinated via covalent bonds within a given double layer. The pressure-induced bridging of electron distribution is highlighted in pink windows in (b).

combination of experimental and theoretical approaches. The pressure-induced electronic properties have been also routinely investigated using first-principle density functional pseudopotential calculations.

The results from angle-dispersive powder X-ray diffraction and *ab-initio* simulation reveal that GeS and GeSe doesn't undergo any structural phase transition up to 94 and 130 kbar, respectively. Also, an anisotropic response of these layered structures to the hydrostatic pressure has been found in both experimental and computational data which show a pressure-induced nonhomogeneous bond bending responsible for this anisotropy. More specifically, the band structure study under compression suggests that the previous reported discontinuity of resistivity of GeSe at 60 kbar can be accounted for by a pressure-induced indirect band gap closure rather than a first-order structural metallic phase transition.

According to the superb agreement between observations and *ab-initio* calculations, it is realised that density functional methods are capable of adequately describing the compressional mechanism of structural and electronic properties in spite of the highly anisotropy of crystal structures. The tremendous success of this methodology will bring a lot of confidence in the pressure studies on other properties, such as the vibrational behaviour under pressure which will be discussed in next chapter.

Chapter 6

Vibrational Properties of Layered Materials

6.1 Introduction

The vibrational properties of low-dimensional layered compounds have been the subject of sustained interest for many years because of different chemical bonding in the unit cell. However, the nature of weak interlayer interaction is still not very well understood. In order to develop a detailed picture of layered solids and also to probe the interlayer coupling, the vibrational studies of layered Ge chalcogenides (as the examples) will be comprehensively studied under pressure using a combination of group theory, high-resolution Raman scattering and *ab-initio* simulation.

According to the structural information provided previously, the lattice dynamics of layered Ge chalcogenides can be directly analysed by well-established group theory. The symmetry properties and optical selection rules derived from group theory considerations give an overall description of the lattice vibrations. However, the distinctively anisotropic features of this quasi-two-dimensional crystal structure can be described more precisely by a diperiodic group (DG) which was developed to model structures

with two-dimensional periodicity and an appreciable thickness along the third dimension. In the limiting case of zero interlayer interaction, DG predicts a Raman-infrared degeneracy of the isolated layer vibrations. Since Davydov-like degeneracy will be lifted by interlayer interaction, a good quantitative estimation of the weak interlayer cohesion can be made by comparing the frequencies of Raman-infrared pairs.

Another distinctive feature of the vibrational properties of layered solids is the existence of low-frequency vibrational rigid-layer modes in which the layers move relative to each other as rigid units. These rigid-layer vibrations originate from the restoring force due to the interlayer interaction and are located at the very low-frequency region with a frequency separation from the intralayer vibrational frequencies. The understanding of rigid-layer modes is therefore helpful to characterise the anisotropy of layered solids.

Since the strength of interlayer coupling is normally of few orders smaller than that of the intralayer binding, it is expected that hydrostatic pressure will have preferential effects on the weak interlayer cohesion. Then, all interlayer properties, such as Davydov splitting and rigid-layer vibrations, are also expected to be modified under compression. The objective of the work in this chapter is to explore different pressure dependence for heirarchical binding in layered materials.

Thus, the organisation of this chapter is as follows. The fundamental group theoretical tools are outlined in Sec. 6.2. The detail of lattice vibrations in GeS and GeSe which include experimental observations and computational calculations at ambient presure are given in Sec. 6.3. The DG analysis and systematic investigations of interlayer coupling are shown in Sec. 6.4. Pressure effects on layered materials , a new scaling law, and the examination of RL approximation under compression are discussed in Sec. 6.5. Eventually, the conclusion is summarised in Sec. 6.6.

6.2 Symmetry Considerations

It is well known that the vibrational properties of solids are related to the symmetries of the crystal structures. Since the symmetry properties can be properly described by the group theory, it is helpful to demonstrate general group-theoretical analyses for understanding the lattice vibrations before entering into the detailed investigations of specific layered materials.

The normal mode is defined as a lattice vibration in which all atoms vibrate from their equilibrium positions in a specific frequency called the normal frequency. However, the atomic oscillation is confined by the space group symmetry of the crystal structure and conventional group theory [146] is therefore a useful tool to describe the vibrational properties for normal modes. Based on the group theory, Bhagavantum and Venkatarayudu (BV) utilised a group decomposition approach to determine the irreducible representations and selection rules for the normal modes of materials with specific space groups. This BV method which will be discussed in Sec. 6.2.1 can be applied generally to any crystal structure with symmetry properties.

A more elegant correlation method is presented in the second part of this section. The correlation method developed by Hornig builds up the connection between the factor group and its subgroups – site groups. Because the lattice vibrations are the combination of the individual atomic oscillation around their equilibrium sites, the symmetries for site groups will reflect the symmetry properties of lattice vibrations. Therefore, this correlation provide an efficient means to study the symmetries, selection rules, and even the directions of the atomic displacements for normal vibrations in the crystal.

Considering the long wavelength lattice vibrations, this section focuses on the zone-centre phonons of layered compounds. The case studies of GeS and GeSe are provided using both the BV and correlation method. This theoretical result will be found consistent with the experimental data in the next section.

6.2.1 Bhagavantum-Venkatarayudu (BV) Method

To study the zone-centre phonons, the first step of the BV procedure is application of factor-group operations which are isomorphic to the relevant point-group operations to all the atoms inside an unit cell. A reducible representation of the factor group is then constructed by the atoms which are invariant under factor-group symmetry operations. Nevertheless, the reducible representation Γ can be reduced to a linear combination of irreducible representations $\Gamma^{(l)}$,

$$\Gamma = \sum_l a_l \Gamma^{(l)} \tag{6.1}$$

According to the *little orthogonality theorem* (LOT) of group theory [146], the reduction coefficient $a(l)$ of each irreducible representation $\Gamma^{(l)}$ is given by

$$a(l) = \frac{1}{h} \sum_R \chi^{(l)}(R)^* \chi(R) \tag{6.2}$$

where h is the order of the group, $\chi^{(l)}(R)^*$ and $\chi(R)$ is the character of each symmetry operation R within the representation $\Gamma^{(l)}$ and Γ, respectively. The summation runs over all symmetry operations of the factor group.

In Eqn. (6.2), $\chi^{(l)}(R)^*$ and h can be easily determined from a standard character table which provides the character value for each irreducible representation of a factor group under different symmetry operations. Further, the character $\chi(R)$ for reducible representation can be evaluated by

$$\chi(R) = \eta(R)[2\cos\theta \pm 1] \tag{6.3}$$

where $\theta = 360^o/n$ is the angle of an n-fold symmetrical axis and $\eta(R)$ is the number of invariant atoms under the operation R. The plus and minus sign corresponds to a pure and an improper rotation, respectively. Once a_l been found, from Eqn. (6.1), the lattice

vibrations can be clearly presented as a full description of irreducible representations.

In the case of layered Ge chalcogenides, GeS and GeSe adopt a orthorhombic crystal structure with a nonsymmorphic space group D_{2h}^{16} ($Pcmn$) which has been discussed in Sec.5.1. The factor group of D_{2h}^{16} is D_{2h} and the character table for this factor group are shown in Table 6.1. To form the reducible representation of this factor

Table 6.1. Character table for the point group D_{2h} [147]. The x, y, and z corresponds to the c, b, and a crystallographic axis, respectively. T denotes a pure translation whereas R represents a pure rotation. The subscript g and u of the representations represents the *gerade* (symmetric) and *ungerade* (anti-symmetric) property respectively.

$D_{2h} \equiv V_h$	E	$C_2(z)$	$C_2(y)$	$C_2(x)$	i	$\sigma(xy)$	$\sigma(zx)$	$\sigma(yz)$	Linear	Bilinear
A_g	1	1	1	1	1	1	1	1		x^2, y^2, z^2
B_{1g}	1	1	-1	-1	1	1	-1	-1	R_z	xy
B_{2g}	1	-1	1	-1	1	-1	1	-1	R_y	zx
B_{3g}	1	-1	-1	1	1	-1	-1	1	R_x	yz
A_u	1	1	1	1	-1	-1	-1	-1		
B_{1u}	1	1	-1	-1	-1	-1	1	1	T_z	
B_{2u}	1	-1	1	-1	-1	1	-1	1	T_y	
B_{3u}	1	-1	-1	1	-1	1	1	-1	T_x	

group, eight symmetry operations listed in the first row of Table 6.1 are applied to all atoms within the unit cell. Then, the $\eta(R)$ and θ referred to relative operation R can be identified from Eqn. (6.3) and the characters for this reducible representation of D_{2h} can be determined. As an example of this procedure, the operation $\sigma(zx)$ of this nonsymmorphic group which is composed of a pure reflection with respect to the ac plane and a nonprimitive translation $\tau(0, 1/2, 0)$ (which corresponds to shifting the whole unit cell with the distance of an half of lattice constant along the direction of the **b** axis)is applied to each atom. A schematic diagram of the atomic transformation under the operation $\sigma(zx)$ is depicted in Fig. 6.1. It can be seen that all atomic positions are identical to the original ones under $\sigma(zx)$ and, therefore, the number of atoms left

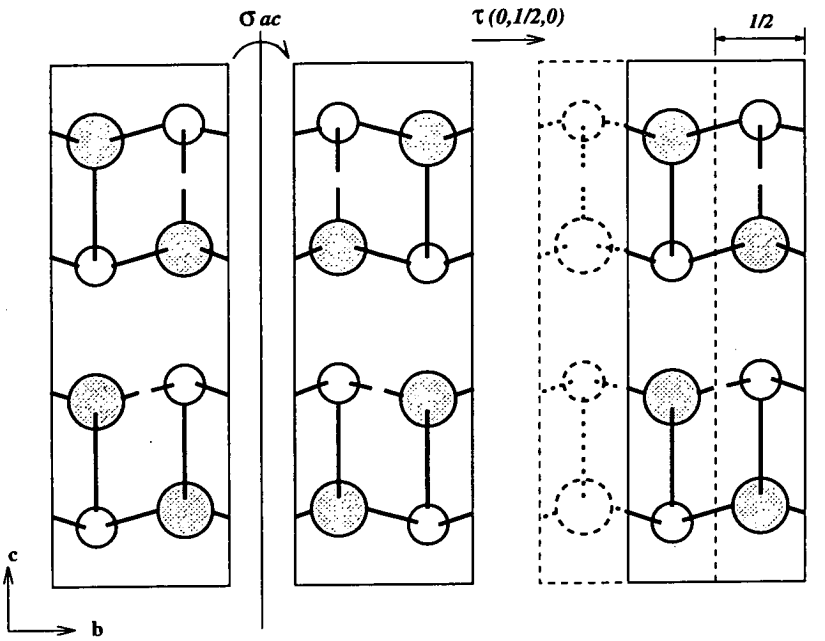

Figure 6.1. Illustration of the symmetry operation $\sigma(zx)$ in which a pure reflection σ_{ac} and a translation $\tau(0, 1/2, 0)$ (defined in text) are involved. Ge and chalcogen atoms are represented as small white and large grey circles, respectively.

invariant by this operation, $\eta(\sigma(zx))$, is 8. Meanwhile, the angle θ corresponding to $\sigma(zx)$ is 0°. Thus, from Eqn. (6.3), the character $\chi(\sigma(zx))$ is equal to 8.

The values for the character $\chi(R)$ associated with the eight symmetry operations can be obtained by the careful examination of each symmetry factor-group operation and are listed in Table 6.2. Consequently, the reduction coefficient $a(l)$ derived from Eqn. (6.2) for the irreducible representations can be obtained directly

$$
\begin{aligned}
a(A_g) &= \frac{1}{8}[1(24) + 1(0) + 1(0) + 1(0) + 1(0) + 1(0) + 1(8) + 1(0)] = 4, \\
a(B_{1g}) &= \frac{1}{8}[1(24) + 1(0) - 1(0) - 1(0) + 1(0) + 1(0) - 1(8) - 1(0)] = 2, \\
a(B_{2g}) &= \frac{1}{8}[1(24) - 1(0) + 1(0) - 1(0) + 1(0) - 1(0) + 1(8) - 1(0)] = 4, \\
a(B_{3g}) &= \frac{1}{8}[1(24) - 1(0) - 1(0) + 1(0) + 1(0) - 1(0) - 1(8) + 1(0)] = 2, \\
a(A_u) &= \frac{1}{8}[1(24) + 1(0) + 1(0) + 1(0) - 1(0) - 1(0) - 1(8) - 1(0)] = 2, \\
a(B_{1u}) &= \frac{1}{8}[1(24) + 1(0) - 1(0) - 1(0) - 1(0) - 1(0) + 1(8) + 1(0)] = 4,
\end{aligned}
$$

Table 6.2. The parameter values of the characters for eight symmetry elements of point group D_{2h}.

Factor-group operation R	$\eta(R)$	θ	$\chi(R)$
E	8	0	24
$C_2(z)$	0	180	0
$C_2(y)$	0	180	0
$C_2(x)$	0	180	0
i	0	180	0
$\sigma(xy)$	0	0	0
$\sigma(xz)$	8	0	8
$\sigma(yz)$	0	0	0

$$a(B_{2u}) = \frac{1}{8}[1(24) - 1(0) + 1(0) - 1(0) - 1(0) + 1(0) - 1(8) + 1(0)] = 2,$$

and

$$a(B_{3u}) = \frac{1}{8}[1(24) - 1(0) - 1(0) + 1(0) - 1(0) + 1(0) + 1(8) - 1(0)] = 4,$$

So, the irreducible representations of D_{2h} are

$$4A_g + 2B_{1g} + 4B_{2g} + 2B_{3g} + 2A_u + 4B_{1u} + 2B_{2u} + 4B_{3u} \tag{6.4}$$

In order to identify the optical selection rule for each irreducible representation, a more detailed consideration of the character table is needed. In Table 6.1, the transformation properties of the irreducible representations are listed in the third and forth column. Considering the fundamental criterion of the infrared absorption, the infrared-active vibrations for an electric dipole transition correspond to the transformation property of a pure linear translation (T) which is the same as that of a Cartesian axes. In addition, the bilinear combination (R) of the specific vibration has the same symmetry

as some elements of the polarisability tensor which implies this mode is symmetry-allowed for Raman scattering. Moreover, the zero-frequency acoustic vibrations are described as the rigid translations of the unit cell along three axis directions. Thus, the 24 lattice vibrations in Eqn. (6.4) can be separated as three acoustic modes (B_{1u}, B_{2u}, and B_{3u}) and 21 optical modes. The expressions and the selection rules for the 21 optical vibrations are deduced as

$$4A_g^{(R)} + 2B_{1g}^{(R)} + 4B_{2g}^{(R)} + 2B_{3g}^{(R)} + 2A_u^{(0)} + 3B_{1u}^{(IR)} + B_{2u}^{(IR)} + 3B_{3u}^{(IR)} \qquad (6.5)$$

where the subscripts (R) and (IR) denote the Raman-active and infrared-active modes, respectively. In addition, based on Table 6.1, the A_u mode without the linear or bilinear transformation property is recognised as an optically silent lattice vibration which is denoted as a subscript (0).

6.2.2 Correlation Method

To implement the correlation method, the symmetry for each site occupied by atoms within the unit cell must be ascertained accurately. The detail of site symmetry for the 230 space groups can be found in the *International Tables for X-ray Crystallography* [148]. The irreducible representations for different site groups within the unit cell are then determined by the relevant character tables [147]. However, only the representations with the linear translational transformation properties (T_x, T_y, and T_z) could be involved because the normal lattice vibrations are only contributed by the combination of linear translational displacements of individual atoms. A correlation table which indicates the relationship between the site-group operations and the factor-group ones is used for subsequent identification of the lattice vibrations. Furthermore, the infrared or Raman activity and the possible eigenvector (atomic displacements) for each normal mode can be also predicted by the correlation method.

As the space group is designated D_{2h}^{16}, there are three possible site groups $2C_i(4)$,

$C_s(4)$, and $C_1(8)$ [148] for the crystal structure of GeS and GeSe. However, four Ge and four chalcogens (S or Se) in the unit cell are in the same symmetry (Sec. 5.1). So, the site groups for Ge and chalcogen are identical and should be one of two candidates $C_i(4)$ and $C_s(4)$. The decision can be made using the crystallography tables with Wyckoff site notation [31] which indicates four equivalent Ge atoms and the other four equivalent chalcogens are both on C_s sites in D_{2h}^{16}. Since the mirror plane (σ_h) for C_s within D_{2h}^{16} lies on the b direction of the unit cell, the character table for site group C_s can be described as Table 6.3.

Table 6.3. Character table for the point group C_s

C_s	E	σ_h	Linear	Bilinear
A'	1	1	$T_x, T_z; R_y$	$x^2, y^2, z^2, x-z$
A''	1	-1	$T_y; R_x, R_z$	$x-y, z-y$

From this character table, it is found that A' representation corresponds to the translational transformation along the x and z directions while the A'' representation transforms as y. Therefore, both A' and A'' must be involved in the correlation.

Now, the correlation between C_s and D_{2h} needs to be considered. The connection between the representations of the factor group D_{2h} and its site group C_s is described in a correlation table [147]. Table 6.4 is the correlation table for the factor group D_{2h} which possesses three possible correlations related to the site group C_s. The proper site correlation is through $\sigma(zx)$ since the Ge (and chalcogen) is on the Wyckoff site(c) which corresponds to site symmetry $\sigma(zx)$ [149]. Therefore, A' in C_s correlates with A_g, B_{2g}, B_{1u}, and B_{3u} in D_{2h} and A'' in C_s correlates with B_{1g}, B_{3g}, A_u, and B_{2u} in D_{2h}. This is shown in a correlation diagram of Fig. 6.2.

The next step is to find out the accurate degrees of freedom for each site-group irreducible representation. In Table 6.3, A' in C_S transforms as x and z, and A'' transforms as y only. The degrees of freedom for A_g, B_{2g}, B_{1u}, and B_{3u} modes originating

Table 6.4. Correlation table for the point group D_{2h} and its subgroups.

D_{2h}	D_2	$C_2(z)$ C_{2v}	$C_2(y)$ C_{2v}	$C_2(x)$ C_{2v}	$C_2(z)$ C_{2h}	$C_2(y)$ C_{2h}	$C_2(x)$ C_{2h}	$C_2(z)$ C_2	$C_2(y)$ C_2	$C_2(x)$ C_2	$\sigma(xy)$ C_s	$\sigma(zx)$ C_s	$\sigma(yz)$ C_s	C_i
A_g	A	A_1	A_1	A_1	A_g	A_g	A_g	A	A	A	A'	A'	A'	A_g
B_{1g}	B_1	A_2	B_1	B_1	A_g	B_g	B_g	A	B	B	A'	A''	A''	A_g
B_{2g}	B_2	B_1	A_2	B_2	B_g	A_g	B_g	B	A	B	A''	A'	A''	A_g
B_{3g}	B_3	B_2	B_1	A_2	B_g	B_g	A_g	B	B	A	A''	A''	A'	A_g
A_u	A	A_2	A_2	A_2	A_u	A_u	A_u	A	A	A	A''	A''	A''	A_u
B_{1u}	B_1	A_1	B_1	B_2	A_u	B_u	B_u	A	B	B	A''	A'	A'	A_u
B_{2u}	B_2	B_2	A_1	B_1	B_u	A_u	B_u	B	A	B	A'	A''	A'	A_u
B_{3u}	B_3	B_1	B_2	A_1	B_u	B_u	A_u	B	B	A	A'	A'	A''	A_u

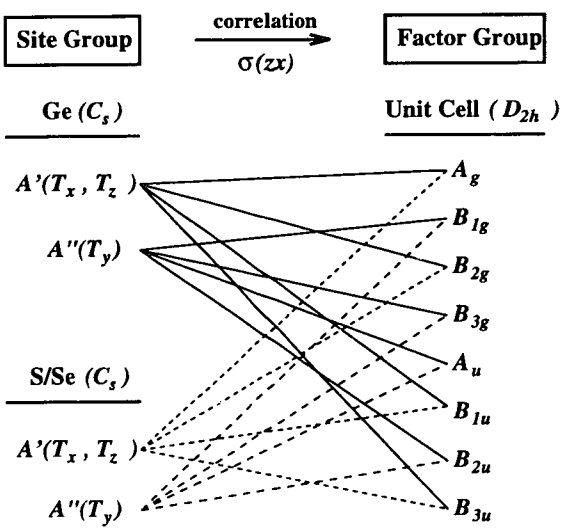

Figure 6.2. Correlation diagram for Ge chalcogenides. The correlation for C_s(Ge)-D_{2h} is indicated by the connecting solid lines and for C_s(S/Se)-D_{2h} is denoted as the connecting dashed lines.

from A' should therefore be two while B_{1g}, B_{3g}, A_u, and B_{2u} remain single degrees of freedom. Further, the irreducible representations associated with the optical lattice vibrations of the crystal (Γ_{vib}) are the sum of the representations contributed by Ge (Γ^{Ge}) and chalcogen ($\Gamma^{S/Se}$) with subtraction of the representations of acoustical vibrations(Γ^{acoust}). In addition to the conditions of selection rules for the acoustic, infrared-active, and Raman-active modes discussed previously, the lattice vibrations can be formed as,

$$\begin{aligned}
\Gamma_{vib} &= \Gamma^{Ge} + \Gamma^{S/Se} - \Gamma^{acoust} \\
&= [2A_g + B_{1g} + 2B_{2g} + B_{3g} + A_u + 2B_{1u} + B_{2u} + 2B_{3u}] \\
&\quad +[2A_g + B_{1g} + 2B_{2g} + B_{3g} + A_u + 2B_{1u} + B_{2u} + 2B_{3u}] \\
&\quad -[B_{1u} + B_{2u} + B_{3u}] \\
&= 4A_g^{(R)} + 2B_{1g}^{(R)} + 4B_{2g}^{(R)} + 2B_{3g}^{(R)} + 2A_u^{(0)} + 3B_{1u}^{(IR)} + B_{2u}^{(IR)} + 3B_{3u}^{(IR)} \quad (6.6)
\end{aligned}$$

The information concerning the displacement polarisations for particular atoms involved in the normal lattice vibrations can be also obtained from the correlation diagram. For instance, the B_{3g} mode, in Fig. 6.2, is derived from the A'' representation of both Ge and chalcogen site group which involves the atomic motions along the y direction. However, the notation of x, y, and z is referred to the c, b, and a direction of the crystallographic axis, respectively. It implies that B_{3g} mode involves the combined motion of the Ge and chalcogen along the b-axis direction. Therefore, two possible normal coordinates for this B_{3g} mode can be easily found due to its particular characteristic and is shown in Fig. 6.3. Finally, the detail for each lattice vibration of the orthorhombic Ge chalcogenides can be characterised using the same scheme and the results are listed in Table 6.5.

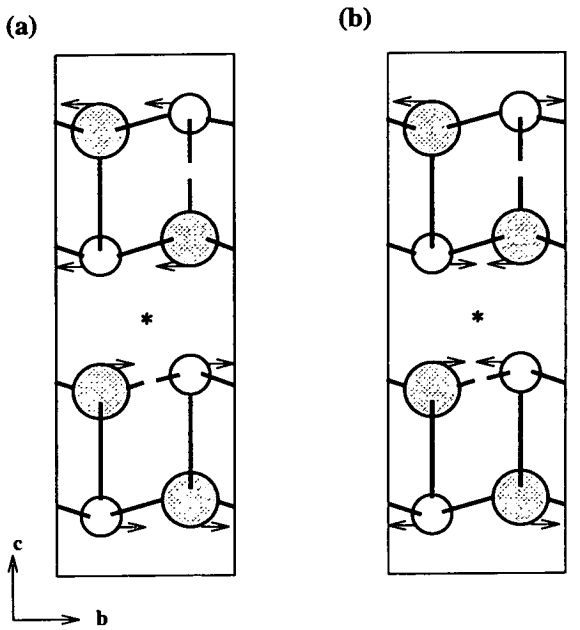

Figure 6.3. Two normal coordinates of B_{3g} modes for Ge chalcogenides are represented as arrows. Ge and chalcogen atoms are denoted as small white and large grey circles, respectively. The inversion centre is indicated by a asterisk symbol.

Table 6.5. Properties of the zone-centre optical lattice vibrations for layered Ge chalcogenides.

Irreducible representation	Activity	Polarisation direction	Atoms involved	Transformation property
A_g	R	a-c plane	Ge + S (or Se)	(aa), (bb), (cc)
B_{1g}	R	b-axis	Ge + S (or Se)	(bc)
B_{2g}	R	a-c plane	Ge + S (or Se)	(ac)
B_{3g}	R	b-axis	Ge + S (or Se)	(ab)
A_u	*Silent*	b-axis	Ge + S (or Se)	-
B_{1u}	IR	a-c plane	Ge + S (or Se)	a
B_{2u}	IR	b-axis	Ge + S (or Se)	b
B_{3u}	IR	a-c plane	Ge + S (or Se)	c

6.3 Lattice Vibrations in GeS and GeSe

The zone-centre normal modes in the layered Ge chalcogenides at ambient pressure have been extensively studied using the first-order Raman scattering. From the single crystal Raman scattering measurements, it will show that not only the phonon frequencies but also assignments for every Raman-active modes can be well-determined using different scattering configurations. This experimental procedure will be outlined in this section.

On the other hand, a first-principle calculation has also been employed to probe the lattice vibrations of GeS and GeSe under ambient condition. The calculated eigenvectors can be assigned by symmetry considerations and provide details of relevant zone-centre optical modes. Also, calculated eigenfrequencies given in this section are in good agreement with the low temperature measurements according to the zero-temperature effects in *ab-initio* calculations.

6.3.1 Observed Raman Spectra

Since GeS and GeSe are opaque to usual visible laser excitation sources, the backscattering setup is the proper Raman scattering geometry for either single crystal or powder samples. However, the symmetry of vibrational properties depends on the spatial symmetry properties of the crystal structure as discussed in Sec. 2.4.1. Hence the selection rules for Raman scattering can be experimentally derived from the spectra of single crystal samples associated with different scattering configurations.

Because of the anisotropy of GeS and GeSe, the sample with perfect ab planes can be obtained by the easy cleavage of the single crystals without polish. The backscattering geometry can be set such that the incident and scattered light is along the c direction and opposite to the c direction ($\bar{c}$), respectively. The a and b axes for the sample can be also identified using a single crystal Laue X-ray diffraction and then the polarisations of incident and scattered photons can be well-defined. Raman spectra were recorded using the experimental aspects which detail is given in Sec. 2.4.3. For both GeS and GeSe

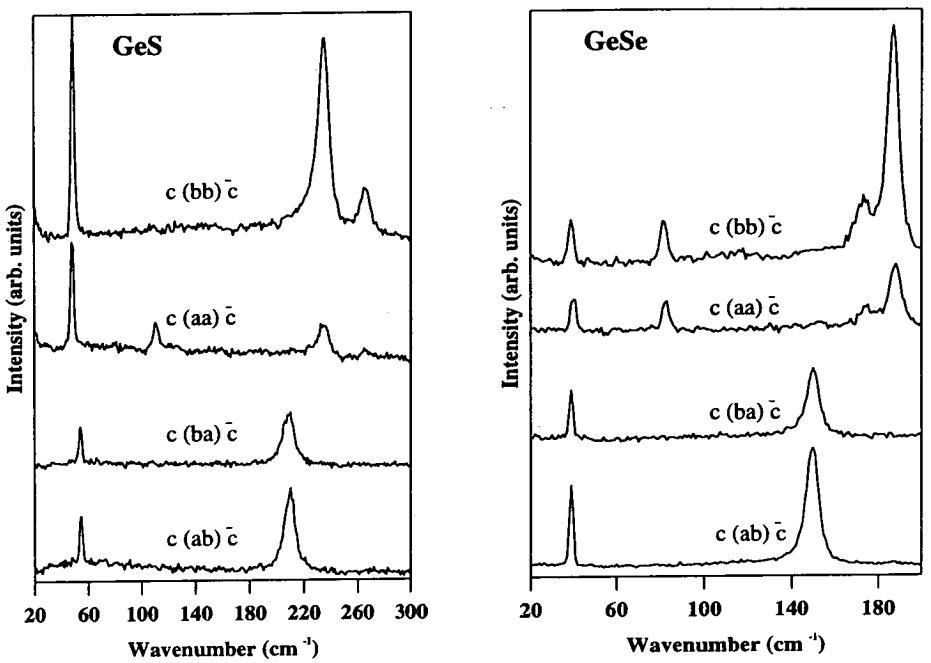

Figure 6.4. Raman-scattering spectra for crystalline GeS and GeSe at room temperature. The notation $x(y,z)\bar{x}$ indicates the direction of incident exciting radiation, the polarisation of the incident and scattered photons, and the scattered direction of radiation, respectively.

single crystal samples, the 6764 Å line of a Kr^+ laser was employed as the excitation source. The laser power was estimated to be 90 mW at the samples. The sizes for four slits S_1, S_2, S_3, and S_4 of the Coderg-800 spectrometer were set at 400, 610, 400, and 400 μm, respectively, which gave a resolution of approximately 1.5 cm^{-1}. The observed spectra with respect to different experimental configurations for GeS and GeSe at room temperature are shown in Fig. 6.4.

The Raman spectra corresponding to diagonal polarisations (aa), (bb), and (cc) [150] give three nonzero components α_{aa}, α_{bb}, and α_{cc} for the 2nd-rank polarisability $\boldsymbol{\alpha}$ (Eqn. (2.21)). This polarisability possesses the same symmetry properties as the irreducible representation A_g of the point group D_{2h}. Also, the observed allowed Raman peaks attributed to the (ab) and (ba) polarisations arise from two off-diagonal components of the polarisability which is specified as the B_{3g} symmetry. Both polarisabilities can be

represented as

$$\alpha(A_g) = \begin{pmatrix} \alpha_{aa} & 0 & 0 \\ 0 & \alpha_{bb} & 0 \\ 0 & 0 & \alpha_{cc} \end{pmatrix} \qquad \alpha(B_{3g}) = \begin{pmatrix} 0 & \alpha_{ab} & 0 \\ \alpha_{ba} & 0 & 0 \\ 0 & 0 & 0 \end{pmatrix}$$

and, thus, the associated raman tensor which is defined as the first derivative of α with respect to normal coordinates holds the same symmetry properties.

However, the remaining Raman-active zone-centre modes derived from other different polarisation geometries have been also reported for GeS [151, 144] and GeSe [150, 152]. In addition, to proceed with the pressure studies, the Raman spectra for the sample loaded in a DAC under ambient condition has also been measured. Without further symmetry condition from specific polarisation configurations, a spectrum with the combination of A_g and B_{3g} modes was observed for the sample and will be shown in Sec. 6.5.1. The other two Raman-active modes, B_{1g} and B_{2g}, corresponding to the $c\bar{c}$ geometry cannot be obtained in our measurements. Further, the low temperature (10 K) Raman scattering for GeS and GeSe have been measured as well. The frequencies of all Raman-active modes for both layered Ge chalcogenides at different temperatures are listed in Table 6.6

6.3.2 *Ab-initio* Simulations for Zone-Center Phonons

In view of the significant success of quantum mechanical simulations for compression mechanism of layered semiconductors (shown in Chapter 5), the zone-centre lattice vibrations for GeS and GeSe were also studied using the first principles simulations, *dynamical matrix diagonalisation method.* This computational methodology is based on *ab-initio* molecular dynamics for calculating the Hellmann-Feynman forces and the detail of this calculation scheme can be found in Sec. 3.2.5.

As shown in Sec. 3.3.2, the construction of the dynamical matrix for a crystal with a particular space group only needs a few atomic distortions and the remaining

Table 6.6. Observed phonon frequencies for all Raman-active modes of GeS and GeSe at different temperature. The frequency is in the unit of wavenumber, cm^{-1}.

	GeS		GeSe	
Symmetry	ν_i (300 K)	ν_i (low T)	ν_i (300 K)	ν_i (low T)
A_g	48^a, 49^b, 48^c	52^a, 51.5^b	40^a, 40^d, 39^e	43^a, 43^d
	112^a, 112^b, 111^c	116^a, 115.5^b	82^a, 82^d, 83^e	84^a, 84^d
	238^a, 239^b, 238^c	244^a, 245^b	175^a, 175^d, 174^e	181^a, 181^d
	269^a, 269^b, 269^c	276^a, 278^b	188^a, 189^d, 188^e	196^a, 197^d
B_{1g}	94^b, 96^c	97^b	78^d, 77^e	80^d
	245^b, 215^c	251^b	166^d, 164^e	171^d
B_{2g}	75^b, 76^c	76.5^b	70^d, 49^e	72^d
	130^b, 132^c	133.5^b	102^d, 102^e	105^d
	281^b, 242^c	290^b	199^d, 178^e	203^d
	329^b	335.5^b	226^d, 225^e	231^d
B_{3g}	56^a, 56^b, 55^c	57^a, 58.5^b	40^a, 39^d, 39^e	42^a, 42^d
	212^a, 213^b, 212^c	219^a, 219.5^b	151^a, 151^d, 151^e	159^a, 159^d

[a] Present work at 10 K. [b] [151] at 20 K. [c] [144]. [d] [152] at 20 K. [e] [150].

elements can be generated by symmetry transformation. In the case of the layered Ge chalcogenides, a full 24×24 dynamical matrix corresponding to eight atoms within a unit cell can be built, in principle, with only three independent displacements of each species of atom through the symmetry of the D_{2h} point group. However, this calculation relies on the simple harmonic (SH) approximation, a test for this approximation is therefore necessary. The test scheme has been presented in Sec. 3.3.2. After the examination for SH approximation, a proper atomic displacement of 0.05 in fractional coordinates along three different axis has been found for Ge and chalcogen atoms.

In practice, the distorted configuration is of lower symmetry than the equilibrium one and the special k points associated with the same Monkhorst-Pack grid (discussed in Sec 3.2.2) have to be regenerated in order to preserve the Brillouin zone sampling density. For instance, to construct the dynamical matrix of GeS, the 16 and 32 special k-point set for the displacement along the a (c) and b direction, respectively, were used to keep the density of k point sampling corresponding to the $4 \times 4 \times 4$ Monkhorst-Pack

grid employed in equilibrium structure determination.

Thus, the diagonalisation of the resulting dynamical matrix gives 24 eigenvalues with relevant eigenvectors which correspond to long wavelength , Γ-point, lattice vibrations of the orthorhombic Ge chalcogenides. Except for three approximately zero-frequency eigenvalues (attributed to acoustic modes), the residual 21 normal modes need to be assigned in order to decide the symmetry and selection rules for each calculated lattice vibration. The mode-assignment procedure can be implemented by applying all point group symmetry operations of the structure to the set of calculated displacement eigenvectors for a given vibrational mode. To underline the usefulness of this quantitative mode-determination, an example for the assignment of the lowest non-zero-frequency mode of GeSe is demonstrated as follows.

The calculated eigenvector $\boldsymbol{\delta}$ with respect to the lowest non-acoustic mode (ν_i = 38.7 cm^{-1}) of GeSe is expressed in a mass-modified displacement unit like ζ in Eqn. (3.66)) referred to the equilibrium atomic positional matrix **A** in fractional coordinates.

$$\mathbf{A} = \left(\begin{array}{ccc} 0.108 & 0.25 & 0.117 \\ 0.608 & 0.75 & 0.383 \\ 0.392 & 0.25 & 0.617 \\ 0.892 & 0.75 & 0.883 \\ \hline 0.498 & 0.25 & 0.854 \\ 0.998 & 0.75 & 0.646 \\ 0.002 & 0.25 & 0.354 \\ 0.502 & 0.75 & 0.146 \end{array}\right) \begin{array}{l} \left.\begin{array}{c} \\ \\ \\ \\ \end{array}\right\} Ge \\ \\ \left.\begin{array}{c} \\ \\ \\ \\ \end{array}\right\} Se \end{array} \qquad \boldsymbol{\delta} = \left(\begin{array}{ccc} 0.00 & -0.36 & 0.00 \\ 0.00 & -0.36 & 0.00 \\ 0.00 & 0.36 & 0.00 \\ 0.00 & 0.36 & 0.00 \\ \hline 0.00 & 0.35 & 0.00 \\ 0.00 & 0.35 & 0.00 \\ 0.00 & -0.35 & 0.00 \\ 0.00 & -0.35 & 0.00 \end{array}\right)$$

Taking into account the symmetry operation, $C_2(z)$ corresponds to a combination of a pure 2-fold rotation operation **R** with respect to the a axis and a nonprimitive translation operation **T** along the direction of $(\mathbf{1/2, 0, 1/2})$ which is in fraction coordinates

of a unit cell. Then, applying $C_2(z)$ on the $\mathbf{A}+\boldsymbol{\delta}$ yields

$$
\begin{aligned}
C_2(z)(\mathbf{A}+\boldsymbol{\delta}) &= (\mathbf{A}+\boldsymbol{\delta})(\mathbf{R}+\mathbf{T}) \\
&= \begin{pmatrix}
0.608 & 0.25+0.36 & 0.383 \\
0.108 & 0.75+0.36 & 0.117 \\
0.892 & 0.25-0.36 & 0.883 \\
0.392 & 0.25-0.36 & 0.617 \\
\hline
0.998 & 0.75-0.35 & 0.646 \\
0.498 & 0.25-0.35 & 0.854 \\
0.502 & 0.75+0.35 & 0.146 \\
0.002 & 0.25+0.35 & 0.354
\end{pmatrix}
=
\begin{pmatrix}
0.108 & 0.25+0.36 & 0.117 \\
0.608 & 0.75+0.36 & 0.383 \\
0.392 & 0.25-0.36 & 0.617 \\
0.892 & 0.75-0.36 & 0.883 \\
\hline
0.498 & 0.25-0.35 & 0.854 \\
0.998 & 0.75-0.35 & 0.646 \\
0.002 & 0.25+0.35 & 0.354 \\
0.502 & 0.75+0.35 & 0.146
\end{pmatrix} \\
&= \mathbf{A}-\boldsymbol{\delta}
\end{aligned}
$$

Hence, the calculated eigenvector for the lowest frequency of GeSe is anti-symmetric under the operation $C_2(z)$ resulting in a character of -1 for this symmetry operation. The character for each symmetry operation can be decided using the same procedure and this eigenvector can be therefore assigned to the B_{3g} symmetry according to the character table for D_{2h} (Table 6.1). Therefore, all the calculated normal modes for GeS and GeSe can be assigned properly and the results are listed in Table 6.7. It should be remembered that this calculation corresponds to zero-temperature conditions. The calculations show excellent agreement with low-temperature experimental Raman data in Table 6.6. The previous room-temperature infrared frequencies for GeS and GeSe are also shown in Table 6.7. However, as mentioned in Sec. 3.4, without including long-range dipolar effect in the phonon calculations presented above, the calculated frequencies of infrared-active phonons may not be as reliable as the ones of Raman-active modes.

Table 6.7. Calculated frequencies for all optical modes of two Ge chalcogenides. The assignment procedure for each calculated eigenvector is given in detail in the text. The room-temperature infrared data are also included for comparison. All frequencies are in the unit of cm^{-1}.

	GeS		GeSe	
Symmetry	ν_i (Calc.)	ν_i (Expt.)	ν_i (Calc.)	ν_i (Expt.)
A_g	52.3		43.5	
	110.2		74.9	
	241.4		173.1	
	280.7		193.8	
B_{1g}	94.5		72.5	
	249.8		166.8	
B_{2g}	77.5		70.7	
	133.1		101.9	
	287.7		197.8	
	318.6		217.8	
B_{3g}	64.0		38.7	
	222.6		158.2	
A_u	88.0	-	70.7	-
	238.8	-	162.6	-
B_{1u}	112.1	118[a]	77.3	88 [b]
	227.4	-	172.6	175 [b]
	267.7	258[a]	189.5	186 [b]
B_{2u}	212.5	201[a]	156.8	150 [b]
B_{3u}	105.0	105[a]	79.1	83 [b]
	209.5	238[a]	161.0	172 [b]
	287.6	280[a]	200.0	198[b]

[a] [144]. [b] [150].

6.4 Interlayer Interactions in Layered Ge Chalcogenides

Since the crystal structure of layered semiconductors GeS and GeSe is mainly dominated by quasi-two-dimensional symmetry properties, a particular group theoretical analysis, diperiodic group theory, which provides the proper symmetry operations of a two dimensional crystal in three dimensional space is used in this section in order to study the lattice dynamics of GeS and GeSe. Comparing different group-theory considerations, a Davydov doublet splitting will be induced due to the weak interaction between isolated layers. This observation implies that the strength of interlayer coupling can be systematically studied by the splitting frequencies of the Davydov doublets. A simple model for measuring the interlayer interaction will be presented in Sec. 6.4.2.

The existence of very-low-frequency zone-centre optical phonons introduces another vital issue in the vibrational properties of layered compounds. The low-frequency modes correspond to layers moving as rigid units and are termed as rigid-layer vibrations. The frequency of the rigid-layer mode depends on the interlayer force. Thus, it will be shown that the comparison between the frequencies of rigid-layer vibrations and intralayer vibrations provide the ratio of interlayer/intralayer force constants which is regarded as a measurement of anisotropy. Therefore, the anisotropy of a layered structure can be categorised by the ratio of different hierarchical force constants. The layerlike characters of GeS and GeSe will be gauged at the end of this section.

6.4.1 Diperiodic Group Analysis

In the conventional group-theory studies, the three-dimensional space group has been employed to probe the vibrational properties of layered compounds. In fact, the layered crystals are characterised by a three dimensional structure with only two-dimensional periodic boundary conditions according to the weak interactions between isolated layers. However, the pure two-dimensional group is not an appropriate description of the

layer structure because it does not allow the existence of the third dimension. In order to underline the structural anisotropy, a *diperiodic* space group which could properly represent the three-dimensional structure confined to two-dimensional infinite periodicity is therefore needed to proceed the theoretical studies for layer structures.

Rather than 230 three-dimensional (triperiodic) space groups and 17 pure two-dimensional groups, 80 DG have been extensively studied by E. A. Wood [153]. The symmetry elements of DG include n-fold axes, screw axes, mirror planes, glide planes, etc., with respect to the atoms in an isolated layer. According to the limitation from the absence of periodicity normal to the plane of diperiodicity, the operations referred to third periodicity, such as glide planes with glide direction out of the plane, screw axes perpendicular to the plane, and n-fold ($n > 2$) axes lying in the plane, are forbidden in DG. In other words, all of the 80 DG do not contain symmetry elements connecting atoms in different layers. The compatibility relation between DG and triperiodic space groups has been specified and reported in elsewhere [153].

In the limiting regime of zero coupling between layers, the vibrations for a single layer can be described by the DG from the correlation method [144, 154]. By turning off the weak interlayer interaction, the isolated single layered Ge chalcogenides adopt a crystal structure with the diperiodic group DG32 [144], in Wood's notation, which is analogous with the space group C_{2v}^7 but without the inversion symmetry. In principle, a single layered Ge chalcogenides containing 4 atoms in a unit cell should give 12 zone-centre lattice vibrations. Within an isolated layer, Ge and chalcogen atoms are at the locations with site group C_s. Based on the correlation table for DG32 (C_{2v}) shown in Table 6.8, the connection between the irreducible representations of C_s and of the layer factor group DG32 (D_{2v}) is illustrated in Fig. 6.5. It shows that the A_1 and B_1 modes in DG32 are originated from A' modes of both species of atoms at C_s in which A'' modes contribute the layered A_2 and B_2 irreducible representations.

Table 6.8. Correlation table for the diperiodic group DG32 (C_{2v}) and its subgroups.

C_{2v}	C_2	$\sigma(zx)$ C_s	$\sigma(yz)$ C_s
A_1	A	A'	A'
A_2	A	A''	A''
B_1	B	A'	A''
B_2	B	A''	A'

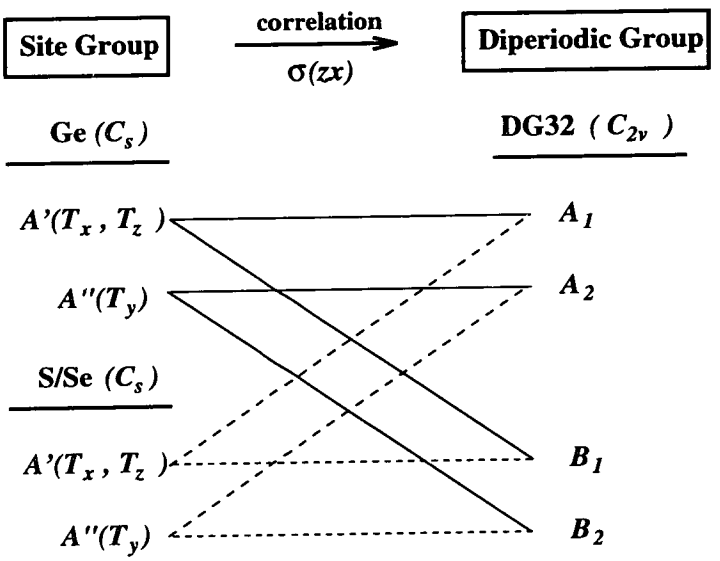

Figure 6.5. Correlation diagram for the isolated layered Ge chalcogenides.

After inspecting the degree of freedom for site groups, the decomposition into irreducible representations is

$$4A_1 + 2A_2 + 4B_1 + 2B_2 \tag{6.7}$$

These 12 normal modes are characterised in Table 6.9. Without any interaction between adjacent layers, 12 lattice vibrations are dominated by the strong coupling between atoms inside a layer. From Table 6.9, the 12 layer fundamentals are separated as 3

acoustic vibrations ($1A_1 + 1B_1 + 1B_2$) and 9 optical modes. Again, considering the transformation properties , the layer-symmetry selection rules for 9 optical modes can be assigned as that three A_1, three B_1, and one B_2 modes are all Raman- and infrared-active while two A_2 modes are Raman allowed only.

Table 6.9. Properties of the zone-centre normal modes for orthorhombic Ge chalcogenides in layer symmetry. The transformation properties in the fifth column can be derived from the character table of C_{2v}

Irreducible representation	Activity	Polarisation direction	Atoms involved	Transformation property
A_1	$IR+R$	a-c plane	Ge + S (or Se)	a, (aa), (bb), (cc)
A_2	R	b-axis	Ge + S (or Se)	(bc)
B_1	$IR+R$	a-c plane	Ge + S (or Se)	c, (ac)
B_2	$IR+R$	b-axis	Ge + S (or Se)	b, (ab)

Now, the weak interlayer interaction has to be considered in order to obtain the irreducible representation for the real crystal structure. The correspondence between DG and crystal factor group for orthorhombic Ge chalcogenides can be derived from the correlation method. Following the relationship described in the character table for D_{2h} (Table 6.4), the correlation between C_{2v} and D_{2h} symmetry is depicted in Fig. 6.6. The degrees of freedom for each irreducible representation of D_{2h} can be propagated directly from the relevant representation of C_{2v}. Thus, the description of the 24 lattice vibrations is

$$4A_g + 2B_{1g} + 4B_{2g} + 2B_{3g} + 2A_u + 4B_{1u} + 2B_{2u} + 4B_{3u} \tag{6.8}$$

The selection rules for three acoustic and 21 optical modes are identical to the result given in Eqn. (6.5).

From the DG analyses, two issues need to be addressed carefully here. Firstly, the Raman-infrared degeneracies of an isolated layer structure without the inversion centre lead to a different conclusion from the space group considerations in which the

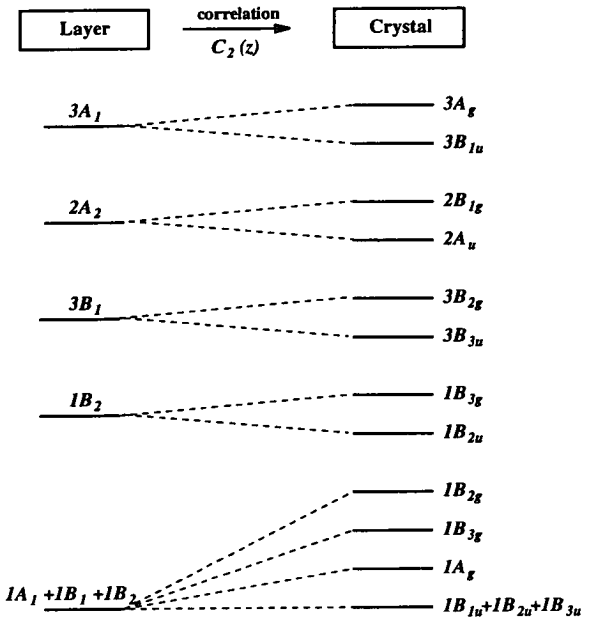

Figure 6.6. Correlations diagram among zone-centre vibrations for individual layers and crystalline structures of layered Ge chalcogenides. To the left of the figure is shown the symmetry elements for DG which are appropriate for the case without interlayer coupling.

Raman-active and infrared-active are mutually exclusive. This optical selection rules of DG is due to the absence of interlayer inversion symmetry in the layer symmetry. Nevertheless, the crystal vibrations involve the combination of vibrations on the adjacent layers will be either even-symmetric or odd-symmetric with respect to the inversion centre located on the middle of two layers. Hence, the symmetry-induced admixture of Raman- and infrared-active vibrations is not permitted in crystals having inversion symmetry.

Another feature shown in Fig. 6.6 is that each normal mode in a layer symmetry is split into a pair of *gerade* (Raman-active) and *ungerade* (infrared-active) lattice vibrations in the corresponding crystal symmetry. This nondegenerate pair of Raman- and infrared-actived crystal modes can be understood as the mode-splitting of the layer vibrations by the weak coupling between layers. Using the DG analysis, the splitting of the Raman-infrared doublets derived from the interlayer interaction has been also observed in other layered compounds, As_2S_3 [154], MoS_2 [155], and Sn chalcogenides

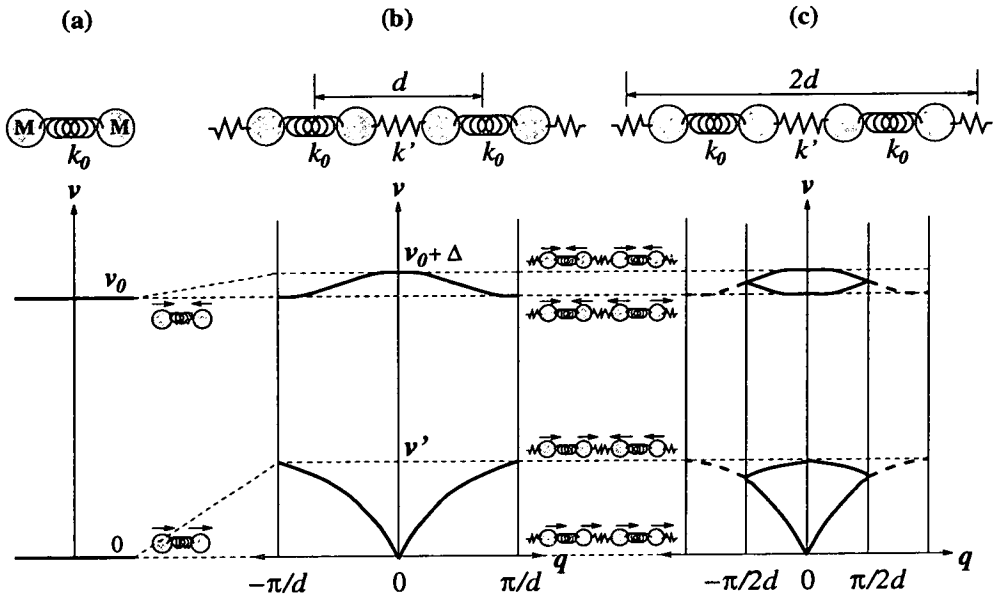

Figure 6.7. One-dimensional spring models and vibrational spectra for layer materials. In (a), the isolated layer is represented by a coupled oscillators connected with an intralayer spring of force constant k_0. Different layers are jointed by a soft interlayer spring of smaller force constant k' to form a linear lattice with (b) one layer and (c) two layers per unit cell. The phonon dispersion curves are shown below corresponding to the models.

[156]. Therefore, a careful comparison of the Raman modes and their infrared counterparts of layered materials provides a means to measure the strength of interlayer interactions.

6.4.2 Interlayer-coupling Induced Davydov Splitting and Rigid-Layer(RL) Vibrations

As the weak-interaction induced Raman-infrared splitting in layer solids, an analogous effect has been found in the molecular crystals and called *Davydov splitting* which gives rise to both mode shift and mode splitting of the molecular spectrum [157]. The character of interlayer-coupling induced Davydov splitting can be captured by a classical spring-ball model. Fig. 6.7 illustrate this simple vibration model only in one-dimensional consideration. In Fig. 6.7(a), the isolated layer is simplified as two identical oscillators of mass M tighten by an *intralayer bond* of a spring of force constant k_0 and

the equilibrium distance between oscillators is d. For this free "layer", there are only two eigenfrequencies corresponding to two degrees of vibrational freedom. The vanishing frequency is recognised as a pure translation of the layer (*acoustic* modes), and the higher one ($\nu_0 = \sqrt{2k_0/M}$) is assigned to the spring *stretching* mode. Both eigenvectors are also displayed in Fig. 6.7(a). Taking into account the interaction between "layers", the "layer" is coupled with its neighbours by a set of soft springs of force constant k' ($k' \ll k_0$) which is responsible for the interlayer cohesion. This linear chain of identical atoms connected by springs of alternating strengths has only one "layer" per unit cell. According to the harmonic approximation, the discrete eigenfrequencies of a single "layer" will spread to two branches:

$$\nu^2(q) = \frac{k_0 + k'}{M} \pm \frac{\sqrt{k_0^2 + k'^2 + 2k_0k' \cos qd}}{M} \tag{6.9}$$

As the wave vector increases from zone centre ($q = 0$) to the zone boundary ($q = \pi/d$), the acoustic branch rises up to $\sqrt{2k'/M}$ whereas the *stretch* branch gives rise to a flat dispersion from $\sqrt{2(k_0 + k')/M}$ to $\sqrt{2k_0/M}$ in Fig. 6.7(b). The displacements associated with zone-centre and zone-edge modes are also demonstrated to give a detail vibrational pictures. Further, a dimerised lattice with double unit cell is introduced to include two layers within a unit cell as the case of GeS and GeSe. The lattice dimerisation causes halving of the Brillouin zone and the modes at the zone edge will be folded back to the zone centre as shown in Fig. 6.7(c). Thus, from the first-order Raman and infrared measurements which detect only zone-centre vibrations, it can be regarded as the mode-splitting from the original layer lattice vibration. In addition, the ratio of zone-centre normal-mode frequencies can be expressed as

$$\frac{\nu'}{\nu_0} = \sqrt{\frac{k'}{k_0}} \tag{6.10}$$

$$\frac{\Delta}{\nu_0} = \sqrt{\frac{k_0 + k'}{k_0}} - 1 = \frac{1}{2}\left(\frac{k'}{k_0}\right) \qquad (k' \ll k_0) \tag{6.11}$$

where the Δ and ν' are the mode splittings from the acoustic and the stretching band, respectively.

The theoretically predicted Raman-infrared splitting of the dimer model can be observed in the experimental and calculated frequencies for lattice vibrations of GeS and GeSe. In practice, the characteristic frequencies with no layer-coupling, ν_0, can be estimated from the obtained Raman-infrared pairs by a simple form,

$$\nu_0 = \sqrt{\nu_+^2 + \nu_-^2} \tag{6.12}$$

where $\nu_\pm$ denotes the frequencies for a Raman-infrared pair. Table 6.10 lists the intralayer Raman-infrared Davydov doublets for GeS and GeSe. The frequency-splittings

Table 6.10. Three pairs of Raman-infrared Davydov splitting for GeS and GeSe. Calculated data are shown in parentheses and all frequencies are in the unit of cm^{-1}. The A_g-B_{1u}, B_{2g}-B_{3u}, and B_{3g}-B_{2u} pair is originated from A_1, B_1, and B_2 layer vibration, respectively.

Raman-Infrared	GeS				GeSe			
doublets	ν_+	ν_-	ν_0	$\Delta_{\nu_+-\nu_-}$	ν_+	ν_-	ν_0	$\Delta_{\nu_+-\nu_-}$
A_g-B_{1u}	269	258	264	11	188	186	187	2
	(280.7)	(267.7)	(274)	(13)	(193.8)	(189.5)	(191.6)	(4.3)
B_{2g}-B_{3u}	329	280	305.5	49	226	198	212.5	28
	(318.6)	(287.6)	(303.5)	(31)	(217.8)	(200)	(209.1)	(17.8)
B_{3g}-B_{2u}	212	201	206.6	11	151	150	150.5	1
	(222.6)	(212.5)	(217.6)	(10.1)	(158.2)	(156.8)	(157.5)	(1.4)

Δ in Table 6.10 are about 10 cm^{-1} for GeS and few wavenumber for GeSe except large discrepancy for the pair of B_{2g}-B_{3u}. From the calculated eigenvectors of *ab-initio* simulations, it is attributed to the admixture of bond stretching and bond bending of B_{2g} which is induced by the complexity of the crystal geometry.

On the other hand, the low-lying frequency crystal modes (below 100 cm^{-1}) originate from the layer acoustic mode and are recognised as a rigid-layer (RL) motions. The idea of the RL mode was identified initially by Zallen and Slade [158] to explain

the origin of very low-frequency zone centre optical modes in layered solids. According to the RL approximation, crystals containing more than one layer in a unit cell exhibit unique lattice vibrations in which the layers move relative to each other as rigid units. The restoring force responsible for the RL mode is due to the weak interlayer cohesion so, the frequency of the RL vibration will be much lower than one of the intralayer vibration.

Since three independent acoustic modes exist along three crystallographic axis of the orthorhombic layer structure, three RL modes are expected to be found in GeS and GeSe. In addition, the opposite directional motions for two layers of orthorhombic Ge chalcogenides ensure that these three RL modes are inversion-invariant and are associated with Raman-active vibrations. As the results of DG analysis and optical measurements shown in Table 6.6, three room-temperature RL vibrations are observed to be $\nu(A_g) = 48$, $\nu(B_{3g}) = 56$, and $\nu(B_{2g}) = 75$ cm^{-1} for GeS while $\nu(A_g) = 40$, $\nu(B_{3g}) = 40$, and $\nu(B_{2g}) = 70$ cm^{-1} for GeSe.

Considering the transformation properties, the low-frequency A_g, B_{3g}, and B_{2g} can be specified as the *shear* RL motion along the a-axis direction, b-axis direction, and the *compressive* RL motion, respectively. From this theoretical prediction of three RL modes, the *frozen phonon* (FP) calculation (Sec. 3.3.3) which assumes a pure rigid-layer eigenvector displacement pattern was also performed to obtain the RL vibrational frequencies. The calculated frequencies obtained from a 0.005 fractional unit displacement of a rigid layer are $\nu(A_g) = 58.6$, $\nu(B_{3g}) = 66.0$, and $\nu(B_{2g}) = 80.5$ cm^{-1} for GeS. In addition, the calculated frequency of RL A_g mode of GeSe at ambient pressure is found to be 47 cm^{-1}. On the other hand, the calculated frequencies for three RL modes using the dynamical matrix diagonalisation technique without a priori bias concerning the eigenvectors have been listed in Table 6.7 as $\nu(A_g) = 52.3$, $\nu(B_{3g}) = 64.06$, $\nu(B_{2g}) = 77.53$ cm^{-1} for GeS and $\nu(A_g) = 43.5$, $\nu(B_{3g}) = 38.7$, $\nu(B_{2g}) = 70.65$ cm^{-1} for GeSe. The calculated eigenvectors for relevant RL vibrations of GeS are given as an example and are displayed in Fig. 6.8. It is evident that the rigid-layer mode

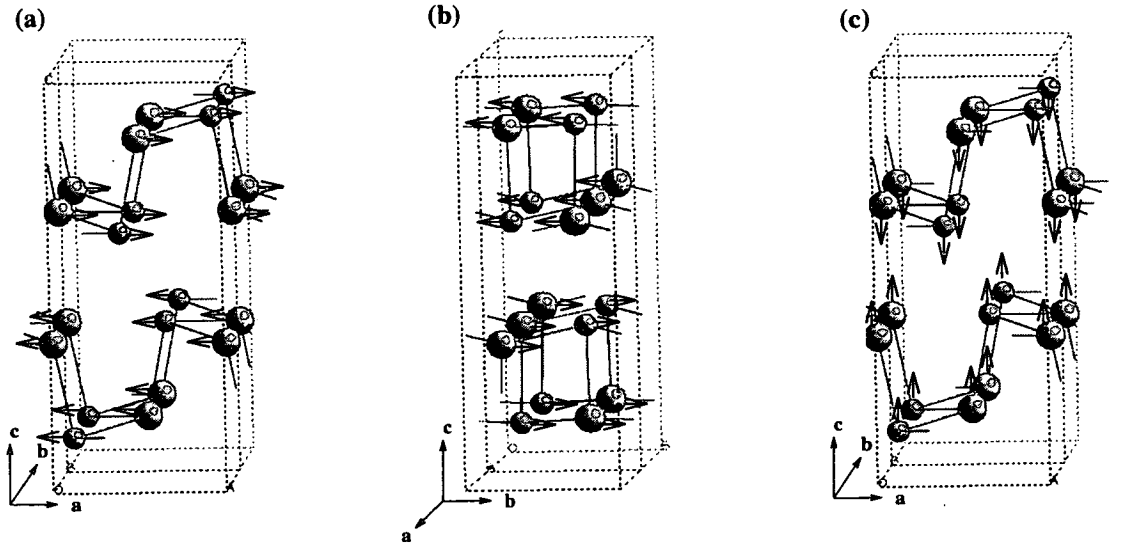

Figure 6.8. Schematic illustrations of the calculated eigenvectors corresponding to three RL vibrations of GeS determined by dynamical matrix diagonalisation at ambient pressure. The shear RL mode along a and b direction are displayed in (a) and (b) respectively. The compressive RL mode is shown in (c). The Ge and S atoms are denoted as small and large spheres respectively. The arrows represent the directions and values of the eigenvectors.

approximation is satisfied under ambient pressure condition.

The RL frequencies have been employed to derive quantitative information on the strength of the interlayer cohesion in chalcogenide crystals [158]. According to Eqn. (6.10), the ratio of interlayer to intralayer force constants can be estimated by the ratio of the RL frequency (ν') to the relevant intralayer covalent-bond-strengthing vibrational frequencies (ν_0). From the inspection of Table 6.7 and 6.10, it obtains three RL-intralyer vibration pairs corresponding to three crystallographic axis for GeS and GeSe. The calculated and experimental interlayer-intralayer force constant ratios proportional to $(\nu'/\nu_0)^2$ for two *shear* modes and one *compressive* mode of GeS and GeSe are shown in Table 6.11 which includes other prototypical layered solids for comparison. It can be seen that average force-constant ratios of GeS and GeSe are about 0.07 and 0.08, respectively, which are much larger than the ratio of graphite ($\sim$ 0.005). These results reveal that the anisotropy of GeS and GeSe is more less than that of graphite.

Table 6.11. The observed and calculated interlayer-intralayer force constant ratios for layered materials. The calculated data for GeS and GeSe are shown in parentheses. All the experimental data corresponds to room-temperature measurements except the ones of As_2S_3 and As_2Se_3 which are obtained at 15 K [158]. The compressive RL modes for the hexagonal GaS and GaSe are forced to be optically silent by strict selection rules and the compressive force constant ratio for these crystals are therefore inaccessible.

Crystal	$(\frac{k'}{k})_{shear}$	$(\frac{k'}{k})_{compr.}$
GeSe	0.058 (0.056)	0.109 (0.114)
GeS	0.052 (0.062)	0.084 (0.065)
As_2Se_3	0.021	~ 0.07
As_2S_3	0.017	~ 0.06
MoS_2	0.014	0.038
GaSe	0.019	-
GaS	0.016	-
Graphite	0.001	0.010

6.5 Pressure Effects on Anisotropic Layered Compounds

The conceptual foundations of pressure effects on first-order Raman spectrum of general materials without structural phase transition have been highlighted in Sec. 2.4.2. It is shown that not only the Raman frequencies but also line-shape of Raman spectrum will be affected by compression. However, the main focus of the present work is to trace the pressure-induced Raman-line shift of layered materials.

The zone-centre Raman-active modes of GeS are measured using the DAC facilities up to about 70 kbar. In order to obtain a spectrum with good quality in the low-frequency region for RL modes, the special experimental considerations are needed and will be given in Sec. 6.5.1. The first-principle simulations result will be also included for comparison. The Raman-frequency blue-shift under pressure can be obtained in both experimental and theoretical studies. Moreover, the pressure-enhanced Davydov splitting will be found here.

Within the quasi-harmonic approximation regime, the change of phonon frequencies

are attributed to the modification of perturbed anharmonicity of the crystal Hamiltonian by the external pressure. The aspects of anharmonic behaviours of phonons in 3-dimensional covalent bonded structures has been well developed and the Grüneisen parameter [60] has been widely used to study the vibrational properties of crystals under nonequilibrium conditions. In addition, a scaling relationship of frequency-shifts between different phonons can be derived from the Grüneisen constant which will be concerned here. However, the Grüneisen model has been found to be inappropriate for a system combining different hierarchical couplings such as layered, chained, and molecular materials [159, 160]. In these anisotropic structures, a modification of the Grüneisen approximation is needed and a new vibrational scaling has been found and will be shown later.

As with the weak interlayer-interaction induced lattice vibrations, the RL modes are expected to be preferentially affected by appling hydrostatic pressures to layered crystal structures. Besides the different scaling parameters for RL and intralayer vibrations found in the low pressure region, a pronounced sublinear pressure response of RL vibrations of GeS has also been observed at modest pressure. This dramatic effect on the RL vibrations has also been reported in some layered semiconductors such as MoS_2 [161] and As_2S_3 [162]. Moreover, inspection of the calculated phonon eigenvectors for GeS reveals that substantial mode admixture occurs under compression. Therefore, a pressure-induced breakdown of RL vibrations is found and account for the unique vibrational behaviour of layered materials. The examination of the validity of the RL approximation under different pressure conditions will be given at the end of this section.

6.5.1 Pressure-Raman Effects in the Layered Compound: GeS

The Raman-active modes of layered GeS have been monitored using a combination of high-pressure Raman scattering and first principle simulations. The basic experimental aspects have been described in Sec. 2.4.3. The pressure-Raman measurements were

performed by loading a tiny single crystal sample (with the diameter size of 0.1 mm) into the Tungsten gaskets which were preindented to a diameter of 0.2 mm. A 0.6 mm culet Diacell B-05 DAC (Sec 2.1.1) with a 4:1 mixture of methanol-ethanol as the transmitting media has been employed. The pressure was calibrated using the ruby fluorescence scale. As with the setup of single-crystal Raman scattering in Sec 6.3.1, the 6764 Å line of a Kr^+ laser was also used and the spectra were recorded using a Coderg T-800 triple grating spectrometer in backscattering geometry. The slit size in the spectrometer was set at 400 μm which gave a resolution of approximately 1.5 cm^{-1}. However, the laser excitation source may be affected by the diamond window of DAC and yield to a relatively defocused beam on the sample. Therefore, a lens having a small focal length was placed between the mirror and sample in order to minimise stray light and optimise the important low-frequency regime of the spectra. In addition, air spectra contamination was reduced by flushing the entire sample chamber with argon and emission lines were eliminated by prism filters and an iris. Each spectrum was collected using a count time of 20 seconds per data point.

The unpolarised room-temperature Raman spectra of GeS up to a hydrostatic pressure of 64.8 kbar is shown in Fig. 6.9. According to the structural anisotropy of GeS, the modes referred to the polarisation normal to the layered plane, B_{1g} and B_{2g}, can't be detected obviously. In Fig. 6.9, the low-frequency portion is complicated by the presence of small amount of residual air contamination and the pressure evolution of the B_{3g} shear RL mode having weaker intensity can't be determined reliably.

Ab-initio calculations has also been employed to probe the pressure dependence of Raman-active phonon frequencies of GeS. The calculated frequencies using a dynamical matrix diagonalisation method at different pressure are shown in Fig. 6.10. Comparison between experimental and relevant calculated Raman-active phonons is made and it shows that a good agreement can be obtained in the low-frequency regime. However, the thermal effect of observed high-pressure phonon frequencies (room temperature) accounts for the the overestimate of calculated results (zero temperature) found in

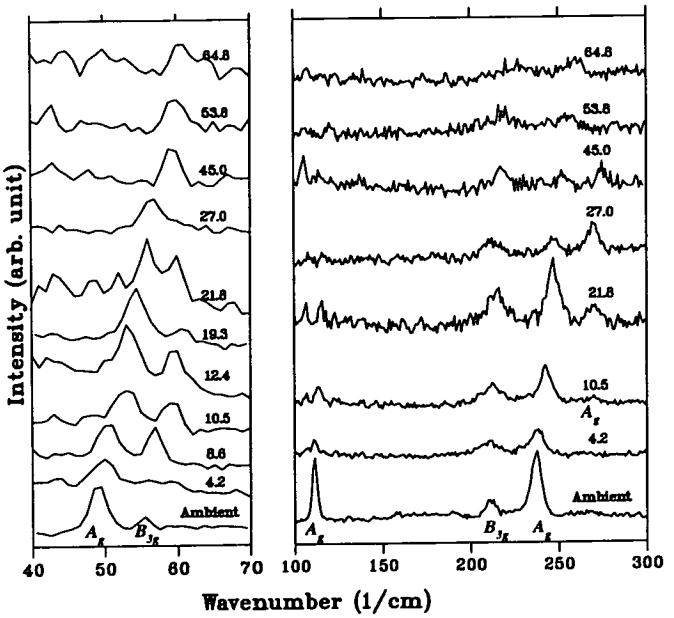

Figure 6.9. Room-temperature Raman spectrum of GeS as a function of hydrostatic pressure up to 64.8 kbar. According to the sample in the $c(ab)\bar{c}$ scattering geometry, a combination of A_g and B_{3g} modes is accessible in these spectra. The assignments are denoted under each spectrum. However, the residual air contamination located at about 60 cm^{-1} obscures the weaker low-frequency B_{3g} shear mode and prohibits the reliable measurements of this RL mode under pressure.

the high-frequency portion. The low-temperature Raman data at ambient pressure are also included in Fig. 6.10 and it implies that the low-temperature high-pressure Raman scattering will reduce the discrepancy between observed and calculated frequencies in Fig. 6.10.

Besides the pressure-induced Raman-frequency shift observed in GeS, a enhancement of the Davydov splittings due to compressions was found using *ab-initio* simulation. The pressure response of all low- and mid-frequency zone-centre optical modes is shown along with their assignments in Fig. 6.11. It is evident that all Raman-infrared splittings increase with pressure and the frequency-gap between interlayer vibrational modes (RL) and intralayer modes is decreased under hydrostatic compressions. These behaviours also recognised in other anisotropic solids [160, 162] are attributed to the enhancement of the interlayer coupling by compression. Moreover, pressure appreciably enforces the interlayer interaction and yields to the calculated crossover between

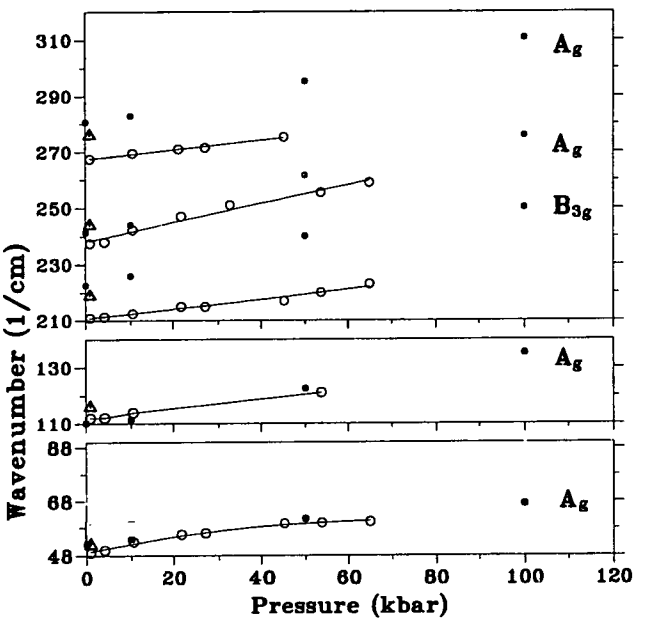

Figure 6.10. Observed and calculated frequencies of Raman modes of GeS as a function of hydrostatic pressure. The experimental data are shown as open circles. The solid lines through data points are guides to the eye. The solid circles represent the calculated frequencies from the dynamical matrix diagonalisation method. The low-temperature (10 K) measurements at ambient pressure are also included for comparison and denoted as open triangles.

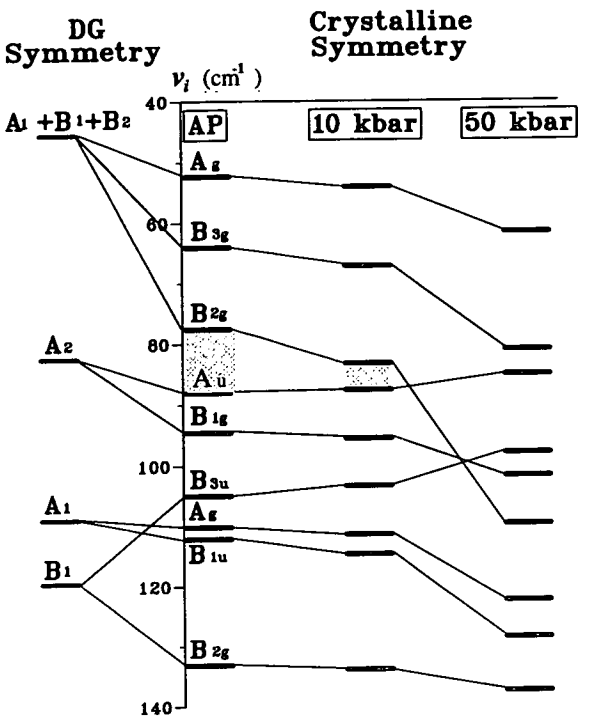

Figure 6.11. Calculated frequency and symmetry labels at ambient and elevated pressure. The DG symmetry assignments are shown to identify the original modes of isolated layers. However, the frequency axis is not appropriate for the DG symmetry assignments. The gap between interlayer and intralayer modes at ambient pressure and 10 kbar are denoted as shaded area. It is evident that the splitting of Raman-infrared doublets increases with increasing pressure. Also, it can be seen that frequency-gap between interlayer and intralayer vibrations decreases gradually with compression and a crossover between RL B_{2g} compressive mode and interlayer A_u, B_{1g}, B_{3u} modes was observed at 50 kbar.

RL B_{2g} mode and intralayer modes (A_{1u}, B_{1g}, B_{3u}) at 50 kbar.

6.5.2 Generalised Vibrational Scaling Law

It is well-known that lattice vibrations in crystals will be affected by the change in the equilibrium volume due to external applied forces, such as pressure, temperature, etc. However, if a rigorous harmonic oscillation was used to model the crystal vibrations, the volume-change only induces a modification of potential energy without altering the lattice dynamics at all. It suggests that the oversimplified harmonic model is not suitable

for the description of lattice dynamics in real crystals. In order to avoid this problem [60], a cubic anharmonic term should be taken into account in the Hamiltonian and a volume-change-induced frequency-shift is thus expected. The normal-mode frequency corresponding to the pressure-induced volume changes leads to the definition of a dimensionless mode-Grüneisen parameter which reflects this anharmonic frequency-shift of phonons.

$$\gamma(\mathbf{q},i) = -\frac{V}{\nu_i(\mathbf{q})}\frac{\partial \nu_i(\mathbf{q})}{\partial V} = -\frac{\partial \ln \nu_i(\mathbf{q})}{\partial \ln V} = B\frac{\partial \ln \nu_i(\mathbf{q})}{\partial P} \tag{6.13}$$

where $\gamma(\mathbf{q},i)$ is the mode-Grüneisen parameter for phonon i with wave vector $\mathbf{q}$. V, P, and B denotes the crystal volume, the external pressure, and bulk mudulus, respectively.

In Grüneisen's assumption, an *overall mode-Grüneisen parameter* γ which is the weighted average of $\gamma(\mathbf{q},i)$ over i and $\mathbf{q}$ enters the coefficient of thermal expansion. Due to the Grüneisen approximation, the pressure coefficient $\partial\nu_i/\partial P$ is proportional to the relevant frequency ν_i of zone-centre phonons ($\mathbf{q} = 0$) and γ is therefore a universal parameter of unity order. Then, the Grüneisen scaling law can be formulated as connecting the force constant k with crystal volume V (k is proportional to ν^2) and Eqn. (6.13) can be rewritten as

$$k \propto V^{-2\gamma} \tag{6.14}$$

The validity of the Grüneisen model has been examined for 3-dimensional tetrahedral semiconductors controlled by single type of bond [160] and a larger value of γ has been observed for the more ionic compounds [163]. However, the Grüneisen model will be shown to be inappropriate for layered GeS as was found in molecular solids [160].

Fig. 6.12 shows the observed pressure sensitivity of phonon frequency, $(1/\nu_i)(\partial\nu_i/\partial P)$, as a function of frequency in GeS at low pressure. It is evident that the value of pressure

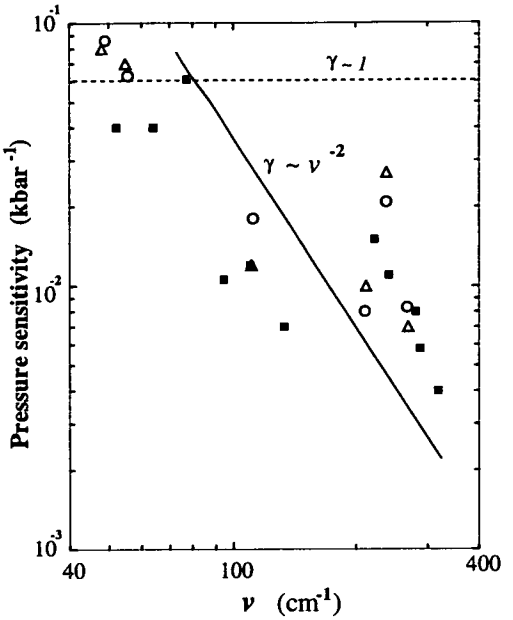

Figure 6.12. Pressure sensitivity, $(1/\nu_i)(\partial\nu_i/\partial P)$, as a function phonon frequency for GeS. Experimental and previous observed (from ambient pressure to 7 kbar) data [165] are represented as open circles and triangles, respectively. The results of calculations are denoted as solid squares. The fitting curve corresponding to $\gamma \propto 1$ and $\gamma_i \propto \nu_i^{-2}$ is shown as dashed and solid lines respectively.

sensitivity for low-frequency phonons decreases from order of 0.1 down to order of 0.01 for high-frequency phonons. This trend departs dramatically away from the Grüneisen scaling which predicts a universal pressure sensitivity for all phonons. In order to scale the phonon behaviour of highly anisotropic materials, a modified Grüneisen scaling law derived from the valence force field model [164] is introduced.

$$\gamma = -\frac{1}{6}\frac{d\ln k}{d\ln l} \qquad \Longrightarrow \qquad k \propto l^{-6\gamma} \tag{6.15}$$

where k and l are the force constant and the relevant bond length, respectively. γ is a bond-scaling parameter of order unity for all type of bonds. This phenomenological scaling law providing a relationship between bond-stiffness and bond-strain can be tested by comparing the ratio of interlayer-intralayer bond length and the ratio of different force constants for layered materials. The result listed in Table 6.12 shows that the value of the exponent is about 6 for a variety of layered crystals. Thus, the

Table 6.12. The length-strength relationship for several layered crystals. l and l' denotes the intralayer and interlayer bond length respectively. The interlayer-intralayer force constant ratio k'/k is from $(k'/k)_{compr.}$ in Table 6.11

Crystal	$\frac{l'}{l}$	$(\frac{k'}{k})_{compr.}$	m (where $k_i = cl_i^{-m}$)
GeS	1.45	0.084	6.7
As_2Se_3	1.51	0.07	6.5
As_2S_3	1.55	0.06	6.4
MoS_2	1.5	0.038	8.1
Graphite	2.36	0.010	5.4

validity of Eqn. (6.15) is corroborated for general layered compounds.

However, the stiffness of the *pseudo* interlayer bond with length of l' is much lower than that of the intralayer bond (l_0). In this case, the scaling exponents corresponding to heirarchical interactions can be connected with relevant mode-Grüneisen parameters by differentiating Eqn. (6.15) and connecting the global strain of the unit cell $\Delta L/L$ where $L = l' + l_0$

$$\frac{\Delta k_0}{k_0} = -6\gamma\frac{\Delta l_0}{l_0} = -6\gamma_0\frac{\Delta L}{L} \tag{6.16}$$

$$\frac{\Delta k'}{k'} = -6\gamma\frac{\Delta l'}{l'} = -6\gamma'\frac{\Delta L}{L} \tag{6.17}$$

where γ_0 and γ' correspond to the intralayer and interlayer mode-Grüneisen parameter, respectively.

For the elemental one-dimensional spring-ball model in Fig. 6.7, the above arguments are applied to three zone-centre optical phonons under the conditions of $k_0 \gg k'$ and $l_0 \simeq l'$. The mode-Grüneisen parameters as a function of frequency are henceforth evaluated as $\gamma_i(\nu') \simeq 2\gamma$, $\gamma_i(\nu_0) \simeq (k'/k_0)2\gamma$, and $\gamma_i(\nu_0 + \Delta) \simeq (k'/k_0)4\gamma$. The result is that the mode-Grüneisen parameter associated with specific interactions is proportional to the inverse of its force constant ($\gamma_0/\gamma' = k'/k_0$). In addition, the relation of $\gamma_i(\nu + \Delta\nu) > \gamma_i(\nu)$ predicts the pressure-enhanced Davydov splitting which has been discussed in Sec. 6.5.1. Moreover, since $\nu_i \propto \sqrt{k_i}$ and $\gamma_i \propto 1/k_i$, the mode-Grüneisen

parameter can be expressed as a function of mode-frequency γ_i as,

$$\gamma_i \propto \frac{1}{\nu_i^2} \tag{6.18}$$

This rough relation included in Fig. 6.12 gives a useful approximation for γ_i and ν_i in anisotropic crystals.

6.5.3 Pressure-Induced Breakdown of Rigid-Layer Approximation

As displayed in Fig. 6.10, the frequencies of Raman-active modes of GeS rise linearly upon compression in the low-pressure region (below 20 kbar). However, the linear dependence between the Raman frequency and pressure is not sustained for the low-frequency RL vibrations of GeS up to about 50 kbar. Instead, a pronounce sublinear pressure response is observed for the RL A_g shear mode. This flattening of frequency versus pressure of RL vibrations is attributed to the pressure-induced decrease of the intralayer/interlayer bond stiffness disparity [162]. In order to investigate this sublinear pressure response in more detail, a first-principle matrix diagonalisation method and the FP calculation have been implemented to simulate the lattice dynamics of the RL A_g vibration of GeS.

Like the phonon calculations of GeS at ambient pressure, the frozen-phonon calculations have been also performed to examine the validity of RL approximation under hydrostatic compression. For instance, a rigid-layer displacement pattern along the crystallographic a-direction was assumed in the FP method to determine the frequencies of the RL A_g shear mode at different pressures. The results for the RL A_g mode in Fig. 6.13 show that the overestimate of the calculated FP frequency of the RL A_g shear mode is 17% higher than the experimental room temperature value and reaches 24% by 50 kbar. This apparent failure of the FP method implies that the rigid-layer approximation must not be valid even under modest pressure.

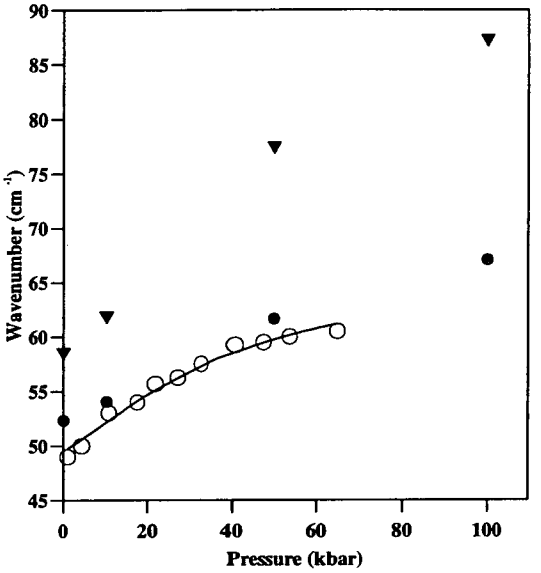

Figure 6.13. The pressure dependence of the lowest-frequency A_g shear mode. The experimental data are determined by Raman scattering up to 64.8 kbar and denoted as open circles. Calculated phonon frequencies using dynamical matrix diagonalisation and frozen-phonon method are shown as solid circles and triangles, respectively, up to 100 kbar.

By contrast, the calculated frequencies obtained from the dynamical matrix diagonalisation method agree well with experimental data for RL modes over the entire experimentally accessible pressure range. The slight overestimate of calculated frequencies for the whole frequency-pressure curve in Fig. 6.13 is due to the temperature effects which are not included in the calculations. Further, the calculated normalised eigenvectors for the RL shear and compressive modes at ambient and elevated pressure are listed in Table 6.13. It can be seen that the minor symmetry-allowed coupling of components on the ac plane of eigenvectors at ambient pressure is gradually enhanced by compression for both A_g and B_{2g} modes. This calculated eigenvectors indicate the mode mixing of approximately RL mode and intralayer vibrations occurs continuously in response to hydrostatic pressure.

The displacement patterns of two RL modes of GeS are illustrated in Fig. 6.14 and it is clear that the simple rigid-layer character is no longer valid at modest pressure. In addition, this pressure-induced admixture of interlayer and intralayer vibrations gives

Table 6.13. Calculated normalised eigenvectors of the A_g shear mode and B_{2g} compressive mode normal to the crystallographic b-axis at several pressures. Ge_1 and S_1 are located on one double-layer whereas Ge_2 and S_2 are located on another double-layer in the unit cell. Note the relatively large increase in the c- and the a-component of the displacements of A_g and B_{2g} mode, respectively, with increasing pressure indicating the breakdown of the RL approximation.

		Ge_1		Ge_2		S_1		S_2	
Symmetry	Pressure	a	c	a	c	a	c	a	c
A_g	Ambient	-0.42	0.11	0.42	-0.11	-0.24	0.00	0.24	0.00
	10kbar	-0.42	0.13	0.42	-0.13	-0.23	0.01	0.23	0.01
	50kbar	-0.42	0.19	0.42	-0.19	-0.20	0.02	0.20	0.02
	100kbar	-0.42	0.20	0.42	-0.20	-0.17	0.04	0.17	0.04
B_{2g}	Ambient	-0.03	0.43	0.03	0.43	-0.01	0.25	0.01	0.25
	10kbar	-0.04	0.43	0.04	0.43	-0.01	0.24	0.01	0.24
	50kbar	-0.11	0.44	0.11	0.44	-0.03	0.22	0.03	0.22
	100kbar	-0.34	0.32	0.34	0.32	-0.11	0.14	0.11	0.14

a microscopic description of the band crossover under pressure which was pointed out in Fig. 6.11, and indicates the complete loss of two-dimensional character of the vibrations. Also, this calculated results provide an explanation for the failure of FP method. Therefore, it is believed that the sublinear behaviour of the pressure response of RL mode frequencies derived from the pressure-induced breakdown of the RL approximation can be found in any other layered compounds.

6.6 Conclusion

In the chapter, the lattice dynamics of layered solids GeS and GeSe have been extensively investigated using both theoretical and experimental methods. Before the systematic studies by experimental observations and computational simulations, the activities of lattice vibrations at ambient pressure can be predicted using the group-theoretical approaches, the BV and the correlation methods. The results of symmetry considerations are consistent with the experimental ambient pressure Raman scattering and first-principle calculations.

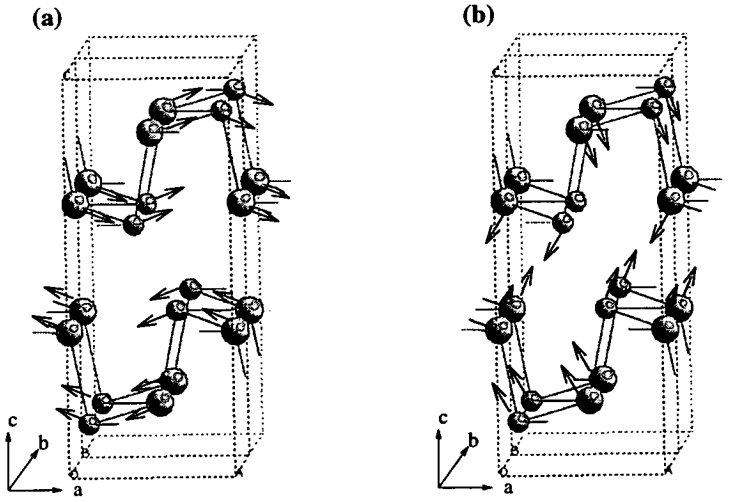

Figure 6.14. Calculated eigenvector corresponding to the (a) shear RL A_g, (b) compressive RL B_{2g} mode vibrations as determined by dynamical matrix diagonalisation at a pressure of 50 kbar. The arrows represent the directions and the values of eigenvectors. Ge and S atom is denoted as the small and the large sphere, respectively.

On the other hand, in order to obtain an appropriate theoretical description of the lattice vibrational properties of layer structures, a diperiodic group has been employed. The DG analysis has given more information for the normal modes and their optical selection rules of layered GeS and GeSe. Moreover, a Davydov doublets splitting attributed to the weak interlayer interaction has been observed by the comparison between the layer symmetry and the crystal symmetry. It was shown that studies of Davydov doublets splitting provide a means to probe the strength of the interlayer coupling. Another characteristic feature of vibrational properties of layered solids, rigid-layer vibrations, has been also deduced from DG investigations and been identified using *ab-initio* calculations. This RL modes correspond directly to the force between adjacent layers and locate at very low-frequency regime isolated with a frequency-gap from intralayer vibrational frequencies. In the case of GeS and GeSe, the ratios of heirarchical force constants estimated from Davydov doublets splittings and the frequency-gap of only 10 cm^{-1} indicate that the vibrational properties of layered Ge chalcogenides at

ambient pressure are not as anisotropic as the structure might suggest. Therefore, the ambient pressure situation of GeS and GeSe is associated to a weak-coupling regime.

Pressure effects on layered GeS and GeSe have been studied as well. Under compression, a pressure-enhanced Raman-infrared Davydov doublets splitting has been predicted by dynamical matrix diagonalisation method. This effects can be addressed as the enforcement of interlayer cohesions by compression. Also, during the low pressure regime, it was revealed that the pressure dependence of phonon frequencies for RL vibrations and intralayer modes can not be interpreted by a conventional Grüneisen approximation. In fact, a general bond-stiffness-bond-strain scaling law has been found to scale the pressure sensitivities of phonons referred to different type of interactions.

However, by 50 kbar, the linear relationship between frequency blue-shift and hydrostatic pressure is no longer appropriate for RL modes. From the first-principle simulations, the failure of the RL model has been shown and a pressure-induced breakdown of the RL approximation which can be observed in other layered materials has been obtained. The admixture of RL modes and intralayer modes is continuous and removes the frequency-gap between interlayer and intralayer vibrations. These conclusions reveal that substantial anisotropy of vibrational properties of anisotropic materials may lose completely although the structure still maintain highly anisotropic under pressure (shown in Chapter 5). It also implies that the pressure will induce more fruitful effects on the less structural materials which will be discussed in the next few chapters.

Chapter 7

Anisotropic Condensed Molecular Systems

7.1 Introduction

Previous chapters mainly concentrated on anisotropic semiconductors involving the strong intralayer covalent bonding and the weaker interlayer interaction in quasi two-dimensional solids. However, in addition to these solid-state materials, there exists a wide variety of condensed matter systems which can be found everywhere. These "soft" condensed molecular systems (molecular crystals, liquid crystals, polymers, and biological materials) are formed by cohesion of widely disparate strengths and have a variety of applications especially in industry. Also, corresponding to this complex cohesive mechanism within these materials, the effect of external fields (not only pressure but also temperature, electric field, etc.) will provide means to control the physical and chemical properties of condensed molecules in order to extend applications. Thereby, the study of such highly anisotropic materials is pivotal to the understanding of complex chemical bonding.

The range of condensed molecular systems covered in this chapter includes quasi-molecular solids and liquid crystals in which strong covalent forces preserve molecular

identity while much weaker (see Chapter 1, van der Waals, short-ranged exponential and thermal-Casimir) interactions define intermolecular correlations. High pressure and variable temperature effects on structural, vibrational, and electronic properties of typical quasi-molecular crystals of Group-V metal triiodides are comprehensively studied using advanced theoretical and experimental approaches given in Chapter 2 and 3. The compressional response of quasi-molecular materials will be demonstrated in Sec. 7.2. Furthermore, the scope is widened to include large flexible liquid crystals. Preliminary studies of the lattice dynamics of thermotropic liquid crystals unique features are discussed in Sec. 7.3. Finally, a summary and a perspective of future work are provided in Sec 7.4.

7.2 Molecular-Nonmolecular Crossover in Quasi-Molecular Solids

Molecular crystalline materials are an interesting area of condensed matter science as a result of the large discrepancy between the strength of intra- and of inter-molecular cohesive forces. However, various types of structures can be obtained using organic chemical synthesis methods to manipulate cohesion. One extreme case is a crystal structure in which molecular shapes are retained from solution or gas phase. This retention of molecular geometry provides the possibility of structural determination for organic molecules using X-ray diffraction. However, another extreme type of structure corresponds to a close proximity of molecules in the solid state. This stronger intermolecular coupling is due to intermolecular charge transfer and therefore new bond formation across molecules.

A good example of these two extreme cases is Group-V metal triiodides in which AsI_3 and SbI_3 approximately keep the molecular identity while it is lost in BiI_3 at ambient pressure. Like the layered semiconductors discussed previously, external pressure is expected to induce a substantial modification of structural and vibrational properties

Table 7.1. Observed structural parameters for AsI_3, SbI_3, and BiI_3 under ambient conditions. The units for lattice constants a and c are in Å and those for internal parameters are in fractional coordinates. Previous data determined from single crystal X-ray diffraction with Patterson projection analyses [166] are shown in parentheses for comparison.

	a	c	z_X	x_I	y_I	z_I
AsI_3	7.208	21.415	0.2001	0.3447	0.3187	0.0772
	(7.208)	(21.436)	(0.1985)	(0.3485)	(0.3333)	(0.0822)
SbI_3	7.505	20.967	0.1812	0.3397	0.3233	0.0816
	(7.480)	(20.900)	(0.1820)	(0.3415)	(0.3395)	(0.0805)
BiI_3	7.527	20.732	0.1693	0.3322	0.3146	0.0797
	(7.516)	(20.718)	($\sim$ 0.1667)	($\sim$ 0.3415)	($\sim$ 0.3395)	($\sim$ 0.0805)

of this quasi-molecular family. In this section, the crystal structure and vibrational spectra of Group-V metal triiodides at various compressions are extensively studied by means of modern experimental techniques. The possible charge transfer under pressure is also probed using *ab-initio* calculations. The results which complement earlier high-pressure studies on quasi-two-dimensional solids are displayed here in detail.

7.2.1 Molecular Geometry of Group-V metal Triiodides

The ambient structure of three Group-V metal triiodides, XI_3(X=As, Sb, Bi), is rhombohedral with space group $C_{3i}^2(R\bar{3})$ [166]. As shown in Fig. 7.1, the atomic positional parameters for metal (X) and iodine (I) atoms are defined as (0,0,z_X) and (x_I, y_I, z_I), respectively, in an equivalent hexagonal cell containing six XI_3 formula units. Although the three structures are all crystallographically equivalent, the geometry of each compound is predominately determined by the free atomic positional parameters. The structural parameters for three Group-V metal triiodides obtained from a synchrotron X-ray angle-dispersive powder diffraction [167] are compiled in Table 7.1.

The crystal structure of three compounds is based on approximate hexagonal close-packing of the iodine atoms with the metal atoms lying in the interstices of alternate layers. In the case of BiI_3, the value of z_{Bi} is close to 1/6 which suggests the bismuth

atom is at the centre of a nearly-perfect octahedron of iodines. Thus, six BiI_3 units in a hexagonal cell form three individual layers in which cations (Bi) occupy the middle of the "*sandwich*" structure and are surrounded octahedrally by six anions (I). Comparing with a more close-packed layered structure of PbI_2, the partial occupation (2/3) of cations in BiI_3 gives rise to a twofold-coordinated anions as outer atomic layers. Therefore, the identical Bi−I bondlength of 3.1 Å within an isolated layer is determined from the internal parameters in Tab. 7.1 and one nearest I−I separation of 4.11 Å is also identified between adjacent layers. Further, the layer separation $d_{sep.}$ defined as $2z_I c$ is obtained as 3.34 Å at ambient condition.

However, the octahedral environment of the metal atom becomes progressively distorted from BiI_3 to AsI_3 since z_X deviates gradually from the perfect value with going up this group. This effect causes a threefold bonding configuration of metal atoms and the relevant intramolecular bondlength of AsI_3 and SbI_3 at ambient pressure is 2.56 Å and 2.88 Å , respectively. A certain amount of molecular character is thus expected to be retained in AsI_3 and SbI_3. Like with layered structures, $d_{sep.}$ corresponds to the molecular separation in this quasi-molecular picture and can also be defined as $2z_I c$ which gives the value of 3.52 Å and 3.37 Å for AsI_3 and SbI_3, respectively. In addition, two nearest intermolecular I−I distances are observed in AsI_3 (4.21 and 4.26 Å) and SbI_3 (4.12 and 4.22 Å).

The evidence of this topological trend in XI_3 can be also stated in terms of the difference between the intramolecular bondlength b_1 and the nearest-intermolecular X−I separation b_2 (defined in Fig. 7.1). In AsI_3 and SbI_3, b_1 is obviously shorter than b_2 while the distinction between b_1 and b_2 is negligible in BiI_3. Indeed, the identical As−I bond length and intramolecular I−As−I bond angle found in both gaseous and crystal phases [166] implies the existence of discernible AsI_3 molecules in the corresponding crystal. However, these gas-phase molecular dimensions are distored in SbI_3 and totally disappear in BiI_3.

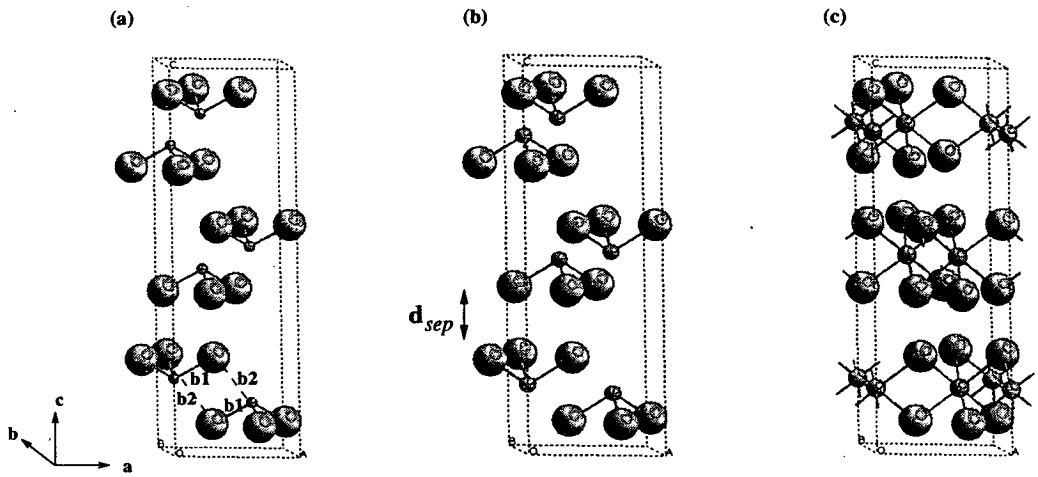

Figure 7.1. Schematic representation of the ambient structures of AsI_3 (a), SbI_3 (b), and BiI_3 (c). As is discussed in the text, the distances b_1 and b_2 are indicated in (a). The molecular (or interlayer) separation $d_{sep.}$ is also defined. It can be seen that the distinction between b_1 and b_2 is applicable only for AsI_3 and SbI_3, for which the intramolecular I–X–I bond angle deviates from 90^o.

7.2.2 Molecular Vibrational Properties

As presented in Sec. 6.2, the vibrational properties of crystals can be systematically analysed using the group theoretical correlation method. For the quasi-molecular Group-V metal triiodides, the correlation method can be performed through two different approaches. The first approach is the ionic representation which treats the crystal of XI_3 as a composition of individual ions. Thus, in the rhombohedral unit cell, two metal atoms (X) and six iodines located on the C_3 and C_1 site, respectively, build the XI_3 crystal with factor group of C_{3i}. By making reference to the character tables of C_3 and C_1 and the correlation table of C_{3i}, the correlation diagram of this ionic picture is shown in Fig. 7.2. The result for the irreducible representations of the unit cell, $\Gamma^{XI_3}_{ionic}$, is then given by subtracting the acoustic vibrations $\Gamma^{XI_3}_{acoust.}$ from the contribution of cations (Γ^X) and anions (Γ^I)

$$\Gamma^{XI_3}_{ionic} = \Gamma^X + \Gamma^I - \Gamma^{XI_3}_{acoust.}$$

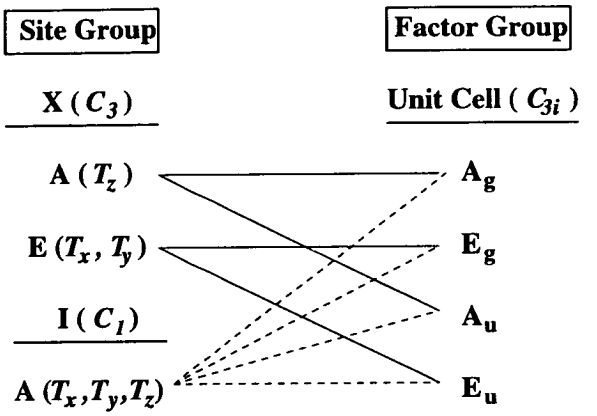

Figure 7.2. Correlation diagram for XI_3 by an ionic approach

$$\begin{aligned} &= (A_g + E_g + A_u + E_u) + 3(A_g + E_g + A_u + E_u) - (A_u + E_u) \\ &= 4A_g^{(R)} + 4E_g^{(R)} + 3A_u^{(IR)} + 3E_u^{(IR)} \end{aligned} \tag{7.1}$$

where A and E denotes respectively the single and double degenerate modes. R stands for the Raman-active mode and IR for the infrared-active one.

However, a better representation for AsI_3 and SbI_3 is the molecular description which concedes the molecular identity of the XI_3 unit. From this consideration, two pyramidal XI_3 molecules is situated at a unit cell having C_{3v} symmetry and the site symmetry of each molecule is C_3. In the molecular approach, the normal modes are mainly due to three parts: intramolecular vibrations, molecular rotations, and molecular translations. However, the pure molecular rotation and translation are Raman-inactive in a purely isolated molecule. The activities of rotational and translational vibrations are induced by the weak intermolecular perturbations inside the crystal. Hence, within a pyramidal XI_3 molecule, X and I occupy the C_{3v} and C_s site, respectively, and the correlation diagram of the isolated molecule is displayed in Fig. 7.3(a). The irreducible representation of the intramolecular vibration $\Gamma_{intra.}^{XI_3}$ is then expressed as

$$\Gamma_{intra.}^{XI_3} = 2A_g^{(R)} + 2E_g^{(R)} + 2A_u^{(IR)} + 2E_u^{(IR)} \tag{7.2}$$

Similarly, the correlation diagram of rotational and translational vibrations of the XI_3 molecule locating at C_3 site is demonstrated respectively in Fig. 7.3(b) and (c). The relevant irreducible representations $\Gamma_{lib.}^{XI_3}$ and $\Gamma_{trans.}^{XI_3}$ corresponding to librations and lattice vibrations are given by

$$\Gamma_{lib.}^{XI_3} = A_g^{(R)}(lib.) + E_g^{(R)}(lib.) + A_u^{(IR)}(lib.) + E_u^{(IR)}(lib.) \quad (7.3)$$

$$\Gamma_{trans.}^{XI_3} = A_g^{(R)}(trans.) + E_g^{(R)}(trans.) + A_u^{(IR)}(trans.) + E_u^{(IR)}(trans.) \quad (7.4)$$

Thus, the zone-centre vibrational modes of XI_3 are derived from the summation of $\Gamma_{intra.}^{XI_3}$, $\Gamma_{lib.}^{XI_3}$, and $\Gamma_{trans.}^{XI_3}$ and subtraction of the acoustic component $\Gamma_{acoust.}^{XI_3}$.

$$\begin{aligned}\Gamma_{molecular}^{XI_3} &= \Gamma_{intra.}^{XI_3} + \Gamma_{lib.}^{XI_3} + \Gamma_{trans.}^{XI_3} - \Gamma_{acoust.}^{XI_3} \\ &= 4A_g^{(R)} + 4E_g^{(R)} + 3A_u^{(IR)} + 3E_u^{(IR)} \equiv \Gamma_{ionic}^{XI_3} \end{aligned} \quad (7.5)$$

In addition to the theoretical considerations, the vibrational properties of three Group-V metal triiodides at ambient pressure have also been experimentally studied using low-temperature Raman scattering. The 6764 Å line of Kr^+ laser was employed as the excitation source. The laser power was estimated to be 30 mW at the powdered sample. A Coderg T-800 triple-grating spectrometer was used to collect spectra with a slit width of 400 μm which gives a resolution of approximately 1.5 cm^{-1}. The 90^o scattering geometry was performed with a count time of 10 seconds per data point. The details of the experimental techniques can be found in Sec. 2.4.3. Ambient pressure first-order Raman spectra collected at different temperatures are exhibited in Fig. 7.4 for three compounds. The lowest-frequency $E_g(trans.)$ in SbI_3 and BiI_3 cannot be observed clearly at this experimental resolution, whereas the other Raman modes can be clearly monitored. Based on previous depolarisation ratio measurements [168], the assignments of eight Raman peaks are given and are consistent with the above group-theoretical prediction. The frequencies of observed zone-centre Raman-active

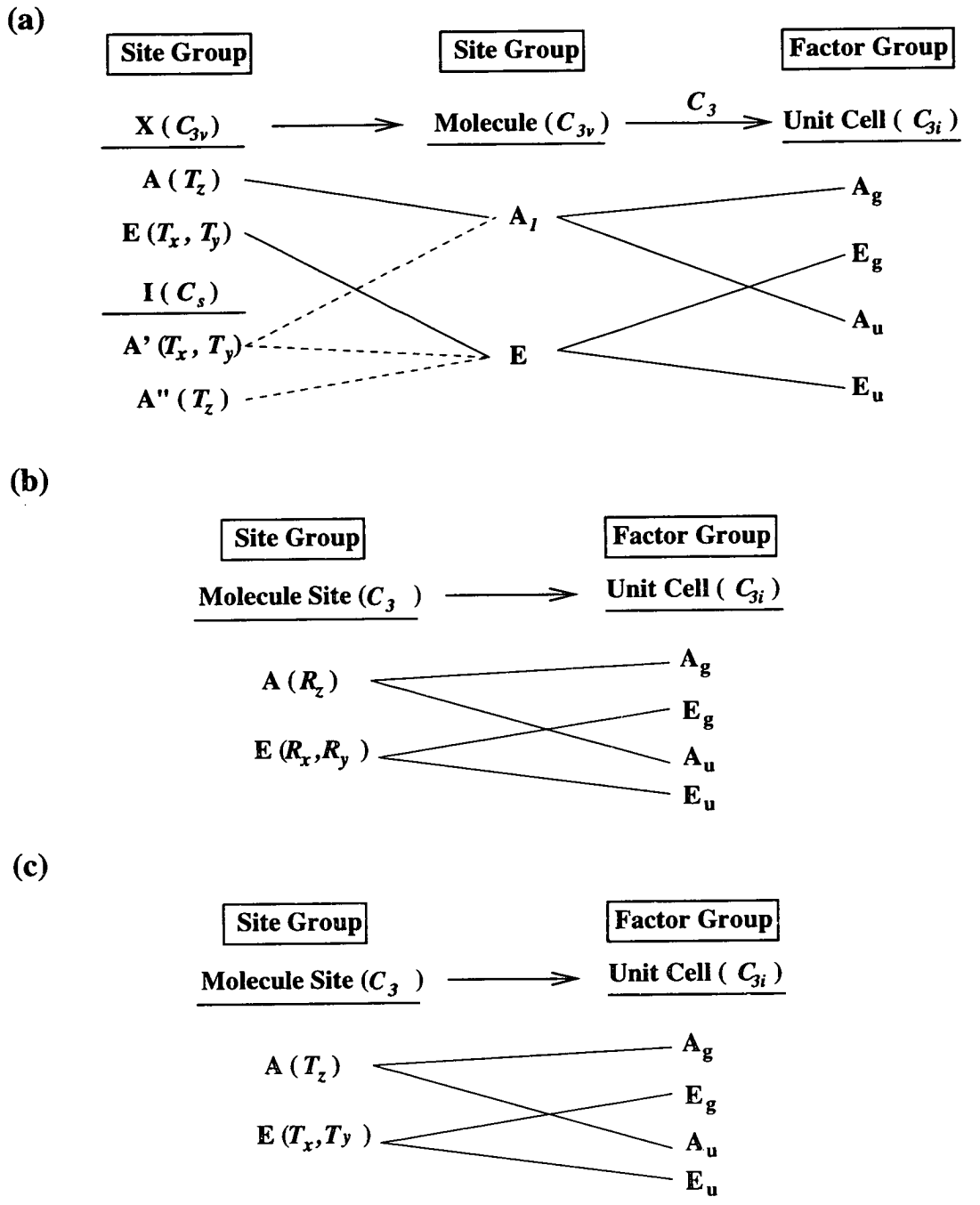

Figure 7.3. Correlation diagram for an individual molecule XI_3 (a), molecular rotations (b), and molecular translations (c).

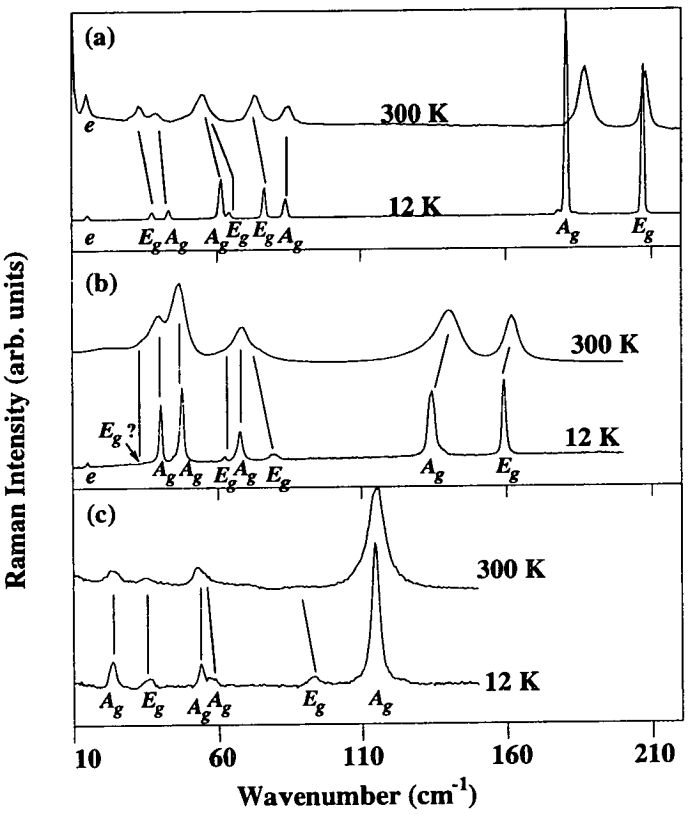

Figure 7.4. Raman spectra at room (300 K) and low (12K) temperature for AsI_3 (a), SbI_3 (b), and BiI_3 (c). The assignment derived from depolarisation ratios [168] is shown for the corresponding peak. The signal of emission line is denoted as *e*.

Table 7.2. Observed first-order Raman frequencies of three Group-V metal triiodides at room and low temperature. The frequency is in a unit of cm^{-1}.

Symmetry	AsI_3		SbI_3		BiI_3		Symmetry
Species	300 K	12 K	300 K	12 K	300 K	12 K	Species (BiI_3)
$E_g(stret.)$	207.5	206.9	160.6	159.1	115.5	114.7	A_g
	208.2[a]	206.5[b]	161.5[a]	158.0[b]	-	113.3[c]	
$A_g(stret.)$	185.5	180.4	138.3	134.7	87.4	94.4	E_g
	187.1[a]	180.0[b]	139.0[a]	132.5[b]	-	95.0[c]	
$A_g(bend)$	84.5	83.8	66.9	67.5	56.3	58.0	A_g
	84.6[a]	83.5[b]	73.0[a]	67.0[b]	-	58.5[c]	
$E_g(bend)$	74.1	76.6	74.2	79.8	52.8	53.7	A_g
	73.9[a]	76.5[b]	-	81.0 [b]	-	53.5[c]	
$E_g(lib.)$	62.0	64.1	60.8	62.2	34.6	34.8	E_g
	-	64.0[b]	-	62.0[b]	-	36.7[c]	
$A_g(tran.)$	57.3	61.2	46.0	47.6	-	-	E_g
	56.0[a]	61.0[b]	45.5[a]	47.5[b]	-	33.5[c]	
$A_g(lib.)$	39.5	43.1	38.5	40.1	22.4	22.6	$A_g(RL)$
	39.0[a]	43.0[b]	38.0[a]	40.0[b]	-	22.8[c]	
$E_g(tran.)$	34.3	37.3	-	-	-	-	$E_g(RL)$
	33.3[a]	37.5[b]	33[a]	35.5[b]	-	12.9[c]	

[a] [170] [b] [168] [c] [169].

vibrational modes for three compounds are listed in Table 7.2 in comparison with the previous reports by Anderson *et al.* [168] and Komatsu *et al.* [169].

Like the zone-centre phonons of layered semiconductors shown in Chapter 6, the Raman frequencies of Group-V metal triiodides can be grouped into two classes associated with *internal* and *external* vibrational modes. In the quasi-molecular system of AsI_3 and SbI_3, four low-frequency external vibrations are due to two molecular librations ($A_g(lib.)$ and $E_g(lib.)$) and two molecular translations ($A_g(trans.)$ and $E_g(trans.)$) which correspond, respectively, to the rigid-molecular rotations and translations. However, the internal group consists of two intramolecular bond-stretching ($A_g(stret.)$ and $E_g(stret.)$) and two bond-bending ($A_g(bend)$ and $E_g(bend)$) modes. As pointed out in group theoretical discussion, six of the eight Raman-active modes (the other two molecular translational modes are acoustic) have their infrared-active counterparts which have been observed in the far-infrared spectra [171]. Moreover,

the gap between the highest external (intermolecular libration) and the lowest internal (intramolecular bond-bending) vibrational frequencies can be used to gauge the intermolecular intercation. The larger inter-intramolecular frequency separation of AsI_3 (12.5 cm^{-1}) is attributed to the weaker intermolecular cohesion and corroborates the conclusion of structural studies which suggest a more pronounced molecular identity in AsI_3.

Nevertheless, this molecular picture is not appropriate for the ionic layered BiI_3. In fact, the molecular libration is not allowed since the pyramidal molecular BiI_3 units link to each other by chemical bonds. The external modes only include one rigid-layer shear mode ($E_g(RL)$) and one compressive mode ($A_g(RL)$), and the remaining Raman modes corresponds to the internal part which contains intralayer breathing, bond-bending, and bond-stretching vibrations. The inter-intralayer frequency difference of 11 cm^{-1} indicates that the anisotropy of BiI_3 is close to that of GeS and GeSe.

7.2.3 Structural Response to Hydrostatic Pressure

Phase behaviour of Group-V metal triiodides under the influence of pressure was extensively studied using high-pressure powder diffraction with an image plate area detector. The details of the experimental apparatus and techniques have been given in Sec. 2.3.2. The Merrill-Bassett DAC (see in Sec. 2.2.1) was used to provide the high pressure condition which is calibrated using ruby fluorescence. In view of the molecular and layered character and therefore preferential cleavage of these compounds, care was taken to load a uniform sample powder so as to reduce complications from potentially severe preferred orientation effects. However, no pressure-transmitting fluid was used because of the moisture sensitivity of samples. The incident beam with a wavelength of 0.4447 Å collimated to a diameter of 75 μm was employed for all measurements. The distance between the sample and the image plate was approximately 300 mm. Exposure times were about 4 hours in length. As the same integration scheme used in structural measurements of GeS, the PLATYPUS software (Sec. 2.3.2) was utilised to integrate the

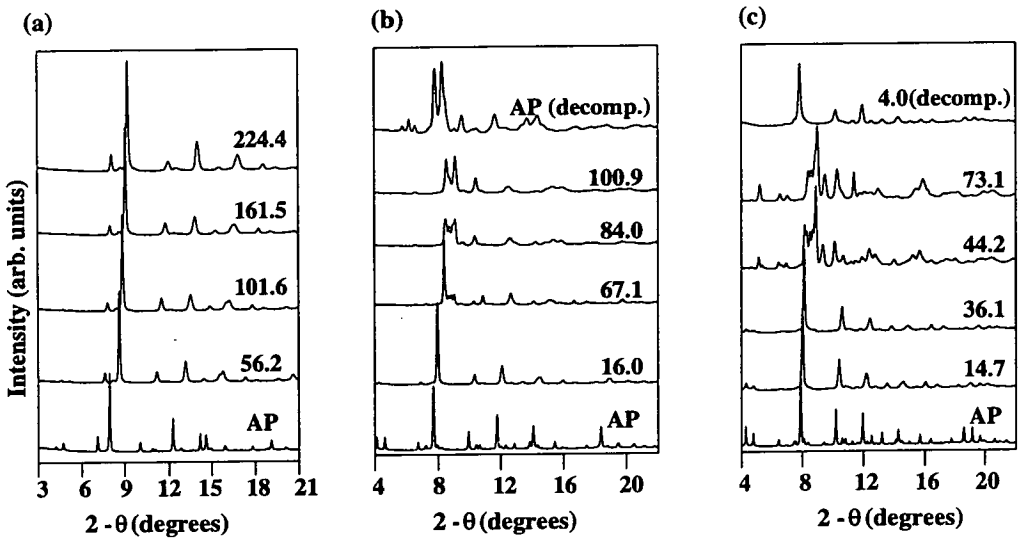

Figure 7.5. The evolution of angle-dispersive X-ray diffraction profiles for AsI_3 (a), SbI_3 (b), and BiI_3(c) at different compressional conditions. The strength of pressure of each pattern is indicated in a unit of kbar.

two-dimensional images here. Subsequently, Rietveld refinement was done using the DBWS-9006 programme (Sec. 2.3.3).

The structural properties of AsI_3, SbI_3, and BiI_3 were investigated up to pressures of 220, 114, and 73 kbar, respectively. The evolution of the patterns under different pressure conditions for three compounds is shown in Fig. 7.5. It is clear from this figure that a pressure-induced structural phase transition was observed in SbI_3 and BiI_3 beyond 70 and 40 kbar, respectively, whereas the hexagonal structure of AsI_3 retains at least up to 220 kbar. Before discussing the high-pressure modification of SbI_3 and BiI_3, it is of interest to study the pressure effects on the molecular geometry of AsI_3 and SbI_3 . Within the pressure region below the structural transformation pressure, lattice constants and the nearest metal-iodine (intramolecular) bondlength b_1 as a function of pressure for three materials is displayed in Fig. 7.6(a) and (b), respectively. It is shown that both lattice constants a and c decrease monotonically with pressure for each material. However, an unexpected pressure response of b_1 was found in both AsI_3 and SbI_3 in which b_1 first increases and then decreases with increasing pressure. The maximum value of b_1 for AsI_3 and SbI_3 is at about 45 and 15 kbar, respectively.

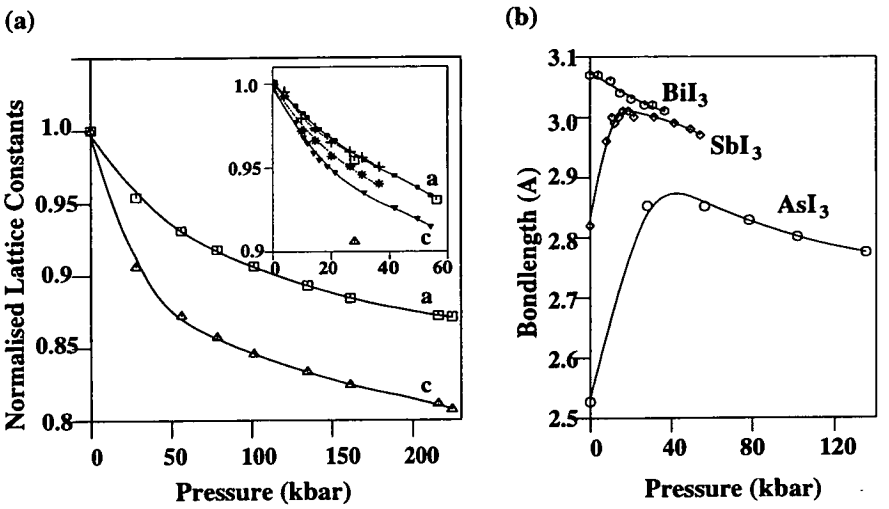

Figure 7.6. Pressure dependence of normalised lattice constants (a) and X−I bondlength (b). In (a), the structural parameters (a and c) for AsI_3, SbI_3, and BiI_3 is represented as the symbol set of (open squares and triangles), (solid squares and triangles), and ('+' and '*'), respectively. The solid and dashed lines are guides to the eye. In (b), the bondlength b_1 for AsI_3, SbI_3, and BiI_3 is denoted as an open circle, diamond, and hexagon, respectively. A nonlinear pressure behaviour of b_1 was found in both AsI_3 and SbI_3.

The characteristic distance ratio b_2/b_1 and I−X−I bond angle as a function of pressure are also depicted in Fig. 7.7. It can be seen that pressure has the effect of preferentially compressing the intermolecular bond (b_2) of both AsI_3 and SbI_3 until the distinction between inter- and intra-molecular (b_1) bonding is lost. Based on the structural refinement of SbI_3, the "knee" in the curve of b_2/b_1 vs pressure corresponding to $b_2 \approx b_1$ with the I−X−I bond angle $\approx 89°$ occurs at the molecular-layered transition pressure of $P_{mole-layer} \leq 20$ kbar at which SbI_3 adopts the layered structure of BiI_3. In AsI_3, this pressure-induced continuous isostructural molecular-layered transition can be only roughly determined as $P_{mole-layer}(AsI_3) \leq 50$ kbar because of the wide pressure intervals of data collection. Therefore, above $P_{mole-layer}$, both AsI_3 and SbI_3 become quasi-two-dimensional layered solids characterised by more-or-less ideal octahedral coordination of the metal atoms. The associated vibrational properties, influenced by pressure, will be discussed in Sec 7.2.4.

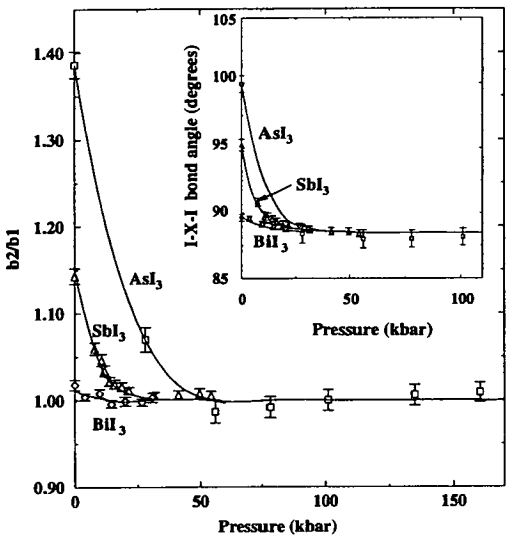

Figure 7.7. Pressure dependence of the ratio of metal-iodine distances b_2/b_1 and the I–X–I bond angles (inset) in Group-V metal triiodides as determined by angle-dispersive X-ray powder diffraction and subsequent Rietveld refinement. The data for AsI_3, SbI_3, and BiI_3 are denoted, respectively, as squares, triangles, and diamonds with an error bar which is propagated from the estimated standard deviations of the structural refinement results. Solid lines through the experimental data are guides to the eye.

High Pressure Mixed Coordination and Hysteresis

Under further pressurisation, a high-pressure phase of SbI_3 mixed with the hexagonal phase was observed at about 70 kbar. In order to elucidate the structural detail of the new modification of SbI_3, a pattern with only a single phase corresponding to 100.9 kbar is used to refine. Based on Rietveld refinement, the calculated profile with a merit factor $R_{wp} = 6.48\%$ (shown in Fig. 7.8(a)) corresponds to a monoclinic structure having space group C_{2h}^5 ($P2_1/c$). The unit cell of monoclinic SbI_3 containing four SbI_3 formula units is characterised by the lattice parameters of $a = 6.636$ Å , $b = 9.375$ Å $c = 8.165$ Å and $\beta = 108.41°$ at 100.9 kbar. The detail of this monoclinic structure is specified by the internal positional parameters listed in Table 7.3. Fig. 7.8(b) indicates that the nearly-perfect octahedral sixfold bonding configuration of metal atoms within previous hexagonal phase is distorted by the application of compression. Indeed, three sets of Sb–I bondlengths inside the layer were observed as (2.90, 2.90 Å), (2.98, 2.99

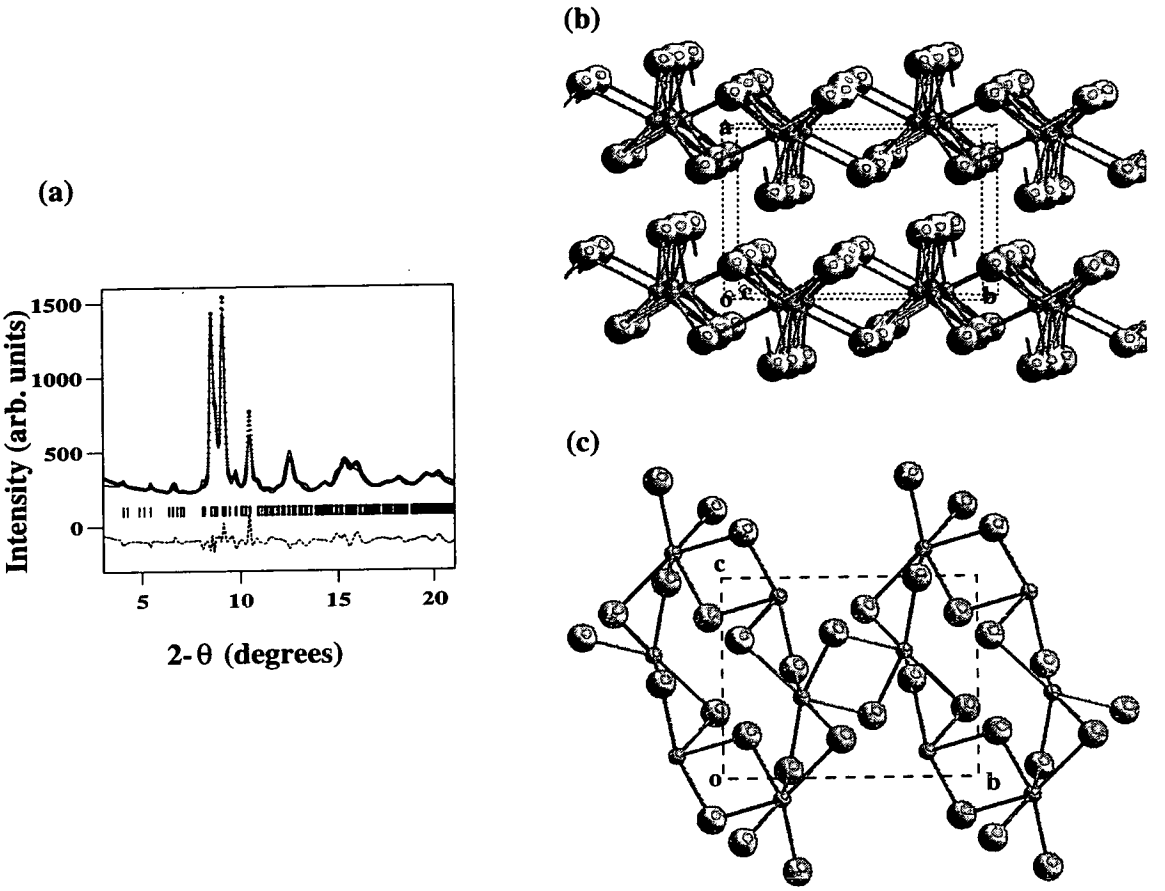

Figure 7.8. Rietveld refinement of powder patterns of SbI_3 observed at 100.9 kbar (a). The fit shown in (a) has been obtained using a (l00) preferred orientation correction. The observed data, calculated reflection, calculated profile, and the discrepancy between the observation and calculation is denoted as the '+' symbol, '|' tics mark, solid line, and dashed line, respectively. Illustration of the relevant puckered layered structure along different view point is shown respectively in (b) and (c) in which the small sphere stands for the Sb atom and the large one for the I atom.

Table 7.3. Refined internal structural parameters in fractional coordinate for SbI_3 at 100.9 kbar

Atom	x	y	z
Sb	0.0209	-0.2078	0.1113
I_1	0.2335	0.0734	0.2065
I_2	0.3689	-0.2642	0.4695
I_3	-0.2017	-0.0510	0.3205

Å), and (3.14, 3.27 Å) and two nearest I−I separations of 3.56 and 3.70 Å were also found across adjacent layers. Hence, the combination of mixed coordinated $2+2+2$ cations and twofold coordinated anions forms two puckered layers inside a unit cell. For BiI_3, a very similar pattern was also found when the external pressure up to 40 kbar. Therefore, the high-pressure modification of BiI_3 is predicted to adopt a similar monoclinic crystal structure composed of puckered layers. However, additional work on refinement for the monoclinic SbI_3 and BiI_3 at various pressures is needed to obtain the relevant equations of state and then to decide the order of this transition. In addition, the decompressed result in Fig. 7.5 reveals that this structural phase transition is reversible in BiI_3, whereas the hexagonal phase of SbI_3 cannot be restored by simply releasing pressure.

7.2.4 Pressure Effects on Raman Spectra

The vibrational properties of quasi-molecular Group-V metal triiodides under compression were investigated by DAC and Raman scattering with a backscattering geometry (see in Sec 2.4.3). In view of the anisotropic structural properties of all three materials mentioned previously, various vibrational responses to external pressure are expected. Again, to explore the molecular identity of XI_3, attention is focussed on the pressure dependence of internal and external Raman modes in the pressure region corresponding to the isostructural hexagonal phase for three triiodides. As an example, the evolution of the room temperature Raman spectrum under compression for AsI_3 up to 72 kbar is shown in Fig. 7.9 in which the general intensity decrease of high-pressure spectra is due to a pressure-induced red shift of the band gap.

In the high-frequency internal vibrational area, the X−I symmetry stretch mode frequencies, $A_g(stret.)$, with the highest Raman intensity are displayed in Fig. 7.10 for three quasi-molecular solids. The pressure dependence of the $A_g(stret.)$ mode for more ionic BiI_3 is unexceptional, increasing linearly with pressure in a pressure sensitivity (defined in Sec. 6.5.2) of 0.003 $kbar^{-1}$. However, an extraordinary behaviour

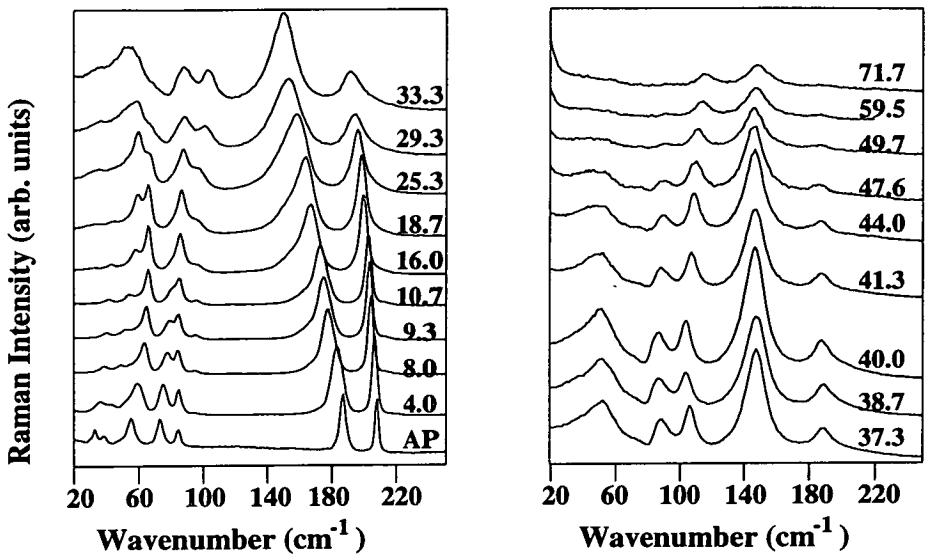

Figure 7.9. Observed Raman spectrum of AsI_3 as a function of pressure. The strength of pressure in a unit of kbar is indicated for the corresponding spectrum.

of the $A_g(stret.)$ mode are found in both AsI_3 and SbI_3. The $A_g(stret.)$ mode frequency initially decreases with pressure suggesting that the metal-iodine bond initially weakens under compression. This mode softening can also be accounted for by the non-monotonic behaviour of the bondlength b_1 under pressure in Fig. 7.6 which shows that the intramolecular bond of AsI_3 and SbI_3 is extended slightly during the initial application of pressure. Nevertheless, this trend of $A_g(stret.)$ is arrested at $\sim$ 45 and 15 kbar for AsI_3 and SbI_3, respectively, after which pressure derivatives of the normal sign are observed. The pressure of the "*turnover*" of the intramolecular $A_g(stret.)$ mode corresponds to the "*knee*" of b_2/b_1 curves found in Fig. 7.7 which indicates that the structural environment of the metal (As and Sb) becomes progressively more symmetric. Hence, the non-linear pressure dependence of the $A_g(stret.)$ mode in two more molecule-like compounds suggests that pressure leads to a gradual suppression of covalent bonding between the metal and its nearest three iodines in favour of ionic bonding between a central cation surrounded by an increasingly symmetric cage of six anions – a progressive loss of molecular character. A conclusive evidence of this pressure-induced charge redistribution can be ascertained from *ab-initio* electronic calculations

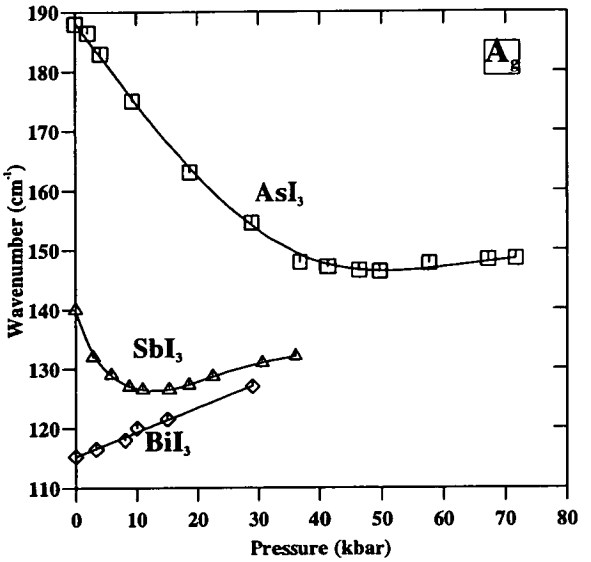

Figure 7.10. Frequencies of the intramolecular X–I symmetry stretching $A_g(stret.)$ mode versus pressure in Group-V metal triiodides. It is clear that the frequency response is non-monotonic for both AsI_3 (squares) and SbI_3 (triangles). Only for BiI_3 (diamonds) does this mode shift to higher frequencies immediately upon pressure increase. The solid lines through experimental data are guides to the eye.

which will be given in Sec. 7.2.5.

We now consider the low-frequency external vibrational region where a more complicated pressure effect is observed in the intermolecular mode regime. As shown in Fig. 7.9, the reversal of relative intensities for intermolecular vibrations under pressure, also found in SbI_3, can be recognised as a character of Fermi resonance [172]. Although this subtle phenomenon cannot be studied by first-order Raman data presented here, it is still possible to trace specific modes at different compressional conditions to elucidate the pressure influence on lattice vibrations. The external lattice translational $A_g(trans.)$ mode as a function of pressure is shown in Fig. 7.11. Like the internal $A_g(stret.)$ mode, the $A_g(trans.)$ of BiI_3 corresponding to a rigid-layer compressive vibration shows a normal linear pressure dependence with a higher pressure sensitivity of 0.006 kbar^{-1}.

However, an anomalous pressure dependence of the $A_g(trans.)$ mode was found in AsI_3 in which the frequency increases initially from ambient pressure, then decreases

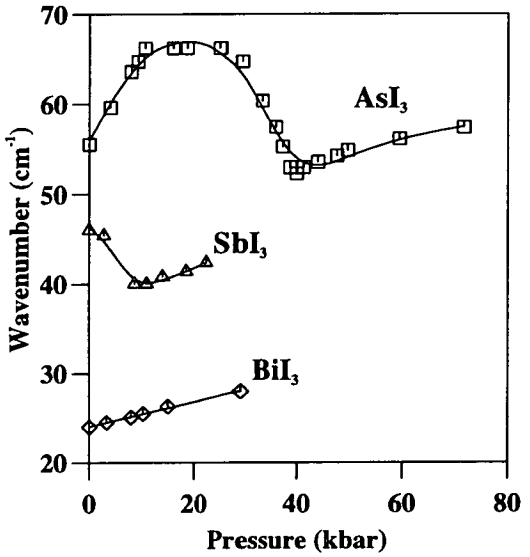

Figure 7.11. Pressure dependence of intermolecular translational $A_g(trans.)$ mode for three XI_3. The observed data of AsI_3, SbI_3, and BiI_3 are shown as open squares, triangles, and diamonds, respectively. The interpretation of anomalous behaviour of $A_g(trans.)$ mode for AsI_3 and SbI_3 can be found in text.

at about 20 kbar at which the mixing of two intermolecular A_g occurs, and, eventually, shifts increasely again while the pressure beyonds 45 kbar. This unusual behaviour can be interpreted by a close look at the structure. As given in Sec. 7.2.1, the molecular identity is retained in the ambient structure of AsI_3. In fact, the molecular separation $d_{sep.}$ of 3.08 Å is smaller than the As–I nonbonded distance b_2 (3.56 Å). It is implied that the intermolecular interaction is fairly weak and can be ignored in lattice vibrations. Thus, a simple spring-pendulum approximation is appropriate for this nearly ideal rigid-molecule vibration $A_g(trans)$ under low compressional condition. However, at a modest pressure such as 28 kbar, b_2 in AsI_3 becomes smaller (2.95 Å) and then the interaction between two pyramidal molecules plays a damping role in this spring-pendulum model. The vibrational frequency is therefore reduced by this constraint although its $d_{sep.}$ is shorter (2.99 Å). The stronger intermolecular interaction at higher pressure introduces a more severe damping effect which induces a mode softening. While the pressure up to 45 kbar, the molecular identity of AsI_3 is lost and a maximum damping factor is reached. At this point, the molecular pendulum of this simple

spring-pendulum model is replaced by a rigid layer and this rigid-molecule mode is transformed into a rigid-layer mode. Finally, the $A_g(tran.)$ mode is found to increase linearly with pressure at ~ 0.15 cm^{-1} per kbar.

In the intermediate molecular-like system of SbI_3, the b_2 (3.25 Å) and $d_{sep.}$ (3.44 Å) are comparable at ambient pressure and the existence of $A_g(trans.)$-$A_g(lib.)$ admixture implies that the molecular damping effect described above is already involved in the molecular vibration. Therefore, the application of external pressure induces initially softening of the $A_g(trans.)$ mode. Similar to AsI_3, a rigid-layer mode is gradually obtained from the breakdown of the rigid-molecule approximation while the pressure is higher than about 15 kbar relating to the molecule-layer transformation of SbI_3. Under higher pressure, a usual pressure dependence of the lattice vibrational $A_g(trans.)$ mode is thus expected and observed just like that found in the quasi-two-dimensional layered compound BiI_3.

7.2.5 Pressure-Induced Electron Transfer

In addition to the previous geometrical descriptions, the structural trend and lattice dynamics of quasi-molecular crystals can be discussed in terms of bonding type as well. The valence electronic structure of Group-V metals is ns^2np^3. Two extreme forms of bonding to construct the crystal structure of triiodides can therefore be envisaged: ionic and covalent. In the ionic extreme, the loss of three p-electrons leave X^{3+} cations with non-bonding s-orbitals, each surrounded octahedrally by six I^- anions. This gives rise to a layered solid in which the value of b_2/b_1 is approximately 1 and the I–X–I bond angle is about 90°, implying that no isolated molecules exist. On the other hand, the bonding feature in the covalent extreme is complete sp^3 hybridisation, with three covalent metal-iodine bonds and one lone pair on each metal atom. This bonding type corresponds to a solid containing distinct XI_3 molecules in which $b_2/b_1 > 1$ with bond angle > 90°. From this view point, the ionic picture appears to be suitable for BiI_3 although a minor rehybridisation process has been found in this layered

Table 7.4. Calculated structural parameters of AsI_3 in a hexagonal cell at different pressures. Lattice constants (a and c) are in the unit of Å whereas internal free parameters for As and I are in fraction coordinate.

Pressure	a	c	z_{As}	x_I	y_I	z_I
Ambient	7.032	20.223	0.1700	0.3357	0.3158	0.086
50 kbar	6.615	18.200	0.1674	0.3311	0.3387	0.079
100 kbar	6.418	17.668	0.1676	0.3338	0.3451	0.077

semiconductor [173, 174], the covalent picture is more appropriate for AsI_3, with SbI_3 being an intermediate case. Further, the perspective of chemical bonding type also provides a means to interpret the pressure-induced mode softening observed in both AsI_3 and SbI_3. The mechanism of this unique phenomenon can be regarded as a process of charge redistribution which depletes electron density from the intramolecular bond b_1, thereby reducing its strength.

In order to explore the aforementioned intermolecular charge transfer under pressure, the studies of electronic properties of the most molecule-like AsI_3 were performed by means of *ab-initio* pseudopotential calculations. Priori to calculating the total valence charge density, the structural detail has to be obtained from first-principle total energy calculations. As mentioned in Sec. 3.2, the calculation parameter of energy cutoff $E_{cutoff} = 320$ eV and Pulay coefficient $\partial E/\partial ln E_{cutoff} = -0.618$ were used to implement the structural simulations. The calculated structural parameters of AsI_3 with respect to three different pressures are listed in Table 7.4 and show quite good descriptions of structural behaviour despite the volume underestimate of LDA.

The relevant calculated total valence charge density of AsI_3 at different pressures is illustrated in Fig. 7.12. At ambient pressure, Fig. 7.12 (a) shows the majority of electron population distributes around the bonding As and I atoms and gives a sp^3 hybridised feature. However, the underestimate of calculated lattice constants causes a shorter molecular separation and gives rise to a minor charge distribution within the nonbonding area between metal and iodines. By applying the hydrostatic pressure up

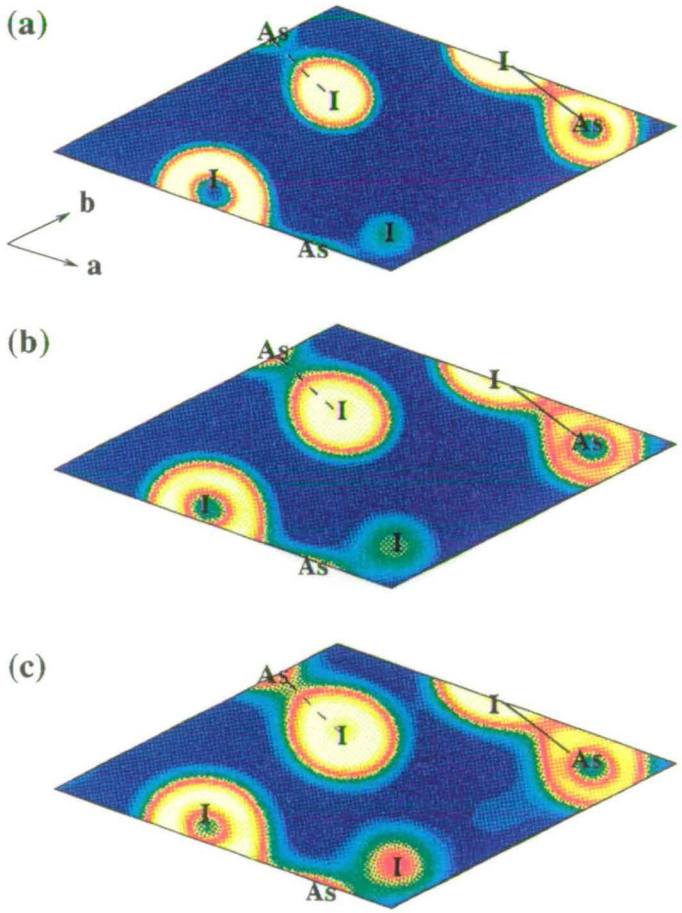

Figure 7.12. Charge-density contour plot of the calculated total valence charge of AsI_3 displayed in a (100) plane at ambient pressure (a), 50 kbar (b), and 100 kbar(c). The bonding and nonbonding state between As and I atom is denoted as a solid and dashed line, respectively. A gradual electron transfer from the intramolecular to intermolecular bond is found with increasing pressure.

to 50 kbar, the valence electrons as shown in Fig. 7.12 (b), gradually migrate into the nonbonding region. This bonding feature transformation is substantially enhanced by more compressional perturbation and then a electronic configuration of As atoms with nearly sixfold symmetry is formed in the calculated charge density corresponding to 100 kbar (Fig. 7.12(c)). Consequently, from the structural, vibrational, and electronic data, the mechanism of the pressure-induced molecular-nonmolecular transition of the quasi-molecular solids can be therefore recognised as a continuous isostructural transformation corresponding to a purely electronic deformation without associated crystallographic symmetry breaking. Moreover, this conclusion indicates that anisotropic materials exhibit a variety of novel presure-induced behaviour.

7.3 Vibrational Properties of Liquid Crystals

Form the point view of structure, liquid crystals exhibit an intermediate case between two extremes of homogeneous isotropic liquids and crystalline solids. Like normal isotropic fluids, the liquid crystals show short-range order in most directions and a few degree of long-range orientational or translational order. Thus, liquid crystals characterised by long-range orientational order are highly anisotropic systems.

Conventionally, the anisotropic molecular units are simplified as rigid rods or ellipsoids, *ie.* molecular detail is ignored. Three basic types of liquid crystals can be classified as nematic, cholesteric, and smectic types by different symmetry elements. In Fig. 7.13(a), uniaxial nematics are specified by a molecular arrangement predominately aligned along one special direction, but the molecular centres of gravity have no long-range order. This special orientation of molecular configuration undergoes a helical distorsion in cholesterics (shown in Fig. 7.13(b)). Further, both translational and orientational order in the smectic phase give rise to a layered structure. However, various alignments of molecules within layers correspond to different types of smectics. A simple example of smectic phase, smectic-A, is depicted in Fig. 7.13 (c).

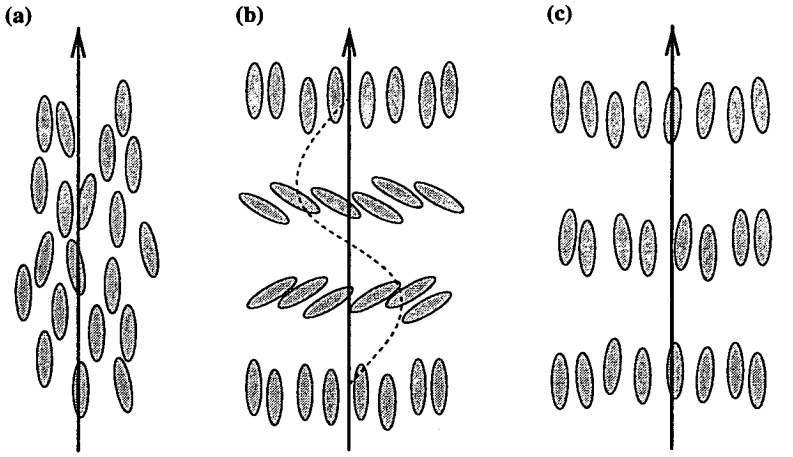

Figure 7.13. The arrangement of molecules for three mesophases of liquid crystals: nematic (a), cholesteric (b), and smectic (c).

Related to the various structures of liquid crystals, vibrational properties of the nematogen and smectogen are comprehensively studied in this section by a combination of high-resolution Raman spectroscopy and *ab-initio* calculations. In such flexible molecular systems, it is possible that the vibrational frequency of some internal modes may be so low as to extend into the external regime. Therefore, in order to determine the possibility of the coupling between internal and external modes and to elucidate the behaviour of vibrational modes near the mesophase transition, the frequency regime of intra- and inter-molecular vibrations of this sufficiently flexible molecular systems is monitored individually with the help of first principles computer simulations. Further, the exploration of a essential vary-low-frequency dynamics of different liquid crystals phases is another main objective of this section.

7.3.1 Structural Flexibility of The Liquid-Crystal Homologous Series of The Cyanobiphenyls (nCB)

The structural requirement for generating the mesophases of liquid crystals is that the object should have a highly anisotropic molecular geometry. Normally, the candidate molecules are small elongated molecules, discoid organic molecules, long helical rods

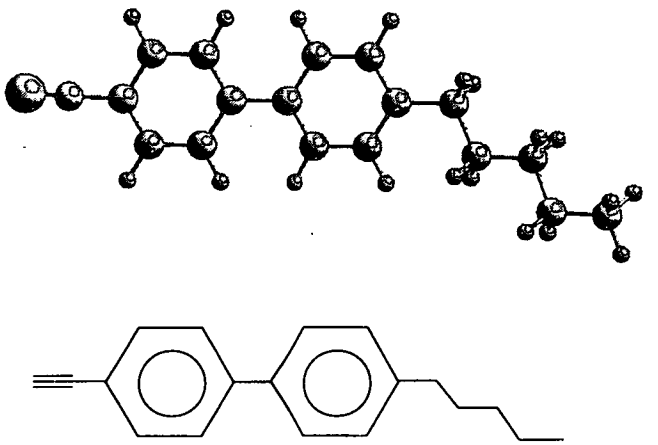

Figure 7.14. Schematic presentation and a simplified expression of a nematic 5CB molecule. The nitrogen, carbon, and hydrogen is denoted as the large, middle, and small sphere, respectively

in a liquid substrate, rigid polymers, or even complex amphiphilic compounds [175]. However, in view of the major commercial requirements of the chemical and photochemical stability, the typical mesogens – cyanobiphenyls (nCB), which is composed of two pheynl (C_6H_6) rings (without any bridge group) and two simple end groups of CN and alkyl chains, are widely used to synthesise liquid crystal (LC) devices [176]. In the whole cyanobiphenyl family, the 4'-pentyl-4-cyanobiphenyl (5CB) containing a short alkyl chain of C_5H_{11} is the lowest weight member to exhibit a nematic phase. Recent deuterium NMR studies [177] and first-principle simulations [178] indicated that a stable nematic 5CB molecule is characterised by a torsion angle between two phenyl rings ($\sim 31°$) and a nearly perpendicular connection between the phenyl ring and the alkyl end. An illustration of the isolated 5CB is shown in Fig. 7.14. Meanwhile, as the lightest member of cyanobiphenyl series which was found in a smectic phase, 4'-octyl-4-cyanobiphenyl (8CB) differs from which of 5CB only in that it contains an 8-membered alkyl tail.

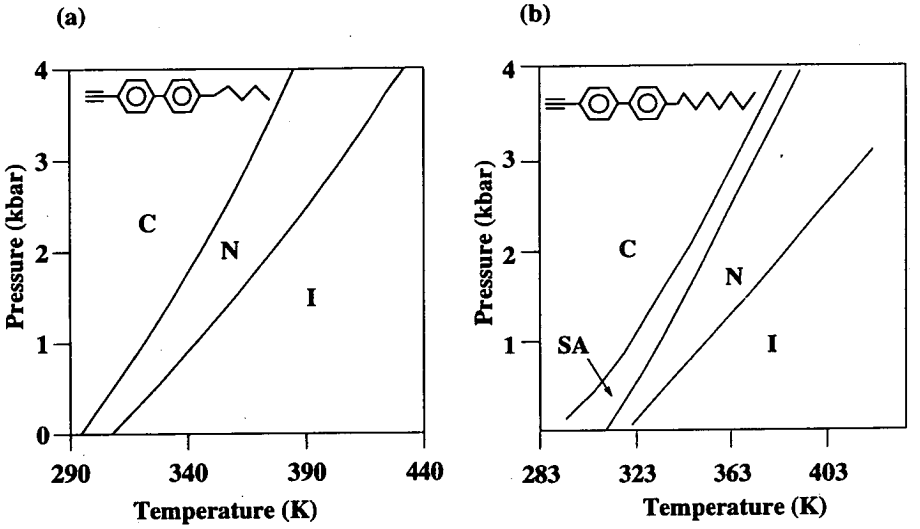

Figure 7.15. Pressure-temperature phase diagram for (a) 5CB [179] and (b) 8CB [181]. The isotropic, nematic, smectic-A, and crystal phase is denoted as I, N, SA, and C, respectively.

According to the long and narrow molecular character, the flexibility of 5CB and 8CB causes an exotic phase behaviour under external fields. The phase diagram of 5CB and 8CB as determined from measurements of refractive indices [179], dielectric constants [180], and transmitted light intensity [181] is summarised in Fig. 7.15 (a) and (b), respectively. Many studies of critical phenomena and order parameter of 5CB and 8CB have also been reported [182, 183, 184, 185, 186]. However, as the typical thermotropic liquid crystals, all liquid crystal phases of 5CB and 8CB can be obtained by varying the external temperature. Under ambient pressure condition, the isotropic-nematic and nematic-crystal transition temperature of 5CB was found respectively at 308 K and 295 K (as shown in Fig. 7.15(a)), and two solid polymorphs with a plate-like and a fine-needle-like crystal structure were observed at 253 K [187]. On the other hand, previous observations [186] suggest the isotropic-nematic, nematic-smectic, and smectic-crystal phase transition of 8CB occurs at 313 K, 307 K, and 294 K, respectively.

7.3.2 Intramolecular Vibrations in Liquid Crystals

At ambient pressure, the lattice dynamics of thermotropic 5CB and 8CB in various phases referred to different temperatures was experimentally investigated using a high-resolution Raman spectroscopy. Concerning about a wide spectral range including the extent very close to the laser line, the extremely good stray light rejection is demanded and an extra high-resolution Raman spectrometer is needed to discriminate the possible mode mixture. According to the fluidity behaviour at ambient temperature, the samples of 5CB (or 8CB) were contained in a sealed capillary which affixed to a copper backing plate for thermal contact. To perform Raman scattering, the 6471 Å line of a Kr^+ laser was used as the exciting light. The laser power at the sample was estimated to be 80 mW. A Coderg T-800 triple-grating spectrometer which provides the high resolution from 1/3 to 1.5 cm^{-1} was employed to collect spectra. The crucial parameter of temperature was controlled by a CTI Cryogenics closed-cycle cryostat and a Lakeshore Cryogenics temperature controller for which temperature control was better than 0.1 K. Spectra were collected in 90^o scattering geometry (see Fig. 2.4.3) using a count-time of 1 second per data point.

In order to elucidate the detail of molecular vibrations, the theoretical calculations of the prototypical nematogen 5CB were implemented using first principles computer simulations [188, 189]. Based on the technique in Sec. 3.2, *ab-initio* density functional theory using non-local pseudopotentials and the generalised-gradient approximation to exchange and correlation was employed to study the vibrational properties of the isolated 5CB after confident tests on several small molecules (C_2H_4 and C_6H_6) [190]. This parameter-free plane wave method for 5CB was carried out on a parallel computer to minimise the electronic energy. To build the dynamical matrix for the 38-atom molecule having no symmetry, 114 displacements are needed to implement. Thus, 108 normal mods plus 3 molecular translations and 3 molecular rotations are generated from the matrix diagonalisation.

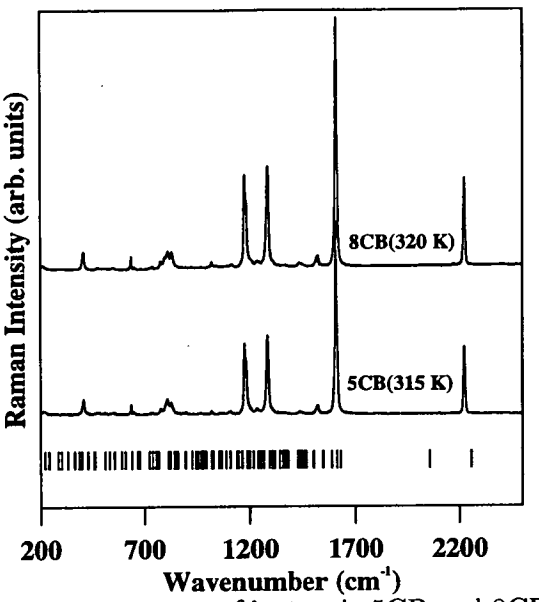

Figure 7.16. Raman spectrum of isotropic 5CB and 8CB within the frequency regime from 200 to 2500 cm^{-1}. The vertical tick marks show the calculated positions of the intramolecular frequency modes for the isolated 5CB molecule.

In view of the structural resemblance of molecular 5CB and 8CB, the overall spectrum of the isotropic phase for these two homologous liquid crystals are expected to be analogous. Excluding the featureless region (0 to 200 cm^{-1}), the spectrum related to isotropic 5CB and 8CB, respectively, is presented in Fig. 7.16 which is mainly contributed from the intramolecular vibrations. Like the Raman spectra of complex organic materials [191], the spectral profile of liquid crystals in high-frequency intramolecular vibrational region is predominated by characteristic frequencies which are strongly related to specific structural components. Without any symmetry inside the isolated molecule of 5CB (or 8CB), all 108 (135 in 8CB) normal modes are both infrared and Raman active. Although the existence of considerable mixing of large number of possible vibrations in this large molecular system will obscure the assignment of each Raman mode, the vibrational detail for the prominent signals still can be identified from the calculated frequencies and eigenvectors indicated in Fig. 7.16. For example, the calculated eigenvector for the mode isolated near 2200 cm^{-1} shows a bond-stretching vibrations of the CN end and a distortion of two pheynl groups (benzene rings) is assigned to the mode situated at 1177 cm^{-1}. A comparison between theoretical predictions

Table 7.5. Calculated and observed Raman mode frequencies of specific intramolecular vibrations in 5CB and 8CB. Experimental temperature for the isotropic 5CB and 8CB is at 315 K and 320 K, respectively. The frequency is in the unit of cm^{-1}. Mode descriptions are determined by calculated eigenvectors.

	5CB		8CB
Mode description	Calc.	Expt.	Expt.
$C \equiv N$ stretch	2255	2223	2223
$C = C$ stretch	1608	1604	1607
$C - H$ deformation (in the alkyl tail)	1302	1284	1284
C_6H_6 bending (mixing with alkyl tail accordions)	1200	1184	1184
C_6H_6 bending	1189	1177	1177

and observations for some particular intramolecular modes determined by calculated eigenvectors is made and listed in Table 7.5.

Further, the intramolecular vibrations as a function of temperature through different phases of 5CB and 8CB are examined and displayed in Fig. 7.17. For 5CB, most Raman signals remain the same frequencies with a slight band sharpening at the isotropic-nematic transition during a cooling procedure. Similar behaviour is also found in 8CB at isotropic-nematic and nematic-smectic transition. This can be attributed to the effects of molecular conformation which suffers more restrain in the more orderly nematic and smectic phase. While the temperature is decreased into the crystal regime, the conformation-constrained effect is more severe and gives rise to a splitting of several broad peaks going with a small frequency shift in both homologs. In addition, new Raman signals were detected in the range of 200 to 500 cm^{-1} and is likely due to the intermolecular dipole-dipole interaction in the crystal structure.

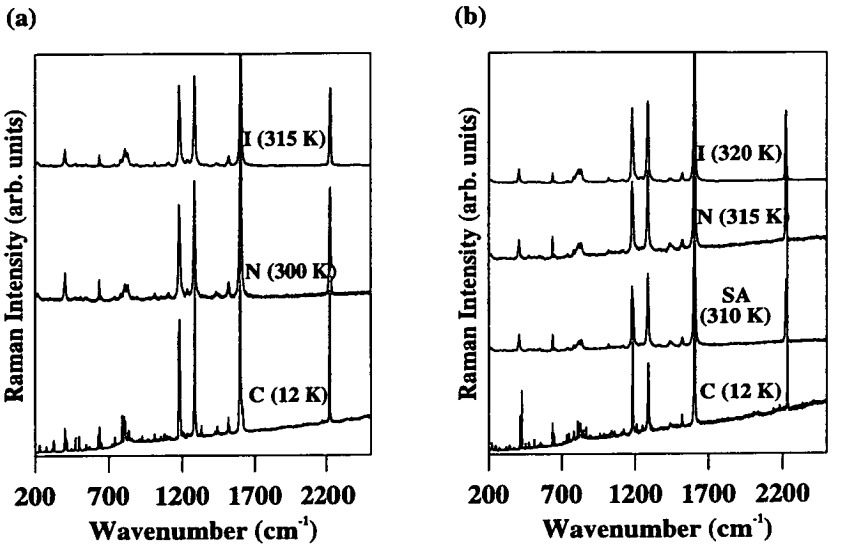

Figure 7.17. Tracing of observed Raman spectra of 5CB (a) and 8CB (b) within the frequency region of 200 to 2500 cm^{-1}. Temperature and corresponding phase is indicated for each spectrum.

7.3.3 Low-Frequency Dynamics of Nematic and Smectic Liquid Crystals

The nature of low-frequency (0 to 200 cm^{-1}) dynamics of the nematogen 5CB is explored using Raman scattering (with a higher resolution of 1 cm^{-1}) across mesomorphic phases at different temperatures. By cooling nematic 5CB from 300 K, three distinct solid phases having discriminative low-frequency features can be observed from different cooling rates. Fig. 7.18(a) shows that extremely rapid cooling procedures produce a glassy solid (G) which is characterised by a flat low-frequency region. Slower cooling results in the formation of two distinct crystalline polymorphs indicated as C_m and C in Fig. 7.18 (b) and (c), respectively, at 270 K. These two distinct spectra may be related to previously observed solid polymorphs of 5CB [187]. On the other hand, the slow heating processes for two solid modifications of 5CB were also performed over the temperature range of 12 K to 315 K. The result of observed low-frequency spectrum shows a gradually broadening of spectral bands while approaching the crystal-nematic transition and exhibits a featureless low-frequency signal in the nematic domain. This

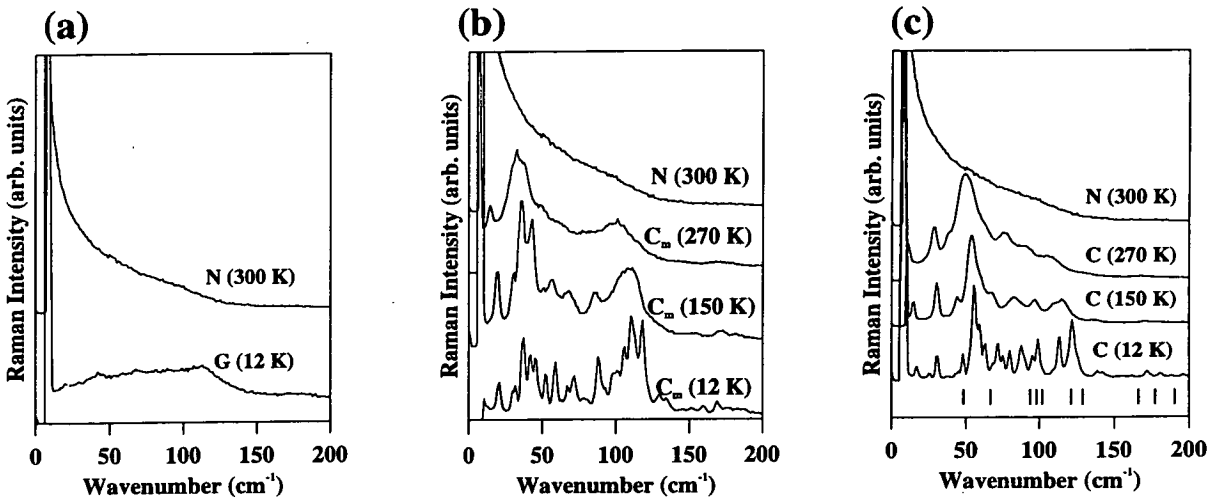

Figure 7.18. Low frequency Raman spectrum of (a) glassy solid (G), (b) metastable solid (C_m), and (c) stable solid (C) which were obtained by cooling nematic 5CB from 300 K in different cooling rates. Calculated eigenvalues for low frequency intramolecular modes are also shown as tick marks in (c) for comparison.

spectral behaviour has also been found in other type of liquid crystals [192]. In addition, it suggests hysteresis in phase behaviour which corresponds to the occurrence of the crystal-nematic transition at 296 K. Moreover, during the warming up procedure, the rearrangement of the crystalline C_m structure in longer time scale gives rise to a structural transformation and favours to another solid phase C. Fig. 7.19 indicates that this complicated thermal perturbed solid structure transition of 5CB takes place at 270 K. Hence, the crystal structure of C_m is recognised as a metastable phase relative to the stable C solid. However, more convincing evidence of this solid polymorphism in 5CB can be obtained from X-ray diffraction measurements.

In order to verify the pretransition effect near crystal-nematic transition which was found initially in the liquid crystal of *p*-Azoxyanisole (PAA) by Bulkin *et al.* [193] who asserted this effect corresponds to a soft-mode-like behaviour, the temperature dependence of the lowest mode of 5CB in the solid C phase is concerned. Considering the mean-field theory of phase transition [194], the square of the frequency as a function

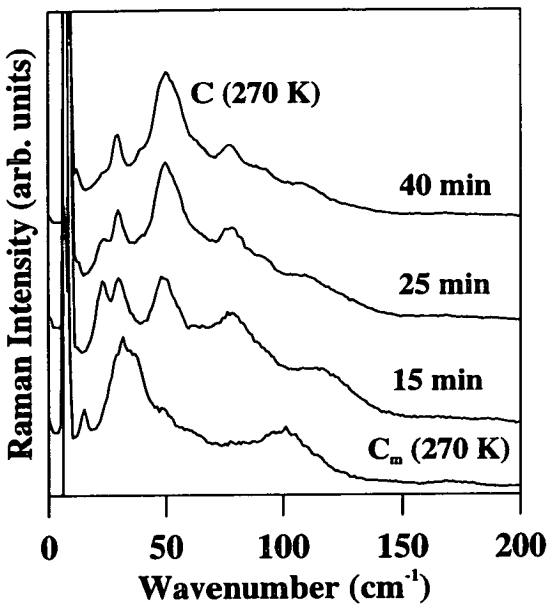

Figure 7.19. Evolution of low-frequency Raman spectrum of 5CB for the transition between two solid polymorphs $C_m \rightarrow C$. The temperature and relaxation time for each spectrum is indicated respectively.

of temperature is shown in Fig. 7.20 and it reveals a mode softening with increasing temperature. However, the crystal-nematic transition of 5CB occurs at a temperature much lower than that at which this low-frequency mode is expected to drop zero. There is no evidence from the observed data of 5CB that the mode softening is linked to the crystal-nematic melting transition as in PAA.

In view of the calculated low frequency modes for the isolated 5CB as determined by diagonalisation of dynamical matrix, Fig. 7.18 (c) manifests the calculated intramolecular mode frequencies overlap the observed low-frequency spectrum over the region 50 to 200 cm^{-1}. Indeed, the calculated eigenvectors of the modes below 100 cm^{-1} show two types of displacement patterns: a long-wavelength transverse vibration along the length of molecule (Fig. 7.21(a))and a molecular conformation with the wagging motion of the alkyl tail (Fig. 7.21(b)). It is concluded that the low frequency Raman spectrum of solid 5CB is composed of mixed inter- and intramolecular vibrations in this material. However, the observed modes with a frequency below 50 cm^{-1} are expected

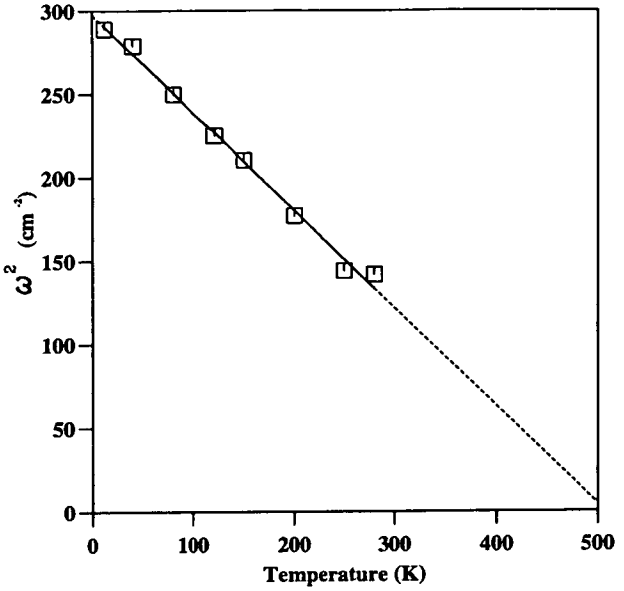

Figure 7.20. Temperature dependence of the square of the lowest frequency mode for the C phase of 5CB. The observed data are denoted as squares and the solid line is a guide of the eye. The dashed line is a linear extrapolation of experimental results. It is clear that the mode frequency is nonzero at melting transition.

to have progressively well-defined lattice vibrational character since no calculated intramolecular modes extend into this frequency regime. Again, the detail assignment of each intermolecular mode can only be obtained from the structural information of the 5CB crystal at low temperature.

Comparing to 5CB, the more significant spectral feature of Octylcyanobiphenyl (8CB) related to the specific smectic-A phase mentioned previously was found. According to the more weaker coupling between smectic layers, the corresponding modes with much lower frequencies than of nematogens is expected and an extreme high-resolution data collection (1/3 cm^{-1}) is therefore necessary. The observed Raman spectra of 8CB during a slow cooling process within even lower frequency regime (3 to 20 cm^{-1}) is shown in Fig. 7.22 (a) at several temperatures. Similar to measurements of 5CB, the spectra recorded in the isotropic and nematic phases of 8CB are also featureless. Continued cooling to the smectic-A phase however, induces a qualitative change in the low-frequency spectrum. Actually, a pronounced broad feature near 9 cm^{-1} is developed in the smectic-A territory. In order to enhance the signal, the overlap of the

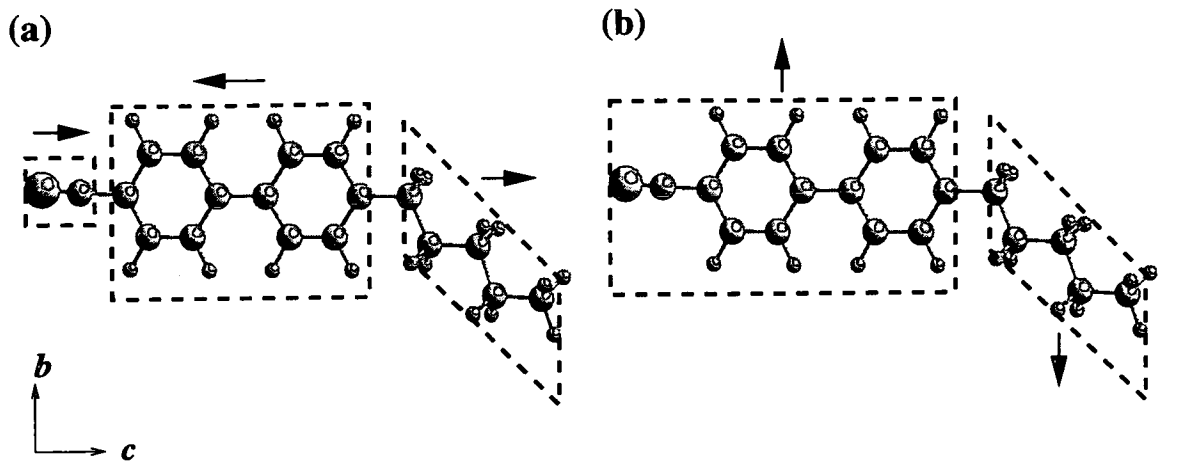

Figure 7.21. Schematic of calculated eigenvectors for two types of low frequency intramolecular modes in an isolated 5CB molecule.

Rayleigh wing was subtracted from the broad band and the result is depicted in Fig. 7.22 (b). This band has a wide width (about 4 cm^{-1}) and vanishes discontinuously at the smectic-A to crystal transition in which the crystal profile of one solid polymorph of 8CB is characterised by a appearance of modes above 20 cm^{-1}. Therefore, this feature can be attributed to a characteristic of the smectic phase and is probably related to the intermolecular cohesion across adjacent layers. Likewise, a similar situation has been observed in another smectic-A compound diethylazoxybenzoate (DEAB) [195] in which a quasi-discontinuous thermal behaviour of a low-frequency (about 14 cm^{-1}) was interpreted as arising from the intermolecular dipole-dipole coupling between adjacent layers.

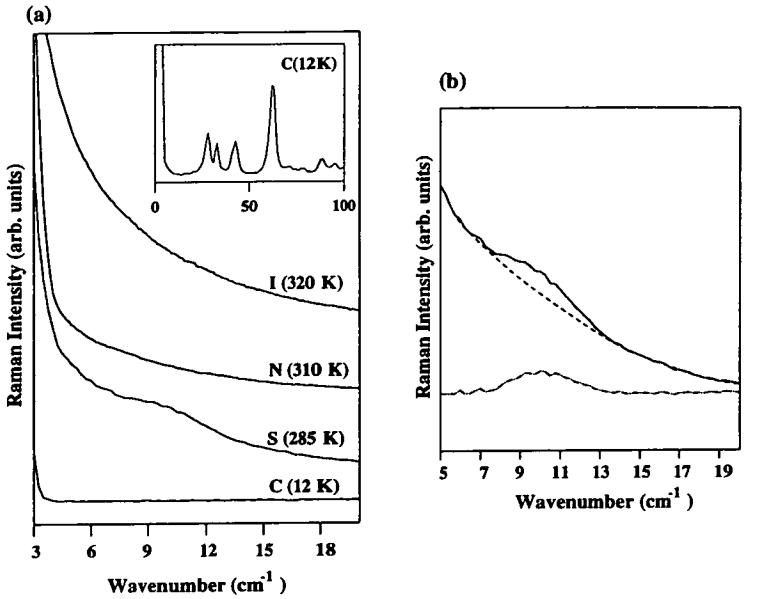

Figure 7.22. Evolution of spectra for different phases at various temperatures is displayed in (a) with an inset of a larger view of the spectrum for the crystalline phase at 12 K. In (b), the broad band of the smectic-A phase (dashed-dotted line) is obtained by subtracting the Rayleight wing (dashed line) from the observed original Raman spectrum (solid line).

7.4 Conclusions and Future Directions

In this chapter, a pressure-induced loss of molecular character in quasi-molecular Group-V metal triiodides has been identified by both structural and vibrational measurements. With the isostructural transition from a molecular solid to a quasi-two-dimensional layered crystal, the loss of molecular identity is attributed to the mechanism of a gradual electron transfer from intramolecular to intermolecular bonds and suppression of sp^3 hybridisation. A distorted puckered layered modification has also been found at modest pressure and which is expected to an intermediate phase before transforming into a three-dimensional network solid under further compression. To probe the subtle electronic behaviour associated with this pressure-induced topological structural transition, both additional high-pressure photoluminescence and first principle simulations give the ability to prove fruitful in further exploring bonding changes in these materials.

Another exciting result came from the studies for low-frequency dynamics of liquid

crystals. It is found that the well-defined internal and external vibrational frequency regimes is blurred in the substantially flexible nematogen 5CB. This strong mixing of inter- and intramolecular vibrational modes is unusual for most molecular solids in which the restoring forces related to lattice modes are well separated from internal vibrations. It is expected that this unique behaviour is particularly common among highly anisotropic large molecular systems. This similarity between inter- and intramolecular force constants implies that molecule shape is strongly coupled to local fields. In addition, a distinct intermolecular mode of smectic 8CB is observed at very low frequency over a temperature range in which no lattice modes are seen. It would be interesting to determine whether atomistic molecular dynamics or monte-carlo simulations of liquid crystals predict that a mode of this type is a generic feature of smectic phases. Also, more insight into the filed of liquid crystals can be provided from Raman spectroscopy under high pressure, or electric, or magnetic field. Furthermore, the detail study of dynamical behaviour in mesophases (such as reorientational dynamics) can be obtained using a new technique of the differential Raman spectroscopy [196] which provide the orientational autocorrelation functions of uniaxial liquid crystals.

Based on the rich pressure effects in anisotropic materials concerned in this thesis, it is fascinating to extend the high-pressure studies into more complicated condensed matter and biomaterials. Indeed, understanding the evolution of physical and chemical properties of condensed phases under compression remains one of the most challenging in modern condensed matter physics and material science. Particularly, after the successful microscopic description of anisotropic materials within this article, it illustrates the vigorous skills combined with recently developed high-pressure techniques, first-principle calculations, and statistical molecular dynamics provides a more powerful tool to probe the most potentially fruitful issues like the static and dynamic properties of complex condensed matters of biological materials.

Bibliography

[1] W. B. Holzaphel. *Rev. Prog. Phys.*, 59:29, 1996.

[2] B. D. Swanson and L. B. Sorensen. *Phys. Rev. Lett.*, 75:3293, 1995.

[3] R. Holyst, D. J. Tweet, and L. B. Sorensen. *Phys. Rev. Lett.*, 75:2153, 1990.

[4] J. Z. Hu, L. D. Merkle, C. S. Menoni, and I. L. Spain. *Phys. Rev. B*, 34:4679, 1986.

[5] J. Crain, G. J. Ackland, and S. J. Clark. *Rep. Prog. Phys.*, 58:705, 1995.

[6] B. A. Weinstein and G. J. Piermarini. *Phys. Rev. B*, 12:1172, 1975.

[7] S. Minomura and H. G. Drickamer. *Phys. Chem. Solids*, 23:451, 1963.

[8] A. W. Lawson and T. Y. Tang. *Rev. Sci. Instrum.*, 21:815, 1950.

[9] P. W. Bridgman. *Collected Experimental Papers.* Harvard University Press, Cambridge MA, 1964.

[10] L. Merrill and W. A. Bassett. *Rev. Sci. Instrum.*, 45:290, 1974.

[11] C. E. Weir, E. R. Lippincott, A. Van Valkenburg, and E. N. Bunting. *J. Res. Natl. Bur. Stand. Sec. A*, 63:55, 1959.

[12] R. M. Hazen and L. W. Finger. *Comparative Crystal Chemistry.* Wiley, New York, 1982.

[13] A. Jayaraman. *Rev. Mod. Phys.*, 55:65, 1983.

[14] S. K. Sharma, H. K. Mao, and P. M. Bell. *Phys. Rev. Lett.*, 44:886, 1980.

[15] R. Boehler. *Nature*, 363:534, 1993.

[16] J. R. Ferraro. *Vibrational Spectroscopy at High External Pressures-The Diamond Anvil Cell.* Academic Press, Inc., Orlando, 1984.

[17] W. F. Sherman and A. A. Stadtmuller. *Experimental Techniques in High-Pressure Research.* Wiley, Chichester, 1987.

[18] G. J. Piermarini, S. Block, and J. S. Barnett. *J. Appl. Phys.*, 44:5377, 1973.

[19] D. H. Liebenberg. *Phys. Lett. A*, 73:74, 1979.

[20] H. K. Mao and P. M. Bell. *Science*, 200:1145, 1978.

[21] G. J. Piermarini, S. Block, and R. A. Forman. *J. Appl. Phys.*, 46:2774, 1975.

[22] A. L. Ruoff. *High Pressure Sci. Technol. AIRAPT Conf. 6th*, 1:754, 1977.

[23] H. K. Mao, P. M. Bell, J. W. Shaner, and D. Steinberg. *High Pressure Sci. Technol. AIRAPT Conf. 6th*, 1:739, 1977.

[24] H. K. Mao, P. M. Bell, J. W. Shaner, and D. Steinberg. *J. Appl. Phys.*, 49:3276, 1978.

[25] Y. R. Shen, T. Gregorian, and W. B. Holzapfel. *High Pressure Res.*, 7:73, 1991.

[26] B. D. Cullity. *Elements of X-ray Diffraction.* Addison-Wesley, Massachusetts, 1978.

[27] R. O. Piltz, M. I. McMahon, J. Crain, P. D. Hatton, R. J. Nelmes, R. J. Cernik, and G. Bushnell-Wye. *Rev. Sci. Instrum.*, 63:700, 1992.

[28] R. J. Nelmes, P. D. Hatton, M. I. McMahon, R. O. Piltz, J. Crain, R. J. Cernik, and G. Bushnell-Wye. *Rev. Sci. Instrum.*, 63:1039, 1992.

[29] J. Crain. *Int. J. Mod. Phys. B*, 7:4555, 1993.

[30] A. Boultif and D. Louër. *J. Appl. Cryst.*, 24:987, 1991.

[31] R. W. G. Wyckoff. *Crystal Structures Vol. I.* Wiley-Interscience, New York, 1963.

[32] H. M. Rietveld. *J. Appl. Cryst.*, 2:65, 1969.

[33] D. J. Bendall, A. N. Fitch, and B. E. F. Bender. *J. Appl. Cryst.*, 16:164, 1983.

[34] D. B. Wiles and R. A. Young. *J. Appl. Cryst.*, 14:149, 1981.

[35] M. M. Hall, V. G. Veeraraghavan, H. Rubin, and P. G. Winchell. *J. Appl. Cryst.*, 10:66, 1977.

[36] J. I. Langford. *J. Appl. Cryst.*, 11:10, 1978.

[37] G. Caglioti, A. Paoletti, and F. P. Ricci. *Nucl. Instrum. Methods*, 35:223, 1958.

[38] G. K. Wertheim, M. A. Butler, K. W. West, and D. N. E. Buchanan. *Rev. Sci. Instrum.*, 11:1369, 1974.

[39] W. A. Dollase. *J. Appl. Cryst.*, 19:267, 1986.

[40] J. I. Langford and D. Louër . *Rep. Prog. Phys.*, 59:131, 1996.

[41] G. Placzek. *Rayleigh-Streuung und Raman-Effect: Handbuch der Radiologie.* E. Marx ed., Leipzig, 1934.

[42] P. Y. Yu and M. Cardona. *Fundamentals of Semiconductors.* Springer, Berlin, 1995.

[43] R. Loudon. *Proc. Roy. Soc. (London)*, page 218, 1963.

[44] J. Twardowski and P. Anzenbacher. *Raman and IR Spectroscopy in Biology and Biochemistry.* Ellis Horwood, Poland, 1994.

[45] H. Balamane, T. Halicioglu, and W. A. Tiller. *Phys. Rev. B*, 46:2250, 1992.

[46] S. J. Clark. *Complex Structures In Tetrahedrally Bonded Semiconductors.* PhD thesis, The University of Edinburgh, 1994.

[47] P. Hohenberg and W. Kohn. *Phys. Rev.*, 136:864B, 1964.

[48] M. Levy. *Proc. Natl. Acad. Sci. USA*, 76:6062, 1979.

[49] E. H. Lieb. *Int. J. Quantum Chem.*, 24:243, 1983.

[50] R. G. Parr and W. Yang. *Density-functional Theory of Atoms and Molecules.* Oxford University Press, Oxford, 1989.

[51] W. Kohn and L. J. Sham. *Phys. Rev.*, 140:1133A, 1965.

[52] D. M. Ceperley and B. J. Alder. *Phys. Rev. Lett.*, 45:566, 1980.

[53] D. C. Langreth and J. P. Perdew. *Phys. Rev. B*, 15:2884, 1977.

[54] R. O. Jones and O. Gunnarsson. *Rev. Mod. Phys.*, 61:689, 1989.

[55] J. D. Perdew, J. A. Chevary, S. H. Vosko, K. A. Jackson, M. R. Pederson, D. J. Singh, and C. Fiolhais. *Phys. Rev. B*, 46:6671, 1992.

[56] J. D. Perdew. Density gradient expansion of the electronic exchange-correlation energy, and its generalization. In E. K. U. Gross and R. M. Dreizler, editors, *Density Functional Theory*, page 51. Plenum Press, 1993.

[57] A. K. Rajagopal. *Adv. Chem. Phys.*, 41:59, 1979.

[58] E. K. U. Gross, C. A. Ullrich, and U. J. Gossmann. Density functional theory of time-dependent systems. In E. K. U. Gross and R. M. Dreizler, editors, *Density Functional Theory*, page 149. Plenum Press, 1993.

[59] Y. Andersson, D. C. Langreth, and B. I. Lundqvist. *Phys. Rev. Lett.*, 76:102, 1996.

[60] N. W. Ashcroft and N. D. Mermin. *Solid State Physics.* Saunders College Publishing, Florida, 1976.

[61] A. Baldereschi. *Phys. Rev. B*, 7:5212, 1973.

[62] D. J. Chadi and M. L. Cohen. *Phys. Rev. B*, 8:5747, 1973.

[63] G. Gilat. *J. Comput. Phys.*, 10:432, 1972.

[64] H. J. Monkhorst and J. D. Pack. *Phys. Rev. B*, 13:5188, 1976.

[65] I. J. Robertson and M. C. Payne. *J. Phys.: Condens. Matter*, 2:8841, 1991.

[66] G. A. Baraff and M. A. Schluter. *Phys. Rev. B*, 19:4965, 1979.

[67] S. Gasiorowicz. *Quantum Physics.* John Wiley and Sons Inc., New York, 2nd edition, 1996.

[68] M. C. Payne, M. P. Teter, D. C. Allen, T. A. Arias, and J. D. Joannopoulos. *Rev. Mod. Phys.*, 64:1045, 1992.

[69] D. R. Hamann, M. Schlüter, and C. Chiang. *Phys. Rev. Lett.*, 43:1494, 1979.

[70] L. Kleinman and D. M. Bylander. *Phys. Rev. Lett.*, 48:1425, 1982.

[71] X. Gonze, P. Kackell, and M. Scheffler. *Phys. Rev. B*, 42:12264, 1990.

[72] E. L. Shirely, D. C. Allen, R. M. Martin, and J. D. Joannopoulos. *Phys. Rev. B*, 40:3652, 1989.

[73] A. M. Rappe, K. M. Rabe, E. Kaxiras, and J. D. Joannopoulos. *Phys. Rev. B*, 41:1227, 1990.

[74] J. S. Lin, A. Qteish, M. C. Payne, and V. Heine. *Phys. Rev. B*, 47:4147, 1993.

[75] M-H. Lee. *Advanced Pseudopotentials.* PhD thesis, The University of Cambridge, 1995.

[76] R. Car and M. Parrinello. *Phys. Rev. Lett.*, 55:2471, 1985.

[77] C. C. Lin and L. A. Segel. *Mathematics Applied to Deterministic Problems in the Natural Sciences.* Macmillan, New York, 1974.

[78] W. H. Press, S. A. Teukolsky, W. T. Vetterling, and B. P. Flannery. *Numerical Recipes in C.* Cambridge University Press, Cambridge, 2nd edition, 1992.

[79] P. E. Gill, W. Murray, and M. H. Wright. *Practical Optimization.* Academic Press, London, 1981.

[80] P. Pulay. *Mol. Phys.*, 17:197, 1969.

[81] G. P. Francis and M. C. Payne. *J. Phys.: Condes. Matter*, 2:4395, 1990.

[82] O. H. Nielsen and R. M. Martin. *Phys. Rev. Lett.*, 50:697, 1983.

[83] M. Parrinello and A. Rahman. *Phys. Rev. Lett.*, 45:1196, 1980.

[84] R. M. Wentzcovitch. *Phys. Rev. B*, 44:2358, 1991.

[85] L. Verlet. *Phys. Rev.*, 159:98, 1967.

[86] H. R. Schober and W. Petry. *Lattice Vibrations*, volume 1, chapter 5. VCH, Weinheim, 1993.

[87] T. Wieting. *Solid State Commun.*, 12:931, 1973.

[88] H. Wendel and R. M. Martin. *Phys. Rev. B*, 19:5251, 1979.

[89] M. T. Yin and M. L. Cohen. *Phys. Rev. Lett.*, 45:1004, 1980.

[90] P. Giannozzi, S. de Gironcoli, P. Pavone, and S. Baroni. *Phys. Rev. B*, 43:7231, 1991.

[91] G. C. Vezzoli. *Phys. Rev. B*, 26:4140, 1982.

[92] E. F. Skelton, A. W. Webb, F. J. Rachford, P. C. Taylor, S. C. Yun, and I. L. Spain. *Phys. Rev. B*, 21:5289, 1980.

[93] Z. Vardeny and O. Brafman. *Phys. Rev. B*, 19:3276, 1979.

[94] H. D. Hochheimer, M. L. Shand, J. E. Potts, R. C. Hanson, and C. T. Walker. *Phys. Rev. B*, 14:4630, 1976.

[95] M. L. Shand, H. D. Hochheimer, M. Krauzman, J. E. Potts, R. C. Hanson, and C. T. Walker. *Phys. Rev. B*, 14:4637, 1976.

[96] A. Blacha, H. Presting, and M. Cradona. *Phys. Status Solidi*, 126:11, 1984.

[97] A. Zunder and M. L. Cohen. *Phys. Rev. B*, 20:1189, 1979.

[98] L. Pauling. *The Nature of the Chemical Bond.* Cornell University Press, Ithaca, 3rd edition, 1960.

[99] J. C. Phillips. *Rev. Mod. Phys.*, 42:317, 1970.

[100] A. García and M. L. Cohen. *Phys. Rev. B*, 47:4215, 1993.

[101] J. R. Chelikowsky. *Phys. Rev. B*, 35:1174, 1987.

[102] J. C. Phillips. *Physics Today*, 23:23, 1970.

[103] A. P. Sutton. *Electronic Structure of Materials.* Oxford University Press Inc., New York, 1993.

[104] M. L. Cohen and J. R. Chelikowsky. *Electronic Structure and Optical Properties of Semiconductors.* Springer-Verlag, Berlin, 1988.

[105] N. R. Serebryanaya, S. V. Popova, and A. P. Rusakov. *Sov. Phys. Solid State*, 17:1843, 1976.

[106] L. Merrill. *J. Phys. Chem. Ref. Data*, 6:1205, 1977.

[107] V. Meisalo and M. Kalliomäki. *High Temp. High Pressure*, 5:663, 1973.

[108] S. Hull and D. Keen. *Phys. Rev. B*, 50:5868, 1994.

[109] R. K. Singh. *Phys. Rep.*, 85:259, 1982.

[110] R. K. Singh and D. C. Gupta. *Phys. Rev. B*, 40:11278, 1989.

[111] H. C. Hsueh, J. R. Maclean, G. Y. Guo, M. H. Lee, S. J. Clark, G. J. Ackland, and J. Crain. *Phys. Rev. B*, 51:12216, 1995.

[112] J. S. Lin, A. Qteish, M. C. Payne, and V. Heine. *Phys. Rev. B*, 47:4174, 1993.

[113] M. H. Lee, J. S. Lin, M. C. Payne, V. Heine, V. Milman, and S. Crampin. (unpublished).

[114] M. H. Lee. (private communication).

[115] J. P. Perdew and A. Zunger. *Phys. Rev. B*, 23:5048, 1981.

[116] D. M. Cepperley and D. J. Alder. *Phys. Rev. Lett.*, 45:1814, 1980.

[117] A. Blacha, N. E. Christensen, and M. Cardona. *Phys. Rev. B*, 33:2413, 1986.

[118] J. M. Besson, J. P. Itié, A. Polian, G. Weill, J. L. Mansot, and J. Gonzolez. *Phys. Rev. B*, 44:4214, 1991.

[119] E. Rapoport and C. W. F. T. Pistorious. *Phys. Rev.*, 172:838, 1968.

[120] K. Reimann and St. Rübenacke. *Phys. Rev. B*, 49:11021, 1994.

[121] S. Ves, D. Glötzel, M. Cardona, and H. Overhof. *Phys. Rev. B*, 24:3073, 1981.

[122] H. Müller, S. Ves, H. D. Hochheimer, and M. Cardona. *Phys. Rev. B*, 22:1052, 1980.

[123] B. Batlogg, J. P. Remeika, and R. G. Maines. *Solid State Commun.*, 38:83, 1981.

[124] W. A. Harrison. *Electronic Structure and the Properties of Solids.* Freeman, San Francisco, 1980.

[125] J. Crain. *Int. J. Mod. Phy. B*, 7:4555, 1993.

[126] A. Okazaki. *J. Phys. Soc. Jpn.*, 13:1151, 1958.

[127] W. H. Zachariasen. *Phys. Rev.*, 40:917, 1932.

[128] J. R. Chelikowsky and J. C. Phillips. *Phys. Rev. B*, 17:2453, 1978.

[129] P. B. Littlewood. *J. Phys. C: Solid St. Phys.*, 13:4855, 1980.

[130] H. C. Hsueh, M. C. Warren, H. Vass, G. J. Ackland, S. J. Clark, and J. Crain. *Phys. Rev. B*, 53:14806, 1996.

[131] H. C. Hsueh, H. Vass, S. J. Clark, G. J. Ackland, and J. Crain. *Phys. Rev. B*, 51:16750, 1995.

[132] N. G. Wright. *Ph.D. thesis.* The University of Edinburgh, Edinburgh, 1994.

[133] Y. Ishihara, Y. Ohno, and I. Nakada. *Phys. Status Solidi B*, 121:407, 1984.

[134] T. Grandke and L. Ley. *Phys. Rev. B*, 16:832, 1977.

[135] Ralph W. G. Wyckoff. *Crystal Structures.* 2nd ed., vol.1, 1963.

[136] J. P. Perdew and A. Zunger. *Phys. Rev. B*, 23:5048, 1981.

[137] Y. Fujii, K. Kitamura, A. Onodera, and Y. Yamada. *Solid State Commun.*, 49:135, 1984.

[138] F. D. Birch. *J. Geophys. Res.*, 91:4949, 1986.

[139] T. Chattopadhyay, A. Werner, and H. G. von Schnering. In C. Homan, R. K. MacCrone, and E. Whalley, editors, *Materials Research Society Symposia*

Proceedings, volume 22, page 93, Pittsburg, 1984. Elsevier Science Publishing Co.

[140] K. L. Bhatia, G. Parthasarathy, D. P. Gosain, and E. S. R. Gopal. *Phys. Rev. B*, 33:1492, 1986.

[141] T. Grandke and L. Ley. *Phys. Rev. B*, 16:832, 1977.

[142] R. B. Shalvoy, G. B. Fisher, and P. J. Stiles. *Phys. Rev. B*, 15:2021, 1977.

[143] E. P. O'Reilly. *J. Phys. C : Solid State Phys.*, 15:1449, 1982.

[144] J. D. Wiley, W. J. Buckel, and R. L. Schmidt. *Phys. Rev. B*, 13:2489, 1976.

[145] G. Valiukonis, F. M. Gashimzade, D. A. Guseinova, G. Krivaite, A. M. Kulibekov, G. S. Orrudzhev, and A. Sileika. *Phys. Stat. Sol. (b)*, 117:81, 1983.

[146] J. P. Elliott and D. G. Dawber. *Symmetry in Physics*, volume 1. The MacMillan Press Ltd., London, 1979.

[147] E. B. Wilson, J. C. Decius, and P. C. Cross. *Molecular Vibrations.* McGraw-Hill, New York, 1955.

[148] Norman F. M. Henry and Kathleen Lonsdale. *International Tables for X-ray Crystallography Vol. I : Symmetry Groups.* The Kynoch Press, Birmingham, 1952.

[149] William G. Fateley, Francis R. Dollish, Neil T. McDevitt, and Freeman F. Bentley. *Infrared and Raman Selection Rules for Molecular and Lattice Vibrations : The Correlation Method.* Wiley-Interscience, New York, 1972.

[150] H. R. Chandrasekhar and U. Zwick. *Solid State Commun.*, 18:1509, 1976.

[151] V. Vorlíček, I. Gergora, and D. Chvostová. *Phys. Stat. Sol. (b)*, 116:639, 1983.

[152] T. Fukunaga, S. Sugai, T. Kinosada, and K. Murase. *Solid State Commun.*, 38:1049, 1981.

[153] E. A. Wood. *Bell Syst. Technol. J.*, 43:541, 1964.

[154] R. Zallen, M. L. Slade, and A. T. Ward. *Phys. Rev. B*, 3:4257, 1971.

[155] J. L. Verble and T. J. Wieting. *Phys. Rev. Letters*, 25:362, 1970.

[156] H. R. Chandrasekhar, R. G. Hymphreys, U. Zwick, and M. Cardona. *Phys. Rev. B*, 15:2177, 1977.

[157] J. D. Wright. *Molecular crystals.* Cambridge University Press, Cambridge, 1995.

[158] R. Zallen and M. L. Slade. *Phys. Rev. B*, 9:1627, 1974.

[159] R. Zallen. *Phys. Rev. B*, 9:4485, 1974.

[160] A. Weinstein and R. Zallen. *Light Scatterings in Solids*, volume IV, chapter 8. Springer Velerg, Berlin, 1984.

[161] S. Sugai and T. Ueda. *Phys. Rev. B*, 26:6554, 1982.

[162] J. M. Besson, J. Cernogora, and R. Zallen. *Phys. Rev. B*, 22:3866, 1980.

[163] S. S. Mitra, O. Brafman, W. B. Daniels, and R. K. Crawford. *Phys. Rev.*, 186:942, 1969.

[164] F. Cerdeira, C. J. Buchenauer, Fred H. Pollak, and Manuel. Cardona. *Phys. Rev. B*, 5:580, 1972.

[165] H. R. Chandrasekhar, R. G. Humphreys, and M. Cardona. *Phys. Rev. B*, 16:2981, 1977.

[166] J. Trotter and T. Zobel. *Z. Krist.*, 123:67, 1966.

[167] H. C. Hsueh, W. C. Poon, V. Hugh, and J. Crain. *Europhys. Lett.*, 35:689, 1996.

[168] A. Anderson, J. A. Campbell, and R. W. G. Syme. *J. Raman Spectrosc.*, 19:379, 1988.

[169] T. Komatsu, T. Karasawa, T. Iida, K. Miyata, and Y. Kaifu. *J. Lumin.*, 24.

[170] W. Kiefer, R. G. Humphreys, and M. Cardona. *Z. Naturforsch., Teil A*, 25:1101, 1970.

[171] A. Anderson and J. A. Campbell. *Phys. Stat. Sol. (b)*, 163:527, 1991.

[172] E. A. Marseglia and W. C. K. Poon. *Molecular Systems Under High Pressure.* Elsevier Science Publisher B. V., North-Holland, 1991.

[173] M. Schlüter, M. L. Cohen, S. E. Kohn, and C. Y, Fong. *Phys. Stat. Sol. (b)*, 78:737, 1976.

[174] M. Schlüter and M. L. Cohen. *Phys. Rev. B*, 14:424, 1976.

[175] P. G. de Gennes and J. Prost. *The Physics of Liquid Crystals.* Oxford University Press, Oxford, 2nd edition, 1993.

[176] M. G. Clark, K. J. Harrison, and E. P. Raynes. *Phys. Technol.*, 11:232, 1980.

[177] S. Sinton and A. Pines. *Chem. Phys. Lett.*, 76:263, 1980.

[178] S. J. Clark, C. J. Adam, G. J. Ackland, and J. Crain. *Mol. Cryst. Liq. Cryst.*, 1996. (submitted).

[179] R. G. Horn. *J. Physique*, 39:167, 1978.

[180] H. -G. Kreul, S. Urban, and A. Würflinger. *Phys. Rev. A*, 45:8624, 1992.

[181] P. E. Cladis, R. K. Bogardus, and D. Aadsen. *Phys. Rev. A*, 18:2292, 1978.

[182] D. Davidov, C. R. Safinya, M. Kaplan, S. S. Dana, R. Schaetzing, R. J. Birgeneau, and J. D. Litster. *Phys. Rev. B*, 19:1657, 1979.

[183] G. B. Kasting, C. W. Garland, and K. J. Lushington. *J. Physique*, 41:879, 1980.

[184] H. Yoshida, Y. Nakajima, S. Kobinata, and S. Maeda. *J. Phys. Soc. Jpn.*, 50:3525, 1981.

[185] J. Thoen, H. Marynissen, and W. Van Dael. *Phys. Rev. A*, 26:2886, 1982.

[186] F. Scudieri, M. Marinelli, U. Zammit, and S. Martellucci. *J. Phys. D: Appl. Phys.*, 20:1045, 1987.

[187] T. Hanemann, W. Haase, I. Svoboda, and H. Fuess. *Liq. Cryst.*, 19:699, 1995.

[188] H. C. Hsueh, H. Vass, F. N. Pu, S, J. Clark, W. C. K. Poon, and J. Crain. *Europhys. Lett.*, 1996. (submitted).

[189] S. J. Clark, C. J. Adam, H. C. Hsueh, F. N. Pu, and J. Crain. *Mol. Crsyst. Liq. Cryst.*, 1996. (submitted).

[190] S. J. Clark, C. J. Adam, G. J. Ackland, J. White, and J. Crain. *Liq. Cryst.*, 1996. (accepted).

[191] P. R. Carey. *Biochemical Applications of Raman and Resonance Raman Spectroscopies.* Academic Press, New York, 1982.

[192] W. J. Borer, S. S. Mitra, and C. W. Brown. *Phys. Rev. Lett.*, 27:379, 1971.

[193] B. J. Bulkin and F. T. Prochaska. *J. Chem. Phys.*, 54:635, 1971.

[194] P. M. Chaikin and T. C. Lubensky. *Principles of condensed matter physics.* Cambridge University Press, Cambridge, 1995.

[195] N. M. Amer and Y. R. Shen. *Solid State Commun.*, 12:263, 1973.

[196] S. Ye. Yakovenko, A. A. Minko, B. Arnscheidt, and J. Pelzl. *Liq. Cryst.*, 19:449, 1995.